



EXCITED STATE DYNAMICS OF EMISSIVE ORGANIC MATERIALS: SINGLET-TRIPLET TRANSITIONS AND OLED DEVICE INTEGRATION

Inaugural-Dissertation

Zur Erlangung des Doktorgrades
der Mathematisch-Naturwissenschaftlichen Fakultät
der Universität zu Köln

vorgelegt von

Elisabeth Pankert

angenommen im Jahr 2025

Begutachtung: Prof. Dr. K. Meerholz
Prof. Dr. A. Griesbeck

Die experimentellen Untersuchungen für die vorliegende Arbeit wurden von April 2021 bis Dezember 2024 im Institut für physikalische Chemie (Institut für Licht und Materialien) der Universität zu Köln unter Anleitung von Prof. Dr. Klaus Meerholz durchgeführt.

Abstract

The development of organic light-emitting diodes (OLEDs) has revolutionized display technology, driven by their high efficiency, flexibility, and superior color quality. A critical challenge in OLED technology is the efficient utilization of triplet excitons, which make up 75% of the excitons generated during charge recombination. Traditional fluorescent OLEDs harness only singlet excitons, limiting their internal quantum efficiency (IQE) to 25%. The introduction of phosphorescent OLEDs, utilizing heavy-metal complexes, e.g. containing iridium, overcame this limitation by enabling triplet exciton emission through strong spin-orbit coupling, achieving near 100% IQE. However, the high cost and limited availability of heavy metals have driven research into alternative mechanisms, including thermally activated delayed fluorescence (TADF) and hybridized locally and charge-transfer (HLCT) excitons that can undergo reverse intersystem crossing (rISC) from higher lying triplet states.

This thesis investigates a range of organic photoluminescent molecules, focusing on their underlying photophysical mechanisms and integration into OLEDs. A combination of steady-state and time-resolved spectroscopy across varying temperatures is employed to analyze these materials.

In the first part a donor-acceptor (D-A) molecules with HLCT character is studied, achieving high photoluminescence quantum yield (PLQY) and the emitter is successfully implemented in an OLED. By studying the excited states in varying environment the relaxation behavior of the compound is unraveled. The second part covers the systematic investigation of D-A molecules incorporating an *N*-phenyl-phthalimide acceptor with varying carbazole-based donors. The effects of donor modifications on the photophysics, particularly TADF behavior, are explored, emphasizing the interplay between molecular structure and TADF efficiency in OLEDs. Part three offers the exploration of a fluorinated acridone derivative demonstrating rISC from the T_2 to the S_1 state. A concept was developed to apply the mechanism in an OLED, showing promising potential for successful implementation. In the fourth part investigations into a D-A TADF emitter with chiral substituent are presented for potential application in a circularly polarised OLED (CP-OLED).

By systematically correlating molecular photophysics with OLED device performance, this work highlights the potential of TADF and related mechanisms as sustainable, cost-effective alternatives to phosphorescent emitters. These findings contribute to the design principles of next-generation OLED technologies.

Kurzzusammenfassung

Die Entwicklung von organischen Leuchtdioden (OLEDs) hat die Displaytechnologie revolutioniert, angetrieben durch ihre hohe Effizienz, Flexibilität und überlegene Farbwiedergabe. Eine zentrale Herausforderung in der OLED-Technologie ist die effiziente Nutzung von Triplett-Exzitonen, die 75% der Exzitonen ausmachen, die während der Ladungsrekombination erzeugt werden. Traditionelle fluoreszierende OLEDs nutzen nur Singulett-Exzitone, wodurch ihre interne Quanteneffizienz (IQE) auf 25% begrenzt ist. Die Einführung von phosphoreszierenden OLEDs, die Metallkomplexe z.B. auf Iridium Basis verwenden, überwinden diese Einschränkung, indem sie durch starke Spin-Bahn-Kopplung die Emission von Triplett-Exzitonen ermöglichen und eine nahezu 100% IQE erreichen. Allerdings haben die hohen Kosten und die begrenzte Verfügbarkeit von Schwermetallen die Forschung nach alternativen Mechanismen vorangetrieben, darunter thermisch aktivierte verzögerte Fluoreszenz (TADF) und hybridisierte lokal angeregte und Ladungstransfer (HLCT) Exzitonen, die durch reverse intersystem crossing (rISC) von höher liegenden Triplett-Zuständen übergehen können.

Diese Arbeit untersucht eine Reihe von organischen photolumineszenten Molekülen und konzentriert sich auf ihre zugrunde liegenden photophysikalischen Mechanismen und ihre Integration in OLEDs. Eine Kombination aus stationärer und zeitaufgelöster Spektroskopie über verschiedene Temperaturen hinweg wird verwendet, um diese Materialien zu analysieren.

Im ersten Teil wird ein Donor-Akzeptor Molekül (D-A) mit HLCT-Charakter untersucht, das eine hohe Quantenausbeute der Photolumineszenz (PLQY) erreicht und erfolgreich in eine OLED integriert wird. Durch die Untersuchung der angeregten Zustände in verschiedenen Umgebungen wird das Relaxationsverhalten der Verbindung aufgedeckt. Der zweite Teil behandelt die systematische Untersuchung von D-A-Molekülen, die einen *N*-phenyl-phthalimid-Akzeptor mit unterschiedlichen carbazolbasierten Donoren kombinieren. Die Auswirkungen von Donormodifikationen auf die Photophysik, insbesondere das TADF-Verhalten, werden untersucht, wobei das Zusammenspiel zwischen molekularer Struktur und TADF-Effizienz in OLEDs im Vordergrund steht. Teil drei bietet die Untersuchung

eines fluorierten Acridon-Derivats, das rISC vom T_2 -Zustand zum S_1 -Zustand zeigt. Ein Konzept wurde entwickelt, um diesen Mechanismus in einer OLED anzuwenden, was vielversprechendes Potenzial für eine erfolgreiche Implementierung zeigt. Im vierten Teil werden Untersuchungen zu einem D-A TADF-Emitter mit chiralen Substituenten für eine potenzielle Anwendung in einer CP-OLED vorgestellt.

Durch die systematische Korrelation der molekularen Photophysik mit der OLED Effizienz hebt diese Arbeit das Potenzial von TADF und verwandten Mechanismen als nachhaltige, kostengünstige Alternativen zu phosphoreszierenden Emittern hervor. Diese Ergebnisse tragen zu den Designprinzipien der nächsten Generation von OLED-Technologien bei.

Contents

1	Introduction	1
2	Motivation	4
3	Theoretical Background	6
3.1	Organic Semiconductors	7
3.2	Organic Light-Emitting Diodes	10
3.3	Charge Injection	12
3.4	Charge Transport	16
3.5	Exciton Formation	18
3.6	Photophysical Processes in OLEDs	21
3.6.1	<i>Franck-Condon</i> Principle	22
3.6.2	Photophysical Processes	22
3.6.3	<i>Kasha's</i> Rule	24
3.6.4	Thermally Activated Delayed Fluorescence (TADF)	24
3.6.5	Energy Transfer Processes	26
3.7	Light Outcoupling	30
3.8	Multi-Layer OLED	32
3.8.1	Substrate	33
3.8.2	Anode	33
3.8.3	Hole Injection Layer (HIL)	33
3.8.4	Hole transport layer (HTL)	34
3.8.5	Emissive Layer (EML)	35
3.8.6	Electron Transport Layer (ETL)	38
3.8.7	Electron Injection Layer (EIL) and Cathode	38
3.9	OLED Processing Techniques	39
3.9.1	Vacuum Thermal Evaporation (VTE)	39
3.9.2	Solution Processing	40

4	Comprehensive Investigation of a HLCT Emitter: Spectroscopic Insights and Photophysical Properties of a Highly Luminescent Blue Chromophore	41
4.1	Publication - Highly Luminescent Blue Emitter with Balanced Hybridized Locally and Charge-Transfer Excited-States Emission	44
4.2	Environmental and Temperature-Dependent Relaxation Effects on Photoluminescence	51
4.2.1	Solvatochromic Effects on Fluorescence	53
4.2.2	Vibronic Effects in Low Temperature Phosphorescence	57
4.2.3	Summary	59
5	Impact of Donor Variation on the Singlet-Triplet Energy Gap and the TADF Process in Donor-Acceptor Emitters	61
5.1	Photophysical Properties	65
5.2	Time-resolved Spectroscopy	67
5.3	Energy Levels and Thermal Properties	74
5.4	Application as Emitters in OLEDs	76
5.5	Summary	80
6	Exploring the HIGHrISC Process of NMArF in OLED Applications	82
6.1	Photophysical Properties	85
6.2	Energy Levels and Thermal Properties	88
6.3	OLED Device Optimization	88
6.4	Summary	91
7	Analysis of TADF Characteristics in a Chiral Donor-Acceptor Emitter	92
7.1	Photophysical Properties	94
7.2	Time-resolved PL in mCBP	97
7.3	Energy Levels and Thermal Properties	100
7.4	Application as Emitters in OLEDs	101
7.5	Summary	103
8	Conclusion and Outlook	105
9	Experimental Part	112
9.1	Material Characterization	113
9.2	Sample Preparation	115
9.3	OLED Characterization	117

9.4 Overview of Used Materials	118
10 Appendix	124
10.1 List of Abbreviations	125
10.2 Supplementary Data	129
10.2.1 Supporting Information for 4.1	129
10.2.2 Supplementary Data for Chapter 5	155
10.2.3 Supplementary Data for Chapter 6	196
10.2.4 Supplementary Data for Chapter 7	197
11 Bibliography	204

1 Introduction

The development of OLEDs has transformed the fields of display technology and solid-state lighting, offering high efficiency, flexibility, and color quality. The journey toward modern OLEDs began in the mid-20th century with groundbreaking discoveries that laid the foundation for this rapidly evolving field.

The earliest observations of organic electroluminescence date back to the work of *Bernanose* et al. at the University of Strasbourg in 1953. They demonstrated that thin films of organic materials could emit light when exposed to high alternating electric fields. Although the efficiency of the light emission was low, this groundbreaking discovery marked the first step in exploring electroluminescent properties in organic compounds.^[1]

In the 1980s, *Tang* and *VanSlyke* at *Kodak* achieved a major breakthrough by developing the first high-efficiency organic light-emitting diode. Their device employed a bilayer structure of small organic molecules, which significantly improved the charge injection and recombination efficiency, resulting in a bright and stable electroluminescence output. This invention provided the conceptual framework for the OLEDs we recognize today.^[2] Further advancements were made in 1990 with the work of *Burroughes* et al., who introduced the concept of polymer-based OLEDs. Their discovery of electroluminescence in conjugated polymers like poly(*p*-phenylene vinylene) opened new possibilities for solution-processable, large-area, and flexible devices.^[3]

While these early devices relied on fluorescence, they faced a fundamental limitation imposed by spin statistics. In OLEDs, charge recombination generates excitons, which are bound electron-hole pairs. Due to quantum mechanical spin rules, 25% of these excitons are singlet excitons, which can emit light via fluorescence, while the remaining 75% are triplet excitons, which are typically non-radiative in fluorescent materials. This inefficiency prompted a search for ways to harness the energy of triplet excitons.

The introduction of phosphorescent OLEDs addressed this challenge. By incorporating heavy-metal complexes such as iridium or platinum, which enable strong spin-orbit coupling, triplet excitons could be converted into emissive states, boosting IQE to nearly 100%.^[4-6]

More recently, the development of thermally activated delayed fluorescence (TADF) has emerged as a promising strategy to utilize triplet excitons without relying on rare and expensive heavy metals. TADF materials facilitate reverse intersystem crossing (rISC) to up-convert triplet excitons into singlet states, enabling efficient delayed fluorescence. This approach is particularly appealing for cost-effective, sustainable OLED manufacturing.^[7-9] Despite the significant progress achieved with TADF materials, ongoing research in this field remains crucial due to several challenges. While TADF enables efficient use of triplet

excitons without relying on expensive heavy metals, the performance of TADF emitters in terms of color purity, operational stability, and device efficiency under high brightness conditions still requires improvement. The quest for better host materials, finely tuned molecular structures, and a deeper understanding of the mechanisms driving rISC are crucial in addressing these limitations.

Beyond TADF, other emerging mechanisms such as hybridized locally and charge-transfer (HLCT) materials and hot exciton (HE) emission offer complementary approaches to achieving high-efficiency OLEDs. HLCT combines the advantages of locally excited (LE) and charge-transfer (CT) states, providing both high radiative decay rates and excellent color purity. This mechanism is particularly promising for blue emitters, a critical challenge in OLED technology. Similarly, HE materials utilize high-energy triplet states to bypass spin statistics constraints, enabling efficient direct singlet exciton formation and light emission.

Moreover, fundamental research into the underlying mechanisms deepens the understanding of exciton dynamics in organic semiconductors. It also lays the groundwork for breakthroughs that could expand OLED applications beyond displays and lighting into areas such as biosensing, photomedicine, and flexible electronics.

2 Motivation

This thesis investigates various organic photoluminescent molecules, focusing on the underlying mechanisms of the photoluminescence (PL). To this end, a combination of steady-state and time-resolved spectroscopic techniques at different temperatures is utilized. Furthermore, these emitters are integrated into OLEDs, and the devices are characterized to assess their performance. This work is structured as follows:

Chapter 3 provides an overview of the scientific background, presenting key aspects of OLEDs and the photophysical processes that underlie their operation. This chapter also establishes the theoretical context for the studies conducted in subsequent chapters.

Chapter 4 part offers a comprehensive study of a donor-acceptor (D-A) molecule, functioning as an HLCT emitter with a singlet excited state exhibiting a balanced locally excited (LE) and charge-transfer (CT) character. This molecule demonstrates an exceptionally high photoluminescence quantum yield (PLQY) close to 100%. Solvatochromic effects are explored and compared with quantum chemical calculations, and the emitter's performance in an OLED is evaluated. The solvatochromic behavior is further investigated with regard to the relaxation behavior of the excited molecule at different temperatures aiming to provide deeper insights into the molecule's photophysical behavior.

Chapter 5 presents a study of a series of D-A molecules, all incorporating an *N*-phenylphthalimide acceptor with structurally varied carbazole-based donors. The influence of donor modifications on the photophysics and PL mechanism is systematically analyzed, and their efficiency in OLEDs is evaluated.

Chapter 6 explores a fluorinated acridone derivative previously reported in the literature for its HIGHrISC mechanism, which involves rISC from a higher excited triplet state. The molecule is investigated in an OLED, and its efficiency is systematically assessed.

Chapter 7 investigates a phenazine-based D-A molecule with a chiral side group for its potential TADF behavior, motivated by similar molecules that exhibit TADF properties. The findings are compared with a known A-D-A molecule from the literature. Additionally, the chiral aspect is investigated to evaluate the potential for application in circularly polarised OLEDs (CP-OLEDs).

Chapter 8 summarizes the key findings of this thesis and provides a critical discussion of the results, along with an outlook on potential future research directions.

Chapter 9 contains all relevant experimental details, including characterization methods, and measurement protocols, ensuring the reproducibility of the results.

Overall, by systematically combining photophysical investigations with OLED device studies, this thesis aims to generate a deeper understanding of the design principles for efficient organic emitters and their integration into next-generation OLED technologies.

3 Theoretical Background

3.1 Organic Semiconductors

Semiconductors are materials with electrical conductivity between that of conductors (like metals) and insulators (like glass). A distinction can be made between inorganic and organic semiconductors.

In inorganic semiconductors, energy bands are formed by the interaction and overlap of atomic orbitals in a solid, creating closely spaced energy levels separated by a small bandgap. This small bandgap enables controlled charge transport, distinguishing semiconductors from metals with overlapping bands and no bandgap, and from insulators with a large bandgap that prevents charge flow. Commonly used semiconductors include silicon, germanium or GaAs and GaN.^[10] The conductivity of inorganic semiconductors can be controlled by doping (adding impurities) and factors like temperature or electric fields, leading to intrinsic conductivity. At room temperature, free charges can be generated through thermal excitation from the valence band to the conduction band.

Organic semiconductors are solid materials composed of π -bonded molecules or polymers primarily made of carbon and hydrogen atoms, sometimes including heteroatoms like nitrogen, sulfur, and oxygen. These materials exhibit typical semiconductor properties such as light absorption and emission in the visible spectrum and sufficient conductivity for devices like OLEDs, solar cells, and field-effect transistors (FETs).

In contrast to their inorganic counterparts, organic semiconductors rely on extrinsic conductivity, resulting from charge injection at electrodes, doping, or the dissociation of photogenerated electron-hole pairs. This difference is due to their lower dielectric constant, which makes Coulomb interactions between electrons and holes significant, binding them with energies of about 0.5–1.0 eV.^[10]

Unlike inorganic semiconductors, organic semiconductors are composed of carbon-based molecules. Neighboring carbon atoms (and hetero-atoms) in these molecules are bonded through σ - and π -orbitals (s. Fig. 3.1 a). Usually the bonding π -orbital and the antibonding π^* -orbital form the **highest occupied molecular orbital (HOMO)** and **lowest unoccupied molecular orbital (LUMO)** respectively.

The semiconducting properties of organic molecules are primarily governed by the HOMO and the LUMO. The energy gap between the HOMO and LUMO serves as the organic counterpart to the band gap in inorganic semiconductors. In inorganic materials, the band gap is the energy difference between the valence band (occupied by electrons) and the conduction band (where electrons can move freely). Similarly, in organic semiconductors, the HOMO can be thought of as analogous to the valence band, while the LUMO

corresponds to the conduction band. When an electron is excited from the HOMO to the LUMO, it can move freely, contributing to the electrical conductivity of the material. This process is essential for applications such as OLEDs, organic solar cells, and organic field-effect transistors (OFETs).

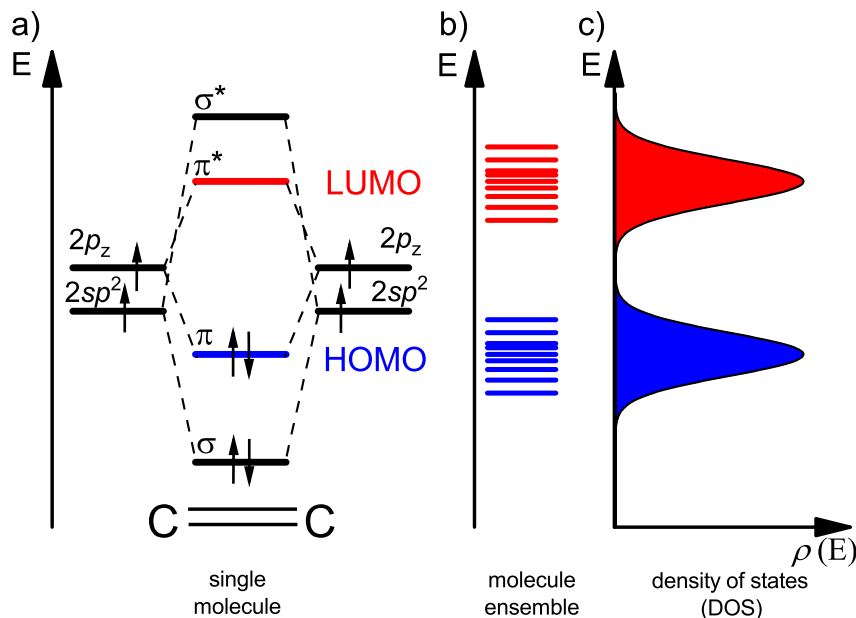


Figure 3.1: a) Bonding (σ and π) and anti-bonding (σ^* and π^*) orbitals in a carbon-carbon double bond with π -orbital being the HOMO and π^* the LUMO (redrawn and modified from^[10]). b) Energetic disorder in molecule ensembles result in small variations in HOMO and LUMO energies. c) This variation, referred to as the density of states (DOS), can be approximated by a Gaussian distribution.

In amorphous, disordered organic materials, the local energy environment around each molecule can vary slightly due to energetic disorder (s. Fig. 3.1 b). As a result, the HOMO and LUMO levels differ from molecule to molecule, leading to a broad distribution of these energy levels. This distribution, known as density of energetic states (DOS) is often described using a *Gaussian* distribution, reflecting the inherent disorder in the material (s. Fig. 3.1 c). The broadening of the HOMO and LUMO levels influences charge transport and overall device performance, making it a critical factor in the design and optimization of organic semiconductor materials.

Organic semiconductors are generally classified into three types^[10]:

1. **Amorphous molecular films:** These are organic molecules deposited as amorphous films, used in devices like OLEDs. These films are typically processed through

techniques such as vacuum thermal evaporation (VTE) or solution-based methods like spin coating or inkjet printing. The choice of processing method depends on various factors, including the thermal stability of the compounds, their evaporation temperature, solubility and film forming properties.

2. **Molecular crystals:** These are crystals formed by molecules like naphthalene or anthracene held together by weak van-der-Waals interactions, with high charge mobility compared to those in noncrystalline organic materials. Molecular crystals can be further divided into single crystals and polycrystalline materials:

- **Single crystalline materials** are highly ordered structures with no grain boundaries, providing the highest charge mobility among organic semiconductors. They are commonly used in applications where high performance is critical, such as organic field-effect transistors (OFETs). Single crystals are typically grown using methods such as solution growth or physical vapor deposition (PVD), which require precise control over the growth environment.
- **Polycrystalline materials** consist of multiple single crystalline grains separated by grain boundaries, which can hinder charge transport compared to single crystals. However, polycrystalline materials are easier and more cost-effective to fabricate, making them suitable for applications like OLEDs and organic solar cells (OSCs). They are often processed through techniques like VTE and solution-based methods (e.g. spin coating).

3. **Polymer films:** Polymers, consisting of covalently bonded molecular repeat units, are processed from solution and offer versatile deposition techniques, making them ideal for blending, short range and large-scale applications. The resulting films are generally amorphous, but crystalline domains can also form depending on the polymer structure, processing conditions, and post-deposition treatments.

While the semiconducting properties of these materials share a common origin related to their electronic structure, their specific excited states and photophysical properties vary based on the material’s structure and molecular order. Localized sites, such as individual molecules or effectively conjugated segments, can feature energy levels that contribute to the material’s overall electronic structure. The density of energetic states (DOS) around these localized sites may exhibit a given width, influencing charge transport and exciton dynamics, and thus the material’s optoelectronic behavior.

3.2 Organic Light-Emitting Diodes

An organic light-emitting diode (OLED) is an electronic thin-film device in which the emissive layer is composed of an organic compound. OLEDs function by converting electrical current into visible light through the process of electroluminescence (EL) in organic semiconducting materials. This chapter deals with the core principles underlying OLED technology, providing a comprehensive understanding of the physical and electrochemical mechanisms at work within these devices. The density of states (DOS) around these localized sites may exhibit a given width, influencing charge transport and exciton dynamics, and thus the material's optoelectronic behavior. As OLEDs continue to gain prominence in modern display and lighting technologies, understanding their operation is crucial for further innovation and application.^[10–12]

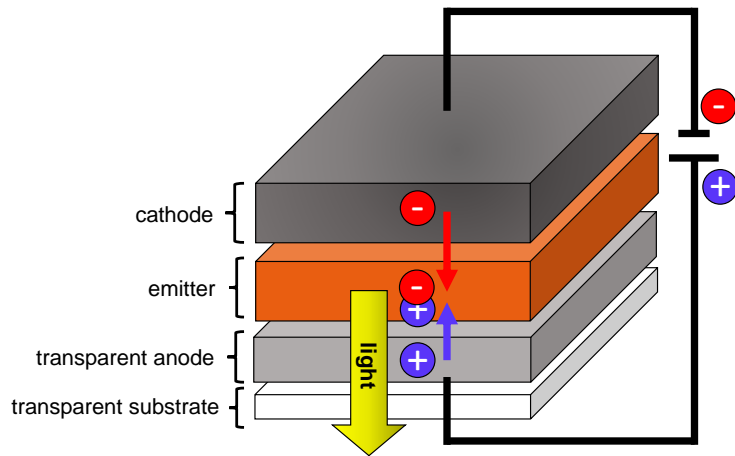


Figure 3.2: Working principle of an OLED: Holes are injected from the transparent anode, while electrons are supplied by the metallic cathode under an applied voltage. The recombination of charges in the emissive layer generates electroluminescence, which is emitted through the transparent anode and substrate.

The basic structure of an OLED is depicted in Fig3.2 and includes a stack of one or more semiconducting organic layers, with at least one being electroluminescent, positioned between two electrodes. For light to be emitted, at least one of the electrodes must be transparent or semi-transparent to visible light. The following four key processes are essential for light emission in an OLED:

1. Injection of electric charge carriers
2. Charge transport
3. Charge recombination and radiative decay of the excited state
4. Light outcoupling

The individual processes are discussed in more detail in the following sections.

3.3 Charge Injection

Organic semiconductors are capable of effectively converting electrical energy into light and vice versa. To achieve this, the organic semiconductor must be connected to an external electrical circuit to either inject or extract charge carriers. During this process, charge carriers may need to overcome energy barriers between the *Fermi* level (E_F) of the electrodes and the transport levels within the organic material.^[10,11]

The injected holes and electrons must overcome the energy barriers ϕ_h and ϕ_e , that exist between the E_F of the anode and cathode and the HOMO and LUMO energy levels of the adjacent organic semiconductor. Electrons aim to occupy the lowest available energy states, holes vice versa. To achieve efficient injection, it is important to minimize ϕ_h and ϕ_e , which should be considered when selecting materials.

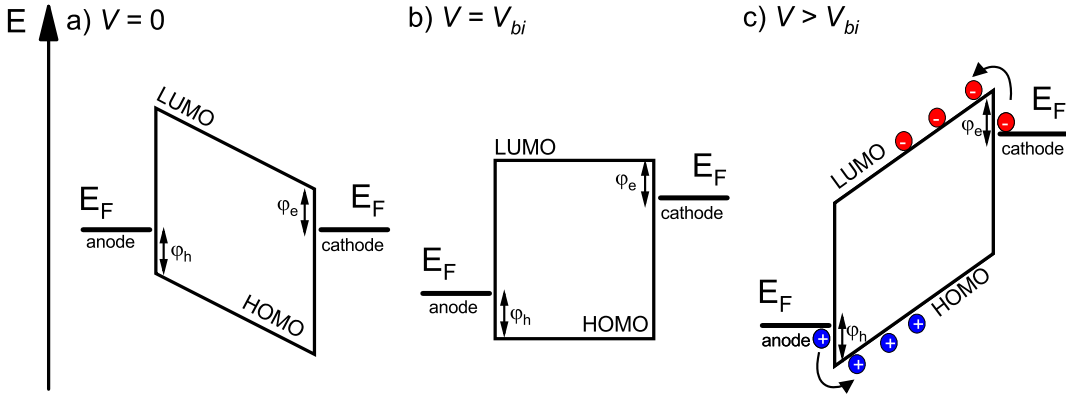


Figure 3.3: Energy across a single-layer device with varying external voltages: a) Under short-circuit conditions ($V = 0$), the Fermi levels of the electrodes align until $E_{F,cathode}$ matches $E_{F,anode}$. The resulting internal electric field inhibits charge transport. b) Applying an external voltage V_{bi} neutralizes the internal built-in field, resulting in a "flat" alignment of the HOMO and LUMO levels. c) When the external voltage surpasses V_{bi} , it facilitates the injection of charge carriers into the organic semiconductor, thereby reaching the operational state.

Fig 3.3 schematically illustrates the energetic conditions within a undoped single-layer OLED under different applied voltages ($V = 0$, $V = V_{bi}$, and $V > V_{bi}$).^[10] For simplicity, the HOMO and LUMO energy levels are shown as single lines, although they actually represent numerous localized states within a *Gaussian* distribution of energy levels (s. Fig. 3.1).

1. **Short circuit** ($V = 0$, s. Fig 3.3 a): When both electrodes are short-circuited, their *Fermi* levels equilibrate, as electrons migrate from the metal with a lower electro-

chemical potential to the one with a higher potential. This alignment causes an electric field distortion in the frontier molecular orbitals (FMOs), dependent on the potential difference between $E_{F,anode}$ and $E_{F,cathode}$, also known as the built-in voltage (V_{bi}).

2. **Flat band** ($V = V_{bi}$, s. Fig 3.3 b): Applying a voltage equal to V_{bi} results in a flat band, where the electronic configuration resembles that of unconnected electrodes in an open circuit.
3. **Operation** ($V > V_{bi}$, s. Fig 3.3 c): When a voltage exceeding V_{bi} is applied, charge carriers may be injected through tunneling or thermionic field-supported mechanisms (s. Fig 3.4). Under the influence of the applied field, charge carriers move towards the counter electrode. During this transit, they may recombine to form excitons, which can subsequently release energy as light (s. 3.5).

OLEDs rely on the efficient injection of charge carriers from electrodes into the organic semiconductor layer. Understanding the mechanisms behind charge injection is crucial for optimizing device performance. In the following, three primary injection mechanisms and their relevance to OLEDs will be presented: *Fowler–Nordheim* tunneling, *Richardson–Schottky* thermionic injection, and thermally activated injection in disordered organic semiconductors (s. Fig 3.4). Each mechanism provides insights into how charge carriers move from the electrodes into the organic layer and their implications for OLED operation.

1. *Fowler–Nordheim* tunneling injection

Fowler–Nordheim tunneling (s. Fig 3.4 a) involves electrons tunneling through a triangular potential barrier created by a strong electric field. The barrier is composed of the metal-vacuum interfaces work function Φ and the applied potential. The current density (J) is related to the electric field (F) by:

$$J_{NF}(F) \cong F^2 \exp\left(-\frac{4\sqrt{2m_{eff}\Phi^3}}{3\hbar eF}\right) \quad (3.1)$$

with m_{eff} being the effective electron mass, \hbar the reduced *Planck* constant and e the elementary charge. In OLEDs, this model presents challenges. The image potential effect, which is significant in disordered organic semiconductors, is not considered in the original *Fowler–Nordheim* model. Additionally, the high electric fields required for effective tunneling in typical OLED structures make this mechanism impractical. Tunneling might be relevant in OLEDs with rough electrode

surfaces where high local electric fields could occur, potentially leading to localized injection or device breakdown.^[10,13]

2. *Richardson–Schottky* thermionic injection

Richardson–Schottky thermionic injection (s. Fig 3.4 b) describes the process of thermally excited electrons overcoming a potential barrier from a metal electrode into a semiconductor. The barrier is defined by the difference between the metal’s work-function Φ and the semiconductor’s electron affinity (E_a). The total potential experienced by the electron includes the barrier, the image potential, and the applied electric field. The injection current density J_{RS} follows:

$$J_{RS} \propto T^2 \exp\left(-\frac{\Delta - \Delta\phi}{k_B T}\right) = T^2 \exp\left(-\frac{\phi - E_a - \beta_{RS} \sqrt{F}}{k_B T}\right) \quad (3.2)$$

where $\Delta\phi$ is the reduction in barrier due to the field, β_{RS} is a constant related to the *Richardson–Schottky* model, and T is the temperature.

In OLEDs, this mechanism is relevant because it accounts for the thermal activation of electrons and the effect of the image charge. However, practical conditions such as inelastic scattering and the disordered nature of organic semiconductors can limit its strict applicability. The field dependence predicted by the *Richardson–Schottky* model provides insights into the behavior of thermionic emission across different conditions.^[10,14,15]

- #### 3. Thermally activated injection in disordered organic semiconductors
- Traditional models like *Fowler–Nordheim* tunneling and *Richardson–Schottky* injection were developed for crystalline, inorganic semiconductors. For disordered organic semiconductors, a refined model is required (s. Fig 3.4 c). This model incorporates image charge effects, hopping transport, and the presence of disorder. According to the model developed by *Gartstein* and *Conwell* electrons thermally activated from the electrodes *Fermi* level jump to tail states within the DOS distribution of the organic material. These electrons must move to neighboring sites with equal or lower energy to continue transport rather than recombine with the image charge. The carrier then undergoes a diffusive random walk in the combined *Coulomb* potential of the image charge and the applied field. The injection current follows a *Poole–Frenkel*-type field dependence:

$$\ln(J_{RN}(F)) \propto \sqrt{F} \quad (3.3)$$

However, when analyzing the temperature dependence of the injection current, discrepancies often arise. The apparent activation energy from experimental data tends to be lower than expected based on the injection barrier. This phenomenon is attributed to the stochastic nature of carrier motion in a disordered energy landscape. The transport energy, which decreases with temperature, affects the actual injection barrier, leading to a lower observed activation energy.^[10,16–18]

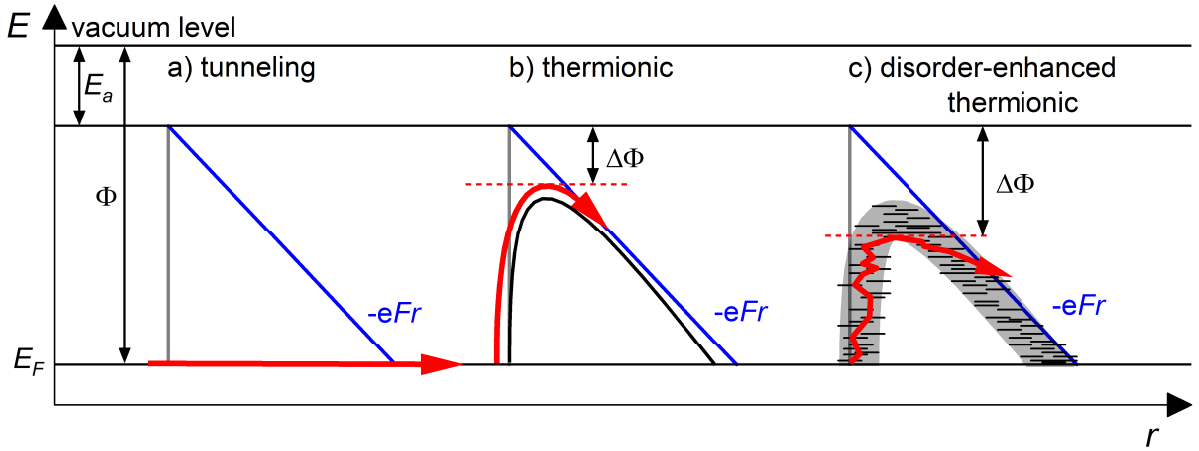


Figure 3.4: Charge carrier injection mechanisms are illustrated, focusing on electrons, but the principles also apply to holes. a) *Fowler-Nordheim* tunneling involves electrons moving through the energy barrier between the electrode and the organic semiconductor. This mechanism is typically negligible due to the usually insufficient external electric field strengths F . b) *Richardson-Schottky* thermionic injection allows charge carriers to surmount the barrier through thermal activation, with the barrier reduced by $\Delta\Phi$ compared to $\Phi - E_a$ due to a mirror charge effect. c) Combining thermal activation with the energetic disorder inherent in organic semiconductors can further reduce the barrier (increase $\Delta\Phi$) as charge carriers can access and traverse through tail states in the energy distribution.

Concluding *Fowler-Nordheim* tunneling is less significant in typical OLEDs, *Richardson-Schottky* thermionic injection offers valuable insights into charge transport across the metal-organic interface. The model for thermally activated injection in disordered semiconductors provides a more accurate depiction of charge dynamics in OLEDs, considering material disorder and hopping transport. Each mechanism contributes to a comprehensive understanding of charge injection processes and their implications for OLED technology.

3.4 Charge Transport

When charges are injected into a semiconductor, they begin to move. Current flow in semiconductors arises from two mechanisms: a gradient in the electrostatic potential, which creates an electric field, and a gradient in the charge concentration. These mechanisms give rise to two distinct types of current: **drift current**, driven by the electric field, and **diffusion current**, driven by the concentration gradient.

The dominant mechanism depends on the relative strengths of these gradients. In inorganic semiconductors, the charge concentration is typically high, leading to significant concentration gradients, while potential differences are minimal due to effective dielectric screening. Consequently, diffusion currents often dominate. In organic semiconductors, the opposite is true. Here, potential gradients are more significant due to weaker dielectric screening, leading to a drift-controlled current.^[10,17,19,20]

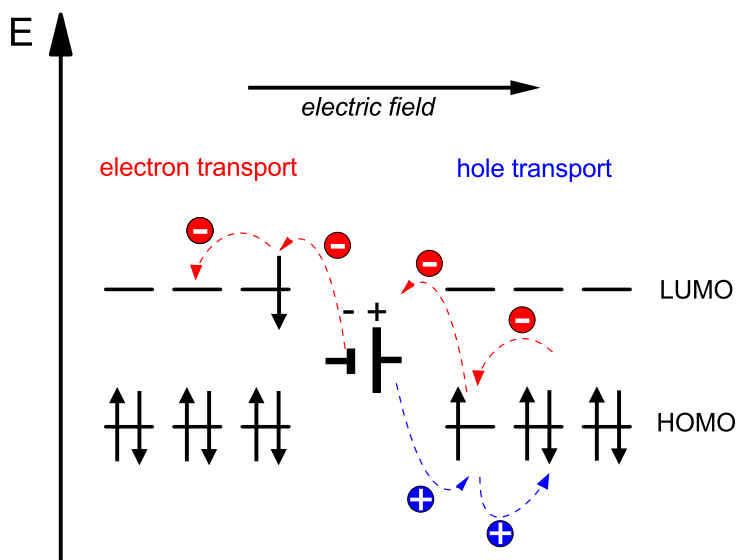


Figure 3.5: Charge transport via hopping mechanism in an organic semiconductor. Charges are transferred from molecule to molecule through successive redox reactions. Electron transport occurs via the LUMO, while hole transport takes place through the HOMO of the individual molecules.

Hopping can be understood as a series of redox reactions between identical molecular units. Fig. 3.5 shows the simplified mechanism of the charge transport for holes and electrons. For hole transport, a hole oxidizes an organic molecule, forming a radical cation. The hole is then transported as an electron moves from the HOMO of a neighboring neutral molecule to the HOMO of the radical cation. In electron transport, injection at the cathode reduces the organic semiconductor, forming a radical anion, and the electron is

transferred from the LUMO of the radical anion to the HOMO of a neutral neighbor molecule. This sequential process results in the movement of the charge carrier.

The *Gaussian* disorder model, developed by *Bässler*, provides a mathematical framework to describe the energy distribution of hopping sites in amorphous organic semiconductors.^[19] The energy distribution of these hopping sites follows a Gaussian distribution, which is given by the formula:

$$g(\varepsilon) = \frac{1}{\sqrt{2\pi}\sigma} \exp\left(-\frac{\varepsilon^2}{2\sigma^2}\right) \quad (3.4)$$

$g(\varepsilon)$ represents the DOS as a function of the energy ε for an individual molecule. This *Gaussian* distribution reflects the energetic disorder caused by molecular fluctuations and varying intermolecular distances in the material. The standard deviation σ , typically around 0.1 eV, quantifies the degree of this disorder and the variations in polarization energies.

The energy of the actual charge transport level, $E_{transport}$, is located below the center of the DOS and can be expressed as:

$$E_{transport} = \frac{5\sigma^2}{9k_B T} \quad (3.5)$$

with the *Boltzmann* constant k_B and the absolute temperature T . This model captures the essence of charge transport in disordered organic semiconductors, where thermal activation is required for hopping to higher energy states, while hopping to lower energy states occurs without energy barriers.

Unlike band transport, hopping is a thermally activated process. Consequently, mobility in organic semiconductors increases with rising temperature and electric field strength.

The efficiency of charge transport in these materials is strongly influenced by the presence of traps. Traps are localized states with energy levels deep within the material's energy gap. Both electron and hole transport can be affected by trap states, which reduce their mobility. For holes, unoccupied sites with higher energy act as traps, requiring thermal activation for the hole to escape, thereby slowing transport. Similarly, for electron transport, an occupied site at a lower energy level can serve as a trap, leading to similar hindrance. Traps can arise from chemical impurities or physical defects.

3.5 Exciton Formation

In the following sections the formation of excitons will be discussed. In an OLED the most relevant process is the exciton formation via charge recombination (electrical formation). Additionally, the exciton formation via optical excitation (absorption of light) is addressed here, as it is relevant for the spectroscopic investigations in this work.

Exciton Formation via Charge Recombination

Excitons are bound states of an electron and a hole, created through charge carrier recombination when their *Coulomb* attraction binds them together. In OLEDs, *Frenkel* excitons dominate due to the low dielectric constant of organic semiconductors, resulting in strongly bound, localized pairs with binding energies of 0.1–1 eV and typical distances below 1 nm. In contrast, inorganic semiconductors exhibit *Wannier-Mott* excitons, which are delocalized quasiparticles across the lattice, with binding energies of a few meV and distances spanning several nanometers.

To achieve EL in organic semiconductors, electrons and holes must recombine to form excitons on an emitter molecule. Exciton formation becomes more probable when the distance between the electron and hole falls below a critical threshold, known as the *Coulomb* capture radius (r_c). This distance determines the point at which the *Coulomb* attraction between the electron and hole is comparable to their thermal energy. The *Coulomb* capture radius is defined as:

$$r_c = \frac{e}{4\pi\epsilon_r\epsilon_0 k_B T} \quad (3.6)$$

with the elementary charge of an electron e , the vacuum permittivity ϵ_0 , the dielectric constant ϵ_r , the *Boltzmann* constant k_B and the absolute temperature T .^[21]

In organic semiconductors, the average hopping distance of charge carriers is smaller than r_c . As a result, when an electron and a hole become localized at nearby transport sites, they tend to form a bound electron-hole pair known as exciton.

The rate R_{Lan} at which excitons form according to *Langevin*, represented as

$$R_{Lan} = \frac{e(\mu_e\mu_h)}{\epsilon_r\epsilon_0} n_e n_h \equiv \gamma_{Lan} n_e n_h \quad (3.7)$$

depends on the concentration of free electrons and holes (n_e and n_h), and the *Langevin* bimolecular recombination rate factor γ_{Lan} which itself is conditional on the hole and electron mobility (μ_e and μ_h).^[21]

A high exciton formation efficiency requires an adequate density of both electrons and holes, balanced mobilities for both types of charge carriers, and a large bimolecular recombination constant. These conditions ensure efficient recombination and maximization of exciton yield, which is crucial for optimal performance in optoelectronic devices like OLED.

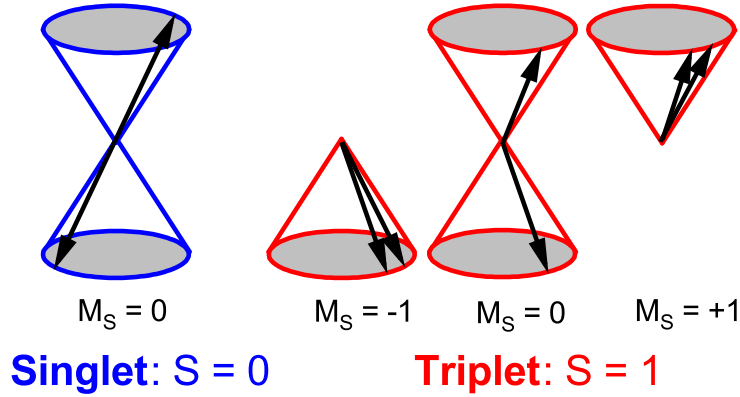


Figure 3.6: The singlet and triplet states of an electron-hole pair are depicted with vector diagrams, illustrating the total spin S and the spin quantum numbers M_S for various orientations. In the singlet state ($S = 0$), the charge carriers have antiparallel spins, meaning their spins are oriented in opposite directions. In contrast, the triplet state ($S = 1$) encompasses three different spin configurations: for $M_S = -1$ and $M_S = +1$, the spins are parallel, while for $M_S = 0$, the spins are antiparallel but aligned in the same direction. The threefold degeneracy of the triplet state explains its higher formation probability. Assuming all configurations are equally probable, 25% of the electron-hole pairs are expected to be in the singlet state, while 75% are expected to be in the triplet state.

When the electron and hole recombine, their respective spins determine whether the exciton formed is in a singlet or triplet state. This spin configuration is governed by the *Pauli* exclusion principle and the spin quantum number M_S :

The electron and hole each have a spin quantum number of $s = \frac{1}{2}$, meaning they can each have two possible spin states: spin-up ($s = +\frac{1}{2}$) or spin-down ($s = -\frac{1}{2}$). During recombination, the spins of the electron and hole can combine in different ways to form excitons. There are four possible combinations of electron and hole spins (s. Fig. 3.6):

One combination leads to a singlet exciton, where the spins are antiparallel, resulting in a total spin of $S = 0$. The other three combinations result in triplet excitons, where the spins are parallel, giving a total spin of $S = 1$.^[22,23]

Since only one of the four possible spin combinations results in a singlet exciton, and the other three lead to triplet excitons, the probability of forming singlet excitons is 25%, while the probability of forming triplet excitons is 75%. This ratio of 1:3 arises naturally from the possible spin configurations during recombination.

Exciton Formation via Optical Excitation

Excitons can also be generated through optical excitation, occurring when the organic semiconductor absorbs photons. This process is essential in devices like OSC, where the objective is to convert light into electrical energy. When a photon is absorbed, an electron in the HOMO is excited to the LUMO, creating an electron-hole pair, or exciton.

In contrast to exciton formation via charge recombination, optical excitation directly generates singlet excitons due to quantum mechanical selection rules governing photon absorption. Specifically, optical excitation is governed by the following selection rules^[22,23]:

Parity selection rule: For electric dipole transitions, the parity of the initial and final states must differ. In molecules with inversion symmetry, this means that an electron must transition between orbitals of opposite parity (such as from a bonding orbital to an anti-bonding orbital). In organic semiconductors, this generally involves excitation from the HOMO (bonding) to the LUMO (anti-bonding).

Spin selection rule: Transitions that preserve the total spin quantum number are allowed. Since photons carry no spin, the total spin of the system cannot change during the absorption process. As a result, optical excitation of singlet ground states can only generate singlet excitons where the spins of the electron and hole are antiparallel, resulting in a total spin of $S = 0$.

The process is crucial in optical spectroscopy for probing the electronic and optical properties of organic semiconductors. By analyzing absorption and emission spectra, insights into energy levels, exciton dynamics, and material efficiency can be gained. This allows for the evaluation and optimization of optoelectronic devices, such as OLEDs and organic solar cells.

3.6 Photophysical Processes in OLEDs

Photophysical processes describe how organic molecules absorb, dissipate, and emit light. These processes are key to understanding the behavior of organic semiconductors and can be illustrated through the diagram in Fig. 3.7 showing the possible transitions between electronic states. To fully grasp these transitions, it is important to introduce the *Franck-Condon* principle, which explains how the overlap between vibrational states influences the likelihood of electronic transitions, and *Kasha's* rule, which governs photon emission pathways.

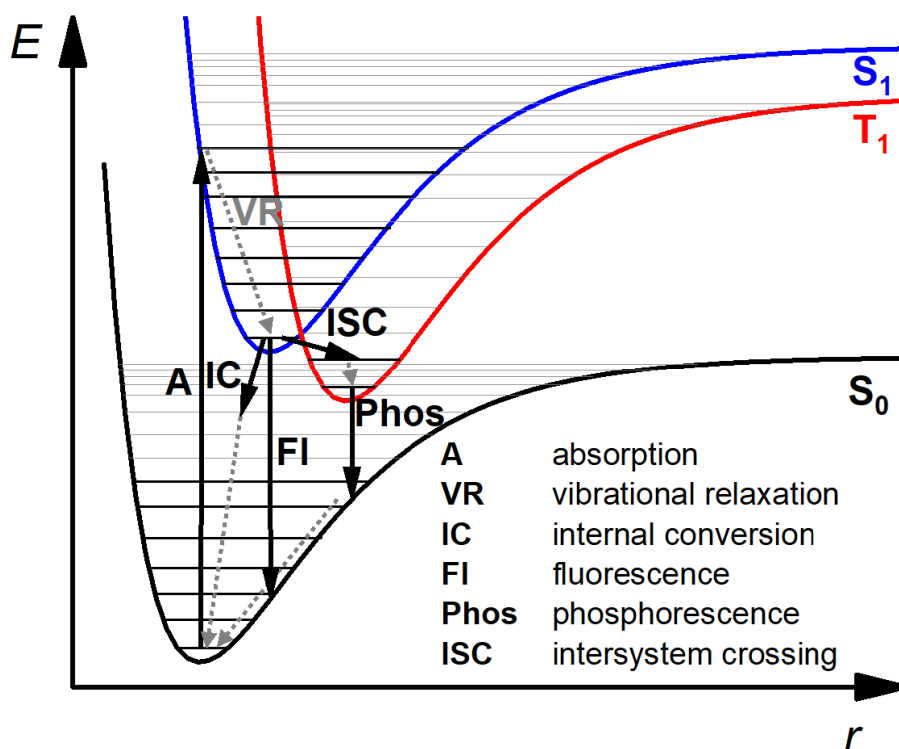


Figure 3.7: Franck-Condon diagram depicts electronic transitions and associated processes in a molecule. It shows how **absorption** elevates the molecule from the ground state (S_0) to an excited singlet state (S_1 or S_2). **Vibrational relaxation** then occurs within the same electronic state, followed by **internal conversion** to a lower singlet state. **Fluorescence** is the radiative transition back to the ground state from the singlet state, while **phosphorescence** involves emission from a triplet state (T_1) to the ground state. **Intersystem crossing** represents the non-radiative transition between singlet and triplet states.

3.6.1 Franck-Condon Principle

The *Franck-Condon* principle describes the transition between electronic states during photon absorption or emission, highlighting the role of nuclear configuration. Since electronic transitions occur much faster than nuclear motion, the nuclei are considered stationary during the transition. As a result, the most probable transitions are those that occur vertically on a potential energy diagram (s. Fig. 3.7), reflecting a rapid change in the electronic state while the molecular structure remains fixed. This explains why excitation and emission spectra often exhibit vibrational structures, with broad absorption bands corresponding to transitions involving different vibrational energy levels.

This behavior can be understood using the *Born-Oppenheimer* approximation, which assumes that the electronic and nuclear motions can be treated separately due to the significant difference in their masses. The approximation allows us to treat the nuclear positions as nearly fixed during electronic transitions, providing the basis for the vertical transitions seen in *Franck-Condon* transitions.^[22–25]

3.6.2 Photophysical Processes

The various processes that occur following the absorption of light are illustrated in Fig. 3.7. The different electronic states of a molecule are shown, including the ground state (S_0), singlet excited states (S_1 and S_2), and triplet excited states (T_1). The diagram also illustrates the pathways by which a molecule transitions between these states, either through radiative or non-radiative processes.^[22,23,26] The key photophysical processes include:

Absorption

When an organic molecule absorbs a photon, an electron is excited from the ground state (S_0) to a higher singlet excited state (S_1). The *Franck-Condon* principle dictates that this transition happens vertically. Absorption occurs on an ultrafast timescale, typically in the range of femtoseconds (10^{-15} s).

Vibrational Relaxation

After excitation, the molecule quickly loses excess vibrational energy within the excited electronic state, a process known as vibrational relaxation. This happens on a timescale of picoseconds (10^{-12} s), bringing the electron to the lowest vibrational level of the excited state (S_1).

Internal Conversion

Internal conversion is a non-radiative process where an electron transitions from a higher singlet excited state (e.g., S_2) to a lower one (S_1) without the emission of light. This process occurs rapidly, typically in picoseconds (10^{-12} s).

Fluorescence

In fluorescence, the electron returns from the lowest excited singlet state (S_1) to the ground state (S_0), emitting a photon. Fluorescence is a radiative process that typically occurs on the timescale of nanoseconds (10^{-9} s) and results in the emission of light. This is the primary radiative decay process for singlet excitons and can be observed in OLEDs and other optoelectronic devices.

Intersystem Crossing (ISC)

Intersystem crossing is a spin-forbidden transition where an electron moves from a singlet excited state (S_1) to a triplet state (T_1). Although the transition is spin-forbidden, it can be enhanced by the presence of spin-orbit coupling, especially in molecules with heavy atoms. The spin-orbit coupling allows for the mixing of singlet and triplet states, which facilitates the intersystem crossing (ISC) process. Typically, ISC occurs on the time scale of nanoseconds to microseconds (10^{-9} s to 10^{-6} s), although this time scale can vary depending on factors such as the molecule's structure, environment, and the strength of spin-orbit coupling. *El-Sayed's* rule governs the likelihood of ISC occurring based on the symmetry of the electronic states and the geometrical changes associated with the transition. According to *El-Sayed's* rule:

1. Spin-forbidden transitions are more likely when the transition involves a significant geometric change that facilitates the mixing of singlet and triplet states.
2. ISC is more efficient when the transition occurs from an excited state with higher spin multiplicity (singlet) to one with lower spin multiplicity (triplet), and this transition involves a change in molecular geometry that allows the spin-orbit coupling to effectively mix the states.

El-Sayed's rule helps explain why ISC is typically more efficient for $n - \pi^*$ transitions than for $\pi - \pi^*$ transitions. The greater geometric changes associated with $n - \pi^*$ transitions allow for better mixing of singlet and triplet states, enhancing the probability of ISC.

Conversely, $\pi - \pi^*$ transitions are generally less likely to undergo ISC unless additional factors, such as strong spin-orbit coupling in the presence of heavy atoms, are involved.

Phosphorescence

Once in the triplet state (T_1), the electron can return to the ground state (S_0) by emitting a photon in a process known as phosphorescence. Phosphorescence is slower than fluorescence due to the spin-forbidden nature of the transition, often occurring on a timescale of microseconds to seconds (10^{-6} s – 1 s) in organic molecules. However, in materials containing heavy metals, such as iridium complexes used in phosphorescent OLEDs (PhOLEDs), spin-orbit coupling is significantly enhanced, allowing phosphorescence to occur on shorter timescales, typically in the range of microseconds (10^{-6} s).

3.6.3 Kasha’s Rule

Kasha’s rule states that photon emission (either fluorescence or phosphorescence) occurs predominantly from the lowest excited electronic state of a given multiplicity. For singlet states, this is the S_1 state, while for triplet states, it is the T_1 state. Even if a molecule is excited to a higher electronic state (e.g., S_2), internal conversion will rapidly relax the system to the lowest excited state (S_1) before any photon emission occurs. This rule explains why fluorescence is generally observed from the S_1 state, regardless of whether excitation occurred at higher energy levels.^[23,27]

Even though the *Kasha* rule applies in many cases there are known exceptions such as azulene which shows strong vibronic coupling, allowing direct emission from a higher excited state S_2 without fully relaxing to the lower singlet excited state S_1 , partly because of the large energy gap between S_1 and S_2 .^[28,29]

3.6.4 Thermally Activated Delayed Fluorescence (TADF)

The process of thermally activated delayed fluorescence (TADF) can effectively harnesses triplet excitons to achieve delayed light emission, combining elements of both fluorescence and phosphorescence. Originally discovered by *Parker* and *Hatchard* for Eosin in 1961^[30,31], the phenomenon of TADF was later referred to as "E-type delayed fluorescence" by *Parker* and *Hatchard*, in reference to Eosin.^[32] Decades later, TADF gained significant attention when *Adachi* and coworkers applied it in OLEDs, dramatically improving device efficiency.^[7-9]

In OLEDs utilizing TADF, the key to high efficiency lies in the ability to harvest both singlet and triplet excitons for light emission. As described in section 3.5, OLEDs generate a mixture of singlet (25%) and triplet (75%) excitons due to spin statistics.

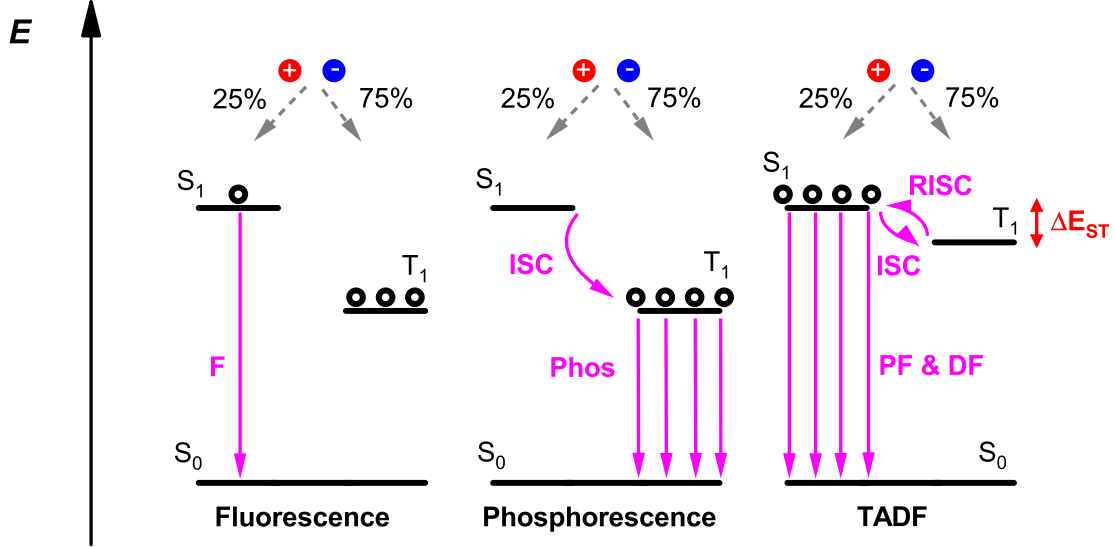


Figure 3.8: Scheme of emission processes in the three generations of OLEDs. Left: fluorescence with a maximum IQE of 25%, middle: phosphorescence with a maximum IQE of 100%, right: TADF with a maximum IQE of 100% due to thermally activated triplet upconversion resulting in delayed fluorescence.

In conventional fluorescent OLEDs which are often described as first generation OLEDs, only singlet excitons contribute to light emission, limiting efficiency. The second generation of OLEDs uses phosphorescent emitters. Efficient ISC allows up to 100% IQEs but they come with the disadvantage of their reliance on costly, less sustainable heavy metals (e.g. Iridium, Platinum). However, TADF (third generation OLEDs) allows triplet excitons, to be converted back into singlet excitons via reverse intersystem crossing (rISC).^[33] The rISC process is thermally activated and occurs because of the small energy gap between the S_1 and T_1 state, known as the singlet-triplet energy gap (ΔE_{ST}). When ΔE_{ST} is small, the thermal energy at room temperature is sufficient to overcome the energy barrier, allowing triplet excitons to transition back to the singlet state. Once the excitons return to the singlet state, they can decay radiatively, emitting photons in form of delayed fluorescence.

The value of 0.1 eV, often used as a benchmark for ΔE_{ST} in TADF materials, is related to the thermal energy available at room temperature (approximately 295 K). The energy provided by thermal activation can be calculated using:

$$E_{thermal} = k_B T = 8.617 \cdot 10^{-5} \frac{\text{eV}}{\text{K}} \cdot 295 \text{ K} = 25 \text{ meV} \quad (3.8)$$

The difference between the room temperature thermal energy ($\sim 25 \text{ meV}$) and the typical maximum ΔE_{ST} ($\sim 100 \text{ meV}$) for TADF materials is due to the *Boltzmann* distribution, which allows some molecules to possess higher energy than the thermal average. Due to their long lifetimes, enough triplet excitons can be thermally excited to singlet states, making rISC efficient despite the larger energy gap.

Unlike phosphorescence, where triplet excitons emit light slowly due to weak spin-orbit coupling (SOC), TADF typically has lifetimes in the range of microseconds to milliseconds. The TADF process takes advantage of weaker SOC in organic materials but still manages to convert triplets back to singlets efficiently, thanks to the small ΔE_{ST} . This mechanism results in delayed fluorescence that significantly enhances the IQE of the OLED, allowing the device to achieve near 100% IQE by utilizing both singlet and triplet excitons.

3.6.5 Energy Transfer Processes

Energy transfer processes are essential to the performance and efficiency of OLEDs, influencing how light is generated and how energy loss can be minimized. Wide-bandgap host materials are commonly used in OLEDs to prevent quenching effects and ensure efficient energy transfer. These hosts provide a stable environment for the guest emitters by confining excitons and charge carriers within the emissive material, avoiding unwanted energy dissipation.

Energy transfer in OLEDs can occur through radiative processes, such as the emission and absorption of photons, or non-radiative processes, where energy is directly transferred between molecules. Two key non-radiative mechanisms are *Förster* resonance energy transfer (FRET) and *Dexter* energy transfer, both critical for moving excitons between host (donor) and guest (acceptor) molecules. Additionally, triplet-triplet annihilation (TTA) can impact the fate of triplet excitons, either enhancing or reducing the overall efficiency of the device. Understanding these energy transfer processes, alongside the role of wide-gap host materials, is vital for optimizing device performance and reducing energy losses.

Förster Resonance Energy Transfer (FRET)

FRET is a non-radiative energy transfer mechanism between chromophores, crucial in OLED host-guest systems and biological applications. In FRET, energy is transferred from a donor to an acceptor (s. Fig 3.9) through dipole-dipole coupling, with the quantum yield of the FRET (Φ_{FRET}) being highly dependent on the spectral overlap of donor emission and acceptor absorption, the dipole orientation of donor and acceptor and the donor-acceptor distance r . Φ_{FRET} is given by:

$$\Phi_{FRET} = \frac{1}{1 + (r \cdot R_0^{-1})^6} \quad (3.9)$$

with the *Förster* distance (R_0) at which the energy transfer efficiency is 50%. Φ_{FRET} decreases with increasing distance, making it sensitive to nanoscale changes. The typical timescale for FRET is in the range of ps to ns.

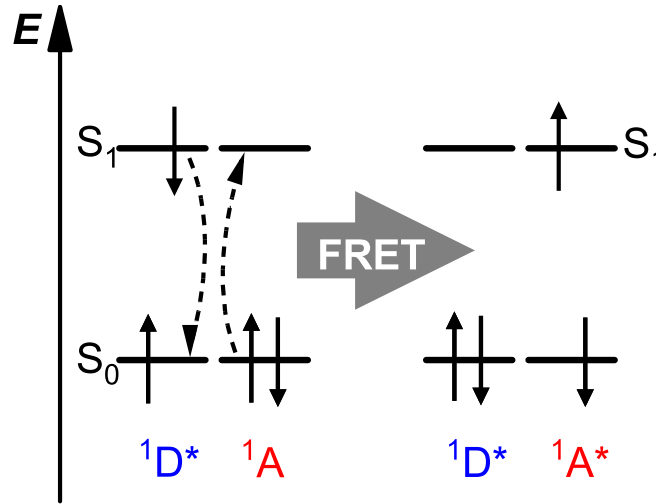


Figure 3.9: Scheme of nonradiative *Förster* resonance energy transfer (FRET). Energy is transferred from an excited donor molecule to an acceptor in the ground state.

In OLEDs, controlling the parameters that influence FRET – distance, spectral overlap, and dipole orientation – is key to optimizing the energy transfer from the host to the guest molecules. The fine-tuning of these interactions leads to more efficient exciton management, resulting in higher quantum yields and better overall device performance.^[34] In biology, FRET acts as a molecular ruler, allowing researchers to measure distances (1–10 nm) between biomolecules, providing insights into molecular interactions and conformational changes.^[10,35–38]

Dexter Transfer

Dexter energy transfer is a short-range, nonradiative mechanism of energy transfer between two chromophores, distinct from FRET, and based on electron exchange interactions.

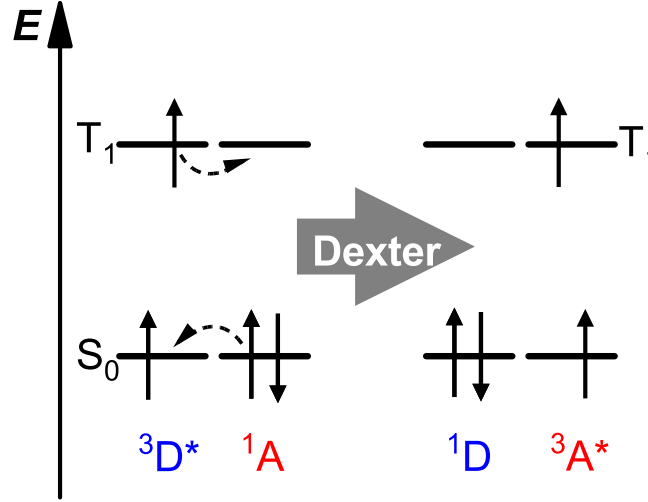


Figure 3.10: Scheme of *Dexter* energy transfer. The nonradiative mechanism involves an excited electron from a donor molecule being transferred to an acceptor molecule through direct orbital overlap, requiring close proximity and electron exchange between the molecules.

Unlike FRET, which relies on dipole-dipole coupling, *Dexter* transfer requires direct orbital overlap between the donor and acceptor molecules, making it highly dependent on their proximity. The quantum yield of the *Dexter* transfer (Φ_{Dexter}) decreases exponentially with the distance between donor and acceptor r and the characteristic distance L over which electron exchange occurs (typically < 1 nm):

$$\Phi_{Dexter} \propto e^{-r/L} \quad (3.10)$$

The typical timescale of the process lies in the range of ns- μ s. In OLEDs, *Dexter* transfer is important for triplet energy transfer (s. Fig 3.10) and can facilitate energy transfer from the host to guest molecules.^[4] Since *Dexter* transfer occurs over very short distances, it ensures that excitons are efficiently transferred to emitters, improving device performance.^[10,23,35,39]

Triplet-Triplet Annihilation (TTA)

Triplet-triplet annihilation (TTA) was detected in pyrene solutions by *Parker* and *Hatchard* in 1962 and referred to as p-type delayed fluorescence.^[32,40] It is a nonradiative process in which two triplet-state excitons interact, resulting in one exciton being excited to a higher singlet state while the other relaxes to the ground state (s. Fig 3.11) while the total spin of the system is conserved. This mechanism is distinct from both *Förster* and *Dexter* energy transfers, as it involves exciton-exciton interactions rather than donor-acceptor pairs. TTA plays a key role in upconversion processes where low-energy triplet excitons combine to generate high-energy singlet excitons capable of emitting light.

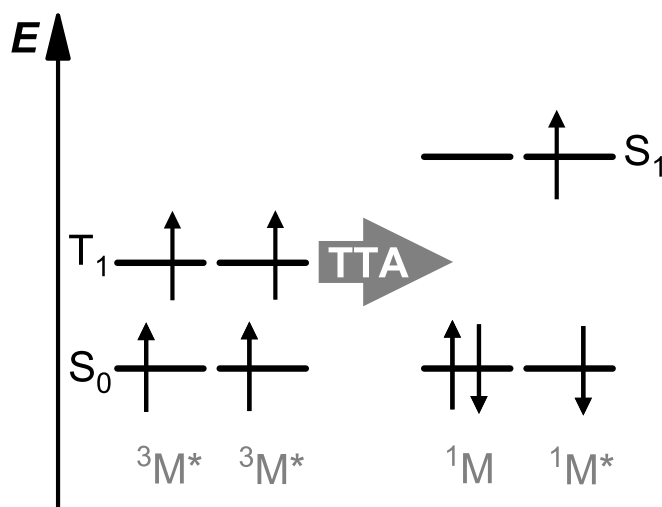


Figure 3.11: Scheme of TTA mechanism. The nonradiative process involves the interaction of two triplet excitons, leading to the excitation of one exciton to a higher singlet state, while the other relaxes to the ground state, enabling energy upconversion.

The efficiency of the process depends on the proximity and mobility of the interacting triplets. The interaction rate increases with the number of triplets in close proximity, making TTA highly dependent on molecular arrangement and diffusion.

In OLEDs, TTA plays a crucial role in generating singlet excitons from triplet states. By efficiently converting triplet excitons into singlet excitons, TTA enhances electroluminescence and helps to overcome the limitations imposed by spin-statistics, which restrict direct singlet exciton formation to only 25% of the total excitons generated during electron-hole recombination.^[41] Furthermore, TTA mechanism is effective for deep blue emission, which is highly sought after in display and lighting applications, overcoming challenges with the large bandgap of phosphorescent and TADF blue emitters.^[42,43]

Additionally, TTA reduces the operating voltage by half, enabling high-energy electroluminescence through electrical-pumped energy up-conversion..^[44]

The reverse process involving the splitting of one singlet exciton into two lower-energy triplet excitons is referred to as singlet fission. This process is useful in photovoltaic applications to harvest more energy from high-energy photons by creating two excitons from one photon.^[35,45]

3.7 Light Outcoupling

In OLEDs, a significant portion of the light generated within the emissive layer is trapped and fails to reach the external environment. This occurs due to internal reflections and light absorption within the layers of the OLEDs resulting in a limited outcoupling efficiency, typically ranging between 20%.

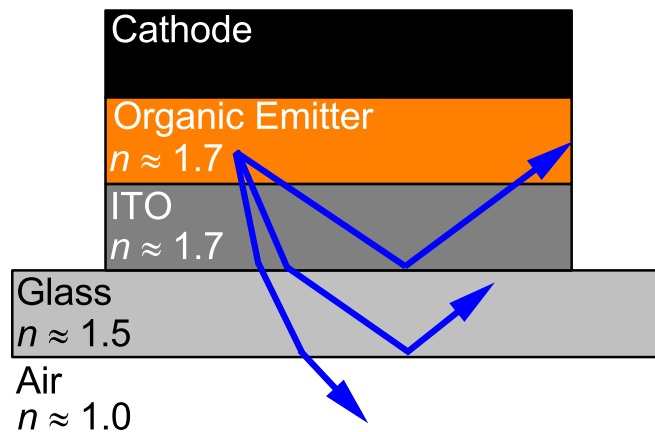


Figure 3.12: Due to the varying refractive indices of the organic layers, ITO, glass, and air, total internal reflection occurs at the interfaces. As a result, light generated within the OLED cavity becomes confined in the glass substrate and organic layers.

Fig 3.12 shows light trapping in OLEDs arising from refractive index mismatches and absorption within various layers of the device. The high refractive index (n) of the organic emissive layer ($n \approx 1.7$) compared to the lower index of the glass substrate ($n \approx 1.5$) leads to substantial internal reflections. Additionally, the indium tin oxide (ITO) layer which is usually used as transparent anode material and metallic electrodes reflect light internally and can cause absorptive losses. Organic transport layers can also absorb light, further contributing to energy losses.^[45]

The light outcoupling efficiency (η_{out}) refers to the fraction of light that escapes the OLED and is emitted to the external environment. For typical OLEDs, this value is constrained by internal optical losses and is usually in the range of 20–30%.^[45,46]

The external quantum efficiency (EQE) of an OLED is a measure of how efficiently the device converts electrical current into emitted light. EQE is dependent on several factors, and its formula is given as:

$$\text{EQE} = \eta_{out} \cdot \text{IQE} \quad (3.11)$$

with η_{out} being the light outcoupling efficiency, which represents how much of the generated light escapes the device. IQE is the internal quantum efficiency, which measures how efficiently excitons are formed and emit photons within the device. It is defined as:

$$\text{IQE} = \eta_r \cdot \gamma \cdot \Phi_{PL} \quad (3.12)$$

η_r is the radiative efficiency which is the fraction of excitons that is allowed to decay radiatively by spin statistics (e.g. 0.25 for fluorescence OLEDs). charge balance factor (γ) is the charge balance, representing how efficiently electrons and holes recombine to form excitons. photoluminescence quantum yield (Φ_{PL}) is the quantum yield of the excitons (the probability that an exciton decays radiatively). Thus, the final equation for EQE is:

$$\text{EQE} = \eta_{out} \cdot \eta_r \cdot \gamma \cdot \Phi_{PL} \quad (3.13)$$

This formula highlights the importance of both internal processes (such as charge balance and exciton formation) and the external process of light extraction in determining the overall efficiency of OLEDs.^[45,47]

Even though there are strategies to improve the light outcoupling, in this work the outcoupling efficiency η_{out} is considered constant and focus will be on the internal processes that affect IQE, specifically through the characterization of emitter molecules.

3.8 Multi-Layer OLED

Multi-layer OLEDs consist of multiple organic and inorganic layers that work together to optimize the efficiency, performance, and stability of the device. Each layer has a specific function and is designed with consideration of the material properties to achieve optimal charge injection, transport, recombination, and light emission. A typical multi-layer OLED is composed of the following layers^[48–51]:

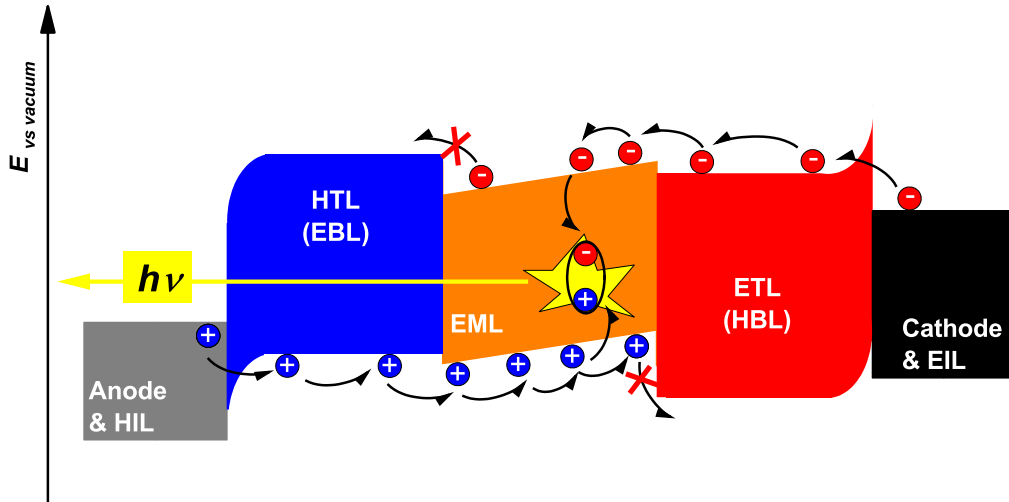


Figure 3.13: Energetic scheme of a multi-layer OLED. Suitable HILs, HTLs, ETLs, and EILs improve the charge injection at anode and cathode and the charge transport through the device. Charge carriers recombine in the EML and the formed excitons emit light during relaxation. Additionally holes are blocked by the ETL (HBL) and electrons by the HTL (EBL).

1. Substrate
2. Anode
3. Hole injection layer (HIL)
4. Hole transport layer (HTL)
5. Emissive layer (EML)
6. Electron transport layer (ETL)
7. Electron injection layer (EIL)
8. Cathode

In the following section the different layers and their purposes will be introduced.

3.8.1 Substrate

The substrate provides mechanical support for the OLED layers and must be transparent to allow light outcoupling. Common materials used for substrates are glass, which is rigid and highly transparent and plastic (e.g., PE, PET), providing flexibility, ideal for bendable and foldable displays.

3.8.2 Anode

The anode is responsible for injecting holes into the organic layers, and for bottom-emitting OLEDs, it must also be transparent to allow light to pass through. It requires a material that is both transparent and conductive, with a work function that aligns well with the hole-injection layer (HIL) to ensure efficient hole injection. The most commonly used anode material is indium tin oxide (ITO), a transparent conductive oxide that efficiently facilitates hole injection. Its work function lies at $\Phi \sim 4.5 \text{ eV}$ [52,53]

3.8.3 Hole Injection Layer (HIL)

To further enhance hole injection and lower the energy barrier, various HIL materials are used between the anode and the hole-transport layer (HTL). These HIL materials help bridge the energy gap between the anode and the organic layers, ensuring efficient hole injection by aligning their work functions or HOMO levels with those of the anode and HTL. The combination of ITO with these HIL materials results in improved charge injection and overall device performance.

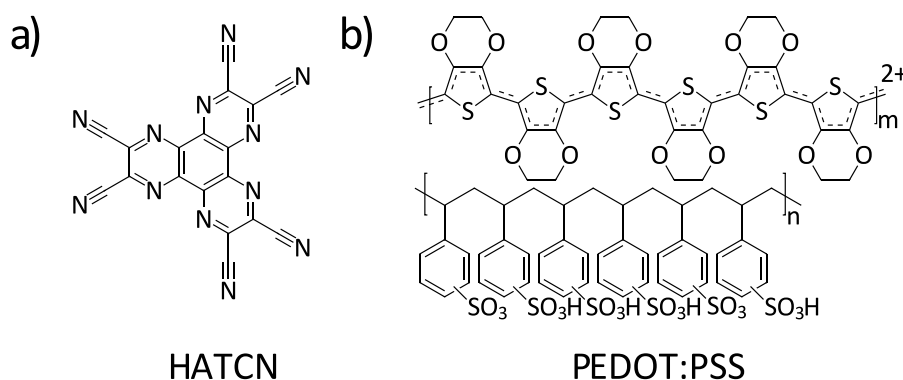


Figure 3.14: Molecular structures of HIL materials a) HATCN and b) PEDOT:PSS.

Common HIL materials include:

HATCN (s. Fig 3.14 a), a small organic molecule that has a relatively low HOMO energy level of around 7.5 eV, making it effective at improving hole injection from the anode to the HTL. It acts as an excellent hole injection facilitator when combined with ITO and is commonly used in thermally evaporated OLEDs. Its workfunction lies at 5.52 eV. ^[54]

PEDOT:PSS (s. Fig 3.14 b), a conductive polymer, with a work function around 5.1 eV, which aligns well with ITO and organic HTLs.^[52] This makes it particularly suitable for improving the hole injection process while also smoothing the ITO surface for better layer deposition. It is commonly used in solution processed OLEDs.

MoO₃ (Molybdenum trioxide) has a high work function of 6.8 eV, making it one of the most effective HIL materials for hole injection, particularly for OLEDs with higher energy barriers.^[52] It ensures excellent alignment with the HOMO levels of adjacent hole transport materials and provides a stable, conductive interface for hole transfer. Even though not strictly an organic material, it is widely used in thermally evaporated organic electronics.

3.8.4 Hole transport layer (HTL)

HTLs are essential in OLEDs, facilitating the efficient movement of holes from the HIL to the Emissive Layer (EML).

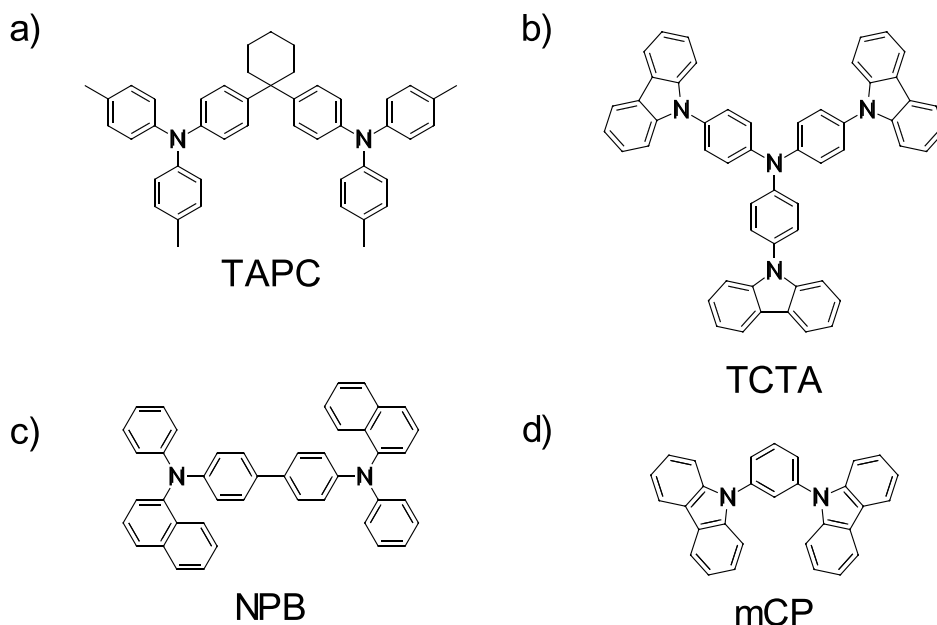
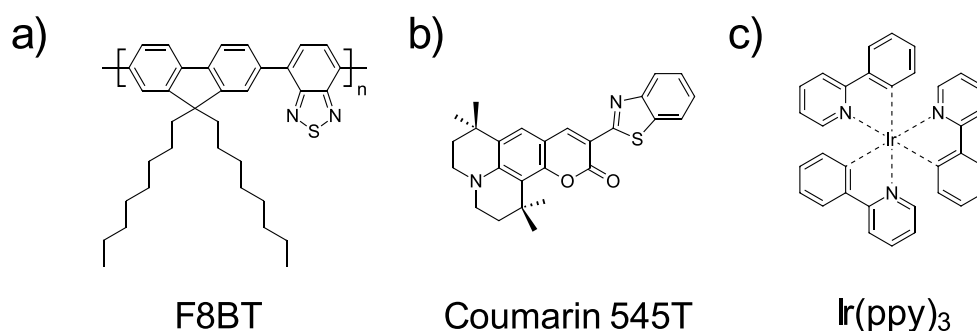


Figure 3.15: Molecular structures of HTLs materials a) TAPC, b) TCTA, c) NPB, d) mCP.

Effective hole transport materials typically incorporate electron rich structural motifs such as di-aryl amines, naphthyl groups, and carbazole units. These motifs can easily be reduced and stabilize positive charges, which are critical for optimal device performance.^[48,55] Fig 3.15 shows some commercially available materials which are commonly used in thermally evaporated OLEDs. Their HOMO energy levels lie between -5.9 and -5.4 eV. High lying LUMO levels can additionally work as electron-blocking layer (EBL).

3.8.5 Emissive Layer (EML)

The EML in OLEDs is where excitons recombine to emit light, and the choice of materials here is crucial for determining device efficiency, brightness, color purity, and stability. Emissive materials can be classified into polymeric emitters and small molecules, each suited to different applications and fabrication techniques.



efficiency and prevent concentration quenching. These emitters can be fluorescent or phosphorescent and provide excellent control over color purity for red, green, and blue emission.

Fluorescent Small Molecule Emitters Fluorescent materials emit light by singlet exciton recombination, which only allows them to utilize around 25% of generated excitons. While less efficient than phosphorescent materials, they have been widely used due to their simplicity and stability. Some examples of common fluorescent emitters include: Alq₃^[2,58] and Coumarin 545T^[59] for green fluorescence, DSA-Ph^[60] for blue fluorescent, Rubrene^[61] for orange fluorescence and DCM for red fluorescence.^[62]

Phosphorescent Small Molecule Emitters Phosphorescent emitters, such as iridium and platinum complexes, can utilize both singlet and triplet excitons, giving them nearly 100% internal quantum efficiency. Common examples include Ir(MDQ)₂(acac) (red)^[63] and Ir(ppy)₃ (green).^[64] However, stable blue phosphorescent emitters remain an ongoing challenge.

TADF Emitters TADF emitters are designed with a donor-acceptor (D-A) or donor-acceptor-donor (D-A-D) structure to achieve efficient reverse intersystem crossing (RISC) by reducing the singlet-triplet energy gap. In these structures, the donor and acceptor units are often twisted at an angle close to 90°, which spatially separates the HOMO and the LUMO. This separation minimizes overlap between the frontier orbitals, reducing the energy difference between singlet and triplet states and facilitating efficient rISC, enabling higher efficiency in light emission.

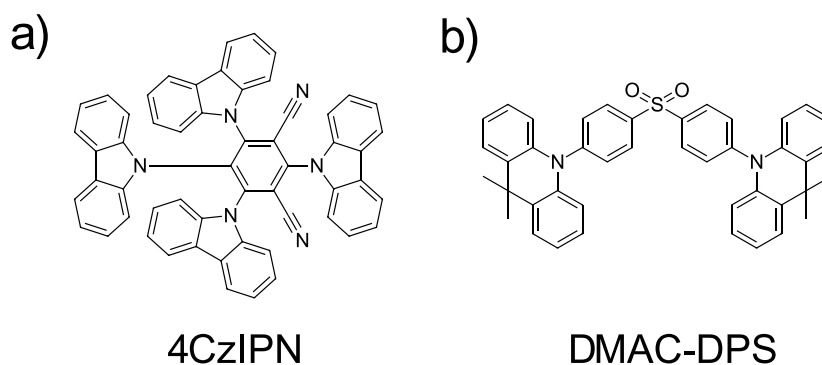


Figure 3.17: Molecular structures of a) green TADF emitter 4CzIPN, b) blue TADF emitter DMAC-DPS.

Common structural motifs include carbazole or triphenylamine, used as a donor unit due to its strong electron-donating properties and ability to stabilize positive charges. Phthalonitrile, phthalimide, acridine or sulfone are often acting as electron-acceptor units. These motifs promote effective charge transfer and optimize the TADF mechanism. Notable examples include 4CzIPN, a green TADF emitter with efficient singlet-triplet conversion^[65], and DMAC-DPS, a blue emitter recognized for its high efficiency in OLED applications^[66,67] (s. Fig 3.17).

Host Materials In small-molecule OLEDs, host materials are used to dilute the emissive dopant, preventing concentration quenching and improving charge recombination efficiency. Additionally, the emitter can act as a charge trap, increasing the probability of exciton formation on the emitter molecule, thus enhancing light emission. For effective performance, a host must have a high triplet energy to avoid quenching the triplet excitons of the emitter and should have well-aligned HOMO and LUMO levels for balanced charge injection.

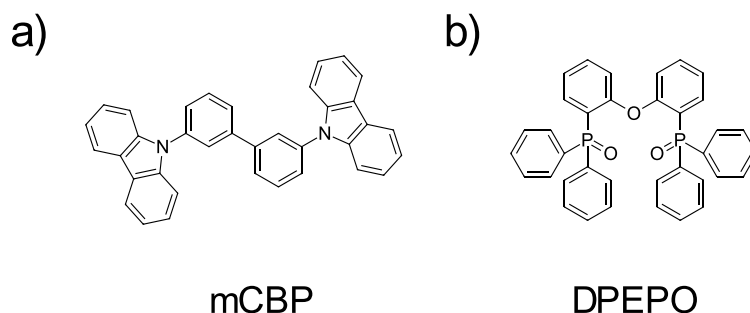


Figure 3.18: Molecular structures of a) mCBP b) DPEPO.

Common hosts include mCP (s. Fig 3.15 d) which is also common as HTL, known for its high triplet energy (2.90 eV^[68]) and suitability for blue phosphorescent and TADF OLEDs. mCBP (2.8 eV^[69]) is favored for blue and green devices due to its efficient hole transport, and DPEPO is (2.98 eV^[70]) often used in blue TADF OLEDs for its very high triplet energy, which prevents back-energy transfer and ensures efficient light emission (s. Fig 3.18).

3.8.6 Electron Transport Layer (ETL)

The electron-transport layer (ETL) in OLEDs is crucial for efficient electron injection and transport to the EML. An ideal ETL should have high electron mobility, good thermal stability, and energy levels that align well with both the EML and cathode to minimize the electron injection barrier. Many ETLs also function as hole blocking layers (HBLs) by preventing holes from leaking out of the emissive layer, thereby improving charge balance and exciton confinement. In addition, excitons are prevented from reaching the cathode, effectively avoiding cathode quenching.

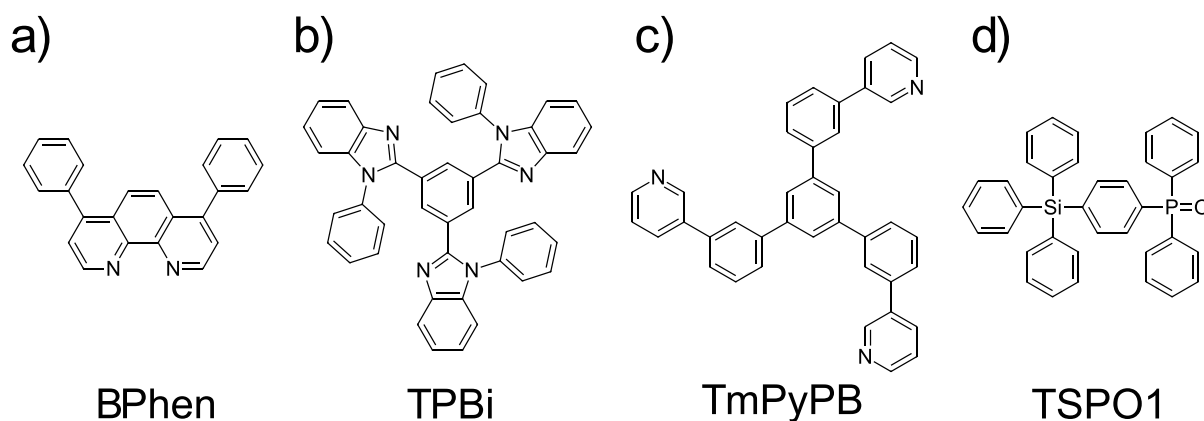


Figure 3.19: Molecular structures of ETLs a) BPhen b) TPBi c) TmPyPB d) TSP01.

Common structural motifs in ETLs include aromatic heterocycles, which contain electron-deficient nitrogen atoms that stabilize negative charges, as seen in materials like TPBi and TmPyPB. Additionally, phenanthroline derivatives, such as BPhen, provide rigid and planar structures that improve electron transport and effectively block holes due to their deep HOMO levels. Phosphine oxides, such as DPEPO and TSP01, are employed as both host materials and ETLs in OLEDs due to their high triplet energy and efficient electron injection properties. The phosphine oxide group is highly polar, which increases electron affinity and further enhances electron injection and transport.

3.8.7 Electron Injection Layer (EIL) and Cathode

Selecting appropriate cathode materials is critical for achieving efficient electron injection in an OLED. Commonly employed metals include calcium (Ca), barium (Ba), and magnesium (Mg) due to their low Fermi energies. These metals are usually applied as thin layers (1–4 nm) on the organic layer through thermal evaporation. Because these

metals are susceptible to oxidation, they are typically covered with a protective layer (100–200 nm) of a more inert metal, such as aluminum (Al) or silver (Ag).

Additionally, fluorides like lithium fluoride (LiF) and cesium fluoride (CsF) serve as electron injection layer (EIL) beneath the aluminum layer. This setup is thought to create an aligned dipole effect at the cathode interface, which improves electron injection efficiency. The aluminum layer induces dipole moments that lower its surface potential, effectively reducing its Fermi energy and facilitating electron transfer.^[71–73]

3.9 OLED Processing Techniques

OLED deposition techniques play a crucial role in determining the performance, scalability, and cost of OLED devices. Depending on the type of material and the application, different deposition methods are employed. The main techniques are VTE, PVD and solution-processed techniques, including inkjet printing and spin coating. Each technique has specific advantages, limitations, and uses that will be addressed in the following sections.

3.9.1 Vacuum Thermal Evaporation (VTE)

VTE is the most widely used deposition method for small molecule OLEDs. The process involves heating the organic material in a vacuum chamber ($10^{-8} - 10^{-6}$ mbar) until it evaporates. The vaporized molecules then travel through the vacuum and condense onto a substrate, forming a thin layer. VTE is ideal for creating high-performance, high-resolution OLED displays, making it the go-to method for smartphones, television displays, monitors, and wearable devices. The primary advantage lies in its precision and ability to produce uniform and well-controlled thin films. This is especially important when depositing multiple layers—such as the hole transport, emissive, and electron transport layers—required in OLED devices. VTE allows for these layers to be stacked without disrupting or damaging the previous ones. However, VTE has notable drawbacks. It is costly due to the need for vacuum chambers and fine metal masks, which are difficult to align. These inefficiencies, along with scalability challenges for large-area displays like OLED TVs, make VTE expensive. Despite this, it remains the dominant technique for small molecule OLEDs due to the high quality and uniformity of deposited layers.

3.9.2 Solution Processing

Solution-processed methods, like inkjet printing and spin coating, are ideal for polymer OLEDs and small molecules that dissolve in organic solvents. Solution-processed OLEDs face challenges in stacking layers for multi-layer devices, as solvents can disturb underlying layers. One commonly used solution is the use of different solvents for each layer to prevent dissolution of previous ones. It must be ensured that the previously deposited layers are not soluble in the solvent that is used for top layers. A second strategy involves organic materials that are chemically modified to form crosslinked bonds after deposition, making the layer insoluble in subsequent solvents. Once the first layer is deposited, it is exposed to heat or light, which triggers a crosslinking reaction. This crosslinked layer becomes resistant to solvents, allowing the next layer to be deposited without affecting the previous one.^[74–76]

Inkjet Printing

Inkjet printing deposits tiny droplets of organic material onto substrates, making it efficient and cost-effective for large-area and flexible OLEDs. It is gaining attention for large, flexible OLED panels, but irregular layer thicknesses, difficulties with material viscosity, solvent compatibility, and issues with substrate adhesion may negatively affect the performance of OLEDs.

Spin Coating

Spin coating, commonly used in research, spreads a solution evenly across a substrate using centrifugal force. It is low-cost but lacks precision for commercial production and multi-layer deposition. Its main limitation is the inability to pattern specific regions, making it more suited to prototyping.

4 Comprehensive Investigation of a HLCT Emitter: Spectroscopic Insights and Photophysical Properties of a Highly Luminescent Blue Chromophore

Despite the advancements in OLED technology, the quest for efficient deep-blue emitters remains a challenge. Blue light emission is critical for full-color displays, yet it is often associated with lower quantum efficiencies and insufficient long-term stability due to degradation compared to red and green emitters.

Understanding the photophysics of organic emitters is vital for the design of efficient materials capable of high quantum yields in solid-state applications. Organic emitters can be classified into various categories based on their emission mechanisms, including fluorescence, phosphorescence, TADF, and HLCT states.

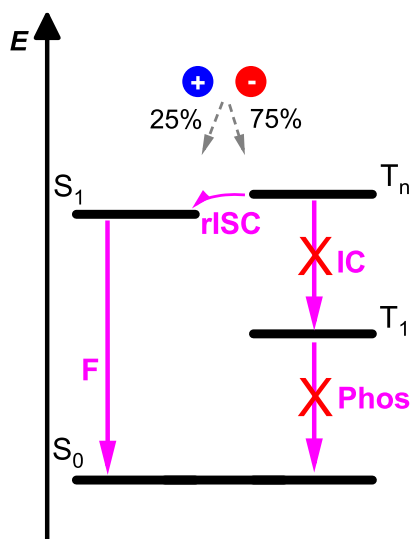


Figure 4.1: Mechanism of hot exciton (HE) processes in HLCT materials. The large T_n-T_1 energy gap in HLCT emitters inhibits internal conversion (IC), while the small T_n-S_1 energy splitting enhances rISC. This enables the conversion of high-energy triplet excitons to singlet excitons, leading to 100% exciton utilization efficiency in HE materials with HLCT properties.

Recent advancements have revealed that emitters with hybridized excited states can optimize light emission by balancing LE and CT character.^[77–81] The key difference between LE and CT states lies in the spatial separation of the excited electron. In an LE state, the electron remains localized on the same molecular fragment as the hole, resulting in strong orbital overlap and a compact exciton. In contrast, a CT state involves the electron being transferred to a different part of the molecule, creating a spatially separated electron-hole pair with a significant dipole moment. The HLCT state is highly efficient for emission in OLEDs because it combines advantages of both, LE and CT excited states. The CT component provides a large dipole moment, enhancing exciton dissociation, which is crucial in OLEDs as it reduces exciton binding energy and improves charge transport and injection

efficiency within an OLED. Meanwhile, the LE component ensures strong orbital overlap, enabling high radiative recombination rates for effective light emission. The combination of these factors also contributes to high color purity, as the LE component ensures a narrow emission spectrum while the CT component minimizes vibronic broadening.^[81] A promising advancement in OLED emitter design is the hot exciton (HE) mechanism shown in Fig. 4.1, which offers a solution to the limitations imposed by spin statistics. In OLEDs, the spin statistics during recombination dictate a 1:3 ratio of singlet to triplet excitons, meaning that only 25% of the excitons can naturally contribute to light emission in fluorescent materials. The HE mechanism overcomes this by efficiently converting high-lying triplet states T_n into singlet states S_m through rISC. This mechanism is particularly significant in HLCT emitters due to their ability to utilize the hybridized state. The LE character ensures high radiative recombination rates through strong orbital overlap, while the CT character facilitates a small energy gap between higher T_n and S_m states, enabling efficient rISC. This process minimizes energy loss by suppressing internal conversion (IC) from T_n to T_1 , ensuring that more excitons contribute to light emission rather than decaying non-radiatively.^[81]

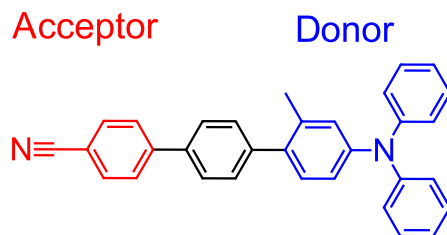


Figure 4.2: Molecular structure of **BN-Ph-MTPA**.

Wiefermann et al. studied **BN-Ph-MTPA**, a novel blue emitter (s. Fig. 4.2), highlighting its photophysical properties, which make it a highly promising candidate for OLED applications.^[82]

In section 4.1 the photophysics of **BN-Ph-MTPA** is examined, focusing on its high PLQY of near 100% in solid state. Additionally, the nature of the excited states involved in the emission process are evaluated, and the potential of the emitter for OLED applications is assessed. By combining experimental photophysical characterization with advanced quantum chemical calculations, insights into the underlying mechanisms and energetic landscape that drive the emitter’s performance are provided. Furthermore, the emitter is successfully implemented in an OLED.

In section 4.2 some additional and more detailed studies on the photophysical properties in different solvents are presented, focusing on the relaxation behavior of the excited states in changing environments and temperatures.

4.1 Publication - Highly Luminescent Blue Emitter with Balanced Hybridized Locally and Charge-Transfer Excited-States Emission

Julia Wiefermann, Jeremy M. Kaminski, **Elisabeth Pankert**, Dirk Hertel, Klaus Meerholz, Christel M. Marian, and Thomas J. J. Müller

Highly Luminescent Blue Emitter with Balanced Hybridized Locally and Charge-Transfer Excited-States Emission

ChemPhotoChem 2023, 7, 1-6

Reprinted with permission from ref. ^[83] ©2022 Wiley-VCH GmbH.

doi.org/10.1002/cptc.202200265

Supporting Information can be found in 10.2.1

Contributions by E.Pankert to this publication:

- Design and fabrication of OLEDs
 - Characterization of OLEDs via L-J-V, EQE and EL spectroscopy
 - Experimentally estimation of ΔE_{ST} via time-resolved and temperature dependent PL spectroscopy.
 - Measurement of PLQY in different solvents.
 - Recording of cyclic voltammetry (CV)
 - Determination of thermal properties via thermogravimetric analysis (TGA)
 - Creating Figure 5 and Figure S12 - S15 (Supporting Information, s.10.2.1) and contributing to writing the manuscript.
-



Highly Luminescent Blue Emitter with Balanced Hybridized Locally and Charge-Transfer Excited-States Emission

Julia Wiefermann^{+, [a]} Jeremy M. Kaminski^{+, [b]} Elisabeth Pankert,^[c] Dirk Hertel,^[c] Klaus Meerholz,^[c] Christel M. Marian,^[b] and Thomas J. J. Müller^{*, [a]}

Dedicated to Prof. Dr. A. Stephen K. Hashmi on the occasion of his 60th birthday

In this work, we perform an in-depth investigation of the optoelectronic properties of a blue emitter (4''-(diphenylamino)-2''-methyl-[1,1':4',1''-terphenyl]-4-carbonitrile), which was reported earlier. Lippert–Mataga analysis of the emission spectra obtained in solvents of varying polarity reveal charge transfer (CT) contributions to the first singlet excited state, S_1 . Multi-reference quantum chemical calculations clearly show a bal-

anced local excitation (LE) and CT character of the S_1 state and suggests the presence of a LE triplet state, T_2 , in its energetic vicinity. Finally, organic light emitting diodes (OLED) revealed blue emission at 451 nm and an external quantum efficiency (EQE) of 2%, corresponding to an internal quantum efficiency (IQE) of circa 10%.

Introduction

In recent years organic electronics paved its way into daily life and has steadily become a focus of research. Organic functional chromophores have attracted wide attention due to flexible processability, low power consumption, and the absence of toxic and expensive heavy metals as an advantageous aspect of sustainability and applicability.^[1] In the first and third generation of organic light emitting diodes (OLEDs) purely organic materials already found entry as emissive materials.^[2] Prerequisite for the application as emissive materials are high luminescence quantum yields in the solid state, good thermal and oxidative stability, and a high color purity.^[3] For full-color displays new materials are indispensable and especially efficient deep-blue emitters are highly demanded.^[4] Spin-

statistics dictate the formation of 25% singlet excitons and 75% triplet excitons upon hole-electron recombination.^[5] According to the underlying mechanism, emissive materials are divided into classical fluorescence,^[6] phosphorescence,^[7] thermally activated delayed fluorescence (TADF),^[8] and hybridized locally excited (LE) and charge transfer (CT) excited state (HLCT) emitters.^[9] In classical fluorescent materials, the triplet excitons remain wasted due to non-radiative deactivation pathways.^[10] And classical fluorescence emitters limit the internal quantum efficiency (IQE) of the OLED to 25%.^[2] For harvesting the remaining 75% triplet excitons phosphorescent heavy-metal complexes have been employed as emitters for the second generation of OLEDs.^[7b] Another approach for harvesting the triplet excitons is the use of TADF emitters. They characteristically possess a small energy gap (ΔE_{ST}) between the lowest lying singlet (S_1) and triplet (T_1) excited states. It enables thermally activated reverse intersystem crossing (rISC) upconversion of triplet excitons to generate singlet excitons, which radiatively relax rapidly as delayed fluorescence to the ground state. Theoretically, the IQE can be optimized up to 100%.^[11] For HLCT materials, a hybridized local and charge transfer excited state occurs, which leads to a high photoluminescence quantum yield (PLQY) Φ_{PL} and high exciton utilization efficiency by rISC from a higher-lying triplet state.^[12]

Here, we present an in-depth investigation of the optoelectronic properties of a highly luminescent blue organic emitter (4''-(diphenylamino)-2''-methyl-[1,1':4',1''-terphenyl]-4-carbonitrile) with balanced LE and CT contributions. The origin of emission is examined by advanced quantum chemical calculations and photophysical experiments. In addition, the suitability for application in OLED devices is investigated.

[a] J. Wiefermann,⁺ Prof. Dr. T. J. J. Müller
Institute of Organic Chemistry and Macromolecular Chemistry
Heinrich Heine University Düsseldorf
Universitätsstraße 1, 40225 Düsseldorf (Germany)
E-mail: Thomas.J.J.Mueller@hhu.de

[b] J. M. Kaminski,⁺ Prof. Dr. C. M. Marian
Institute of Theoretical and Computational Chemistry
Heinrich Heine University Düsseldorf
Universitätsstraße 1
40225 Düsseldorf (Germany)

[c] E. Pankert, Dr. D. Hertel, Prof. Dr. K. Meerholz
Department of Chemistry
University of Cologne
Greinstraße 4–6
50939 Köln (Germany)

[*] These authors contributed equally to this work.

Supporting information for this article is available on the WWW under <https://doi.org/10.1002/cptc.202200265>

An invited contribution to a Special Collection on Emissive Materials for Organic Light Emitting Diodes

© 2022 The Authors. ChemPhotoChem published by Wiley-VCH GmbH. This is an open access article under the terms of the Creative Commons Attribution Non-Commercial License, which permits use, distribution and reproduction in any medium, provided the original work is properly cited and is not used for commercial purposes.

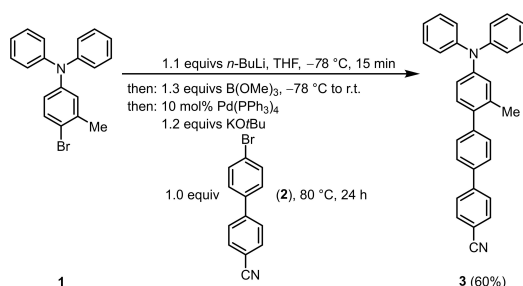
Results and Discussion

Synthesis

Recently, we showed that functional donor-acceptor TADF chromophores are efficiently accessed by one-pot methodologies.^[13] This approach was also successfully applied to study effects of extended π -conjugation with steric hindrance in a series of four terphenyl based blue emitters.^[14] Here, we selected the most intensely emissive molecule **3** with PLQYs of 0.96 and higher in solution (toluene, dichloromethane), in the solid state and in a PMMA film. The synthesis takes advantage of practical one-pot bromine-lithium exchange borylation-Suzuki (BLEBS) sequence^[15] starting from 4-bromo-3-methyl-*N,N*-diphenylaniline (**1**) as the donor part and 4'-bromo-[1,1'-biphenyl]-4-carbonitrile (**2**) as acceptor coupling partner (Scheme 1).

Photophysical properties

Absorption and emission spectra were recorded in nine solvents of variable solvent polarity with different orientation polarizations (Δf) (Figure 1). Evidently, the absorption is not significantly affected by the solvent polarity, indicating the weak dipole moment in the ground state. The compound reveals two distinctly separated absorption maxima in each



Scheme 1. BLEBS sequence for the synthesis of the *p*-phenylene bridged D-A compound **3**.

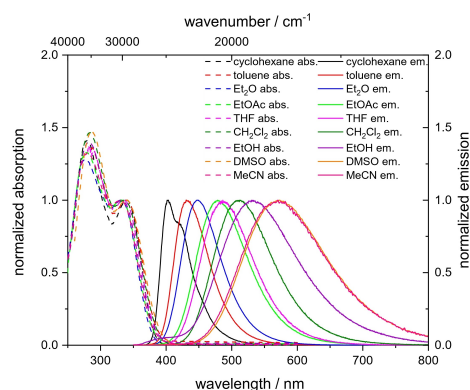


Figure 1. UV/Vis absorption (dashed) and emission spectra (solid) of compound **3** in different solvents normalized on the longest wavelength absorption band (recorded at $T = 293$ K, $c(\mathbf{3}) = 10^{-5}$ M for absorption spectra and $c(\mathbf{3}) = 10^{-6}$ M for emission spectra, $\lambda_{exc} = \lambda_{max,abs}$).

solvent. The absorption maximum at higher energy lies between 277 nm (diethyl ether) and 290 nm (THF). The absorption maximum at lower energy appears in a range from 330 to 340 nm.

The emission strongly shifts bathochromically for solvents of higher polarity, ranging from 404 to 572 nm ($\Delta\tilde{\nu} = 7,270$ cm^{-1}). This positive solvatochromism is easily visible to the naked eye and covers the color spectrum from blue (cyclohexane) to yellow orange (dimethylsulfoxide) accompanied by large Stokes shifts of up to 12,790 cm^{-1} (Table 1, Figure 2).

Emission bands in nonpolar solvents, such as cyclohexane and toluene, have a FWHM (full width at half maximum) of 0.36 and 0.39 eV, respectively. In cyclohexane, a shoulder on the low energy side is observed, indicating some vibrational structure and a significant local contribution to the excited state of **3**.^[16] Emission bands become broader with increasing solvent polarity up to a FWHM value of 0.59 eV. The substantial solvatochromism indicates a CT character of the first excited singlet state. However, the high radiative rate constant of $2.53 \cdot 10^8$ s^{-1} in dichloromethane, derived from mono-exponential fitting of

Table 1. Selected photophysical properties of compound **3**.

	$\lambda_{max,abs}$ [nm] (ϵ [$\text{M}^{-1}\text{cm}^{-1}$])	λ_{em} [nm] (Φ_F) ^[a]	τ [ns]	k_f [s^{-1}]	k_{nr} [s^{-1}]	Δf ^[b]	Stokes shift ^[c] [cm^{-1}]	FWHM ^[d] [nm] [eV]	CIE
cyclohexane	280 (40570), 340 (28620)	404 (0.97)	1.28	$7.58 \cdot 10^8$	$2.34 \cdot 10^7$	-10.00165	4660	49 (0.36)	0.159, 0.031
toluene	287 (33750), 339 (24830)	431 (0.99)	1.86	$5.32 \cdot 10^8$	$5.38 \cdot 10^6$	0.01324	6300	61 (0.39)	0.153, 0.059
Et ₂ O	277 (27600), 331 (21650)	448 (0.91)	2.15	$4.23 \cdot 10^8$	$4.19 \cdot 10^7$	0.16700	7890	70 (0.43)	0.150, 0.098
EtOAc	279 (32450), 330 (24360)	478 (0.83)	2.78	$2.99 \cdot 10^8$	$6.12 \cdot 10^7$	0.19964	9380	91 (0.48)	0.171, 0.264
THF	290 (39150), 335 (29100)	487 (0.88)	2.93	$3.00 \cdot 10^8$	$4.10 \cdot 10^7$	0.20728	9320	93 (0.46)	0.182, 0.312
CH ₂ Cl ₂	284 (37360), 336 (25580)	512 (0.99)	3.91	$2.53 \cdot 10^8$	$2.56 \cdot 10^6$	0.21710	10230	104 (0.48)	0.250, 0.455
EtOH	282 (47530), 330 (33750)	532 (0.50)	2.24	$2.23 \cdot 10^8$	$2.23 \cdot 10^6$	0.26301	12020	132 (0.59)	0.325, 0.471
DMSO	286 (34300), 339 (23290)	572 (0.49)	4.43	$1.11 \cdot 10^8$	$1.15 \cdot 10^6$	0.28874	11500	149 (0.55)	0.434, 0.505
MeCN	280 (43170), 330 (32560)	571 (0.63)	3.96	$1.59 \cdot 10^8$	$9.34 \cdot 10^7$	0.30542	12790	149 (0.55)	0.426, 0.504
in the solid state ^[14]	402	450 (0.98)	8.16	$1.20 \cdot 10^8$	$2.45 \cdot 10^6$	–	2650	46 (0.28)	0.150, 0.088
in 1 wt% PMMA film ^[14]	362	430 (0.96)	2.22	$4.32 \cdot 10^8$	$1.80 \cdot 10^7$	–	4370	61 (0.41)	0.155, 0.060

[a] Absolute quantum yields determined using an integrating sphere. [b] $\Delta f = \frac{f_y - 1}{2f_x + 1} - \frac{n^2 - 1}{2n^2 + 1}$. [c] $\Delta\tilde{\nu} = \frac{1}{\lambda_{max,abs}} - \frac{1}{\lambda_{max,em}}$. [d] Full width at half maximum.

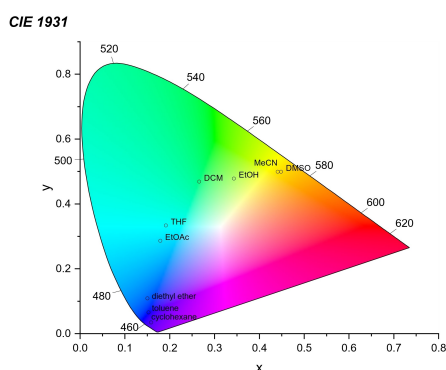


Figure 2. CIE diagram expressing the positive emission solvatochromicity of compound 3.

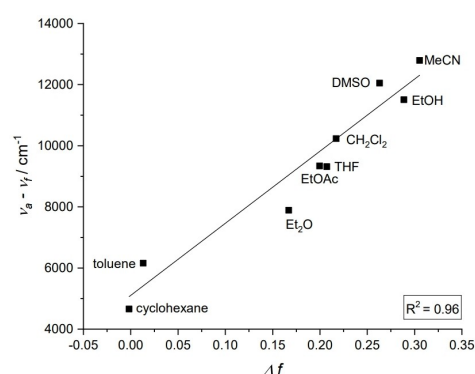


Figure 3. Lippert-Mataga plot for compound 3 ($R^2 = 0.96$).

the luminescence decays and demonstrating a single emissive species,^[14] is untypical for pure CT transitions, typically occurring around 10^6 s⁻¹, and evidence for some LE contribution to the S₁ state.

Fluorescence lifetimes between 1–4 ns fall into a typical range for organic chromophores.^[17] In nonpolar solvents such as cyclohexane and toluene, the compound reveals short lifetimes of 1.28 and 1.86 ns, respectively. With increasing solvent polarity, the lifetime prolongates up to 4.43 ns in DMSO, with the exception of the lifetime in ethanol (2.24 ns), which is even shorter than in ethyl acetate (2.78 ns). This can be rationalized by nonradiative deactivation of the excited state by hydrogen bonding via amine and nitrile groups.^[18] The general trend of increased lifetimes in more polar solvents corresponds to the bathochromic shift in emission and the cubic dependence of the spontaneous emission probability on the transition frequency.^[17]

The emission solvatochromism is explained by a change in the dipole moment of the fluorophore upon excitation and dipole relaxation of the surrounding solvent molecules.^[18] Therefore, it was further assessed by applying the Lippert-Mataga model.^[19] The Stokes shift correlates linearly with the Lippert-Mataga polarity parameter Δf (Figure 3) indicative of a large change in dipole moment $\Delta\mu$ from the ground to the excited state upon excitation. From the slope of the fit using the Lippert-Mataga equation (see Equation S1) $\Delta\mu \approx 21$ D was obtained, where an Onsager radius of 5.60 Å was estimated from the optimized geometry and crystal structural data.^[14]

Low-temperature measurements at 110 K in toluene/cyclohexane allow for estimating a $\Delta E_{S_1-T_1}$ value of 0.82 eV (see Figure S12) in good agreement with quantum chemical calculations (0.76 eV; see below). Therefore, we conclude that reverse intersystem crossing (rISC) of the T₁ population is highly unlikely,^[20] and **3** can be classified as typical singlet emitter.

Quantum chemical calculations

In order to rationalize why **3** is such a highly efficient emitter, its electronic and structural properties were analyzed using combined density functional theory (DFT) and multireference configuration interaction (MRCI) methods. Geometry optimizations of the excited states were performed using time-dependent density functional theory^[21] (TD-DFT) in conjunction with range-separated hybrid density functional ω B97X-D^[22] and the def2-TZVP^[23] basis set. During an optimal tuning procedure,^[24] the optimal value for the range-separation parameter was found to be $\omega = 0.14$ a.u.⁻¹ (see Figure S16). The influence of solvation was considered via the polarizable continuum model^[25] (PCM) using the solvent excluding surface (SES) implemented in Gaussian16.^[26] Note, that the PCM includes only the instantaneous response of the solvent environment to the electronic excitation of the solute and does not account of solvent reorganization effects. Excitation energies, dipole moments and photophysical properties were calculated subsequently with the DFT/MRCI^[27] approach and the R2016^[28] parametrization, which is specially designed for organic systems consisting of various chromogenic units.

The calculated absorption spectrum of **3** in toluene solution comprises two strong and two medium strong singlet transitions in the wavelength region between 350 and 280 nm. The first peak in the experimental absorption spectrum ($\lambda_{\text{max}} = 339$ nm) is assigned to the very intense S₀→S₁ transition found at 350 nm in our calculations with an oscillator strength of $f = 0.789$ and a huge change of the static electric dipole moment by more than 24 D indicating substantial contributions of LE as well as CT character.

The second peak with maximum at 4.32 eV ($\lambda_{\text{max}} = 287$ nm) in toluene is composed of three electronic transitions according to our calculations, i.e., a medium strong ($f = 0.248$) local excitation (LE) on the donor moiety at 4.18 eV (297 nm), a strong ($f = 0.667$) excitation at 4.41 eV (281 nm) and a close-by weaker ($f = 0.177$) transition at 4.43 eV (280 nm), both with mixed CT and LE character on the acceptor moiety. Interestingly, four triplet excited states (3.02 eV, 3.27 eV, 3.39 eV,

3.42 eV) are lying energetically below the first excited singlet state (S_1 , 3.54 eV).

Analyses of the transition densities via the program package TheoDOR^[29] confirm that the first excited singlet state S_1 adopts a hybrid electronic structure of roughly 50% CT and 45% LE single excitation character in the Franck-Condon region ($S_1@S_0$, Figure 4D). The remaining 5% originate from double excitations or even higher excitations. The percentage of the CT and donor LE to the wavefunction slightly decreases in favor of the acceptor LE when the molecular geometry is relaxed in the S_1 state ($S_1@S_1$, Figure 4D). The change of the wavefunction composition is mainly brought about by a flattening of the torsional angle between the donor and acceptor units and a reduction of the C–C bond connecting them. The increased delocalization of the π -system affects a substantial enhancement of the emission oscillator strength ($f = 1.455$) by roughly a factor of two compared to absorption. The natural transition orbitals (NTOs) also show that the *p*-phenylene bridge is fully involved in the electronic transition (Figure 4A) and cannot be considered an innocent spacer.

The fluorescence with calculated emission wavelength of 462 nm and radiative rate constant ($k_f = 4.5 \cdot 10^8 \text{ s}^{-1}$) is predicted to be highly anisotropic, with the electric transition dipole vector pointing along the axis connecting the donor and acceptor subunits. A ¹HLCT excited state with an optimal blend of LE and CT character can take advantage from both – having

a strong and fast radiative fluorescence emission to compete with nonradiative pathways next to fast rISC from nearby ³CT or ³LE states via a hot exciton channel.^[9a]

In the following, the ability of compound **3** to undergo triplet-to-singlet up-conversion will be investigated in more detail. The optimized T_1 state shows about 30% CT and 65% LE character (Figure 4D). The NTOs (Figure 4B) suggest that the LE character mainly originates from the acceptor moiety. Its adiabatic energy is found to be 2.25 eV including zero-point vibrational energy (ZPVE) correction, resulting in a large singlet–triplet splitting between S_1 and T_1 of 0.76 eV, in good agreement with experiment (0.82 eV; see above). This result confirms the assumption that a thermally activated T_1 -to- S_1 up-conversion is energetically not feasible. Excitons populating the T_1 state can, therefore, not be harvested for the fluorescence process. The forward S_1 -to- T_1 ISC, for which we compute a rate constant of $k_{ISC} = 2.2 \cdot 10^6 \text{ s}^{-1}$ in Condon approximation using the VIBES program,^[30] cannot compete against the 200 times faster fluorescence, thus explaining the high PLQY value close to 1 observed in experiment. A very small adiabatic energy difference is found between the S_1 and T_2 state. The optimization of the T_2 geometry leads to an adiabatic energy of 2.96 eV including ZPVE correction, only 0.05 eV below the S_1 state. Due to the small energy gap, forward and backward ISC between S_1 and T_2 might therefore be possible.

T_2 is a multiconfigurational state that cannot be described by a single pair of NTOs (Figure 4C). With more than 80% LE character, evenly distributed on the donor and acceptor moiety (Figure 4D), one might expect its spin-orbit coupling to the S_1 state to be higher than between pure CT excited states. However, these expectations are not fulfilled because the rISC rate constant (T_2 to S_1) is only in the order of 10^4 s^{-1} in Condon approximation, i.e., by far not competitive with the non-radiative transition to the T_1 state. Therefore, triplet excitons will contribute to the luminescence to a minor extent only, if at all. An overview of the kinetic scheme based on our computational results is presented in Scheme 2.

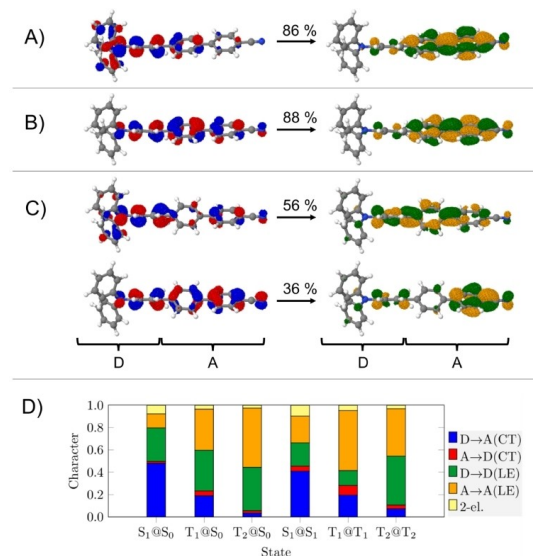
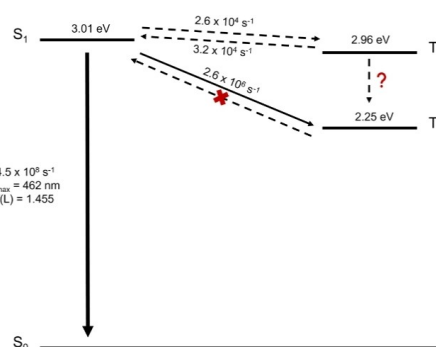


Figure 4. NTOs for (A) the S_1 state, (B) the T_1 state and (C) the T_2 state at their respective minimum geometries in toluene. The NTO from which the excitation takes place is shown in blue and red, the NTO into which the electron is excited is depicted in green and yellow. The numbers (86%, 88%, 56 + 36%) indicate the relative importance in describing the excitation by the given pair of NTOs. (D) Analysis of the excitation characters of the S_1 , T_1 and T_2 states at the S_0 geometry (Franck-Condon region) and at the respective minimum geometries of the excited states (D: donor and A: acceptor).



Scheme 2. Adiabatic energies with ZPVE correction, rate constants for radiative (fluorescence) and nonradiative transitions (ISC and rISC) based on our theoretical results in toluene solution.

OLED fabrication

In order to assess the potential of compound **3** as an OLED emitter, we fabricated via evaporation in high-vacuum devices of the following structure: ITO/MoO₃ (6 nm)/NPB (60 nm)/mCP (10 nm)/EML (20 nm)/DPEPO (10 nm)/Bphen (20 nm)/LiF (3 nm)/Al (100 nm) (see SI/experimental for details) (Figure 5). Here, ITO (indium tin oxide) serves as transparent anode (bottom contact) and MoO₃ as hole-injection layer. NPB (*N,N'*-di(1-naphthyl)-*N,N'*-diphenyl-(1,1'-biphenyl)-4,4'-diamine) and mCP (1,3-bis(*N*-carbazolyl)benzene) were used as hole-transport materials, respectively. As emissive layer (EML), we tested compound **3** in a DPEPO-matrix (10 wt%) (bis[2-(diphenylphosphano)phenyl]-ether oxide) (**device 1**) and as a neat film (**device 2**). DPEPO and Bphen (bathophenanthroline) were utilized as electron-transport and hole-blocking layers, respectively. Finally, lithium fluoride and aluminium served as cathode material (top contact).

Both device types showed deep blue emission with an EL maximum at 451 nm and a FWHM of 60 nm. The respective CIE coordinates ($x=0.150$, $y=0.104$) fall within the range recommended by ITU-R for blue emitters in OLED displays. Comparison of the two devices shows, that **device 1** has a stronger "roll-off" at higher voltages as compared to **device 2**, indicating a better charge carrier balance in the latter case. We attribute this to a broader emission zone and reduced exciton density due to a higher number of recombination centers. Therefore, the brightness at an applied voltage of 8 V reached ca. 12 cd/m² (177 cd/m²) for **device 1** and **device 2**, respectively. Both devices reached a current (power) efficiency of ~2.8 Cd/A (~1.9 lm/W), corresponding to an EQE of ca. 2% and an IQE of ca. 10% for **device 2**, assuming an outcoupling efficiency of 20%.^[31] This is about 40% of the maximum to be expected for a singlet emitter, assuming 25% singlet formation efficiency upon recombination and 94% experimental PLQY. These results prove the potential of compound **3** as a singlet emitter, but

further optimization of the layer stack is needed to enhance the brightness and EQE of the device.

Conclusion

We performed an in-depth study of the strongly blue fluorescent twisted diphenylamino cyano terphenylene dye **3**. Its electronic properties classify compound **3** as a balanced HLCT photoluminescence emitter, further substantiated by quantum chemical calculations. Emission is strongly solvatochromic, exhibiting large Stokes shifts, while the absorption is not affected by solvent polarity. The analysis of the wavefunction contributions in the first excited state indicates a balanced HLCT state, responsible for high quantum yields also in polar solvents. Moreover, compound **3** reveals a strong and fast radiative emission. Regarding the molecular design the extension of the π -system by *p*-phenylene bridging is apparently crucial for obtaining balanced LE and CT contributions. The ligating *p*-phenylene bridge is strongly involved in the electronic transitions and, therefore, represents a handle for their finetuning and altering in future studies that are underway.

Application in OLED devices shows deep-blue emission in the range of recommended values for blue emitters in OLED displays by ITU-R, but the low IQE of about 10% suggests that only singlet excitons are harvested in these devices. The large energetic splitting of the first excited singlet and triplet states prevents the up-conversion of the T₁ population to the S₁ state by reverse intersystem crossing. Our calculations locate the T₂ state in close energetic proximity of the S₁. However, due to the low T₂-to-S₁ rISC rate constants, caused by the small mutual spin-orbit coupling between these states, only a low contribution of triplet excitons to the electroluminescence is expected.

Experimental Section

All experimental details, such as referenced and described, absorption and emission spectra, cyclic voltammetry, thermogravimetric analysis, differential scanning calorimetry, OLED characteristics as well as quantum chemical calculations are included in the Supporting Information.

Acknowledgements

The authors cordially thank the DFG (396890929/RTG 2482-1, Mu 1088/9-1) and the Fonds der Chemischen Industrie. Open Access funding enabled and organized by Projekt DEAL.

Conflict of Interest

The authors declare no conflict of interest.

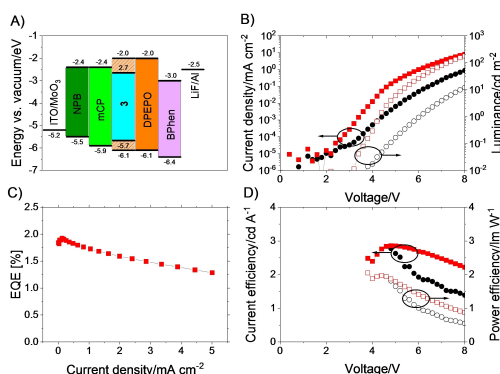


Figure 5. A) Energy diagram of **device 1** (EML: 10 wt % of compound **3** in a DPEPO matrix) and **device 2** (EML: **3** in neat film); B) luminance (open symbols)-current density (solid symbols)-voltage (L-J-V) characteristics; C) EQE-current density characteristics; D) Current (solid symbols) and power (open symbols) efficiencies, respectively. The lines are guide to the eye.

Data Availability Statement

The data that support the findings of this study are available from the corresponding author upon reasonable request.

Keywords: density functional calculations · donor-acceptor systems · optoelectronics · organic light-emitting diodes · solvatochromism

- [1] a) S. E. Root, S. Savagatrup, A. D. Printz, D. Rodriguez, D. J. Lipomi, *Chem. Rev.* **2017**, *117*, 6467–6499; b) J.-H. Jou, S. Kumar, A. Agrawal, T.-H. Li, S. Sahoo, *J. Mater. Chem. C* **2015**, *3*, 2974–3002; c) N. Sun, C. Jiang, Q. Li, D. Tan, S. Bi, J. Song, *J. Mater. Sci. Mater. Electron.* **2020**, *31*, 20688–20729.
- [2] G. Hong, X. Gan, C. Leonhardt, Z. Zhang, J. Seibert, J. M. Busch, S. Bräse, *Adv. Mater.* **2021**, *33*, e2005630.
- [3] B. Geffroy, P. Le Roy, C. Prat, *Polym. Int.* **2006**, *55*, 572–582.
- [4] Y. Im, S. Y. Byun, J. H. Kim, D. R. Lee, C. S. Oh, K. S. Yook, J. Y. Lee, *Adv. Funct. Mater.* **2017**, *27*, 1603007.
- [5] S.-J. Su, E. Gonmori, H. Sasabe, J. Kido, *Adv. Mater.* **2008**, 4189–4194.
- [6] C. W. Tang, S. A. VanSlyke, *Appl. Phys. Lett.* **1987**, *51*, 913–915.
- [7] a) M. A. Baldo, S. Lamansky, P. E. Burrows, M. E. Thompson, S. R. Forrest, *Appl. Phys. Lett.* **1999**, *75*, 4–6; b) Baldo, Thompson, Forrest, *Nature* **2000**, *403*, 750–753.
- [8] H. Uoyama, K. Goushi, K. Shizu, H. Nomura, C. Adachi, *Nature* **2012**, *492*, 234–238.
- [9] a) T. Liu, X. Chen, J. Zhao, W. Wei, Z. Mao, W. Wu, S. Jiao, Y. Liu, Z. Yang, Z. Chi, *Chem. Sci.* **2021**, *12*, 5171–5176; b) W. Li, Y. Pan, R. Xiao, Q. Peng, S. Zhang, D. Ma, F. Li, F. Shen, Y. Wang, B. Yang, Y. Ma, *Adv. Funct. Mater.* **2014**, *24*, 1609–1614; c) N. Sharma, M. Y. Wong, D. Hall, E. Spuling, F. Tenopala-Carmona, A. Privitera, G. Copley, D. B. Cordes, A. M. Z. Slawin, C. Murawski, M. C. Gather, D. Beljonne, Y. Olivier, I. D. W. Samuel, E. Zysman-Colman, *J. Mater. Chem. C* **2020**, *8*, 3773–3783; d) S. Zhang, L. Yao, Q. Peng, W. Li, Y. Pan, R. Xiao, Y. Gao, C. Gu, Z. Wang, P. Lu, F. Li, S. Su, B. Yang, Y. Ma, *Adv. Funct. Mater.* **2015**, *25*, 1755–1762.
- [10] S. Reineke, M. A. Baldo, *Phys. Status Solidi A* **2012**, *209*, 2341–2353.
- [11] Z. Yang, Z. Mao, Z. Xie, Y. Zhang, S. Liu, J. Zhao, J. Xu, Z. Chi, M. P. Aldred, *Chem. Soc. Rev.* **2017**, *46*, 915–1016.
- [12] a) X. Tian, M. Yao, X. Liang, C. Zhou, S. Xiao, Y. Gao, H. Liu, S.-T. Zhang, B. Yang, *Dyes Pigm.* **2022**, 110463; b) J. Li, M. Zhang, T. Li, D. Guo, T. Tian, H. Zhang, *J. Mater. Chem. C* **2022**, *10*, 13124–13136.
- [13] G. A. Sommer, L. N. Mataranga-Popa, R. Czerwieniec, T. Hofbeck, H. H. H. Homeier, T. J. J. Müller, H. Yersin, *J. Phys. Chem. Lett.* **2018**, *9*, 3692–3697.
- [14] J. Wiefermann, P. Schmeinc, C. Ganter, T. J. J. Müller, *Chem. Eur. J.* **2022**, e202200576.
- [15] A. Franz, T. Müller, *Synthesis* **2008**, 2008, 1121–1125.
- [16] J. Yang, Q. Guo, J. Wang, Z. Ren, J. Chen, Q. Peng, D. Ma, Z. Li, *Adv. Opt. Mater.* **2018**, *6*, 1800342.
- [17] in *Principles of Fluorescence Spectroscopy*; (Ed. J. R. Lakowicz), Springer US, Boston, MA, **2006**, pp. 205–235.
- [18] C. Reichardt, T. Welton, *Solvents and Solvent Effects in Organic Chemistry*; Wiley-VCH Verlag GmbH & Co. KGaA, Weinheim, Germany, **2010**, 384–386.
- [19] a) N. Mataga, Y. Kaifu, M. Koizumi, *BCSJ* **1956**, *29*, 465–470; b) E. Lippert, *Berichte der Bunsengesellschaft für physikalische Chemie* **1957**, 962–975.
- [20] a) C. Adachi, *Jpn. J. Appl. Phys.* **2014**, *53*, 60101; b) X. Liu, W. Liu, W. Dongyu, X. Wie, L. Wang, H. Wang, Y. Miao, H. Xu, J. Yu, B. Xu, *J. Mater. Chem. C* **2020**, *8*, 14117–14124.
- [21] a) E. Runge, E. K. U. Gross, *Phys. Rev. Lett.* **1984**, *52*, 997–1000; b) A. Dreuw, M. Head-Gordon, *J. Am. Chem. Soc.* **2004**, *126*, 4007–4016; c) F. Furche, R. Ahlrichs, *J. Chem. Phys.* **2002**, *117*, 7433–7447; d) S. Hirata, M. Head-Gordon, *Chem. Phys. Lett.* **1999**, *314*, 291–299; e) R. Beig, B.-G. Englert, U. Frisch, P. Hänggi, K. Hepp, W. Hillebrandt, D. Imboden, R. L. Jaffe, R. Lipowsky, H. v. Löhneysen, I. Ojima, D. Sornette, S. Theisen, W. Weise, J. Wess, J. Zittartz, C. Fiolhais, F. Nogueira, M. A. L. Marques, Eds, *A Primer in Density Functional Theory*, Springer Berlin Heidelberg, Berlin, Heidelberg, **2003**, 144–158.
- [22] a) J.-D. Chai, M. Head-Gordon, *Phys. Chem. Chem. Phys.* **2008**, *10*, 6615–6620; b) J.-D. Chai, M. Head-Gordon, *J. Chem. Phys.* **2008**, *128*, 84106.
- [23] a) A. Schäfer, H. Horn, R. Ahlrichs, *J. Chem. Phys.* **1992**, *97*, 2571–2577; b) F. Weigend, *Phys. Chem. Chem. Phys.* **2006**, *8*, 1057–1065.
- [24] a) D. Jacquemin, B. Moore, A. Planchat, C. Adamo, J. Autschbach, *J. Chem. Theory Comput.* **2014**, *10*, 1677–1685; b) R. Baer, E. Livshits, U. Salzner, *Annu. Rev. Phys. Chem.* **2010**, *61*, 85–109; c) L. Kronik, T. Stein, S. Refaely-Abramson, R. Baer, *J. Chem. Theory Comput.* **2012**, *8*, 1515–1531; d) L. Kronik, S. Kümmel, *Adv. Mater.* **2018**, *30*, e1706560.
- [25] a) E. Cancès, B. Mennucci, J. Tomasi, *J. Chem. Phys.* **1997**, *107*, 3032–3041; b) R. Cammi, S. Corni, B. Mennucci, J. Tomasi, *J. Chem. Phys.* **2005**, *122*, 104513; c) G. Scalmani, M. J. Frisch, B. Mennucci, J. Tomasi, R. Cammi, V. Barone, *J. Chem. Phys.* **2006**, *124*, 94107.
- [26] M. J. Frisch, G. W. Trucks, H. B. Schlegel, G. E. Scuseria, M. A. Robb, J. R. Cheeseman, G. Scalmani, V. Barone, G. A. Petersson, H. Nakatsuji, X. Li, M. Caricato, A. V. Marenich, J. Bloino, B. G. Janesko, R. Gomperts, B. Mennucci, H. P. Hratchian, J. V. Ortiz, A. F. Izmaylov, J. L. Sonnenberg, D. Williams-Young, F. Ding, F. Lipparini, F. Egidi, J. Goings, B. Peng, A. Petrone, T. Henderson, D. Ranasinghe, V. G. Zakrzewski, J. Gao, N. Rega, G. Zheng, W. Liang, M. Hada, M. Ehara, K. Toyota, R. Fukuda, J. Hasegawa, M. Ishida, T. Nakajima, Y. Honda, O. Kitao, H. Nakai, T. Vreven, K. Throssell, J. A. Montgomery, Jr., J. E. Peralta, F. Ogliaro, M. J. Bearpark, J. J. Heyd, E. N. Brothers, K. N. Kudin, V. N. Staroverov, T. A. Keith, R. Kobayashi, J. Normand, K. Raghavachari, A. P. Rendell, J. C. Burant, S. S. Iyengar, J. Tomasi, M. Cossi, J. M. Millam, M. Klene, C. Adamo, R. Cammi, J. W. Ochterski, R. L. Martin, K. Morokuma, O. Farkas, J. B. Foresman, D. J. Fox, Gaussian 16, Revision A.03, Gaussian Inc. **2016**.
- [27] a) C. M. Marian, A. Heil, M. Kleinschmidt, *Wiley Interdiscip. Rev. Comput. Mol. Sci.* **2019**, *9*; b) S. Grimme, M. Waletzke, *J. Chem. Phys.* **1999**, *111*, 5645–5655; c) M. Kleinschmidt, C. M. Marian, M. Waletzke, S. Grimme, *J. Chem. Phys.* **2009**, *130*, 44708.
- [28] I. Lyskov, M. Kleinschmidt, C. M. Marian, *J. Chem. Phys.* **2016**, *144*, 34104.
- [29] F. Plasser, *J. Chem. Phys.* **2020**, *152*, 84108.
- [30] a) M. Etinski, J. Tatchen, C. M. Marian, *Phys. Chem. Chem. Phys.* **2014**, *16*, 4740–4751; b) M. Etinski, J. Tatchen, C. M. Marian, *J. Chem. Phys.* **2011**, *134*, 154105.
- [31] W. Brütting, J. Frischeisen, T. D. Schmidt, B. J. Scholz, C. Mayr, *Phys. Status Solidi A* **2013**, *210*, 44–65.

Manuscript received: October 6, 2022

Revised manuscript received: December 21, 2022

Accepted manuscript online: December 22, 2022

Version of record online: January 18, 2023

4.2 Environmental and Temperature-Dependent Relaxation Effects on Photoluminescence

The solvatochromic studies in Fig. 4.3 were conducted by *Julia Wiefermann* (reprinted from ^[83]) and reveal pronounced positive solvato-chromism in the steady-state fluorescence of **BN-Ph-MTPA**.

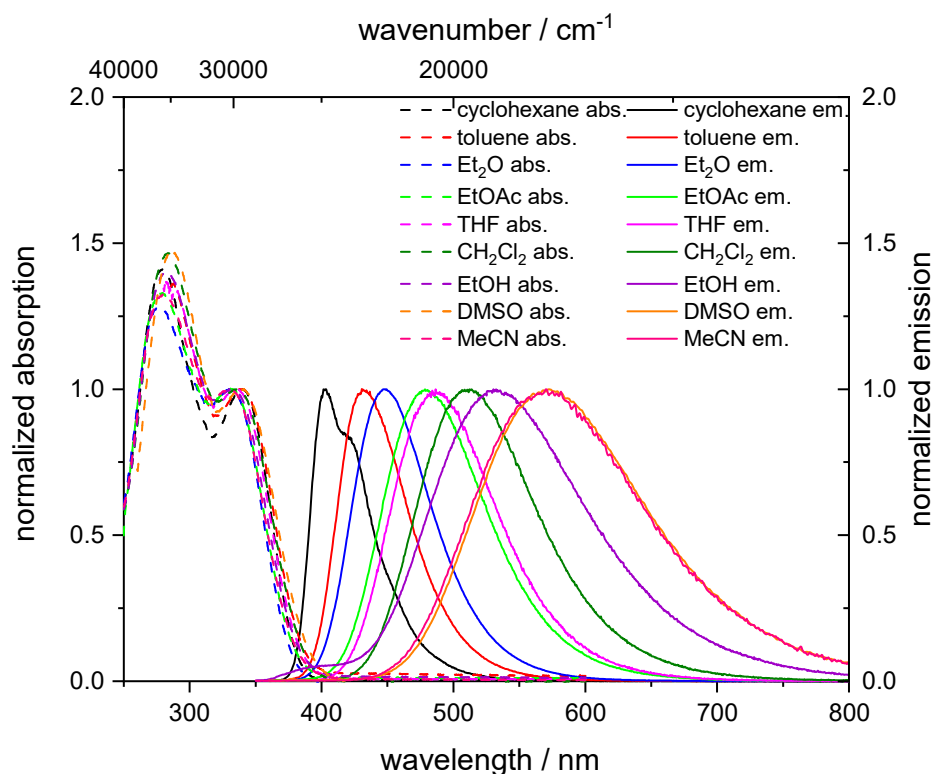


Figure 4.3: UV/vis absorption (dashed) and emission spectra (solid) of **BN-Ph-MTPA** in different solvents normalized on the longest wavelength absorption band (recorded at $T = 293$ K, $c = 10^{-5}$ M for absorption spectra and $c = 10^{-6}$ M for emission spectra, $\lambda_{exc} = \lambda_{max,abs}$). Reprinted with permission from ^[83].

To gain further insight into the underlying dynamics of this process, a more detailed investigation was conducted using time-resolved photoluminescence measurements in two distinct solvents at different temperatures. This approach provides valuable insights into the molecular interactions and environmental factors that influence the solvatochromic response.

In the following section, investigations are presented for **BN-Ph-MTPA** in two different solvent environments: a non-polar 1:1 mixture of toluene (Tol) and methylcyclohexane (MCH), and a significantly more polar medium using 2-methyltetrahydrofuran (MTHF).

4. Comprehensive Investigation of a HLCT Emitter: Spectroscopic Insights and Photophysical Properties of a Highly Luminescent Blue Chromophore

Both, MCH:Tol and MTHF form excellent glasses at low temperatures, making them ideal for experiments conducted in the frozen state (matrix spectroscopy). Tab. 4.1 presents the characteristic transition temperatures of the used solvents.

Table 4.1: Glass transition temperature (T_g), melting temperature (T_m) and dielectric constant (ϵ_r) at 293 K of solvents used for PL spectroscopy. The transition temperatures for the mixture of MCH:Tol (1:1) were estimated from the spectroscopic data.

solvent	T_g /K	T_m / K	ϵ_r
Toluene (Tol)	115 ^[84]	178 ^[85]	2.4 ^[86]
Methylcyclohexane (MCH)	85 ^[84]	147 ^[87]	2.02 ^[88]
Mixture MCH:Tol	~105	~155	
2-Methyltetrahydrofuran (MTHF)	91 ^[89]	137 ^[90]	6.97 ^[88]

4.2.1 Solvatochromic Effects on Fluorescence

In Fig. 4.4, the prompt fluorescence spectra of **BN-Ph-MTPA** in MCH:Tol (a) and MTHF (b) at different temperatures are shown. A pronounced bathochromic shift of the emission at room temperature can be observed in the polar MTHF compared to the non-polar MCH:Tol mixture in accordance to the observed positive solvatochromism in Fig. 4.3.^[83] Since the absorption is nearly independent of the solvent's polarity, this behavior can be attributed to a more effective stabilization of the excited dipolar state in MTHF.

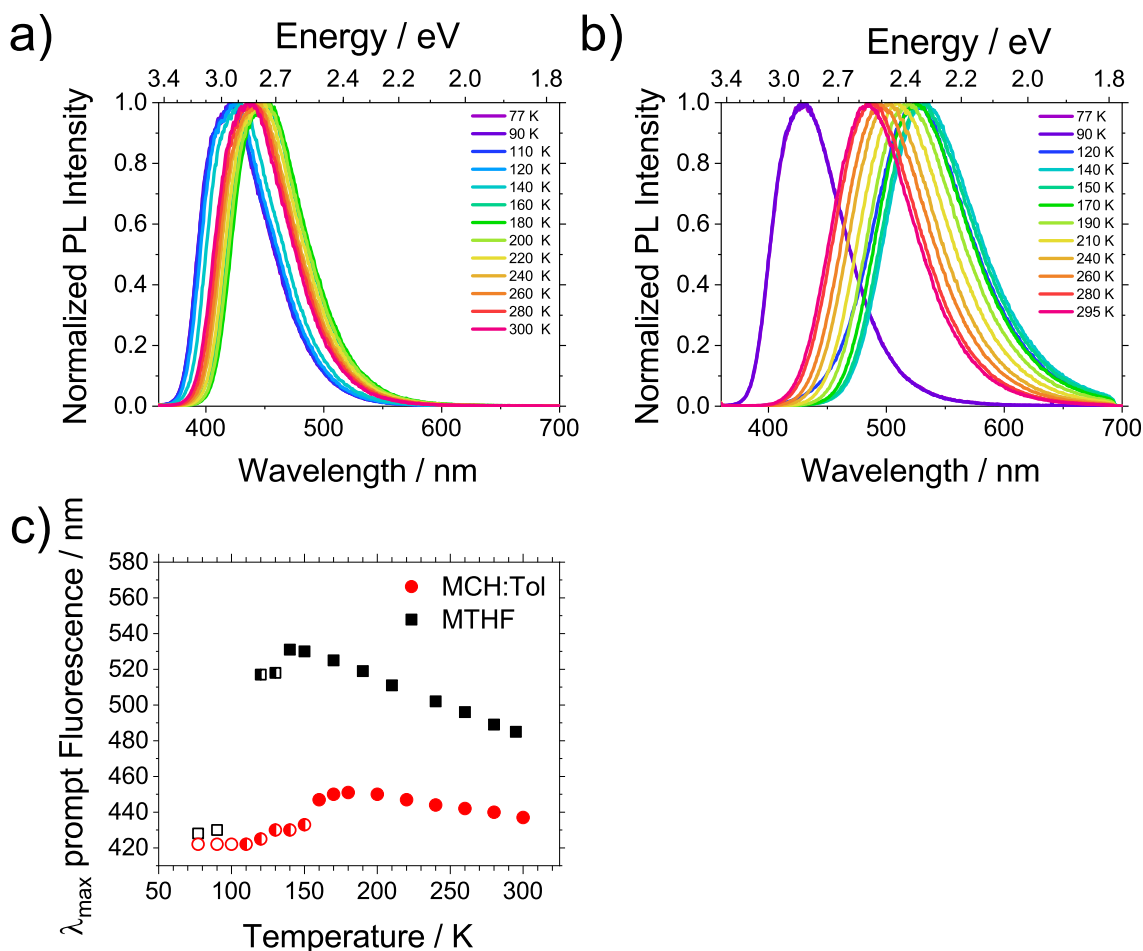


Figure 4.4: Prompt fluorescence spectra of **BN-Ph-MTPA** in a) MCH:Tol and b) MTHF with $c = 10^{-5} \text{ mol L}^{-1}$ at different temperatures. c) Wavelength of fluorescence maxima in MTHF and MCH:Tol in liquid and solid solution at different temperatures. Three different temperature regimes are marked: glass (open symbols), supercooled (half open symbols), liquid (solid symbols).

Fig. 4.4 c illustrates the wavelength of the maxima of the (prompt) fluorescence spectra

4. Comprehensive Investigation of a HLCT Emitter: Spectroscopic Insights and Photophysical Properties of a Highly Luminescent Blue Chromophore

at different temperatures, and a clear temperature dependence of fluorescence can be observed. The dependence is more pronounced in MTHF than in MCH:Tol, although both follow a similar trend.

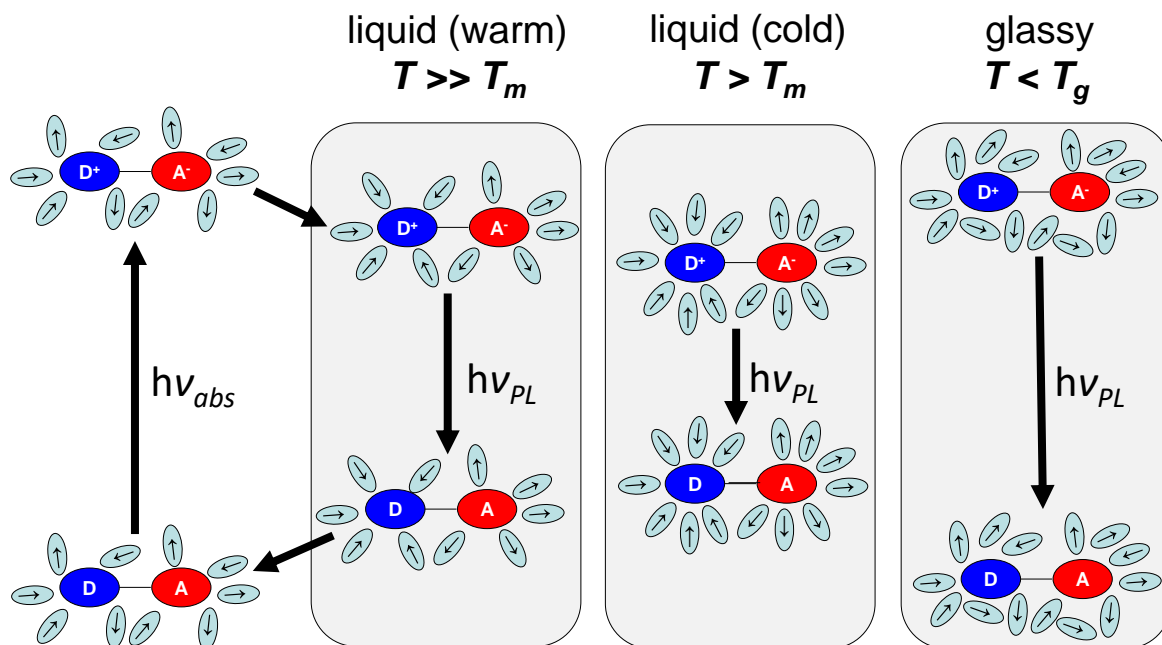


Figure 4.5: Illustration of temperature-dependent solute-solvent interactions. $T \gg T_m$: At higher temperatures, solvent molecules can rapidly reorient around the excited-state dipole of the chromophore, leading to significant stabilization of the excited state and a pronounced redshift in fluorescence. $T > T_m$: The stabilization is enhanced as the solvent density increases during cooling, raising the refractive index and dielectric constant, further stabilizing the excited dipolar state. Additionally, the reduced thermal motion at lower temperatures decreases the entropic cost of solvation, improving solvation efficiency. $T < T_g$: In this amorphous, glassy state, solvent molecules are immobilized, resulting in minimal stabilization of the excited state and a blue shift in the fluorescence spectrum due to the lack of molecular reorientation. Redrawn from ^[91].

The temperature dependence of the fluorescence can be categorized into three distinct regimes that are depicted in Fig. 4.5:

Regime I, $T < T_g$ (glassy): When the solution is rapidly cooled below glass transition temperature (T_g), it forms a glassy, amorphous state. In this regime, the solvent molecules are immobilized, lacking the ability to reorient or relax around the solute in response to its excited-state dipole moment. As a result, the stabilization of the excited state is minimal. This restriction increases the energy gap between the ground and excited state, leading to a blue shift in the fluorescence spectrum. The immobility of the solvent molecules in the glassy state makes it difficult for the system to reach a lower energy, more stabilized configuration, thus the fluorescence appears at higher energy (shorter wavelength).

Regime II, $T_g < T < T_m$ (supercooled): In this intermediate regime, the solvent enters a supercooled phase, where molecular mobility is significantly reduced, but not entirely absent. The solvent molecules may exhibit some limited, sluggish reorientation. As the temperature approaches T_g , the solvent can still partially stabilize the excited-state dipole of the solute, but less effectively than in the liquid phase. This partial stabilization results in a smaller redshift in fluorescence compared to higher temperatures, but the system may still show shifts associated with some degree of molecular motion.

Regime III, $T > T_m$ (liquid): At temperatures above the melting point, the solvent is in the liquid state. Solvent molecules are free to rapidly reorient around the dipole of the chromophore's excited state, leading to significant stabilization of this state. It is particularly pronounced for **BN-Ph-MTPA** because it has a larger dipole moment in the excited state than in the ground state. Upon cooling, the solvent density increases, raising its refractive index and dielectric constant^[92] and enhancing the stabilization of the excited dipolar state. Additionally, the reduced thermal motion of solvent molecules decreases the entropic cost of solvation, further improving the solvation efficiency. The solvatochromic and thermochromic shifts can be explained by the Onsager model, which attributes these shifts to dipole-dipole and dipole-induced-dipole interactions between **BN-Ph-MTPA** and the solvent molecules. In polar solvents (MTHF), these effects are more pronounced due to their higher dielectric constant, resulting in a larger redshift of the emission spectrum. However, in nonpolar solvents, the shifts are primarily driven by changes in density and refractive index, leading to comparatively smaller stabilization effects. The dynamic interaction of these solvent properties with the chromophore highlights the critical role of environmental polarity and temperature in tuning its photophysical behavior.^[92–94]

4. Comprehensive Investigation of a HLCT Emitter: Spectroscopic Insights and Photophysical Properties of a Highly Luminescent Blue Chromophore

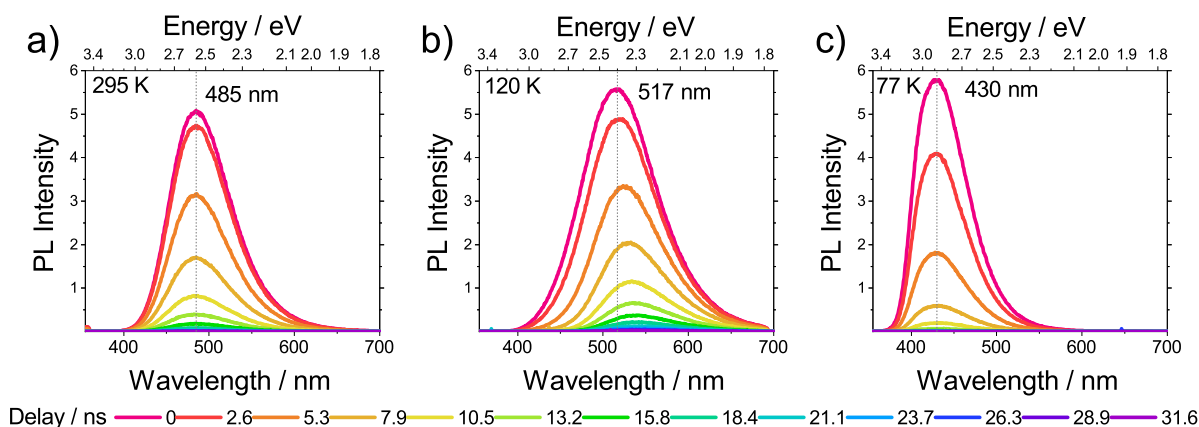


Figure 4.6: Prompt Fluorescence of **BN-Ph-MTPA** at different delay times (0 ns - 31.6 ns) in MTHF solution at a) 295 K (liquid), b) 120 K (supercooled), c) 77 K (glassy).

At both, high temperatures (295 K) as well as very low temperatures (77 K), the wavelength of the fluorescence intensity maximum in MTHF remain unchanged over time as shown in Fig. 4.6. However, in the intermediate supercooled temperature regime (120 K), a notable bathochromic shift of the fluorescence spectra is observed with increasing delay time (s. Fig. 4.6 b). The remaining molecular motion is still sufficient to allow the molecular geometry to relax into a more energetically favorable state. This relaxation process is slow enough to be detectable on the nanosecond timescale, unlike the faster dynamics seen at higher temperatures.

4.2.2 Vibronic Effects in Low Temperature Phosphorescence

While the fluorescence provides insights into the nature of the excited singlet state, phosphorescence offers information about the triplet state. In section 4.1, it was demonstrated that the energy of the triplet state can be determined from a phosphorescence spectrum. Here, additional insights derived from spectra obtained in MCH:Tol at different temperature regimes are provided.

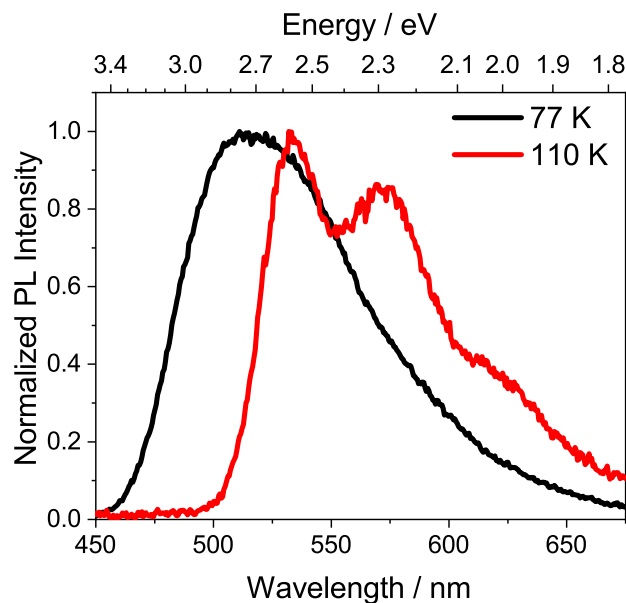


Figure 4.7: Phosphorescence spectra of **BN-Ph-MTPA** in MCH:Tol at 77 K and 110 K.

At low temperatures other non-radiative decay pathways are suppressed, which allows for the detection of phosphorescence. Fig. 4.7 shows the phosphorescence spectra of the **BN-Ph-MTPA** in MCH:Tol. At 77 K the emission spectrum shows a broad maximum at 515 nm while at 110 K it exhibits vibronic features with maximum at 534 nm. At 77 K (**regime I**, glassy solid), the emitter molecules are in an amorphous and disordered environment of solvent molecules, which remain fixed in space due to the reduced thermal energy. Upon optical excitation, no molecular reorganization of the solvent environment occurs around the excited molecule. Consequently, the excited state, even after undergoing ISC into the triplet state, exhibits large energetic differences compared to the relaxed geometry. The radiative decay to the ground state thus occurs from these non-relaxed triplet states. Since the amorphous solvent environment differs slightly for each emitter molecule, the specific energetic states of the excited triplet levels also vary. This leads to

significant differences in the energy of the emitted phosphorescence, resulting in a broad and unstructured spectrum.

At 110 K (**regime II**), the supercooled state of the solvent allows partial structural relaxation, resulting in a red shift in the phosphorescence spectrum. The vibrational fine structure that emerges at this temperature is attributed to radiative relaxation into distinct vibrational sublevels of the ground state.

The wavelengths of the intensity maxima are located at 534 nm, 573 nm, and 618 nm. The vibrational splittings were converted into wavenumbers (cm^{-1}) and are presented in Tab. 4.2. The obtained values lie at 1345 cm^{-1} and 1270 cm^{-1} . A comparison of these values with the infrared (IR) absorption spectrum of triphenylamine (TPA) published by *Munchi* et al. reveals good agreement, as TPA exhibits absorption bands at 1327 cm^{-1} and 1278 cm^{-1} . These bands were assigned by *Munchi* et al. to specific vibrational modes: C–N–C bending, phenyl ring twisting, and C–H bending (1327 cm^{-1}) as well as C–N stretching and C–H bending (1278 cm^{-1}).^[95]

Table 4.2: Estimated λ_{max} of the phosphorescence at 110 K in MCH:Tol with corresponding wavenumber $\tilde{\nu}$, the vibrational splitting $\Delta\tilde{\nu}$ and corresponding wavenumber $\Delta\tilde{\nu}_{TPA}$ of the triphenylamine (TPA) IR spectrum.^[95]

λ_{max} /nm	$\tilde{\nu}$ / cm^{-1}	$\Delta\tilde{\nu}$ / cm^{-1}	$\Delta\tilde{\nu}_{TPA}$ / cm^{-1}
534	18798	1345	1327
573	17453	1270	1278
618	16182		

4.2.3 Summary

This chapter presents the in-depth investigation of the photophysical properties and device performance of **BN-Ph-MTPA**, a blue fluorescent dye, with focus on its electronic characteristics, PL behavior, and application potential in OLEDs.

In section 4.1 **BN-Ph-MTPA** is identified as an emitter with balanced hybridized locally and charge-transfer (HLCT) excited state. This classification is supported by experimental observations and quantum chemical calculations. The latter were instrumental in elucidating the HLCT character of **BN-Ph-MTPA**, highlighting the balanced contributions of locally excited (LE) and charge-transfer (CT) excited state character to the S_1 state. These calculations also emphasized the crucial role of the *p*-phenylene bridging unit in facilitating this balance, providing a detailed understanding of the electronic transitions that govern the dye's photophysical behavior.

BN-Ph-MTPA exhibits an extraordinary PLQY of 98% in neat thin films, underlining its potential for optoelectronic applications and demonstrates a remarkably short fluorescence lifetime with 8.16 ns in the solid state and 1.86 ns in toluene, showing the efficiency of the radiative decay processes.

The molecular design, particularly the π -system extension via a *p*-phenylene bridging unit, plays a crucial role in achieving the balanced HLCT state. This design facilitates strong solvatochromism, with significant Stokes shifts observed in polar solvents, while absorption spectra remain unaffected by the solvent polarity. These results point to the balanced LE and CT contributions to the excited state, enabling high quantum yields across diverse environments.

Experimental determination of the energetic splitting between the first excited singlet and triplet states (ΔE_{ST}) using time-resolved and temperature-dependent PL spectroscopy yielded a value of 0.82 eV, in good agreement with the calculated value of 0.76 eV.

The determination of thermal stability and electrochemical properties was essential, highlighting the compound's suitability for integration into OLED technologies. Electrochemical properties were used to estimate the HOMO and LUMO values, which are found to be -5.7 eV and -2.7 eV, respectively. Additionally, the compound is thermally stable up to 377°C, making it suitable for processing via PVD and ensuring stability during device operation.

Applications in OLED devices reveal deep-blue narrow band emission. However, the IQE of approximately 10% suggests limitations in triplet exciton harvesting due to inefficient rISC. The large energetic splitting between S_1 and T_1 , coupled with minimal spin-orbit

coupling between the T_2 and S_1 states, limits the up-conversion of triplet excitons to singlet states.

Section 4.2 examines **BN-Ph-MTPA** in different solvent environments at various temperatures with respect to the photoluminescence. In MCH:Tol, a slight fluorescence shift occurs with temperature changes, while in MTHF, a stronger shift is observed. This is due to MTHF's better stabilization of the excited state, resulting from its larger dipole moment.

At low temperatures, both systems show a glassy state, causing high-energy blue fluorescence. Upon heating, the emission shifts to red, more prominently in MTHF due to its polarity. In the liquid state, solvent reorganization stabilizes the excited state, leading to a bathochromic shift of the fluorescence maxima. Just above the melting point, the solvent's higher density leads to better stabilization of the excited state, resulting in a larger fluorescence wavelength compared to room temperature. Phosphorescence studies in MCH:Tol reveal temperature-dependent spectral changes, with unstructured phosphorescence at 77 K and vibronic fine structure at 110 K, linked to the triplet state's relaxation.

5 Impact of Donor Variation on the Singlet-Triplet Energy Gap and the TADF Process in Donor-Acceptor Emitters

Organic D-A molecules, with their intrinsic ability to facilitate efficient intramolecular charge transfer are a widely used material class as emissive component in OLEDs. In the context of OLED emitters, twisted molecular architectures are very common because, as described in section 3.8.5, they favour small ΔE_{ST} values and can lead to the occurrence of TADF.^[96–98] Promising and frequently investigated structural building blocks for such twisted D-A molecules are carbazole donor and phthalimide acceptor moieties (s. Fig. 5.1).^[99–103]

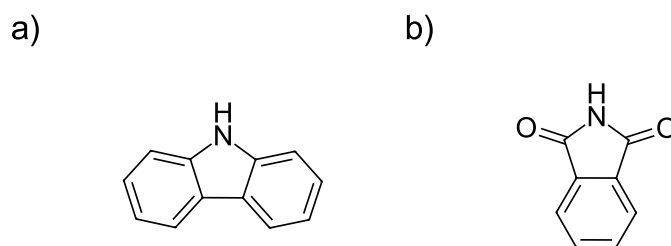


Figure 5.1: Molecular structures of a) carbazole and b) phthalimide.

Both building blocks provide beneficial properties such as a planar and rigid structure which can reduce non-radiative decay pathways and thereby increase the quantum efficiency of an emitter. In addition, both moieties exhibit a high thermal and photochemical stability, which is advantageous for processing via PVD on the one hand and for the durability of the device on the other. Donor and acceptor can easily be functionalized, allowing for the fine-tuning of their electronic properties and emission wavelengths. This versatility is essential for designing materials that can emit across the visible spectrum. Carbazole moieties possess good hole-transport capabilities due to their conjugated structure and electron-rich nature. This property ensures efficient charge carrier mobility, contributing to the high efficiency of OLEDs. The high electron affinity of phthalimide moieties aids in the formation of stable anionic states, which is beneficial for achieving balanced charge injection and transport in OLEDs.

This chapter presents an investigation of various *N*-phenylphthalimide and carbazole-based D-A emitters that were designed and synthesized by *Christopher Wallerius*. The acceptor component, *N*-phenylphthalimide, was kept unchanged while the donor component, based on carbazole, was systematically modified (s. Fig. 5.2). The donor and acceptor were linked at the 4-position of the phthalimide, following the findings of *Feng et al.*, which demonstrated increased PLQY and efficiencies compared to the 3-position linkage.^[103]

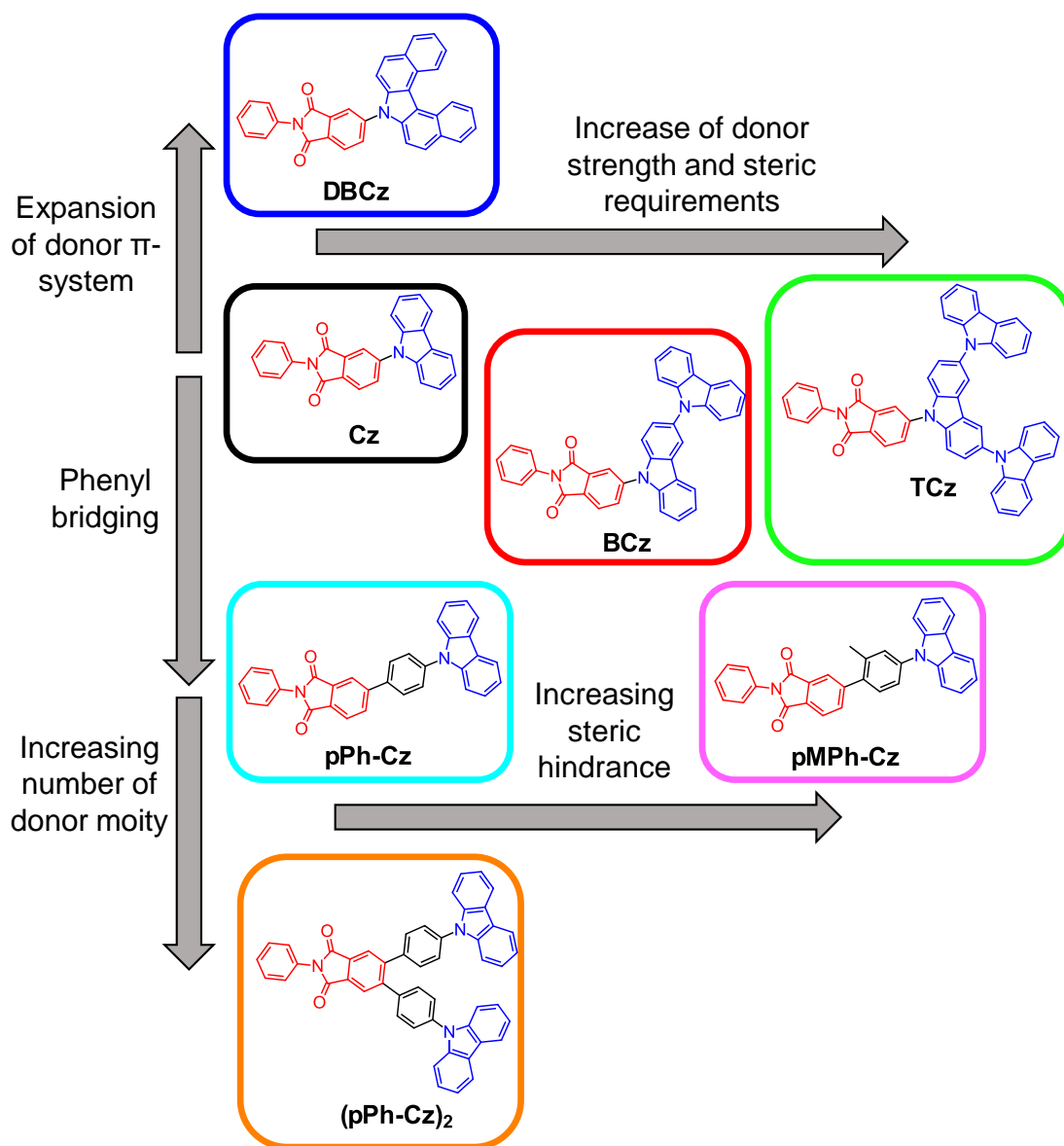


Figure 5.2: Molecular structures of investigated D-A compounds with used acronym. Since the acceptor unit remains the same for all compounds, the acronym is derived solely from the donor part of the molecule. The donor units are mono-carbazole (**Cz**), bis-carbazole (**BCz**), tris-carbazole (**TCz**), dibenzocarbazole (**DBCz**), carbazole with a *para*-phenylene bridge (**pPh-Cz**), a *para*-methyl-phenylene bridge (**pMPh-Cz**), and two *para*-phenylcarbazole donors (**(pPh-Cz)₂**).

5. Impact of Donor Variation on the Singlet-Triplet Energy Gap and the TADF Process in Donor-Acceptor Emitters

Since the acceptor unit remained unchanged, the naming of the D-A molecules was based solely on the donor unit. The donor structures included mono-carbazole (**Cz**), bi-carbazole (**BCz**), and tris-carbazole (**TCz**) units to investigate varying donor strengths and steric requirements, and their impact on photophysical properties and OLED performance. Additionally, a dibenzocarbazole (**DBCz**) was evaluated as a donor to assess the influence of an expanded π -system. Furthermore, the introduction of a phenylene bridge between the donor and acceptor was explored (**pPh-Cz**). This included testing a molecule with two bridged donor units (**(pPh-Cz)₂**), as well as a molecule with a methyl group attached to the *p*-phenylene bridge (**pMPH-Cz**) to introduce steric hinderence and determine the influence of the twist angle between the donor and acceptor.

A synthetic route for **Cz** was already published by *Gonda et al.*^[100] Additionally, *Feng et al.* synthesized and investigated the compound regarding its photophysical properties in toluene solution and in crystalline state.^[103,104] Nevertheless, for comparison purposes and to investigate the properties relevant to OLED environments, specifically in a host-guest system, the compound was included in this study. The remaining six compounds are not yet described in the literature.

The primary goal of this study is to evaluate the suitability of the molecules as emitters in OLEDs. To achieve this, their photophysical properties are of particular interest. While many studies focus on spectroscopy in solution, the aim of this work is to investigate the molecules in an environment that closely resembles practical applications. Therefore, the focus is on examinations within a host-guest system, where the molecules are embedded in the host material mCBP (3,3'-Di(9H-carbazol-9-yl)-1,1'-biphenyl). mCBP is an excellent host material for TADF OLEDs due to its high triplet energy of 2.8 eV, which prevents energy loss through non-radiative decay, and its good charge transport properties, which enhance device efficiency. Additionally, its thermal stability and compatibility with various TADF emitters make it a reliable choice for stable and efficient OLED performance.^[69]

The insights gained from the photophysical investigations will subsequently be compared with the properties and performance of the OLEDs into which the molecules were imbedded.

5.1 Photophysical Properties

To investigate how the photophysical properties are influenced by the alteration of donor parts, thin films were fabricated via thermal vapor deposition on glass substrates. The emitters were co-evaporated with the host material mCBP to produce doped films with 8 wt% of the emitter. The concentration was chosen based on *Li et al.*, as the OLED stack used in their study was also employed, and the photophysical investigations should closely reflect the conditions in the OLED environment, which will be discussed in the following section.^[99] Additionally, the absorbance of neat films was studied, as the absorption of mCBP overlaps with the bands of the emitter molecules (s. Fig. 10.1).

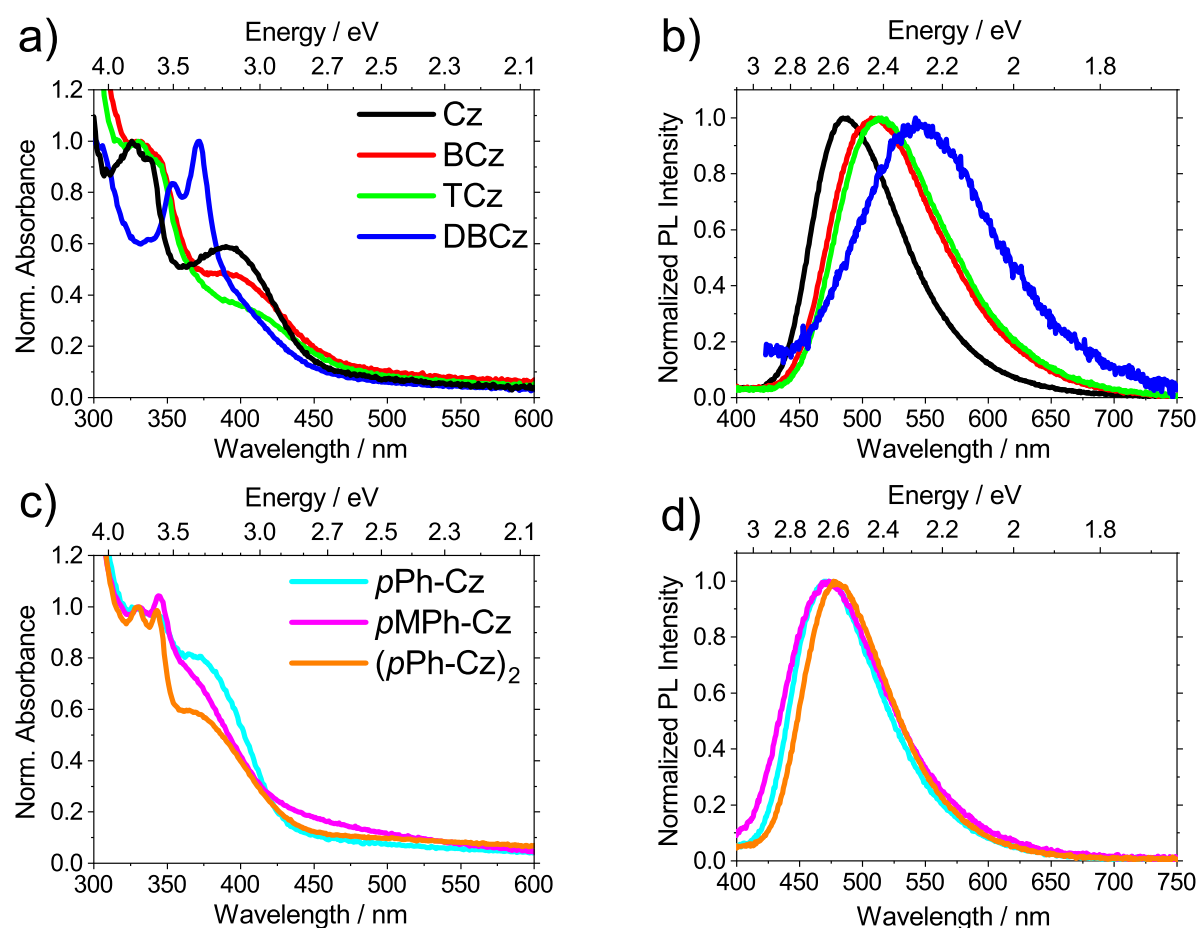


Figure 5.3: Normalized absorbance in neat film of a) non-bridged compounds, c) phenylene-bridged compounds and normalized steady-state PL spectra of 8wt% emitter in mCBP thin films of b) non-bridged compounds, d) phenylene-bridged.

The absorbance spectra of all compounds are shown in Fig. 5.3 a & c. Except for **DBCz** all exhibit a broad, undefined band around 400 nm, which can be attributed to a CT

5. Impact of Donor Variation on the Singlet-Triplet Energy Gap and the TADF Process in Donor-Acceptor Emitters

transition. Furthermore, they display a more structured double band at approximately 330 nm, which can be assigned to an n- π^* -transition. For the compound **DBCz**, the n- π^* band is redshifted to 360 nm due to the enlarged π -system of dibenzocarbazole, indicating a dominant LE state.

The steady-state PL spectra of the doped films in mCBP are shown in Fig. 5.3 b & d. The emission maximum for **Cz** is observed at 487 nm (s. Tab. 5.1). For **BCz**, a redshift to an emission maximum of 508 nm is noted. **TCz** shows only a minimal redshift compared to the **BCz**, with an emission maximum at 513 nm. **DBCz** exhibits the longest wavelength emission, with a maximum at 544 nm. The bridged compounds, on the other hand, all exhibit an emission maximum around 475 nm. Compared with **Cz**, it is confirmed that the phenylene group has only little impact on the emission color and does not enlarge the donor or acceptor unit.

Cz exhibited the highest PLQY at 0.65, followed by **BCz** (0.52) and **TCz** (0.55), which showed similar values. In contrast, **DBCz** demonstrated a significantly lower PLQY of only 0.13. Compared to the non-bridged compounds, the bridged ones generally have lower quantum yields (s. Tab. 5.1).

Table 5.1: Wavelength of PL maximum and PLQY of 8wt% emitter in mCBP thin film at an excitation wavelength of 300 nm.

		$\lambda_{max,PL}$ /nm	Φ_{PL}
non-bridged	Cz	487	0.65
	BCz	508	0.52
	TCz	513	0.55
	DBCz	544	0.13
phenylene-bridged	pPh-Cz	473	0.36
	pMPh-Cz	471	0.26
	(pPh-Cz)₂	478	0.41

5.2 Time-resolved Spectroscopy

To obtain information about the nature of the excited states relevant for photo- and electroluminescence, time-resolved and temperature-dependent PL spectroscopy was used. *Feng et al.* already demonstrated TADF behavior for **Cz** and showed that even small structural changes can lead to detectable room-temperature phosphorescence.^[103] Therefore, the emitters were examined with respect to both phenomena.

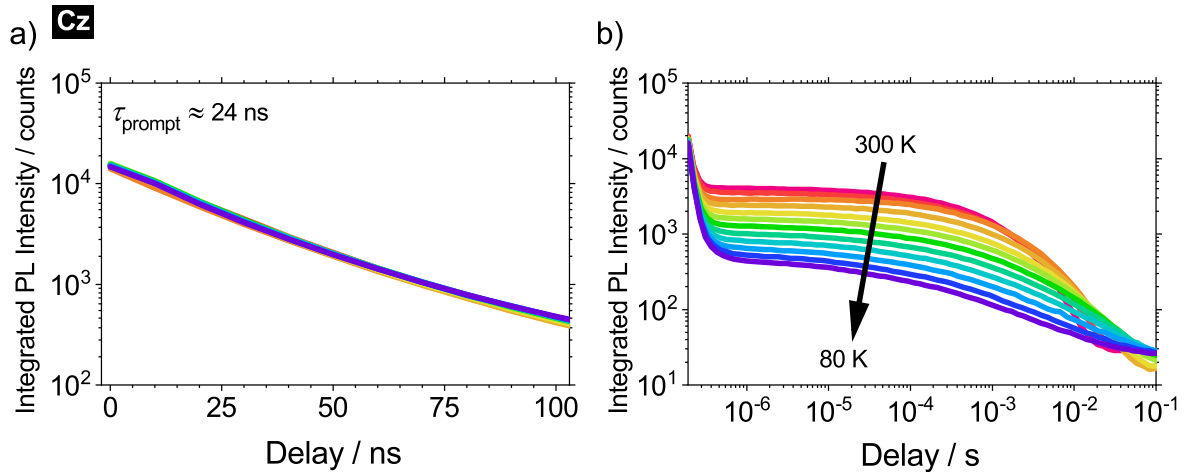


Figure 5.4: PL decay of **Cz** (8wt% in mCBP film). a) prompt decay detected with 100 ns gate and b) delayed decay detected with 1 ms gate at temperatures from 300 K to 80 K in 20 K steps. Corresponding fits for the decay times can be found in Fig. 10.5-10.8. The fitted decay times are summarized in Tab. 10.1.

Exemplary decay curves of the prompt and delayed PL at different temperatures for **Cz** are shown in Fig. 5.4. The prompt fluorescence remains nearly unchanged in intensity and decay ($\tau_{prompt} \approx 24$ ns) at different temperatures. The delayed component exhibits a clear temperature dependence, with its intensity increasing at elevated temperatures compared to lower ones.

5. Impact of Donor Variation on the Singlet-Triplet Energy Gap and the TADF Process in Donor-Acceptor Emitters

The exponentially fitted decay times τ for the prompt and delayed component are plotted as a function of the temperature in Fig. 5.5. While the decay times for the prompt fluorescence of **Cz** remain constant at around 24 ns (Fig. 5.5 a), the decay of the delayed component shows a clear temperature dependence (Fig. 5.5 c). Between 300 K and 180 K, the decay time for **Cz** increases from 1.4 ms to 3.9 ms, indicating TADF. At lower temperatures, an opposite trend is observed, suggesting the presence of a different process. Similar temperature activated behavior is observed for **BCz**, **TCz** and *p***MPh-Cz** (s. Fig. 5.5).

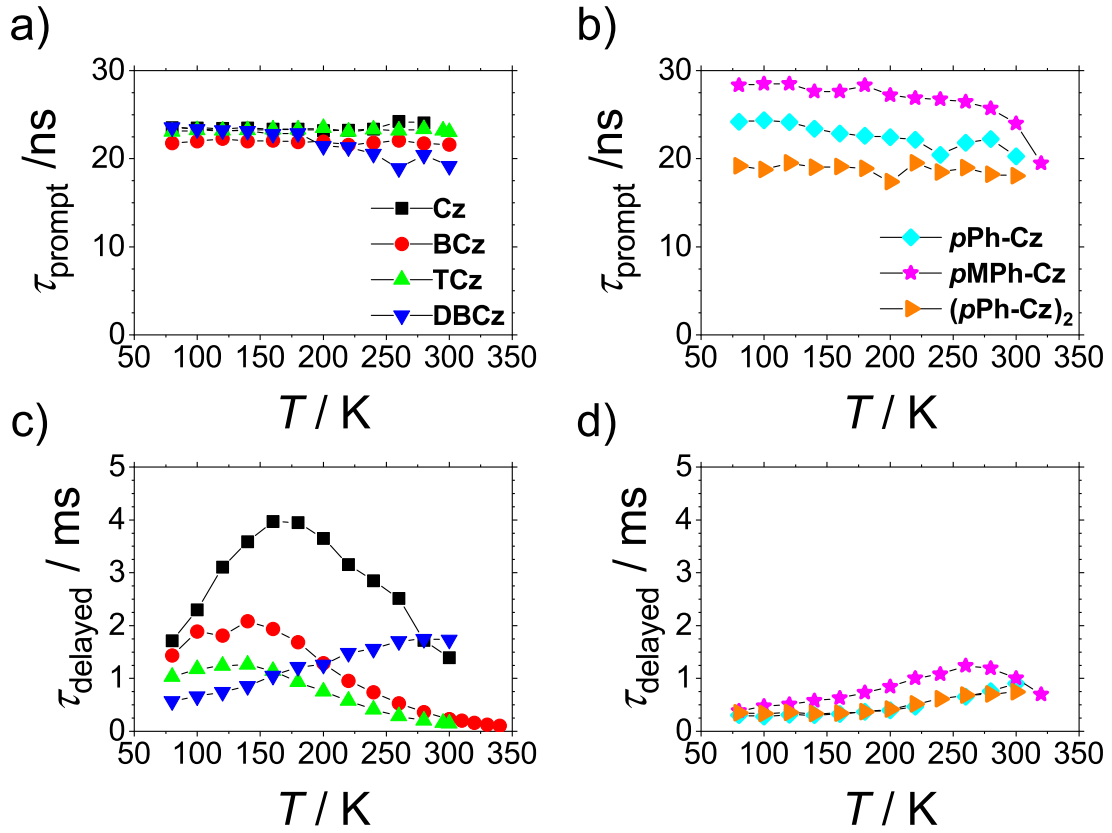


Figure 5.5: Temperature dependent decay times: prompt fluorescence of a) non-bridged compounds and b) bridged compounds; delayed photoluminescence of c) non-bridged compounds and d) bridged compounds (8wt% emitter in mCBP films). Decay curves can be found in Fig. 10.2 and Fig. 10.3.

The TADF process is attributed to a small energy gap between the S_1 and T_1 states. To determine this energy gap, the Arrhenius relationship is used. The inverse decay time corresponds to the experimentally determined rate constant (k_{exp}) (s. Eq. 5.1). According to Eq. 5.2, the energy gap ΔE_{ST} can be calculated from the slope of the linear fit plotting the natural logarithm of k_{exp} against the inverse temperature. (s. Fig. 5.6).^[105] The fit

5. Impact of Donor Variation on the Singlet-Triplet Energy Gap and the TADF Process in Donor-Acceptor Emitters

parameters can be found in Fig. 10.4. The calculated energy barriers are summarized in Tab. 5.2.

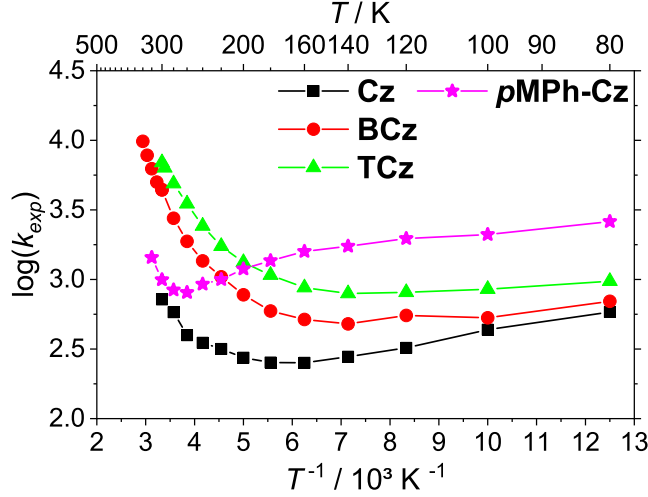


Figure 5.6: Arrhenius plot for all emitters showing TADF behavior. The corresponding fits can be found in Fig. 10.4.

Table 5.2: ΔE_{ST} calculated from plot. Arrhenius

	ΔE_{ST} /meV
Cz	99.8
BCz	121.6
TCz	99.3
DBCz	x
pPh-Cz	x
pMPh-Cz	102.5
(pPh-Cz)₂	x

$$k_{exp} = \frac{1}{\tau_{delayed}} \quad (5.1)$$

$$\log(k_{exp}) = a - \frac{\Delta E_{ST}}{2.303 \cdot k_b T} \quad (5.2)$$

The decrease in photoluminescence lifetime with increasing temperature is a key indicator of TADF. However, analyzing the integrated intensity across all wavelengths can be misleading, as it does not distinguish between different emitting states. Therefore, it is valuable to examine the photoluminescence spectra to reveal energy differences in the emission that may indicate the presence of multiple emitting states. To this end, spectra were recorded for all emitters at 300 K and 80 K. Additionally, the spectra were investigated with delays in the nanosecond and millisecond range.

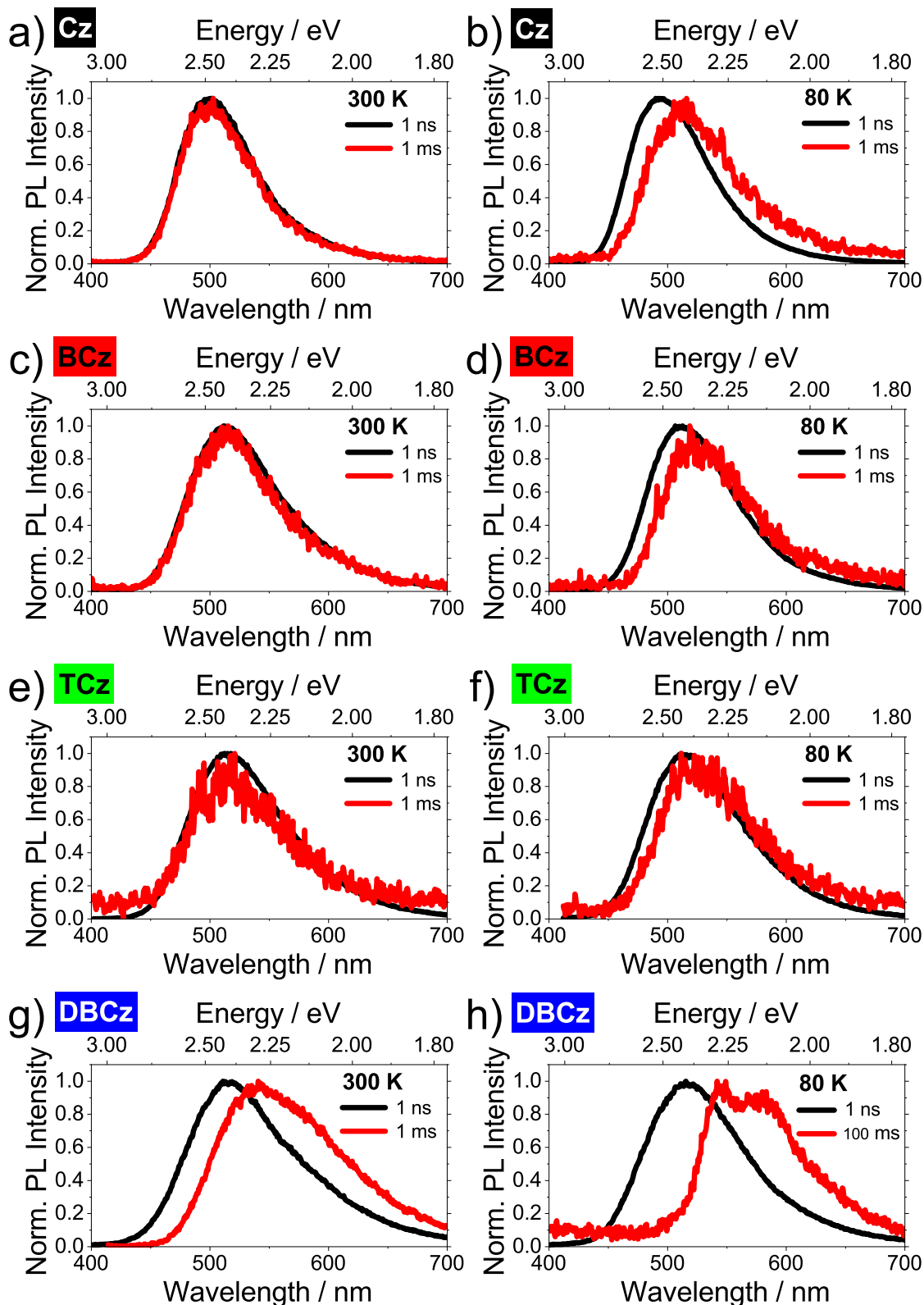


Figure 5.7: Prompt (black) and delayed (red) PL spectra of non-bridged compounds in mCBP film: **Cz** at a) 300 K b) 80 K; **BCz** at c) 300 K d) 80 K; **TCz** at e) 300 K f) 80 K; **DBCz** at g) 300 K h) 80 K.

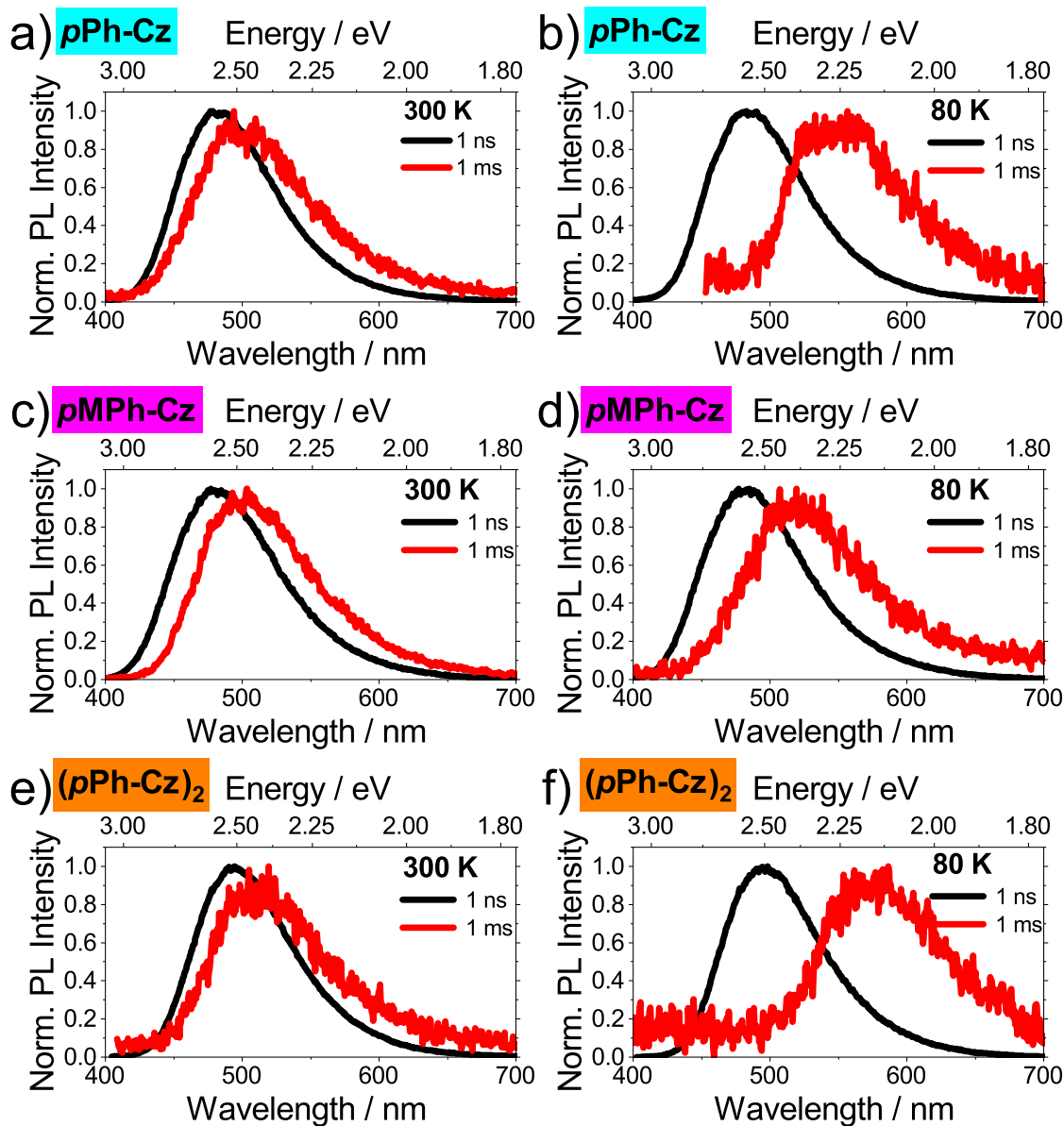


Figure 5.8: Prompt (black) and delayed (red) PL spectra of bridged compounds in mCBP film: *pPh-Cz* at a) 300 K b) 80 K; *pMPh-Cz* at c) 300 K d) 80 K; *(pPh-Cz)₂* at e) 300 K f) 80 K.

At 80 K, most thermally activated processes that can influence photoluminescence should no longer be observable. This includes not only TADF but also thermally activated diffusion of charge carriers and excitons, as well as thermally activated non-radiative transitions. The latter involves processes where excited states are thermally activated into non-radiative states, leading to energy loss that is dissipated as heat.

At low temperatures, many organic emitters exhibit phosphorescence due to the suppression of non-radiative decay pathways that typically quench triplet excited states at higher temperatures. Thermal energy at ambient conditions facilitates molecular vibrations and interactions that enable non-radiative decay, competing with phosphorescence. By cooling the system to low temperatures, these vibrations are significantly reduced, decreasing the efficiency of non-radiative transitions. As a result, the triplet states have a higher probability of decaying radiatively, leading to observable phosphorescence.

Fig. 5.7 presents the normalized PL spectra of all non-bridged compounds. For compounds **Cz**, **BCz** and **TCz** there is minimal difference between the prompt and delayed PL at 300 K, with the spectra being nearly identical, which is characteristic of TADF. At low temperatures, a slight redshift is observed. This shift occurs because the lower thermal energy reduces the efficiency of upconversion from triplet to singlet states, allowing phosphorescence to become more prominent. However, the redshift is minimal, as the energy difference between the S_1 and T_1 states is small.

In contrast, **DBCz** exhibits a notable redshift in the delayed PL even at 300 K, indicating effective ISC that competes with fluorescence and contributes to the low PLQY. As the temperature decreases, this redshift becomes even more pronounced due to the increased intensity of phosphorescence. At these low temperatures, a spectral shift of approximately 412 meV between prompt fluorescence and phosphorescence can be detected. This significant energy difference between the S_1 and T_1 states explains the absence of TADF, as there is an insufficient amount of thermal energy to facilitate upconversion. Additionally, the room temperature phosphorescence does not significantly enhance the PLQY, since it is a spin-forbidden process, making non-radiative decay pathways more likely and further contributing to the reduced overall emission efficiency.

Fig. 5.8 displays the normalized spectra of the phenylene-bridged compounds. At 300 K, all spectra show a slight redshift in the delayed PL compared to the prompt PL, indicating room temperature phosphorescence. At low temperatures, **pPh-Cz** and **(pPh-Cz)₂** exhibit a more pronounced redshift in both the prompt and delayed PL, strongly suggesting the presence of phosphorescence. The spectral shift corresponds to an energy difference of 404 meV for **pPh-Cz** and 277 meV for **(pPh-Cz)₂**. In contrast, **pMPh-Cz** shows a

5. Impact of Donor Variation on the Singlet-Triplet Energy Gap and the TADF Process in Donor-Acceptor Emitters

much smaller shift of about 113 meV. This finding is in agreement with the energy gap calculated from the Arrhenius plot (102.5 meV) and suggests that the additional methyl group in **pMPh-Cz** may improve the orientation between the donor and acceptor parts of the molecule by steric hindrance, thereby facilitating upconversion.

However, despite this structural advantage, the PLQY of **pMPh-Cz** remains low at 0.26. This suggests that while the methyl group enhances the potential for upconversion, the phenylene unit promotes non-radiative decay processes by decoupling donor and acceptor resulting in an increase of vibrational relaxation and a reduced PLQY.

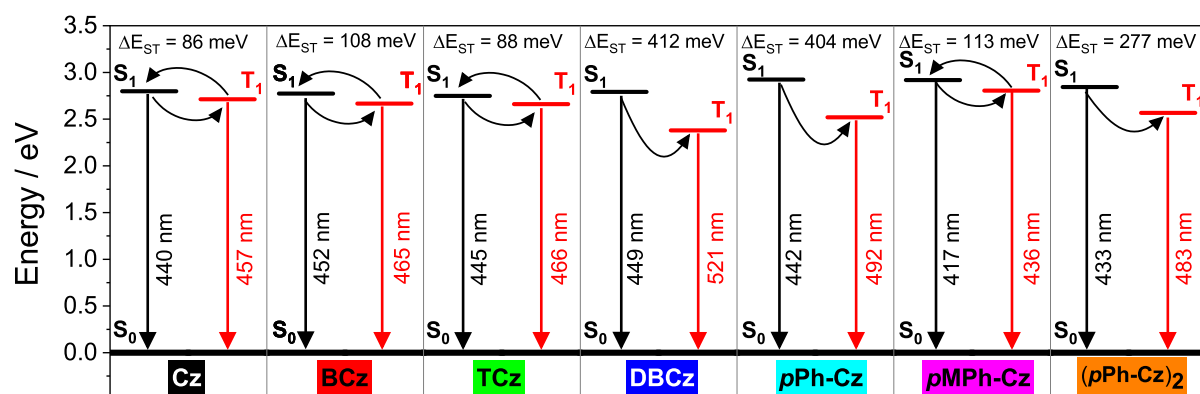


Figure 5.9: Energies of excited states and ΔE_{ST} with onset wavelength of prompt fluorescence at 300 K and phosphorescence at 80 K.

The spectroscopic investigation of the seven compounds focused on the nature of their excited states, yielding important insights that are summarized in Fig. 5.9. Notably, the three non-bridged compounds **Cz**, **BCz**, and **TCz** exhibited TADF. This conclusion was supported by their characteristic delayed PL lifetimes, the congruence of prompt and delayed PL spectra, the temperature-activated decrease of delayed PL decay times, and the analysis of low-temperature spectra that revealed a sufficiently small ΔE_{ST} (86 eV, 108 eV and 88 eV) conducive to TADF.

In contrast, **DBCz** demonstrated different behavior, showing room-temperature phosphorescence instead of TADF. This was accompanied by a significantly lower PLQY of 0.13 and the absence of temperature-activated PL. Furthermore, low-temperature measurements revealed an energy gap of 412 nm, which is too large to support TADF.

The phenylene-bridged compounds exhibited substantially lower PLQY values (0.26-0.41) due to the decoupling of donor and acceptor units resulting in increase of non-radiative vibrational relaxation. Low-temperature measurements allowed the exclusion of TADF for **pPh-Cz** and **(pPh-Cz)₂**, as their large energy gaps (404 eV and 277 eV) precluded

this mechanism. For **pMPh-Cz**, however, a temperature-activated PL component was observed, and the low-temperature spectrum suggested a relatively small ΔE_{ST} of only 113 meV. Nevertheless, the presence of significant non-radiative processes severely suppressed its PLQY, limiting it to 0.26.

These findings collectively highlight the diverse photophysical behaviors of these compounds, emphasizing the critical influence of structural features on their excited-state properties.

5.3 Energy Levels and Thermal Properties

In addition to the photophysical properties, which provide insights into the suitability of a material as an OLED emitter, other characteristics are also crucial. When considering processing options, solubility is important for solution-processed manufacturing, while thermal stability is essential for vacuum processing. In this work, vacuum processing is employed because it typically yields higher efficiencies due to greater material purity and more uniform layers. Therefore, the thermal stability of the emitters up to the evaporation temperature is critical. Moreover, thermal stability at elevated temperatures within the device itself is also important to ensure long-term performance and reliability.

Table 5.3: Melting temperature (T_m), decomposition temperature (T_d) defined as 5% weightloss, oxidation and reduction half wave potential measured in DCM solution vs. Fc/Fc^+ and according to Eq. 9.3 estimated HOMO and LUMO energy values and band-gap energy values.

	T_m /°C	T_d /°C	$E_{ox}^{1/2}$ /V	$E_{red}^{1/2}$ /V	HOMO /eV	LUMO /eV	band-gap /eV
Cz	253	326	0.99	-1.78	-6.19	-3.42	2.77
BCz	315	415	0.78	-1.72	-5.98	-3.48	2.50
TCz	X	496	0.80	-1.71	-6.00	-3.49	2.51
DBCz	258	417	0.76	-1.73	-5.96	-3.47	2.49
pPh-Cz	268	397	0.89	-1.78	-6.08	-3.41	2.67
pMPh-Cz	283	399	0.86	-1.82	-6.06	-3.37	2.69
(pPh-Cz)₂	278	486	0.86	-1.78	-6.06	-3.41	2.65

The thermal properties were determined by *Christopher Wallerius* and *Freia Scharbert* using combined TGA and differential scanning calorimetry (DSC) measurements. The recorded data is presented in Fig. 10.33, and the measured T_m and the T_d , at which a 5%

mass loss was observed, are listed in Tab. 5.3.

For vacuum evaporation, temperatures between 120°C and 200°C are required. Since T_d for all compounds is above 300 °C, the thermal stability is sufficient.

In addition to thermal properties, the alignment of the FMO energy levels is of significant importance for selecting suitable layer structures and compatible materials in an OLED. These energy levels can be approximated by determining the oxidation and reduction potentials by use of CV. *Christopher Wallerius* and *Freia Scharbert* recorded the cyclic voltammograms in dichloromethane (DCM) solution, and the data is presented in Fig. 10.34. The half-wave potentials for oxidation and reduction, as well as the according to Eq. 9.3 estimated HOMO and LUMO values derived from them, are listed in Tab. 5.3. The reduction potential and the corresponding LUMO values remain relatively consistent across the compounds, as expected, since the acceptor, *N*-phenylphthalimide, is identical for all. The LUMO lies within a range of -3.37 eV to -3.49 eV. The additional irreversible reduction signal observable between 0.7 and 0.4 V for all compounds except for **DBCz**, can be assigned to dimerisation of the carbazole unit as described by *Karon et al.*^[106]

In contrast, the oxidation potentials vary significantly among the compounds due to differences in the donor components. Notably, **Cz** exhibits a considerably higher oxidation half-wave potential of 0.99 V. The single, non-bridged carbazole unit is the smallest of all investigated donor moieties, resulting in less delocalization and stabilization of the positive charge. For the remaining compounds, the HOMO energy level lies within a range of -5.96 eV to -6.08 eV.

5.4 Application as Emitters in OLEDs

To complete the evaluation of the compounds' suitability as OLED emitters, all seven compounds were implemented in devices. In line with the spectroscopic studies in 5.1, the emitters were integrated into a host-guest system with mCBP as host material, and a doping concentration of 8 wt%. The OLED structure was adapted from *Li et al.*^[99], as their work used similar compounds and achieved high EQE.

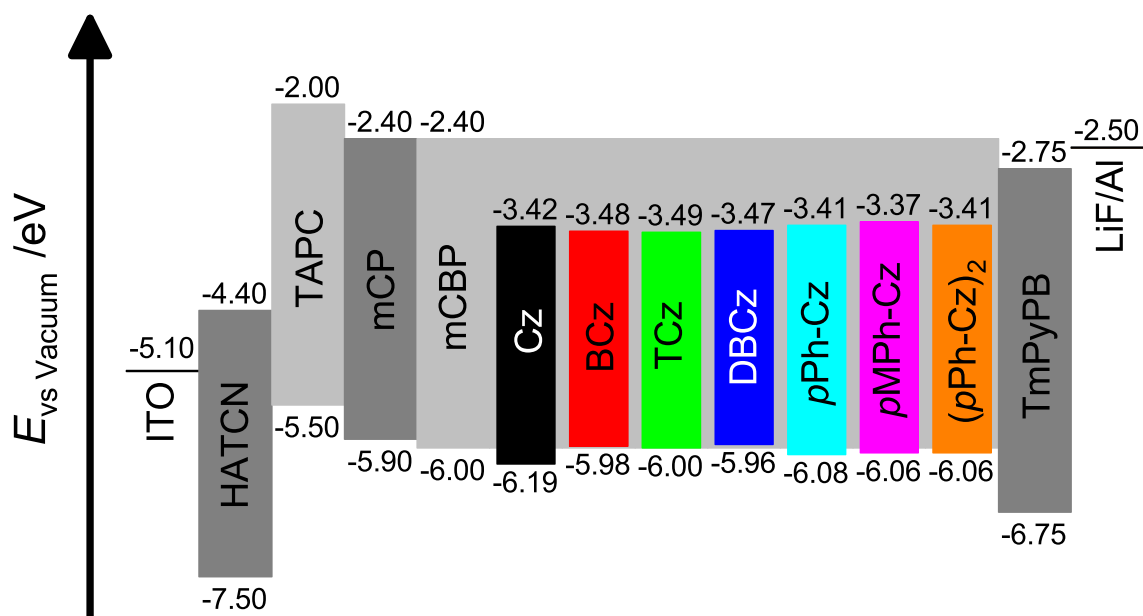


Figure 5.10: Scheme of HOMO and LUMO levels of the used materials in the OLED stack: ITO, HATCN (10 nm), TAPC (30 nm), mCP (10 nm), mCBP (10 nm), 8wt% Emitter in mCBP (25 nm), TmPyPB (45 nm), LiF (1 nm), Al (100 nm). Energy levels of the emitters are estimated from CV measurements. The energy levels of the standard materials are taken from literature (s. 9.4).

Several modifications were made to the device structure, following optimization experiments. A supplemental mCP layer was introduced as a hole transport layer, as experiments indicated that this change led to higher efficiencies. Additionally, the thicknesses of LiF and Al in the cathode was optimized. The used device structure is illustrated in Fig. 5.10. The chemical structures of all used materials can be found in 9.4. HATCN serves as HIL, TAPC and mCP as HTL, mCBP as HTL and host for the emitter and TmPyPB as ETL. ITO is the anode and LiF/Al the cathode material (s. Fig. 5.10).

5. Impact of Donor Variation on the Singlet-Triplet Energy Gap and the TADF Process in Donor-Acceptor Emitters

Fig. 5.11 shows the electrical characteristics of the devices and Tab. 5.4 summarizes the key parameters.

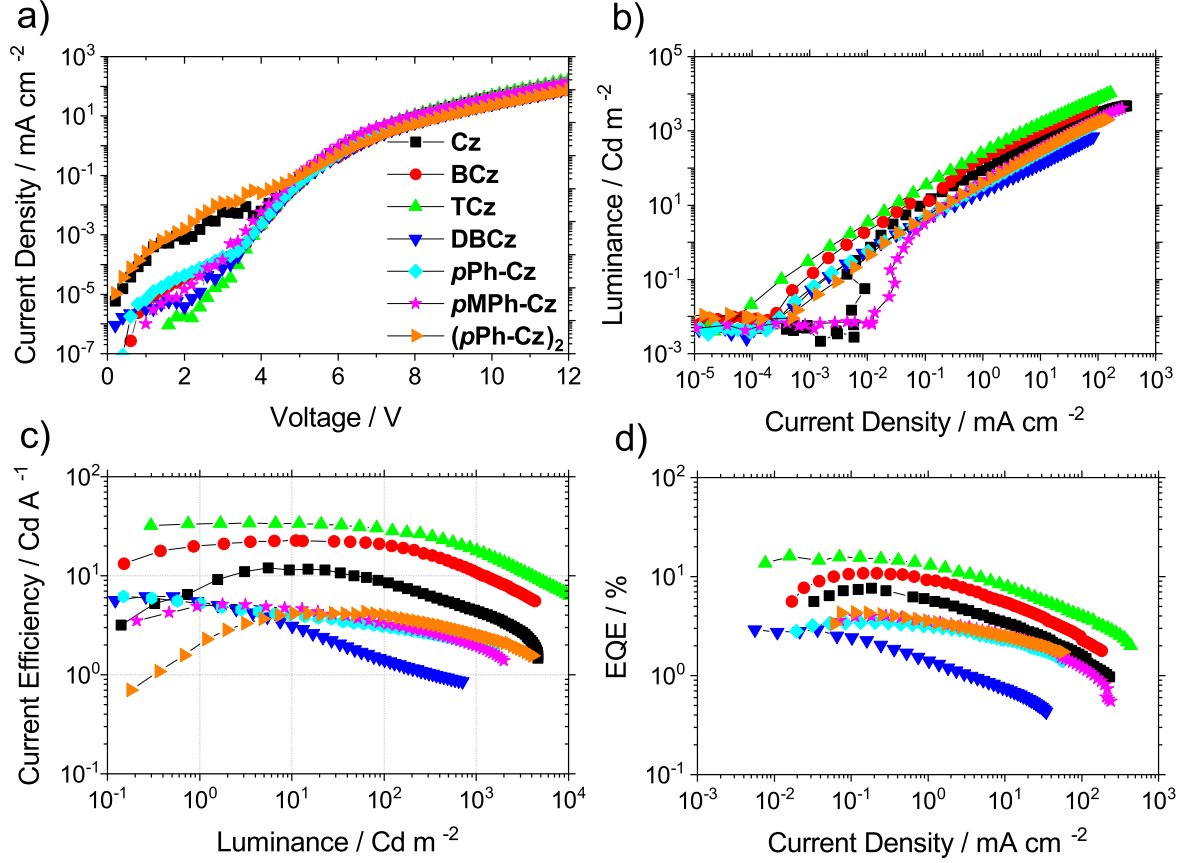


Figure 5.11: Characteristics of OLEDs with different emitters. The OLED stack can be found in Fig. 5.10. a) current density, b) luminance, c) current efficiency, d) external quantum efficiency.

TCz exhibits the highest maximum efficiency as well as EQE with 33.9 cd A^{-1} and 16.0%, respectively. Given that **TCz** has already been shown to exhibit a small ΔE_{ST} and TADF, along with a PLQY of 0.55, the observed high efficiency is consistent with expectations. The slightly reduced EQEs observed for **BCz** is in accordance with the somewhat higher ΔE_{ST} compared to **TCz**. **Cz**, on the other hand, deviates slightly from the expected behavior. Despite exhibiting a comparable ΔE_{ST} to **TCz** and a higher PLQY, its maximum EQE reaches only 7.7%. This behavior can be attributed, firstly, to the prolonged lifetime of the delayed emission component of **Cz** compared to **TCz** (s. Fig. 5.5) indicating a lower rISC rate, which in turn reduces the exciton utilization efficiency of triplet excitons. Secondly, the less steric demanding donor and more compact molecular structure of **Cz** compared to **TCz** may lead to reduced charge injection and stabilization, limiting its

5. Impact of Donor Variation on the Singlet-Triplet Energy Gap and the TADF Process in Donor-Acceptor Emitters

performance. As anticipated from its very low PLQY of only 0.13, **DBCz** exhibits the lowest EQE among the studied compounds. Furthermore, its room-temperature phosphorescence does not appear to provide a significant contribution to improving efficiency.

Table 5.4: Luminance at an applied voltage of 12 V, maximum current efficiency, maximum power efficiency, external quantum efficiency at maximum and at 1000 Cd m^{-2} .

Device	L_{12V}	CE	PE	EQE_{max}	$\text{EQE}_{1000 \text{ Cd m}^{-2}}$
	$/\text{Cd m}^{-2}$	$/\text{Cd A}^{-1}$	$/\text{lm W}^{-1}$	$\%$	$\%$
Cz	336	12	7.8	7.7	3.0
BCz	4339	22.6	13.2	10.8	6.2
TCz	10321	33.9	26.4	16.0	10.5
DBCz	708	6.2	4.6	2.9	-
<i>p</i>Ph-Cz	1576	6.2	4.9	3.4	1.5
<i>p</i>MPh-Cz	1995	5.1	3.5	4.0	1.8
(<i>p</i>Ph-Cz)₂	1678	4.3	2.3	4.3	1.9

The three bridged compounds also exhibit low EQEs and efficiency values, with the performance characteristics of their OLEDs showing minimal differences. On the one hand, the PLQY values for all these compounds are relatively low. On the other hand, the ΔE_{ST} values for ***p*Ph-Cz** and **(*p*Ph-Cz)₂** are too large for TADF to serve as an effective up-conversion mechanism. While ***p*MPh-Cz** does exhibit TADF, its PLQY of 0.26 remains very low, which may be attributed to either the limited efficiency of the TADF process or additional competing non-radiative decay pathways. The efficiency in these cases may also be limited by charge injection and stabilization. This could further contribute to the observed low EQEs and performance across all three phenylene-bridged compounds.

5. Impact of Donor Variation on the Singlet-Triplet Energy Gap and the TADF Process in Donor-Acceptor Emitters

Fig. 5.12 a shows the EL spectra of the investigated OLEDs at an applied voltage of 7 V. The spectra align closely with the PL spectra shown in Fig. 5.3. Fig. 5.12 b presents the corresponding CIE coordinates within a CIE chromaticity diagram. It is evident that **DBCz** exhibits yellow light emission, whereas **TCz** and **BCz** fall within the green region. **Cz** and **(pPhCz)₂** display cyan-colored emission, while **pMPh-Cz** and **pPh-Cz** are located in the blue region.

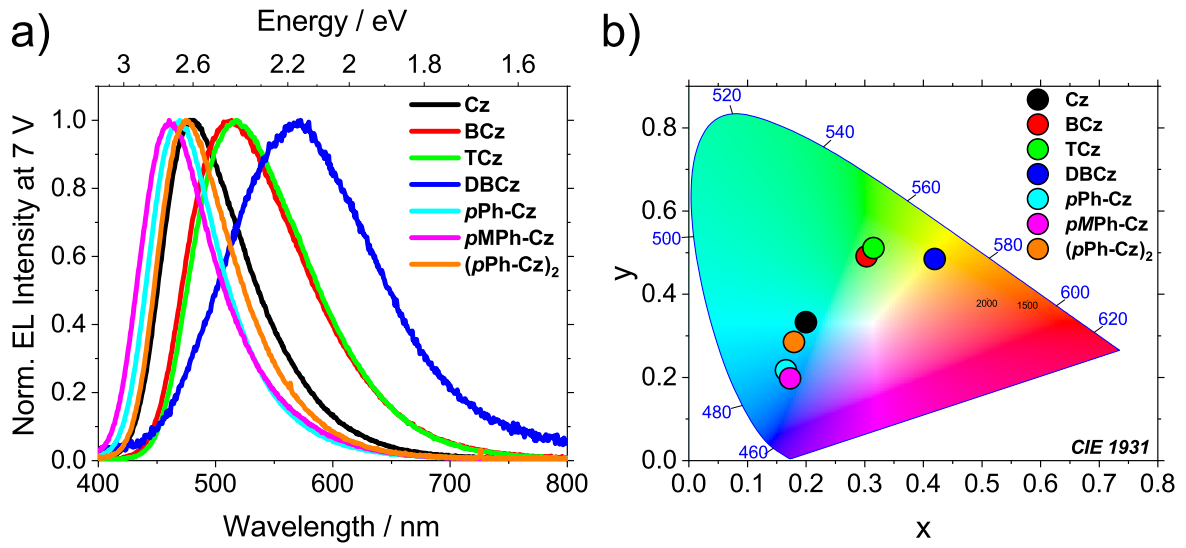


Figure 5.12: a) OLED EL spectra at 7 V applied voltage and b) CIE diagram showing respective color of the EL emission.

Table 5.5: EL characteristics: Maximum wavelength and corresponding energy, full width half maximum and CIE values of EL at 7 V.

Device	λ_{EL} /nm (/eV)	FWHM /nm (/eV)	CIE (x, y)
Cz	479 (2.59)	86 (0.46)	(0.198, 0.332)
BCz	513 (2.42)	115 (0.55)	(0.304, 0.491)
TCz	519 (2.39)	113 (0.53)	(0.315, 0.511)
DBCz	571 (2.17)	143 (0.55)	(0.424, 0.493)
pPh-Cz	469 (2.64)	72 (0.41)	(0.164, 0.215)
pMPh-Cz	461 (2.69)	75 (0.44)	(0.172, 0.197)
(pPh-Cz) ₂	476 (2.61)	77 (0.43)	(0.177, 0.285)

5.5 Summary

This chapter investigated seven carbazole-based D-A molecules with *N*-phenylphthalimide as the acceptor, exploring how modifications to the donor structure affect their photophysical properties and OLED performance.

The photophysics of the emitters was examined, and the absorbance spectra reveal an energetically favored CT state for all the emitters, except for **DBCz**, where an LE state appears to dominate. This is due to the larger conjugated π -system of the dibenzocarbazole donor compared to carbazole. The steady-state PL spectra of the doped films in mCBP show that **Cz** exhibits a cyan colored emission while **BCz**, **TCz** show a bathochromic shift to a green emission. **DBCz** shows the longest wavelength emission in the yellow while the bridged compounds all exhibit an emission maximum in the blue area, indicating that the bridging has little effect on the emission color and does not enlarge the donor or acceptor units. **Cz** showed the highest PLQY at 0.65, followed by **BCz** (0.52) and **TCz** (0.55), which showed similar values. In contrast, **DBCz** had a significantly lower PLQY of only 0.13, and the bridged compounds generally exhibited lower quantum yields compared to the unbridged compounds.

Time-resolved spectroscopy revealed TADF behavior for **Cz**, **BCz**, **TCz**, and **pMPh-Cz**. A small ΔE_{ST} was found for **TCz**, with a value of 88 meV due to the steric demanding donor unit which seems to be beneficial for achieving an optimal alignment of the donor and acceptor compared to **BCz**. **DBCz** exhibited room-temperature phosphorescence and a very large ΔE_{ST} , which prevents TADF. Additionally, **pPh-Cz** and **(pPh-Cz)₂** did not show TADF behavior. The methyl group in **pMPh-Cz** appears to play a crucial role in positioning the donor and acceptor at an optimal angle for TADF to occur.

The OLED characteristics of the investigated compounds show varying efficiencies and emission properties. **TCz** exhibits the highest maximum current efficiency of 33.9 cd A⁻¹ and EQE of 16%, consistent with its favorable photophysical properties. **BCz**, with a slightly higher ΔE_{ST} , shows a reduced EQE compared to **TCz**. Although the photophysical properties of **Cz** suggest it is an excellent emitter with high PLQY, a small ΔE_{ST} and a thermally activated component in the PL the OLED characterization does not reflect this. The reduced EQE of 7.7% may be attributed to poor charge injection and stabilization, potentially due to the more compact nature of the **Cz** structure. **DBCz**, which displays room-temperature phosphorescence and a large energy gap, has the lowest EQE, highlighting the limited contribution of its phosphorescence to efficiency.

The bridged compounds, including **pPh-Cz**, **pMPh-Cz**, and **(pPh-Cz)₂**, generally ex-

hibit lower EQEs (3.4%, 4.0% and 4.3%) and PLQYs (0.36, 0.26 and 0.41), with **pMPh-Cz** showing TADF but still limited by the low PLQY and potential charge injection issues.

The CIE coordinates reveal distinct emission colors for each compound, with **DBCz** emitting yellow light, **TCz** and **BCz** in the green region, and **Cz** and **(pPh-Cz)₂** in the cyan region and **pPh-Cz** and **pMPh-Cz** in the blue area.

6 Exploring the HIGHrISC Process of NMAAdF in OLED Applications

Innovative approaches in OLED technology are essential to overcoming current limitations and advancing next-generation displays, with blue OLEDs being a particular focus. Despite notable progress in organic emitter development, achieving blue TADF emitters that combine the demanding requirements of efficiency, color purity, and stability for real-world applications remains elusive. Despite several promising candidates have been discovered, challenges related to the optimization of these properties hindered the commercialization of blue TADF emitters. This makes the discovery of new materials and with enhanced photophysical properties a critical area of research.

In this context, the work of *Thom et al.* has shown the potential of *N*-methyl-difluoroacridone (NMA dF) as a promising candidate for blue OLED applications (s. Fig. 6.1).^[107] Their study employs spectroscopic and quantum chemical methods to explore the accessibility and characteristics of the higher triplet states of NMA dF , which are crucial for optimizing the performance of this emitter for OLEDs.

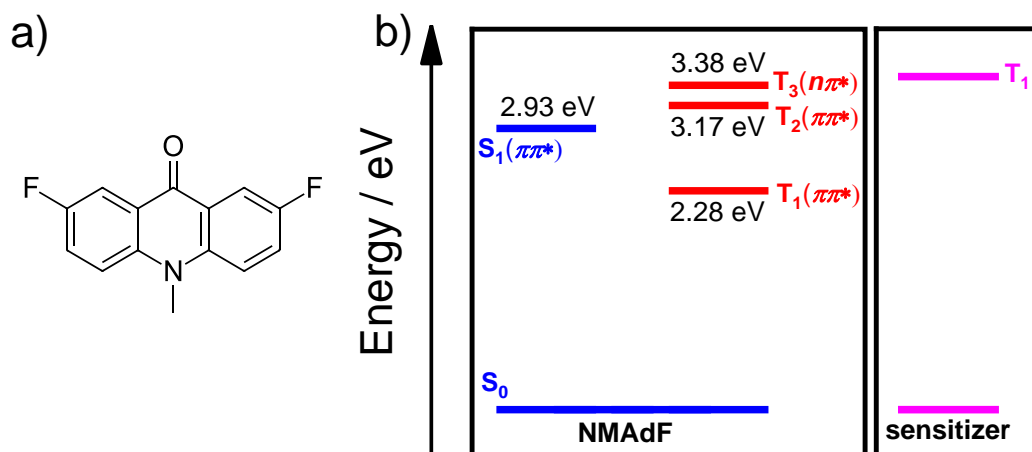


Figure 6.1: a) Structure of NMA dF and b) quantum chemically determined energy values of excited singlet and triplet states and triplet state of sensitizer 1,4-dichlorobenzene taken from ^[107].

Unlike conventional TADF emitters, where the T_1 state typically governs the rISC process to populate the S_1 state, NMA dF offers a distinct advantage: the T_2 state can also contribute to this process. This distinction is particularly significant because leveraging the T_2 state instead of the T_1 state in rISC results in a shorter lifetime of the radiative process. Since the upconversion occurs from the energetically higher T_2 state, rather than the lower-lying T_1 state, non-radiative decay channels are less likely, enhancing the overall efficiency and stability of the emitter.

Experiments by *Ziegenbein et al.* and *Thom et al.* demonstrated that the T_2 state

can be populated through two pathways: optical excitation from the T_1 state or energy transfer from a triplet sensitizer (1,4-dichlorobenzene).^[107,108] The electronically excited sensitizer transfers energy from its high-lying T_1 state directly to the T_2 state of the emitter. These findings, obtained in solution, pave the way for the exploration of this mechanism in OLED devices. The ultimate aim of this research is to evaluate the impact of the HIGHrISC process on OLED performance while providing critical insights into the fundamental mechanisms that could guide future emitter and device design.

The energetic positions of the relevant energy levels of **NMA \mathbf{dF}** are shown in Fig. 6.1 b, based on the detailed analysis by *Thom* et al.^[107,108]. Their computations place the 0–0 energy of the S_1 state ($^1\pi\pi^*$) at 2.93 eV, which aligns well with the experimental value of 2.87 eV. The T_1 state ($^3\pi\pi^*$), positioned at 2.28 eV, is energetically unable to contribute to delayed fluorescence.

Thom et al. identify two higher triplet states via quantum chemical computations that are accessible from the T_1 state of an additional sensitizer. These states are the higher $^3\pi\pi^*$ state (T_2 , 3.17 eV) and the lowest $^3n\pi^*$ state (T_3 , 3.38 eV). Both are proposed to contribute to rISC to the S_1 state. Notably, the $T_2 \rightarrow S_1$ transition is El-Sayed forbidden, with a calculated rate constant of $6 \times 10^9 \text{ s}^{-1}$, whereas the competing internal conversion ($T_2 \rightarrow T_1$) occurs much faster, at $5 \times 10^{12} \text{ s}^{-1}$. As a result, only about 0.1 % of the population in T_2 reaches the S_1 state.^[107]

In contrast, the T_3 state ($^3n\pi^*$) features an El-Sayed allowed transition ($T_3 \rightarrow S_1$) with a rate constant of $7 \times 10^{10} \text{ s}^{-1}$. Competing internal conversion ($T_3 \rightarrow T_2$) occurs at a comparable rate ($4 \times 10^{10} \text{ s}^{-1}$), leading to a significant fraction (60 %) of the population transitioning to S_1 . This branching ratio matches well with the experimental fluorescence efficiency (η_∞).^[107]

Thom et al. note that the computed energy separation between T_2 and T_3 is only 0.2 eV, which lies within the confidence interval ($\pm 0.2 \text{ eV}$) of the employed DFT/MRCI method. This, combined with the limitations of the simplified solvent model, introduces uncertainty in the predicted sequence of these states. The experimental findings suggest an inverted ordering, where T_3 ($^3n\pi^*$) is lower in energy than T_2 ($^3\pi\pi^*$), which better explains the observed population dynamics leading to the S_1 state.^[107]

Based on these insights, *Thom* et al. infer that the T_2 state corresponds to the $^3n\pi^*$ state. The rapid equilibration between T_2 and T_3 on a femtosecond timescale ensures efficient population transfer to S_1 , consistent with experimental results. Direct population of the T_1 state during energy transfer from the sensitizer may occur but is less significant, as indicated by the relatively unfavorable Franck-Condon factors for this pathway.^[107]

6.1 Photophysical Properties

The current understanding of NMA₂F is based either on quantum chemical calculations or on experimental studies in solution. However, to evaluate the suitability of the emitter for application in an OLED, it is necessary to study its properties in an appropriate environment, specifically in a thin film. While many emitters exhibit promising optical properties in highly diluted solutions, these properties can be significantly diminished in films due to quenching effects. Therefore, the concentration-dependent behavior of the emitter was initially investigated in the inert matrix polymethyl methacrylate (PMMA). The corresponding absorbance and emission spectra, as well as the PLQY, are presented in Fig. 6.2.

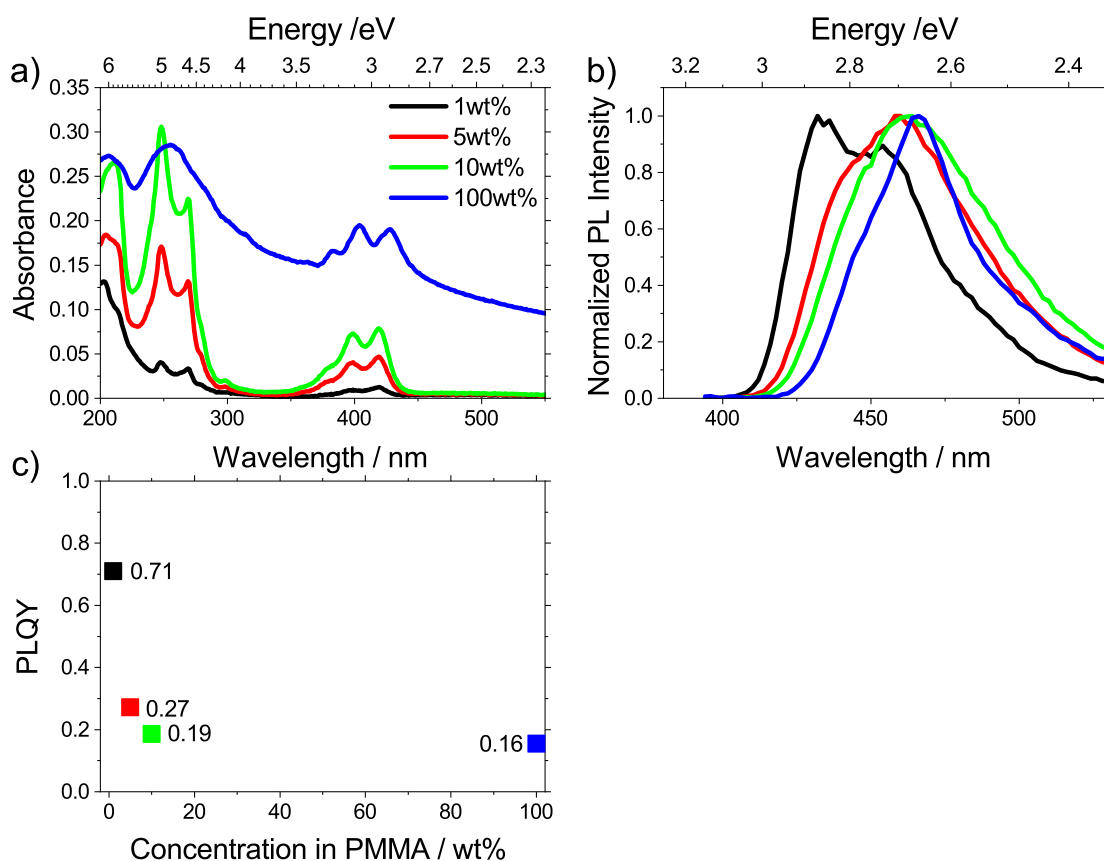


Figure 6.2: a) Absorbance, b) normalized PL intensity, and c) PLQY of NMA₂F in varying concentrations in PMMA matrix.

In highly diluted samples, the high PLQY observed in solution-based measurements can nearly be reproduced, reaching 71% compared to 87% in methanol, as reported by *Thom et al.*^[107]

At higher concentrations, a significant decrease in the PLQY is observed, with the yield dropping to merely 16% in the neat film. The planar character of the molecule likely promotes π -stacking interactions between emitter molecules, leading to non-radiative deactivation processes. The absorbance spectrum is independent of the concentration, although scattering effects are observed in the neat film due to crystallization. The emission at high concentrations is red-shifted ($\lambda_{em,max} = 466$ nm) compared to low concentrations ($\lambda_{em,max} = 432$ nm) and no longer exhibits a distinct double-band structure.

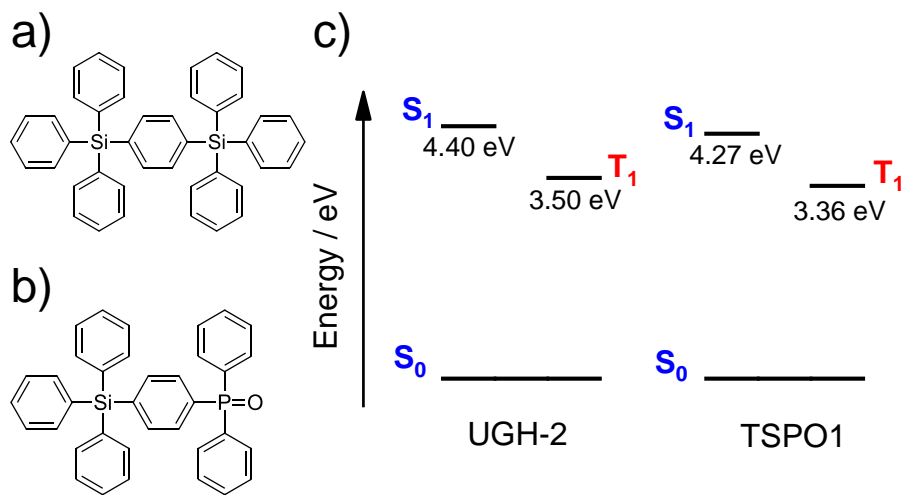


Figure 6.3: Chemical structure of host material a) UGH-2, b) TSPO1 and c) their experimentally determined excited state's energy levels taken from [109,110].

To transfer the concept of solution-based experiments into an OLED, a suitable host material must be identified. The host material should act as a sensitizer and ideally, recombination should occur on the host material, as recombination on the emitter molecule does not guarantee that the 75% statistically formed triplet excitons will populate the T_2 states. However, excitons generated on the host material can transfer to the T_2 state of the emitter molecule, provided the energy levels are properly aligned.

To ensure efficient energy transfer, the host material must have a T_1 state energy higher than the T_2 state of the emitter, which lies at 3.17 eV. Many commonly used host materials fail to meet this requirement. However, arylsilane-based high-gap materials are known to exhibit sufficiently high triplet energies due to their unique molecular characteristics.^[109–111] The weak conjugation between the sp^3 -hybridized silicon atom and the attached aryl groups limits electronic delocalization, preserving high-energy levels. Additionally, the steric bulk of the silicon atom reduces π - π stacking and aggregation, which helps to maintain high triplet state energies. Among these materials, UGH-2 and

TSPO1, both commercially available and depicted in Fig. 6.3, were chosen for this study. Their photophysical properties were initially investigated in guest-host single layers, as shown in Fig. 6.4.

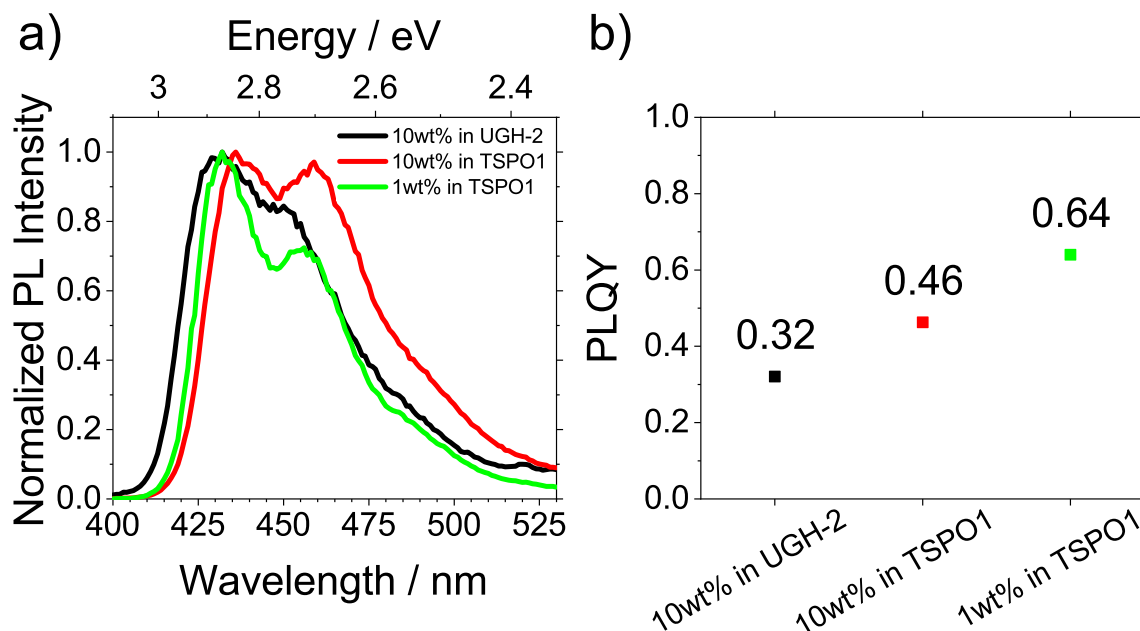


Figure 6.4: a) PL spectra and b) PLQY of NMA dF in UGH-2 and TSPO1 thin film.

The limited solubility of the host materials rendered the use of solution-processed methods for layer deposition impossible; therefore, the layers were fabricated via vacuum thermal evaporation. A concentration of 10 wt% emitter in the host material was chosen to evaluate the fundamental suitability of the system. The PL spectrum in UGH-2 is slightly blue-shifted compared to that in TSPO1, which can be attributed to the nonpolar nature of UGH-2. This nonpolarity results in weaker stabilization of the excited state, leading to the observed shift. The PLQY reached 32% in UGH-2, whereas a higher value of 46% was observed in TSPO1. A further increase in PLQY to 64% and blue-shift of the spectrum was achieved in TSPO1 by reducing the emitter concentration to 1 wt%.

6.2 Energy Levels and Thermal Properties

The energy levels and thermal properties of the emitter are key parameters for its suitability in OLED applications. Accurate energy levels are essential for optimizing charge injection and recombination processes, while robust thermal stability ensures reliable performance during device fabrication and operation.

The electrochemical properties of the emitter were determined using cyclic voltammetry (s. Fig. 10.35), yielding an oxidation potential (E_{ox}) of 1.05 eV and a reduction potential (E_{red}) of -2.17 eV. From these values, the HOMO and LUMO energy levels were estimated according to Eq. 9.3 to be -6.20 eV and -2.98 eV, respectively, as summarized in Tab. 6.1.

Table 6.1: Oxidation and reduction half wave potential, according to Eq. 9.3 estimated HOMO and LUMO energy values, melting temperature (T_m) and decomposition temperature (T_d) of **NMA_dF**.

	$E_{ox}^{1/2}$ /eV	$E_{red}^{1/2}$ /eV	HOMO /eV	LUMO /eV	T_m /°C	T_d /°C
NMA_dF	1.05	-2.17	-6.20	-2.98	243	258

The thermal properties of the emitter were evaluated using TGA/DSC (s. Fig. 10.36), revealing a melting temperature T_m of 243 °C and a decomposition temperature T_d of 258 °C (Tab. 6.1). Such high thermal stability values are essential for vacuum deposition, as they ensure that the material retains its structural integrity during the fabrication process and maintains morphology under operational conditions, which is critical for the long-term reliability of OLED devices.

6.3 OLED Device Optimization

To adapt the HIGHrISC process for application in OLEDs, the emitter was implemented into devices. Initially, a simple device structure was selected and gradually optimized. The optimization steps and the final optimized device structure (Nr. 5) can be found in Tab. 6.2. Fig. 6.5 shows the FMO energy levels of the optimized device stack.

Table 6.2: Optimization of OLED stack. By introducing a hole injection layer consisting of MoO₃ and C₆₀, exchanging the host material from UGH-2 to TSPO1, reducing the emitter concentration in the host-guest system from 10 wt% to 1 wt% and removing the ETL 3TPYMB the device efficiency could be improved (s. Fig. 6.2).

	1	2	3	4	5
PEDOT:PSS	35 nm	35 nm	35 nm	35 nm	35 nm
MoO ₃	x	6 nm	6 nm	6 nm	6 nm
C ₆₀	x	5 nm	5 nm	5 nm	5 nm
TCTA	40 nm	40 nm	40 nm	40 nm	40 nm
NMA ₂ F	10wt%	10wt%	10wt%	1wt%	1wt%
in UGH-2	20 nm	20 nm	x	x	x
in TSPO1	x	x	20 nm	20 nm	20 nm
3TPYMB	35 nm	35 nm	35 nm	35 nm	x
LiF	1 nm	1 nm	1 nm	1 nm	1 nm
Al	100 nm	100 nm	100 nm	100 nm	100 nm

As a starting point for optimization, a simple device structure was chosen (OLED 1). It consisted of an ITO anode and PEDOT:PSS, which was used both as a HIL and for smoothing the surface. TCTA was employed as the HTL due to its low HOMO level.^[112] The emitter **NMA₂F** was doped into the silylaryl host material UGH-2 at a weight concentration of 10 wt%. 3TPYMB was utilized as the ETL, and the cathode consisted of LiF/Al.

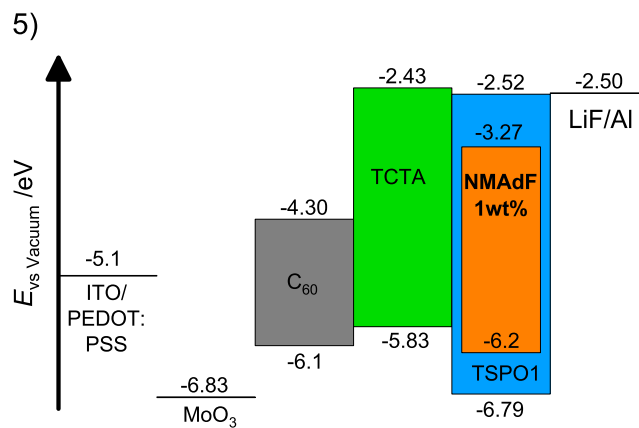


Figure 6.5: Optimized OLED stack. Layer thicknesses can be found in Tab. 6.2, column 5.

The device was optimized in several steps (s. Tab. 6.2). First, a MoO₃/C₆₀ layer was

introduced to improve hole injection (OLED 2).^[113] Subsequently, the host material was changed from UGH-2 to TSPO1 (OLED 3), which had already demonstrated higher a PLQY (0.32 in UGH-2, 0.46 in TSPO1) in prior studies (s. Fig. 6.4). The emitter concentration was then reduced from 10 wt% to 1 wt% (OLED 4), as PL studies indicated that PLQY is higher at lower concentrations (0.46 at 10 wt%, 0.64 at 1 wt% in TSPO1). Finally, the ETL layer was omitted altogether (OLED 5) as TSPO1 already possesses excellent electron transport properties, and its LUMO level aligns well with the cathode's work function.

This optimization process resulted in an OLED with a characteristic diode-like current-voltage curve (s. Fig. 6.6 a) and a maximum efficiency of 0.4 cd/A (s. Fig. 6.6 c). The wavelength of the EL maximum intensity lies at 436 nm (s. Fig. 6.6 d).

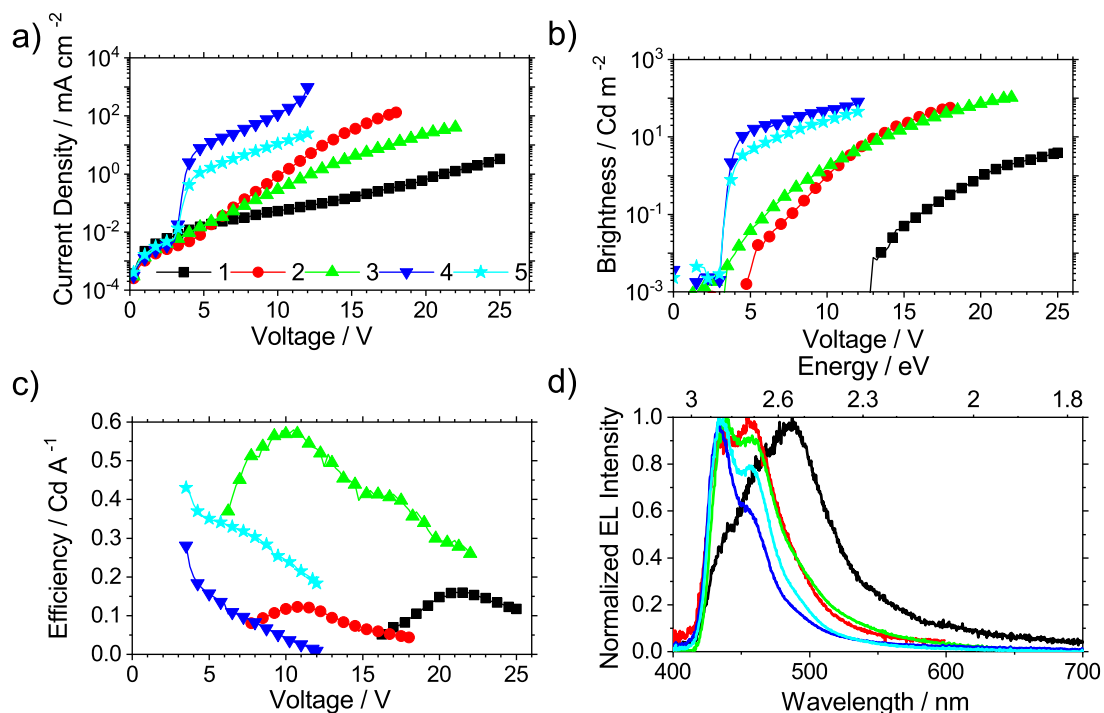


Figure 6.6: Characteristics of NMA₂F based OLEDs. The OLED stacks can be found in Fig. 6.5. a) Current density, b) brightness, c) current efficiency and d) EL spectra of the five devices.

Unfortunately, the optimization process was complicated by the extreme volatility of NMA₂F. During thermal evaporation in vacuum, even at temperatures as low as 80°C, evaporation rates were detectable. This caused contamination of the vacuum chamber, and the molecule was found in all subsequent samples, making further optimization of the

device unfeasible.

Additionally, solution processing was not an option due to the poor solubility of the host materials in solvents such as THF, which also dissolve NMA dF . A promising strategy for future experiments could involve the development of host materials with high T_1 states but improved solubility, allowing for solution-based processing. Another possible approach would be to modify NMA dF with larger substituents that do not significantly alter its electronic properties, thereby increasing its sublimation point and enabling more reliable thermal vacuum deposition.

6.4 Summary

This chapter provides an analysis of the properties of the fluorinated acridone NMA dF for OLED applications. The photophysical properties in solid state were investigated, and it was found that NMA dF tends to form aggregates that red-shift and quench the emission of the compound. However, in diluted PMMA layers high PLQY values of up to 0.71 and a deep-blue emission color (432 nm) could be achieved.

The host materials UGH-2 and TSPO1 were identified as possible candidates to facilitate energy conversion from their high lying T_1 states to the T_2 state of NMA dF to enable the beneficial use of rISC from T_2 to S_1 for conversion of non-radiative triplet excitons to radiative singlet states.

CV was used to estimate the energy levels of the HOMO at -6.2 eV and the LUMO at -3.27 eV from the found oxidation and reduction potential. Determination of thermal properties showed a decomposition temperature of 258°C , which is sufficient for PVD processing.

NMA dF was successfully integrated into an OLED device, and through careful optimization of the device structure a stable OLED was obtained. However, the efficiency remained relatively low, at only 0.4 cd A^{-1} . The extreme volatility of the compound made further device optimization unfeasible. For future developments, materials with similar electronic properties but reduced volatility should be designed, or alternative processing methods should be adopted.

7 Analysis of TADF Characteristics in a Chiral Donor-Acceptor Emitter

Donor-acceptor D-A molecules have emerged as essential materials in the development of advanced optoelectronic devices due to their tunable electronic and photophysical properties. These molecules utilize the interplay between electron-donating and electron-accepting moieties to achieve desired properties such as narrow ΔE_{ST} , CT character, and efficient luminescence.

In this study, a novel D-A molecule that combines a dihydrophenazine donor with a benzothiazol acceptor (s. Fig. 7.1) is investigated. The dihydrophenazine unit, known for its strong electron-donating capabilities and robust chemical stability, has been utilized in TADF applications as an electron donor in similar systems^[114,115]. Benzothiazol has found application as an electron acceptor in various studies, demonstrating its effectiveness in facilitating efficient charge transfer.^[59,115–117]

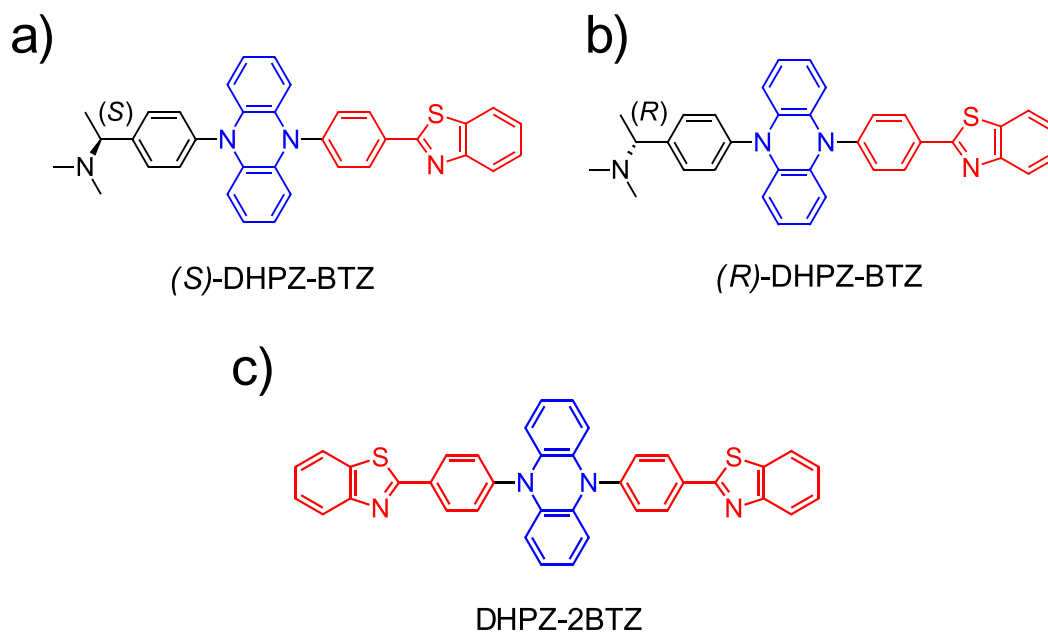


Figure 7.1: Structure and nomenclature of the two enantiomers a) & b) of *N,N*-Dimethyl[1-(*p*-(10-[*p*-(1,3-benzothiazol-2-yl)phenyl]-5,10-dihydro-5-phenaziny)-phenyl)-ethyl]amine. The donor **dihydrophenazine** is marked blue, the acceptor **phenylene-benzothiazol** is marked red. The chiral *N,N*-dimethyl-1-phenylethylamines unit is marked black. c) Structure of the A-D-A compound **DHPZ-2BTZ**, which is well described in the literature and used here as a reference compound (adapted from ^[115]).

The design and synthesis of the compounds was performed by *Dirk Laux* from the group of *Prof. Arne Lützen* and is inspired by prior research on acceptor-donor-acceptor (A-D-A) molecules.^[115] By focusing on a simpler D-A architecture, it is aimed to explore the effects of a single donor and acceptor interaction, enhanced by a chiral side group, on the TADF

performance. The chiral side group *N,N*-dimethyl-1-phenylethylamines introduces potential for chirality-induced phenomena such as circularly polarized luminescence, expanding the scope of this material for advanced applications in CP-OLEDs.

The following sections will explore the photophysical behavior of this molecule, including its singlet-triplet gap, emission characteristics, and delayed fluorescence properties. A comparative analysis with existing A-D-A systems will provide insights into the influence of molecular symmetry and architecture on TADF efficiency.

In this chapter, in addition to photophysical properties, the thermal and electrochemical properties of the molecule are investigated to evaluate its suitability for application in OLEDs. Finally, the molecule is implemented into an OLED, which is then characterized in terms of its electroluminescence and LIV properties.

Although the primary focus of this work is the study of thermally activated upconversion of excited triplet to radiative singlet states, this chapter also addresses the chiral aspect of the molecule to analyze its potential application in CP-OLEDs.

7.1 Photophysical Properties

S-DHPZ-BTZ is studied within the achiral polymer matrix PMMA. As both enantiomers are expected to exhibit identical behavior in an achiral environment as long as no polarization-dependent measurements are performed, only the (*S*)-enantiomer is analyzed to investigate its aggregation behavior and the concentration-dependent effects on its photophysical properties. Absorbance and photoluminescence spectra as well as PLQY of the investigated thin films with different emitter concentrations are shown in Fig. 7.2. The absorbance spectrum remains nearly independent of the emitter concentration, with only the absorbance intensity increasing with higher concentrations. The structureless broad absorbance band at 375 nm suggests the presence of a charge-transfer (CT) state. In contrast, the emission exhibits a clear concentration dependence, showing a pronounced bathochromic shift from 562 nm at 1 wt% to 615 nm in the neat film. This behavior suggests that the emitter molecules aggregate at higher concentrations. Additionally, the PLQY decreases significantly with increasing concentration, dropping from 0.27 at 1 wt% to 0.08 in the neat film. This reduction further supports the conclusion that aggregation adversely affects the photophysics of the emitter. Furthermore, the absorbance of the neat film exhibits pronounced scattering effects, indicating that the film is likely polycrystalline rather than amorphous.

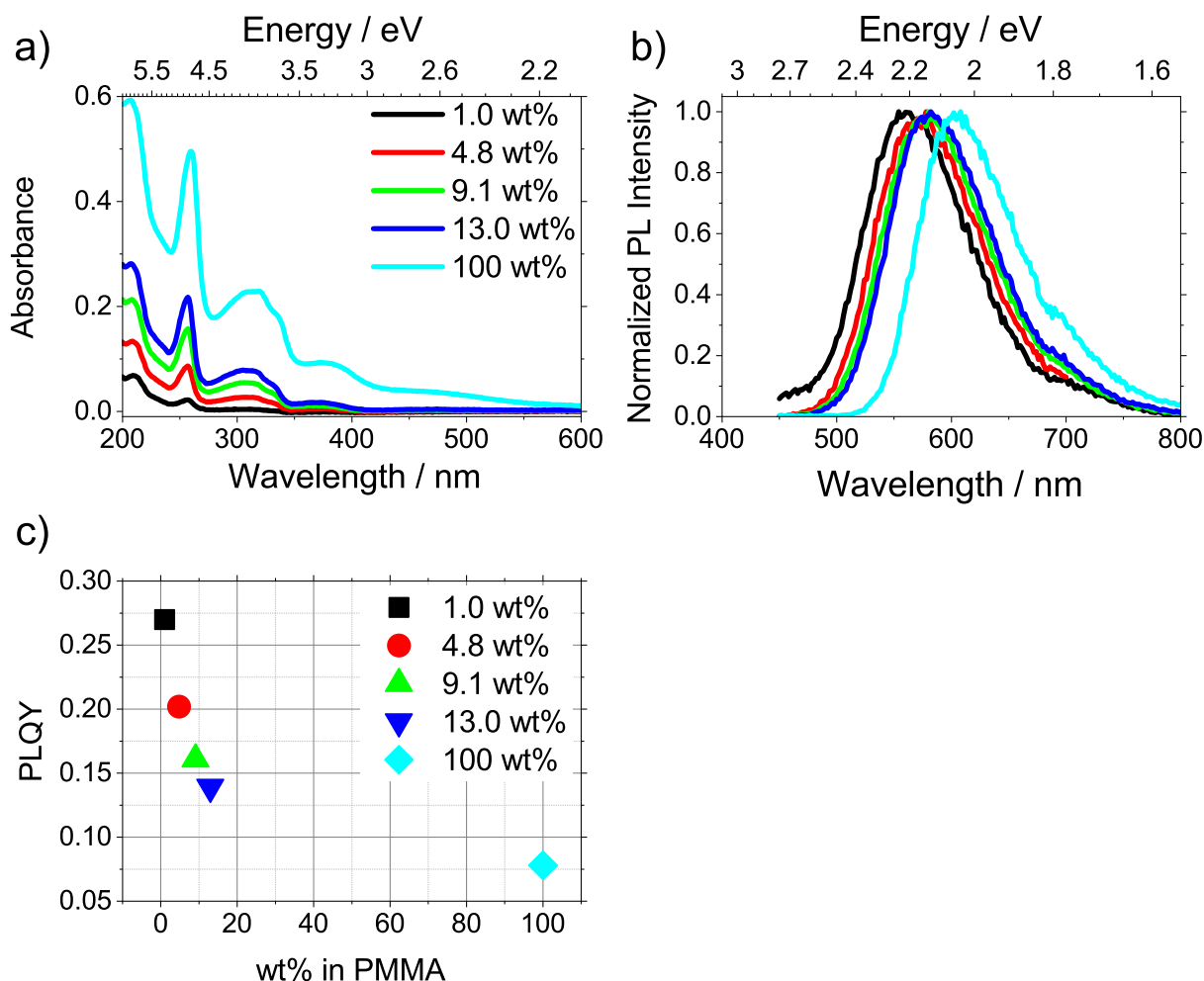


Figure 7.2: a) Absorbance and b) PL spectra, c) PLQY at an excitation wavelength of 310 nm and d) CD spectra of *S*-DHPZ-BTZ in PMMA thin films at different weight concentrations.

In addition to studies in PMMA, the emitter was also investigated in an mCBP matrix. mCBP was chosen as it is a commonly used host material in TADF OLEDs with a high lying T_1 state at 2.8 eV^[69], and **DHPZ-2BTZ** has already been studied in this matrix. To ensure comparability, a concentration of 6 wt% was selected, as reported by *Lee et al.*^[115] The absorbance and PL of the emitter were analyzed under these conditions and the spectra are presented in Fig. 7.3. To distinguish the absorbance and emission of the emitter from those of mCBP, neat films of both materials were also investigated. The broad, unstructured emission band of (*S*)-DHPZ-BTZ in mCBP peaks at 590 nm and is significantly red-shifted compared to the structured emission band of mCBP, which appears at approximately 400 nm. In the host-guest system, no emission is detectable

at the maximum of mCBP, indicating an efficient energy transfer from mCBP to **(S)-DHPZ-BTZ**. The PLQY of the host-guest film is 0.27. In comparison, **DHPZ-2BTZ**, as reported in the literature, exhibits a PL maximum at 577 nm and a slightly higher PLQY of 33%, with its emission being distinctly blue-shifted relative to **(S)-DHPZ-BTZ**.^[115] In the neat film, the emission of **(S)-DHPZ-BTZ** is slightly red-shifted compared to the host-guest system.

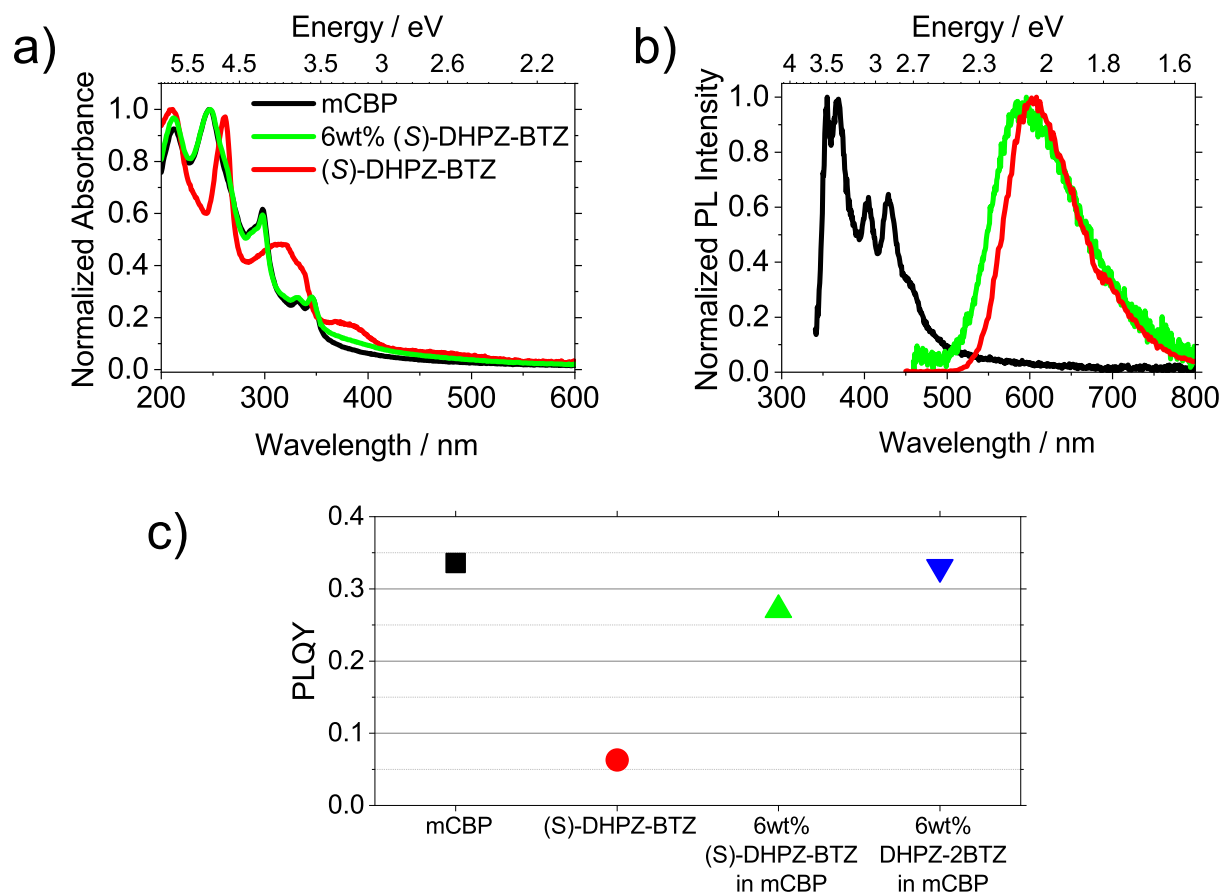


Figure 7.3: a) Absorbance, b) PL spectra, c) PLQY at an excitation wavelength of 300 nm for host material mCBP, 6wt% **(S)-DHPZ-BTZ** in mCBP and neat film of **(S)-DHPZ-BTZ**. PLQY of **DHPZ-2BTZ** taken from ^[115] is included for comparison.

7.2 Time-resolved PL in mCBP

To investigate the emitter's ability regarding TADF, time-resolved spectroscopy experiments were conducted at different temperatures. Fig. 7.4 shows the decay curves of the prompt and delayed PL along with the corresponding exponentially fitted decay times. The prompt fluorescence at 300 K has a decay time of 10.2 ns, with only minor changes observed as the temperature decreases (13.1 ns at 80 K). In contrast, the delayed component shows significant variations: at 300 K, the decay time is 7.8 μ s, while at 80 K, it increases to 101.1 μ s. This can be explained by the fact that at lower temperatures, less energy is available to overcome the energy barrier between the T_1 and S_1 , resulting in longer lifetimes. This behavior suggests the presence of a TADF mechanism.

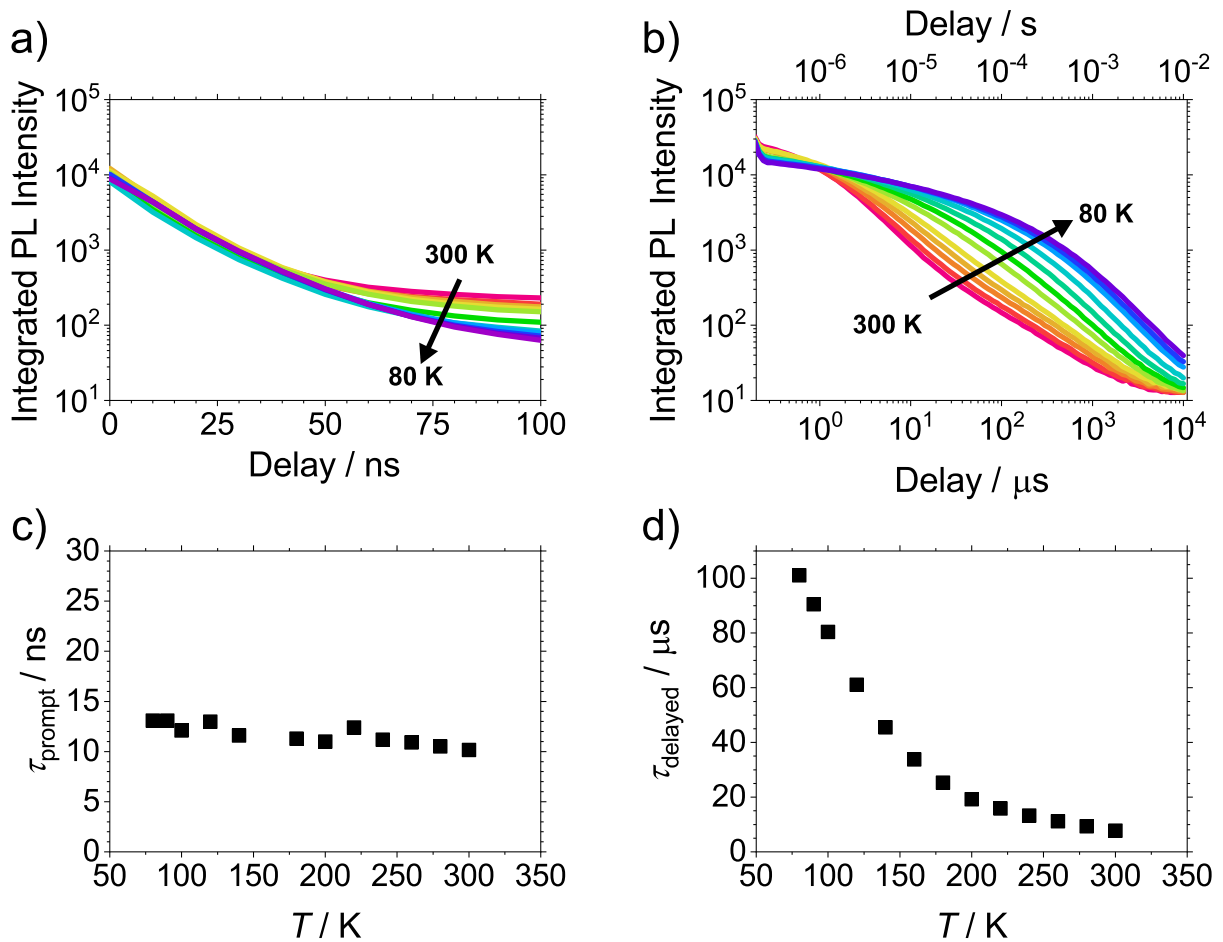


Figure 7.4: Photoluminescence decay of a) prompt and b) delayed PL of 6 wt% (S)-DHPZ-BTZ in mCBP at temperatures between 300 K and 80 K in 20 K steps. Exponentially fitted decay times of c) prompt and d) delayed PL in dependence of the temperature.

To estimate the energy gap ΔE_{ST} , the Arrhenius relationship is employed. By plotting the experimentally determined rates against the inverse temperature (s. Fig. 7.5) and analyzing the slope of the resulting graph, ΔE_{ST} is calculated to be 50 meV. In comparison, **DHPZ-2BTZ** exhibits a delayed component decay time of approximately 1 μ s and a prompt decay time of 12 ns. The determined ΔE_{ST} is close to 0 eV, as derived from the comparison of fluorescence and phosphorescence spectra, though the slight noise in the data may affect the reliability of this value.^[115] A-D-A structures like **DHPZ-2BTZ** facilitate more effective intramolecular charge transfer due to the presence of two acceptor units flanking the donor. This configuration promotes better delocalization of the excited states, leading to a smaller ΔE_{ST} and enhancing the efficiency of TADF compared to the D-A system in (*S*)-**DHPZ-BTZ**.

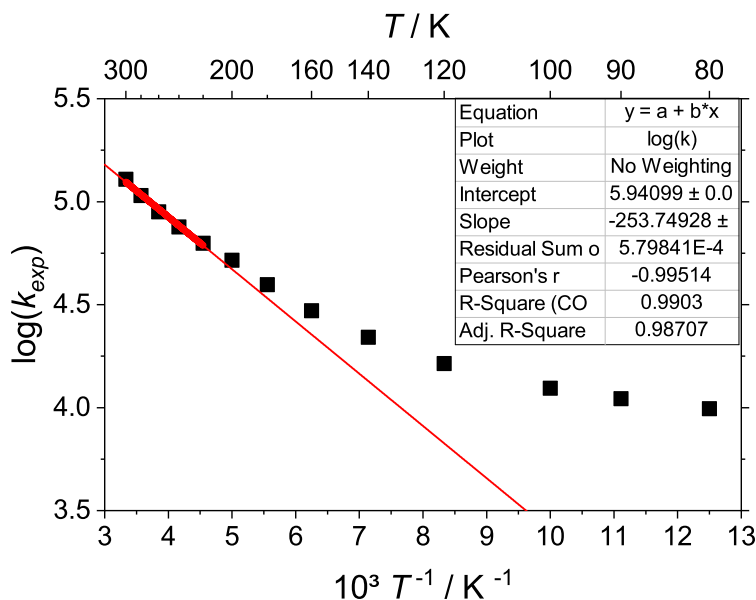


Figure 7.5: Arrhenius plot of experimentally determined delayed PL decay rate constants at different temperatures for 6 wt% (*S*)-**DHPZ-BTZ** in mCBP. The slope of the plot is used to estimate ΔE_{ST} , which is determined to be 50 meV.

Fig. 7.6 presents the PL spectra of the prompt and delayed components at 300 K and 80 K. For a TADF emitter, it is expected that at 300 K, the spectra of the prompt and delayed fluorescence would coincide, as both originate from radiative relaxation of the same S_1 state. At low temperatures, however, the thermal energy is insufficient to enable the conversion from T_1 to S_1 . This makes the T_1 states sufficiently long-lived for phosphorescence to occur, which is typically red-shifted compared to fluorescence.

At 300 K (Fig. 7.6 a), the spectra of the prompt and delayed components are predomi-

nantly identical, as expected. However, the delayed spectrum shows an additional blue-shifted shoulder. This phenomenon can be attributed to the presence of a higher-lying S_1 state, which results from a larger ΔE_{ST} . Consequently, fluorescence from these higher-lying S_1 states is blue-shifted compared to emission from the low energy S_1 states.

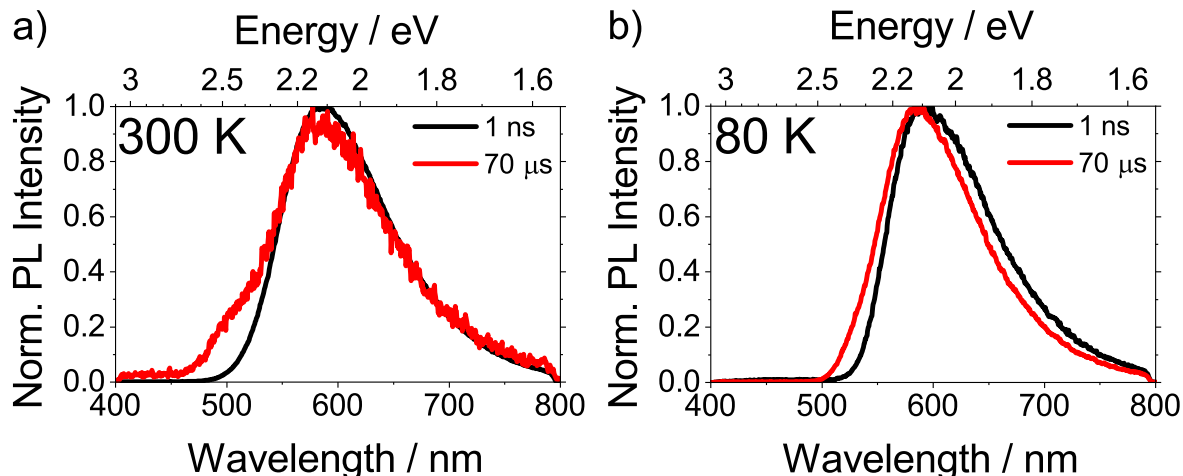


Figure 7.6: Normalized PL spectra of 6 wt% *(S)*-DHPZ-BTZ in mCBP at a) 300 K and b) 80 K at delay times of 1 ns and 70 μ s. An additional plot comparing the spectra at different delay times is presented in Fig. 10.37.

A similar observation was made by *Püschel et al.* in a dihydrophenazine-based A-D-A emitter.^[114] Their quantum chemical calculations demonstrated that the torsional angle between the dihydrophenazine core and the acceptor significantly affects ΔE_{ST} . When the torsional angle approaches 90° , ΔE_{ST} is minimized, allowing for efficient TADF. However, ΔE_{ST} also exhibits additional local minima at certain other torsional angles, reflecting the complex interplay between molecular geometry and electronic structure. Deviations from these optimal angles increase ΔE_{ST} , altering the emission properties by enabling higher-lying S_1 states. Additionally, since these measurements were performed in a film, molecular motion, while not entirely frozen, is significantly restricted. This limitation can trap the molecule in geometries corresponding to other local energetic minima, where torsional angles deviate from 90° , causing the blue shift in the emission.

At 80 K (Fig. 7.6 b), the blue-shifted shoulder is observed but is less pronounced compared to 300 K. This is because the thermal energy at this temperature is insufficient to fully populate the higher-lying S_1 states. In contrast, at 300 K, enough energy is available to overcome the larger ΔE_{ST} of the twisted emitter, enabling access to these higher S_1 states. However, the rISC rate remains relatively low, causing emission from these states to become apparent only at longer delay times. At 80 K (Fig. 7.6 b), the blue-shifted

shoulder is observed but is less pronounced compared to 300 K. Simultaneously, the slight blue shift of the spectrum at 80 K and long delay times, compared to the prompt PL, argues against the occurrence of phosphorescence, which would typically be red-shifted. This behavior suggests a small ΔE_{ST} , as even at 80 K, sufficient thermal energy is available to enable rISC from T_1 to S_1 . This observation is supported by the relatively small energy gap of 50 meV, determined using the Arrhenius relationship shown in Fig. 7.5. To obtain a more distinct phosphorescence spectrum, measurements should be conducted using liquid helium as a coolant, enabling cooling to 4 K.

7.3 Energy Levels and Thermal Properties

The energy levels and thermal properties of the emitter are crucial for its performance in OLEDs. Accurate energy levels enable efficient charge transport and recombination, while high thermal stability ensures reliability during fabrication and operation.

The energy levels of the emitter were determined using cyclic voltammetry (s. Fig. 10.42), yielding oxidation and reduction potentials ($E_{ox} = -0.15$ eV, $E_{red} = -2.41$ eV). These values were used to estimate the HOMO and LUMO energy levels at -5.00 eV and -2.74 eV, respectively, as summarized in Tab. 7.1.

Table 7.1: Oxidation and reduction half wave potential, according to Eq. 9.3 estimated HOMO and LUMO energy values, melting temperature (T_m) and decomposition temperature (T_d) of **(S)-DHPZ-BTZ**.

	$E_{ox}^{1/2}$ /eV	$E_{red}^{1/2}$ /eV	HOMO /eV	LUMO /eV	T_m /°C	T_d /°C
DLS	-0.15	-2.41	-5.00	-2.74	242	349

Thermal characterization was performed using TGA/DSC (s. Fig. 10.43), which identified a melting temperature (T_m) of 243 °C and a decomposition temperature (T_d) of 258 °C (s. Tab. 7.1). These high thermal stability parameters are crucial for vacuum deposition, ensuring the material's morphology and structural integrity are preserved during fabrication and under operating conditions.

7.4 Application as Emitters in OLEDs

The obtained insights were applied to test the emitter in an OLED device. Based on the device structure described by *Lee et al.*, a similar OLED architecture (s. Fig.7.7) was chosen to ensure comparability.^[115] Deviating from *Lee et al.*, PEDOT:PSS was used as the hole injection layer instead of HATCN, as experiments demonstrated that this layer leads to a more stable dark current. This is likely because the polymer is better suited to compensate for irregularities in the ITO layer, creating a smoother and more uniform interface with the subsequent NPB layer. NPB was employed as the HTL, and the emitter was embedded in an mCBP host at a weight concentration of 6 wt%, consistent with the photoluminescence experiments in sections 7.1 and 7.2. TPBi was used as the ETL, and LiF/Al served as the cathode.

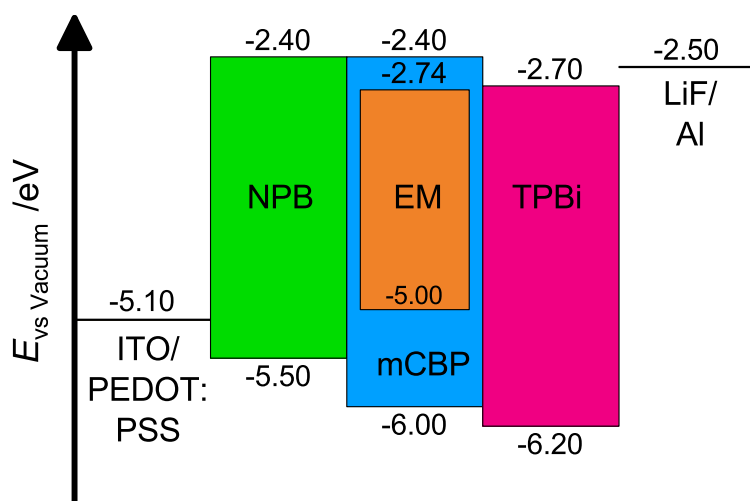


Figure 7.7: OLED stack based on ^[115]: PEDOT:PSS (35 nm), NPB (35 nm), 6wt% (**S**)-**DHPZ-BTZ** in mCBP (15 nm), TPBi (65 nm), LiF (1 nm), and Al (100 nm).

The LIV characteristics (s. Fig.7.8) reveals a current efficiency of up to 8.2 cd A⁻¹ and an EQE of up to 2.7%, compared to 5% reported for **DHPZ-2BTZ** OLED in the literature.^[115] This appears plausible due to the slightly lower PLQY (0.27 compared to 0.33) and the somewhat larger ΔE_{ST} , which results in a reduced rISC rate and, consequently, a lower triplet exciton utilization efficiency. The spectrum of the orange EL

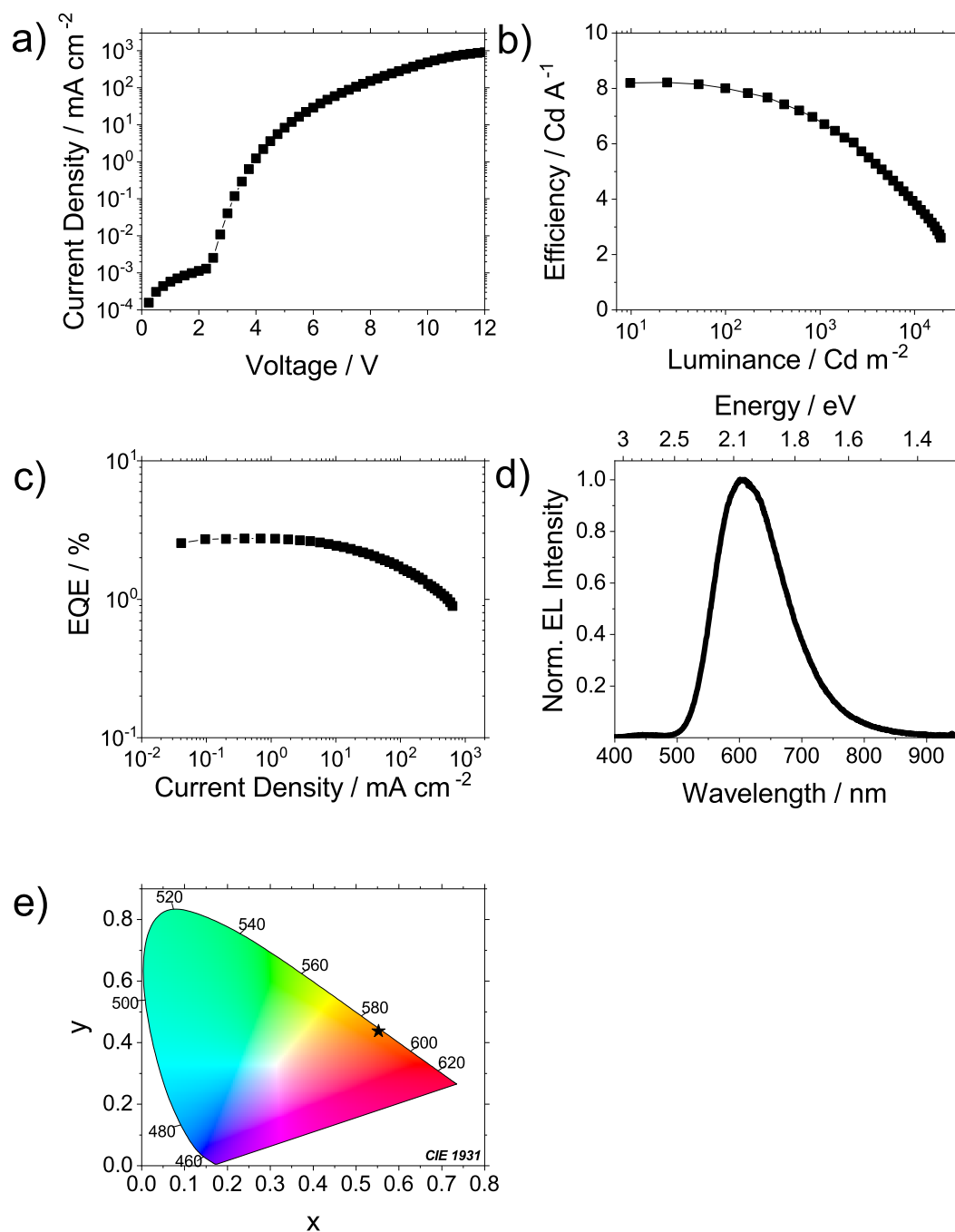


Figure 7.8: Characteristics for (S)-DHPZ-BTZ OLED: a) Current density vs. applied voltage, b) Current efficiency as a function of brightness, c) EQE vs. current density, d) EL spectrum at 7 V applied voltage, and e) CIE 1931 color coordinates.

closely matches the PL spectrum shown in Fig. 7.3 b. Polarization-dependent measurements of the EL spectrum revealed no intensity difference between right- and left-polarized electroluminescence. Thus, while the emitter can be classified as a TADF emitter, it is not suitable for application in circularly polarized OLEDs.

Table 7.2: Characteristics of (**S**)-**DHPZ-BTZ** OLED. Turn-on voltage, maximal luminance, power and current efficiency, external quantum efficiency, wavelength of EL maximum intensity, full width half maximum and CIE of EL.

V_{on}	L_{max}	PE	CE	EQE (max, 1000)	λ_{EL}	FWHM	CIE
/V	/Cd m ⁻²	/lm W ⁻¹	/Cd A ⁻²	/%	/nm	/nm	(x, y)
2.5	19500	8.2	8.2	2.7, 2.2	605	129	(0.55, 0.44)

7.5 Summary

In this chapter, the chiral D-A molecule **S-DHPZ-BTZ** was investigated, and its properties were compared to those of a literature-known symmetric A-D-A emitter **DHPZ-2BTZ**. The relevant data is summarized in Tab. 7.3.

Table 7.3: Comparison of experimental findings on **S-DHPZ-BTZ** with literature described **DHPZ-2BTZ**^[115]. Photophysical and OLED data was determined with 6 wt% emitter in mCBP matrix.

	S-DHPZ-BTZ	DHPZ-2BTZ
structure	D-A	A-D-A
$\lambda_{PL,max}$	590 nm	577 nm
PLQY	0.27	0.33
τ_{prompt}	10.2 ns	12 ns
$\tau_{delayed}$	7.8 μ s	1 μ s
ΔE_{ST}	50 meV	\sim 0 meV
EQE _{max}	2.7%	5%
$\lambda_{EL,max}$	605 nm	601 nm

In the OLED host material mCBP, **S-DHPZ-BTZ** showed an emission maximum at 590 nm and a PLQY of 0.27 was determined at a weight concentration of 6 wt% emitter. These values are comparable to the literature values for the A-D-A molecule, which exhibits an emission maximum at 577 nm and a PLQY of 0.33. The overall moderate

quantum yield suggests high rate constants for non-radiative processes such as IC.

To gain insight into the nature of the excited states, time-resolved PL measurements were performed at different temperatures, and the PL decay was analyzed. The prompt fluorescence was found to be nearly temperature-independent and exhibited a decay time of 10.2 ns at 300 K. The delayed PL showed a decay time of 7.8 μ s at 300 K.

The decay time increased with decreasing temperature, consistent with TADF behavior. An Arrhenius plot was used to determine a ΔE_{ST} of 50 meV, further supporting the classification as a TADF emitter.

The emitter was implemented into an OLED, achieving an EQE of 2.7%. Compared to the A-D-A emitter, which exhibits an EQE of 5%, the efficiency is reduced. This reduction can be attributed to the slightly lower PLQY and the larger ΔE_{ST} of **S-DHPZ-BTZ**, which results in a lower rISC rate.

Polarization-dependent measurements of the EL spectrum showed no variation in intensity between right- and left-circularly polarized electroluminescence. Since the chiral group is not part of the emitter's conjugated system, it has no influence on the polarization of the emitted light.

8 Conclusion and Outlook

In this work various organic emitter molecules are extensively examined in terms of their spectroscopic properties and potential applications in organic light-emitting diodes (OLEDs). Key properties such as the emission color were analyzed, along with the underlying mechanisms of the photoluminescence, including singlet-triplet transitions (and the reverse processes), fluorescence, phosphorescence, and the dynamics and relaxation behavior of excited states. The choice of environment in which the molecules are studied is crucial, as it significantly influences the molecular properties and behavior of the emitter molecules, which in turn has direct implications for the performance and efficiency of OLEDs.

Chapter 3 provides an overview of the theoretical background. It explains the fundamental physical processes that govern the operation of OLEDs, such as charge injection, charge transport, exciton formation, and radiative decay. The chapter also includes a historical perspective on the development of OLED emitters, tracing the evolution from early fluorescent materials to modern phosphorescent and thermally activated delayed fluorescence (TADF) emitters. Furthermore, key photophysical processes relevant to OLED performance are explained, including singlet and triplet exciton dynamics, energy transfer mechanisms, and non-radiative decay pathways. The chapter concludes with an overview of the fabrication techniques used in OLED production.

In **chapter 4** the blue emitting organic compound **BN-Ph-MTPA** was investigated as a promising blue emitter, focusing on its photophysical properties, electronic characteristics, and potential applications in OLEDs (**section 4.1**). The identification of **BN-Ph-MTPA** as an emitter with a balanced hybridized locally and charge-transfer (HLCT) excited state by highlights its photophysical behavior. The classification was supported by experimental observations and quantum chemical calculations, which revealed the crucial role of the *p*-phenylene bridging unit in achieving a well-balanced HLCT character in the first singlet state (S_1).

The compound demonstrated an outstanding PLQY of 98% in neat thin films, coupled with short fluorescence lifetimes of 8.16 ns in the solid state and 1.86 ns in toluene, demonstrating its efficient radiative decay processes. Strong positive solvatochromism of the photoluminescence (PL), and stable absorption spectra across environments further validated the balanced contributions of locally excited (LE) and charge-transfer (CT) states. Thermal and electrochemical analyses revealed **BN-Ph-MTPA**'s suitability for OLED integration, including high thermal stability up to 377°C and HOMO/LUMO estimated

energy levels of -5.7 eV and -2.7 eV, respectively. These properties enable its compatibility with thermal vapor deposition processes and device stability under operational conditions. Despite these advantages, the compound exhibits limitations in OLED applications due to challenges in harvesting triplet excitons. The low internal quantum efficiency (IQE) of approximately 10% is attributed to inefficient reverse intersystem crossing (rISC), driven by the large energetic splitting between the S_1 and T_1 states ($\Delta E_{ST} = 0.82$ eV). Additionally, weak spin-orbit coupling between the second triplet state T_2 and S_1 limits the efficiency of up-conversion from T_2 and S_1 . As a result, both TADF and hot exciton mechanisms fail to play a significant role in enhancing the device efficiency.

Overall, **BN-Ph-MTPA** demonstrates excellent PLQY and radiative decay time, thermal stability, and suitable electronic characteristics, making it well-suited for OLED applications. However, its device efficiency is limited by the low IQE, emphasizing the need for further optimization of triplet exciton utilization.

Section 4.2 provides a study of **BN-Ph-MTPA** in two selected solvent environments across different temperature ranges using time resolved photoluminescence spectroscopy. Initially, the prompt fluorescence was examined. In the nonpolar solvent mixture MCH:Tol, a slight shift in fluorescence occurred with temperature changes, while in the more polar MTHF, a much stronger shift was observed. This can be explained by the improved stabilization of the excited state in MTHF compared to MCH:Tol. The polar character of MTHF, with its larger dipole moment in the excited state compared to the ground state of **BN-Ph-MTPA**, causes positive solvatochromism of the fluorescence.

At very low temperatures, both systems exhibit a glass-like state (regime I) of the solvent. Due to the lack of solvent reorganization around the excited molecule, the excited state retains high energy, resulting in blue fluorescence. As the solvent is heated above the glass transition point the system is in a supercooled state (regime II). The emission shifts to the red region, with a much stronger shift in MTHF due to its polarity. Reorganization occurs as the solvent in the supercooled state, though viscous, remains mobile. This is also evident in the spectra, where the timescale of reorganization is on the nanosecond scale and the reorganization of solvent can be observed in time resolved spectroscopy. After further heating the solvent to temperatures above the melting point, the solvent is in a liquid state (regime III). The solvent can effectively stabilize the excited state through reorganization. Within the liquid temperature regime, the fluorescence also shows significant differences in the PL maximum. Near the melting point, the PL is shifted to lower energies than at room temperature due to the higher solvent density at lower temperatures, which leads

to better stabilization of the excited state.

Phosphorescence was observed in MCH:Tol, with the shape of the phosphorescence spectrum found to vary depending on the temperature of the solvent environment. At 77 K in the glassy state, the phosphorescence is broad, unstructured, and blue-shifted compared to 110 K, where a vibronic fine structure appears, and the spectrum shifts to longer wavelengths. This shift is due to the lack of relaxation of the triplet state into an optimal geometry at 77 K. The vibronic fine structure is not visible at 77 K because, without solvent relaxation, the energies of individual molecules can vary greatly depending on the local environment. The vibronic fine structure at 110 K can be assigned to vibronic transitions of the MTPA donor.

The investigations highlight the importance of considering the environment when characterizing emitters, especially their excited states, as photophysical properties are influenced by surroundings. Therefore, characterizations under conditions that mimic OLED environments, such as solid-state or host-guest systems, are advisable for relevant insights. In solution studies, it is important to consider the relaxation dynamics, especially at low temperatures, where limited solvent relaxation can significantly affect photophysical properties.

While time-resolved measurements in OLED environment (thin films) were not performed in this case, the large ΔE_{ST} suggests that relaxation effects have little impact on rISC. However, for TADF emitters with smaller singlet-triplet separations, relaxation dynamics could play a crucial role in enhancing rISC and influencing efficiency.

Future studies of promising OLED emitters could focus on performing time-resolved measurements in thin films to better understand the influence of the solid-state environment on excited-state dynamics. Matrix materials with different polarities and dipole moments could be explored to study how the emission color and the nature and energetic position of the excited states change. This could help in optimizing the design of OLEDs by fine-tuning the emitter’s environment to enhance performance.

Chapter 5 investigated seven carbazole-based donor-acceptor (D-A) molecules with *N*-phenylphthalimide as the acceptor, focusing on how modifications of the donor structure influence photophysical properties and OLED performance. The study highlights the significant role that molecular design plays in determining emission color, PLQY, and TADF behavior.

Absorbance spectra revealed a CT character for most emitters, except for **DBCz**, where a LE state dominates due to the extended π -conjugation of the dibenzocarbazole donor.

Steady-state PL spectra of the emitters in mCBP-doped films, where mCBP is a widely used commercial OLED host material chosen to simulate the environment within an OLED, revealed emission colors ranging from cyan (**Cz**) to green (**BCz**, **TCz**), yellow (**DBCz**), and blue (bridged compounds). The quantum yield was highest for **Cz** (0.65), followed by **TCz** (0.55) and **BCz** (0.52), while **DBCz** (0.13) and the bridged compounds (0.26-0.41) generally exhibited lower PLQY, reflecting less efficient radiative decay processes.

Time-resolved spectroscopy confirmed TADF behavior for **Cz**, **BCz**, **TCz**, and **pMPh-Cz**. The sterically demanding donor in **TCz** yielded the smallest ΔE_{ST} of 88 meV, optimizing donor-acceptor alignment for TADF. In contrast, **DBCz** exhibited room-temperature phosphorescence with a large ΔE_{ST} , preventing TADF. Bridged compounds generally lacked TADF, except for **pMPh-Cz**, where the methyl group appears to improve donor-acceptor orientation.

OLED devices fabricated with these emitters demonstrated varying efficiencies and emission properties. **TCz** exhibited the best performance with a maximum current efficiency of 33.9 cd/A and an EQE of 16%, reflecting its superior photophysical properties. **BCz**, with a slightly larger ΔE_{ST} , had reduced efficiency. Despite high PLQY and favorable photophysical properties, **Cz** demonstrated a lower EQE (7.7%) due to charge injection or stabilization issues, likely linked to its compact structure. **DBCz** had the lowest EQE, consistent with its large ΔE_{ST} . Even the contribution of room-temperature phosphorescence was insufficient to effectively utilize triplet excitons, resulting in limited efficiency in both PLQY and OLED performance.

The bridged compound OLEDs, generally showed lower efficiencies (EQE of 3.4-4.3%). The decoupling of donor and acceptor by introducing a phenylene bridge result in reduced PLQY due to nonradiative decay paths and in case of **pPh-Cz** and **(pPh-Cz)₂** in a large ΔE_{ST} preventing TADF.

Future emitter design should leverage these insights by focusing on D-A systems that avoid spatial separation of the donor and acceptor through bridging structures, as such configurations lead to reduced PLQY. Among the tested compounds, the sterically demanding donor **TCz** exhibited the highest efficiency, suggesting that structural motifs with significant steric bulk should be prioritized. However, care must be taken to avoid excessive extension of the donor's conjugated system as shown for **DBCz**, as this can promote non-radiative decay pathways.

For further development using carbazole as a donor, sterically demanding substituents could be strategically introduced. These modifications would optimize the donor's align-

ment relative to the acceptor while simultaneously providing a stabilizing effect on the hole, enhancing overall device performance.

Chapter 6 highlights the distinct properties of the fluorinated acridone emitter **NMA₂F**, offering insights into its potential for OLED applications. Unlike conventional TADF emitters, **NMA₂F** benefits from utilizing the T_2 state for rISC to the S_1 state, rather than relying on the T_1 state. This mechanism reduces the likelihood of non-radiative decay and shortens the radiative process lifetime, enhancing efficiency and stability.

Photophysical investigations revealed that **NMA₂F** exhibits high PLQY values of up to 0.71 with deep blue emission when incorporated into diluted PMMA layers. However, aggregation in the solid state causes red-shifted and quenched emissions, highlighting the importance of environment and host material selection. The hosts UGH-2 and TSPO1 were identified as promising candidates for facilitating energy transfer from their high-lying T_1 states to the T_2 state of **NMA₂F**, enabling efficient rISC.

Electrochemical analysis estimated the HOMO and LUMO energy levels at -6.2 eV and -3.27 eV, respectively, and thermal stability tests confirmed a decomposition temperature of 258°C, suitable for thermal vapor deposition processing. After several optimization steps, the integration of **NMA₂F** into an OLED device resulted in stable performance with deep blue emission. However, the device efficiency was limited to 0.4 cd A⁻¹. Due to the compound's extreme volatility no further device optimization was performed.

Future research should focus on designing emitters with similar advantageous electronic properties but reduced volatility to enable improved device fabrication and optimization. One approach could be to introduce additional substituents to increase the molecular weight, thereby raising the evaporation temperature. However, the steric demand should not be too large, as this could potentially disrupt the energy transfer from the host to the emitter.

Additionally, exploring alternative processing techniques or stabilizing host matrices could reduce the challenges associated with high volatility. Further investigations into host materials that can effectively manage energy transfer to the T_2 state and suppress aggregation effects in solid films could unlock the full potential of **NMA₂F** and similar emitters for high-efficiency, stable OLEDs.

Once a stable OLED is obtained, further investigations into the underlying processes can be pursued. For example, low-temperature EL studies could potentially force phosphorescence emission from the T_2 state, providing exclusive evidence of its population. Such findings could serve as a direct confirmation of the T_2 to S_1 conversion process, supporting

the presence of HIGHrISC fluorescence emission from the S_1 state at room temperature. Additionally, magneto-electroluminescence experiments could offer valuable insights into the role of the T_2 state in the EL process, further elucidating its contribution to the device's performance.

In **chapter 7**, the properties of the chiral D-A molecule **S-DHPZ-BTZ** were explored and compared to those of the symmetric A-D-A emitter **DHPZ-2BTZ**, previously documented in the literature.^[115])

When doped into the mCBP host material, **S-DHPZ-BTZ** demonstrated an emission maximum at 590 nm and a PLQY of 0.27. These results are similar to those of **DHPZ-2BTZ**, which emits at 577 nm and achieves a slightly higher PLQY of 0.33. The relatively modest quantum yield for both emitters points to a significant influence of non-radiative pathways, such as internal conversion (IC).

To better understand the excited-state characteristics, temperature-dependent time-resolved PL measurements were conducted. At room temperature, the prompt fluorescence exhibited a decay time of 10.2 ns and showed minimal temperature dependence. The delayed fluorescence, in contrast, had a decay time of 7.8 μ s at 300 K, increasing at lower temperatures. This behavior aligns with expectations for TADF emitters. An Arrhenius analysis of the delayed fluorescence yielded a ΔE_{ST} of 50 meV, further supporting the TADF classification.

Integration of **S-DHPZ-BTZ** into an OLED resulted in an EQE of 2.7%. While notable, this is lower than the 5% EQE achieved by **DHPZ-2BTZ**. The reduction in efficiency is likely due to the slightly lower PLQY of **S-DHPZ-BTZ** and its larger ΔE_{ST} , which may hinder the rate of reverse intersystem crossing (rISC), ultimately limiting the device's performance.

The introduction of the chiral side group (*N,N*-dimethyl-1-phenylethylamine) did not result in detectable circularly polarized electroluminescence, suggesting that this approach is not promising from this perspective.

For future similar emitter design, A-D-A structures should be preferred over D-A as they showed a slightly better performance, although both exhibit TADF behavior. However, the low PLQY observed for both, D-A and A-D-A limits the IQE in OLED applications. If further research into chiral TADF emitters for circularly polarised OLED (CP-OLED) is pursued, reconsidering the choice of the chiral component seems crucial. Molecules with inherently chiral core structures, such as helicenes, could provide a promising alternative in this regard.

9 Experimental Part

9.1 Material Characterization

UV-vis Absorbance Spectroscopy

UV-vis spectra of thin films prepared on glass or quartz glass substrates were investigated via UV-Vis spectroscopy using a *Varian Cary 50 Scan* spectrometer with transmission setup in dual-beam mode (fast mode). Spectra were recorded at wavelength from 200 nm / 300 nm (on quartz glass / on glass) to 800 nm.

Photoluminescence Spectroscopy (PL)

PL spectra were recorded with a Cary Eclipse spectrometer by *Varian*. Excitation wavelengths were chosen between 300 nm and 400 nm regarding the absorption behavior of the investigated organic compound.

Photoluminescence Quantum Yield (PLQY)

PLQY values were determined with a C9920-02 absolute quantum yield measurements system by *Hamamatsu*. The setup uses a L9799-01 CW-Xenon light source for optical excitation, a A10080-01 monochromator to adjust excitation wavelength and an integrating sphere connected to a CCD spectrometer (C10027 Photonic Multichannel Analyzer, *Hamamatsu*) by an optical fiber. The setup is located in a glovebox under a nitrogen atmosphere.

Time-resolved Photoluminescence Spectroscopy

For time-resolved emission measurements, the samples were placed in a cold finger cryostat (Optistat, *Oxford instruments*). The samples were excited using the third harmonic (355 nm) of a Nd:YAG laser (*InnoLas*) operated at a repetition rate of 10 Hz. The excitation intensity was adjusted using appropriate filters. The PL was collected and focused onto the entrance slit of a polychromator (Acton Spectra Pro 275, 150 l/mm, 2 nm spectral resolution) and detected by an intensified CCD camera (ICCD, PIMAX 4, *Roper Scientific*). The ICCD was operated in gated mode, which allows to vary and simultaneously delay the width of the detection window with respect to optical excitation. The instrument response function is about 1.7 ns. For phosphorescence lifetime measurements the repetition rate of the laser was reduced. For temperature-dependent measurements in solution, the sample was rapidly cooled to 77 K to prevent solvent crystallization and

achieve a glass-like frozen state. Measurements were then performed as the temperature was gradually increased. In contrast, for thin-film samples, measurements began at the highest temperature and were conducted while gradually decreasing the temperature. This approach was chosen to avoid crystallization during thawing resulting in poly crystalline instead of amorphous samples. Measurements in chapter 5 and chapter 7 were done with a gate of 100 ns (prompt fluorescence) and 1 ms (delayed PL). Decay curves are the integrated PL intensity of the spectra at corresponding delay times. Fits were performed with OriginPro 2021. The decay times were fitted with 1, 2 or 3 decay times according to Eq. 9.1 with instrumental weighting based on the integrated intensity.

$$y = y_0 + A_1 \cdot e^{-\frac{x - x_0}{t_1}} + A_2 \cdot e^{-\frac{x - x_0}{t_2}} + A_3 \cdot e^{-\frac{x - x_0}{t_3}} \quad (9.1)$$

Decay times for prompt and delayed PL are the amplitude weighted average of the fitted decay times.

$$\tau = \frac{A_1 \cdot t_1 + A_2 \cdot t_2 + A_3 \cdot t_3}{A_1 + A_2 + A_3} \quad (9.2)$$

Cyclic Voltammetry (CV)

Cyclic voltammograms were recorded with an Autolab PGSTAT302N (*Metrohm*) workstation under argon atmosphere with a one-compartment cell. Disk shaped platinum ($A = 0.2 \text{ mm}^2$) was used as working electrode, a platinum grid as counter electrode and a silver wire as reference electrode. Tetrabutylammonium-hexafluorophosphate (TBAPF_6) from Fluka (puriss. Electrochemical grade) was used as supporting electrolyte (0.15 mol L^{-1}). Acetonitrile, DCM or THF, bubbled with argon for 30 min was used as solvent and the emitter was dissolved with a concentration of $10^{-3} \text{ mol L}^{-1}$. The voltammogram was recorded at scan rate of 10 mV s^{-1} . Ferrocene (Aldrich, 98%) or Decamethylferrocene (Aldrich, 97%) was added at the end of the measurement for calibration. The oxidation potential $E_{\text{Ox}}^{1/2}$ is calculated as the average of the anodic and cathodic peak potentials, respectively. To estimate the HOMO energy level the following equation is used

$$E_{\text{HOMO}} = E_{\text{Ox}}^{1/2} - 5.15 \text{ eV} \quad (9.3)$$

Thermogravimetric analysis (TGA/DSC)

Thermogravimetric analysis was performed with a TGA-DSC 1 by *Mettler-Toledo* at a heating rate of $10\text{ }^{\circ}\text{C min}^{-1}$ under nitrogen flow (30 mL min^{-1}).

9.2 Sample Preparation

Substrate Preparation

Quartz Glass Substrates

Quartz glass substrates were purchased by *Nano Quartz Wafer GmbH* (25 mm x 25 mm x $1000\mu\text{m} \pm 150\mu\text{m}$, fused silica, double side polished $\text{Ra} 1\text{nm}$, POT824 / 10016002) and prepared using the following procedure:

1. 10 minutes in CHCl_3 at $40\text{ }^{\circ}\text{C}$ in an ultrasonic bath
2. 10 minutes in acetone at $40\text{ }^{\circ}\text{C}$ in an ultrasonic bath
3. 10 minutes in a 2% aqueous solution of *Mucosol* at $60\text{ }^{\circ}\text{C}$ in an ultrasonic bath
4. Rinsing with deionized water
5. Rinsing with deionized water and subsequent drying in nitrogen flow in a substrate cleaning machine

Subsequently, the substrates were treated with ozone. For this purpose, they were placed in a custom-made ozonization chamber with a pulsed xenon-excimer lamp (*Osram*, Xeradex 20) for 10 min. The step ensures purification from organic impurities.

ITO-Coated Substrates

Unstructured ITO-coated (ca. 150 nm) display glass (sheet resistance: $20\text{ }\Omega\text{ cm}^{-2}$) was cut (26 mm x 26 mm) and the middle of each substrate was covered with a circular ($\varnothing 15.8\text{ mm}$) acid resistant sticker (*ORACAL*) before they were dipped into a hot ($80\text{ }^{\circ}\text{C}$) etching solution comprising 5 M FeCl_3 and 6 M HCl . The subsequent cleaning and ozonization procedure was the same as described for quartz glass substrates.

Processing of PEDOT:PSS

PEDOT:PSS was purchased from *Heraeus* (Clevios P VP. AI4083) and spin coated in air (humidity: 35-45%, temperature $25\text{ }^{\circ}\text{C}$) under clean room conditions on cleaned and ozone treated glass, quartz glass or ITO coated glass substrates. The PEDOT:PSS dispersion was deposited on the substrate through a PDFV syringe filter ($0.45\mu\text{m}$). The substrate

was spun at 2000 rpm for 30 s on a *Süss Microtec Delta 20* spin coating system and a PEDOT:PSS film of 45 nm was obtained. The coated substrates were transferred into a nitrogen filled glove box (*M. Braun*) and thermally cured at 150 °C for 10 min via a hot plate to remove residual water and obtain insoluble PEDOT:PSS films.

Spin-Coating

For the preparation of emitter:PMMA films, solutions were spin-coated under a nitrogen atmosphere inside a glovebox (*M. Braun*) using a spin coater (*Süss Microtechnik*) equipped with an inert PTFE substrate holder. The solutions contained 30 mg mL⁻¹ PMMA along with the corresponding concentration of the emitter. Spin coating was performed at speeds ranging from 1000 to 3000 rpm, depending on the desired film thickness. **NMA-dF** & PMMA was spincoated from THF solution, **(S)-DHPZ-BTZ** & PMMA was spincoated from toluene solution.

Substrates were placed on the spin coater, and 100–200 μ L of the spin-coating solution was dispensed onto the substrate in a single portion. The spin coater was started immediately to minimize the risk of layer inhomogeneities.

Vacuum Processing

The evaporated materials are commercially available and were used as received. MoO₃ and all organic materials were deposited in a customized *Lesker* evaporation chamber. Devices were transferred from a glovebox under dry nitrogen atmosphere into the evaporation chamber. The evaporation process was started at a maximum of 5 x 10⁻⁶ mbar and a rate of 0.2-0.5 Å s⁻¹. The layer thickness was monitored via quartz sensors during the evaporation. After deposition of the organic material and without breaking the vacuum another shadow mask was used to define the active area (7.85 mm⁻²) of the OLED and lithium fluoride and aluminum were evaporated as cathode materials.

Layer Thickness Determination

Layer thicknesses were determined using a *DekTak150* from *Veeco Instruments Inc.* with a tip diameter of 12.5 μ m. With a scalpel a line was scratched into the layer. Its depth was measured at three different points during scans orthogonal to the scratch. The resulting values were averaged. The inaccuracy lies at about 5 nm.

9.3 OLED Characterization

LIV

To determine LIV characteristics, measurements were performed under nitrogen atmosphere using a photodiode calibrated with a luminance meter *Chroma Meter CS-100* (*Konica Minolta*). The photodiode was connected to a picoammeter (model 6485 (*Keithley*)) and a *Source Meter*® (model 2400 (*Keithley*)). The OLEDs were fixed in a custom-made LIV measuring holder. The seven pixels as well as the anode were contacted by round gold-tips and the applied voltage was changed in 0.2 V steps. The measurement data were recorded with a *Labview* program developed in the research group.

Electroluminescence Spectroscopy (EL)

EL spectra were recorded by use of an Ocean Optics SD 2000 dual channel spectrometer attached to an optical fibre. Calibration of the spectrometer was performed by use of an Ocean Optics LS-1-CAL light source. EL spectra were determined at a constant applied voltage.

External Quantum Efficiency

EQE and additional EL measurements were performed under nitrogen atmosphere using an external quantum efficiency measurement system (C9920-11) by *Hamamatsu*. An integrating sphere, equipped with a custom-made device holder with electrical contacts is connected to a CCD spectrometer (C10027 Photonic Multichannel Analyzer by *Hamamatsu*). The voltage is increased stepwise by use of a *SourceMeter*® (*Keithley*, model 2400). An EL spectrum is recorded at every voltage step.

9.4 Overview of Used Materials

Table 9.1 provides an overview of all commercially procured materials, including the respective suppliers and their stated purity levels.

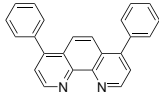

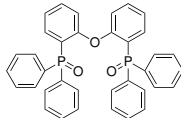
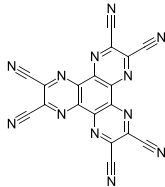
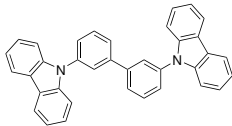
Table 9.1: Supplier and purity of used materials.

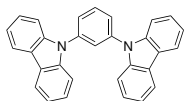
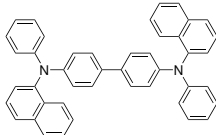
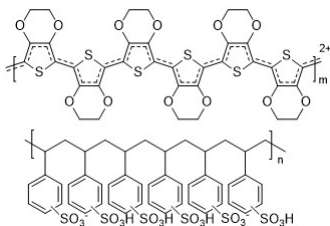
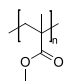
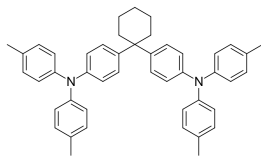
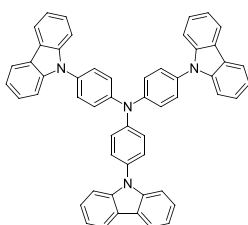
Acronym	Supplier	Purity
BPhen	Sigma Aldrich	purified by sublimation, >99%
C ₆₀	CreaPhys	purified by sublimation, >99.99%
DPEPO	Sigma-Aldrich	>98%
HATCN	Sigma-Aldrich	purified by sublimation, >98%
mCBP	TCI	purified by sublimation, >99%
mCP	TCI	purified by sublimation, >99%
NPB	Ossila	purified by sublimation, >99%
PEDOT:PSS	Heraeus	CLEVIOS TM P VP Al 4083
PMMA	Sigma-Aldrich	(M _n =15000 g mol ⁻¹)
TAPC	TCI	98%
TCTA	Thermo Fisher	99%
TmPyPB	Ossila	purified by sublimation, >99%
TPBi	BLDPharm	98%
TSPO1	Lumtec	purified by sublimation, >99%
UGH-2	Lumtec	purified by sublimation, >99%
MoO ₃	Alfa Aesar	99.95%
LiF	Alfa Aesar	99.99%
Al	Alfa Aesar	granules 8-12 mm, 99.99%

BN-Ph-MTPA was designed and synthesized by *Julia Wiefermann* in the group of *Prof. Thomas Müller* at Heinrich-Heine University in Düsseldorf. **Cz**, **BCz**, **TCz**, **DBCz**, **pPh-Cz**, **pMPh-Cz** and **(pPh-Cz)₂** were designed and synthesized by Christopher Wallerius in the group of *Prof. Klaus Meerholz*. **NMA₂F** was designed and synthesized in the groups of *Prof. Constantin Czekelius* and *Prof. Peter Gilch* at Heinrich-Heine University in Düsseldorf. **(S)-DHPZ-BTZ** and **(R)-DHPZ-BTZ** were synthesized by *Dirk Laux* in the group of *Prof. Arne Lützen* at Rheinische Friedrich-Wilhelms-University Bonn. Tab 9.2 provides a summary of the organic materials used for the preparation of thin films and OLEDs in this thesis while Tab 9.3 provides an overview of the emitters

characterized in this thesis. The acronyms used in this thesis are complemented by the molecular structures, the *International Union of Pure and Applied Chemistry* (IUPAC) names and the respective FMO energies.

Table 9.2: Acronyms, molecular structures, IUPAC names and FMO energies of used Materials.

Acronym & Molecular Structure	IUPAC Name	HOMO& LUMO /eV
BPhen 	Bathophenanthroline	-6.4 & -3.0 ^[118]
C₆₀ 	(C60-Ih)[5,6]fullerene	-6.1 & -4.3
DPEPO 	Bis[2-(diphenylphosphino) -phenyl]ether oxide	-6.53 & -2.53 ^[70] T ₁ = 2.98 eV ^[70]
HATCN 	1,4,5,8,9,11-Hexa -azatriphenylene -hexacarbonitrile	-9.62 & -5.42 ^[54]
mCBP 	3,3'-Di(9H-carbazol-9-yl) -1,1'-biphenyl *HOMO was estimated from CV oxidation half-wave potential in ^[69]	6.0 & 2.5* T ₁ = 2.8 eV ^[69]

Acronym & Molecular Structure	IUPAC Name	HOMO& LUMO /eV
mCP 	1,3-Bis(N-carbazolyl)benzene	-5.9 & -2.3 ^[119] $T_1 = 2.90 \text{ eV}$ ^[68]
NPB 	N,N'-Di(1-naphthyl)-N,N'-diphenyl-(1,1'-biphenyl)-4,4'-diamine	-5.4 & -2.4 ^[119]
PEDOT:PSS 	Poly(3,4-ethylenedioxythiophene) : poly(styrenesulfonate)	$E_F = -5.1$ (on ITO)
PMMA 	Poly(methyl methacrylate)	
TAPC 	1,1-Bis[(di-4-tolylamino)phenyl]- cyclohexane	5.8 & -2.4 ^[120]
TCTA 	Tris(4-carbazoyl-9-ylphenyl)amine	-5.7 & -2.4 ^[112]

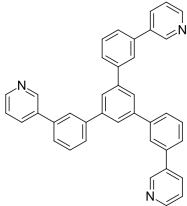
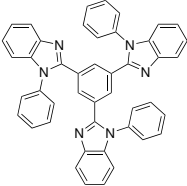
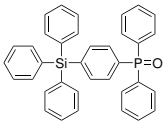
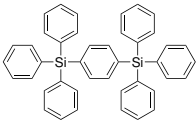
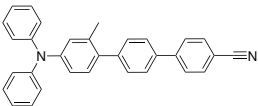
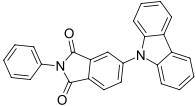
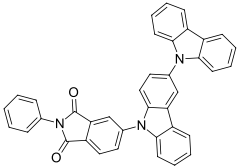
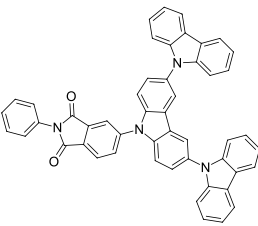
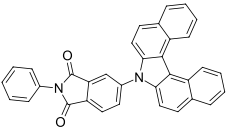
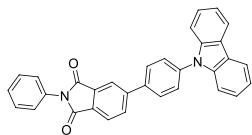
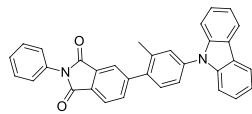
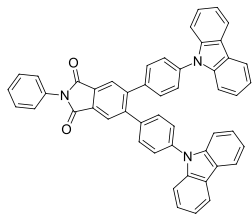
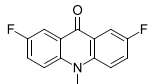
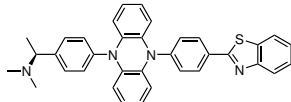
Acronym & Molecular Structure	IUPAC Name	HOMO& LUMO /eV
TmPyPB 	1,3,5-Tris(3-pyridyl-3-phenyl)-benzene	-6.82 & -2.87 ^[121]
TPBi 	2,2',2''-(1,3,5-Benzinetriyl)-tris(1-phenyl-1-H-benzimidazole)	-6.7 & -2.7 ^[112]
TSPO1 	Diphenyl[4-(triphenylsilyl)-phenyl]phosphine oxide	-6.79 & -2.52 ^[110] $T_1 = 3.36 \text{ eV}^{[110]}$
UGH-2 	1,4-Bis(triphenylsilyl)benzene	-7.2 & -2.8 ^[109] $T_1 = 3.50 \text{ eV}^{[109]}$

Table 9.3: Acronyms, molecular structures, IUPAC names and FMO energies of investigated compounds.

Investigated in	Acronym & Molecular Structure	IUPAC Name	HOMO& LUMO /eV
Chapter 4	BN-Ph-MTPA 	4''-(diphenylamino)- 2''-methyl- [1,1':4',1''-terphenyl]- 4-carbonitrile	-5.7 & -2.7
Chapter 5	Cz 	4-Carbazolyl- N-phenyl phthalimide	-6.19 & -3.42
Chapter 5	BCz 	4-(4-Biscarbazolyl)- N-phenyl phthalimide	-5.98 & -3.48
Chapter 5	TCz 	5-(9H,9'H,9''H-9,3':6',9'' -Tercarbazol-9'-yl)- 2-phenyl- 1,3-isoindolinedione	-6.00 & -3.49
Chapter 5	DBCz 	4-[3,4,5,6-Dibenzocarbazolyl]- N-phenyl phthalimide	-5.96 & -3.47

Investigated in	Acronym & Molecular Structure	IUPAC Name	HOMO& LUMO /eV
Chapter 5	<i>p</i>Ph-Cz 	5-[<i>p</i> -(9-Carbazolyl)phenyl]- 2-phenyl- 1,3-isoindolinedione	-6.08 & -3.41
Chapter 5	<i>p</i>MPh-Cz 	5-[4-(9-Carbazolyl)-2-tolyl]- 2-phenyl- 1,3-isoindolinedione	-6.06 & -3.37
Chapter 5	(<i>p</i>Ph-Cz)₂ 	5,6-Bis[<i>p</i> -(9-carbazolyl)- phenyl]-2-phenyl- 1,3-isoindolinedione	-6.06 & -3.41
Chapter 6	NMA-dF 	<i>N</i> -methyl-difluoro-acridone	-6.20 & -2.98
Chapter 7	<i>S</i>-DHPZ-BTZ 	<i>N,N</i> -Dimethyl[(<i>S</i>)-1-(<i>p</i> -(10-[<i>p</i> -(1,3-benzothiazol-2-yl)-phenyl]-5,10-dihydro-5-phenazinyl)-phenyl)ethyl]amine	-5.00 & -2.74

10 Appendix

10.1 List of Abbreviations

c	concentration
CIE	Commission Internationale de l'Éclairage
CP-OLED	circularly polarised OLED
CT	charge-transfer
CV	cyclic voltammetry
D-A	donor-acceptor
DCM	dichloromethane
DOS	density of energetic states
DSC	differential scanning calorimetry
e	elementary charge $1.602 \cdot 10^{-19}C$
E_a	electron affinity
EIL	electron injection layer
ϵ_0	vacuum permittivity
ϵ_r	dielectric constant
EBL	electron-blocking layer
E_F	<i>Fermi</i> level
EL	electroluminescence
EML	Emissive Layer
E_{ox}	oxidation potential
ϵ_r	dielectric constant
EQE	external quantum efficiency
E_{red}	reduction potential
η_{out}	light outcoupling efficiency
η_r	light outcoupling efficiency
ETL	electron-transport layer
ΔE_{ST}	singlet-triplet energy gap
F	electric field

FET	field-effect transistor
FMO	frontier molecular orbital
FRET	<i>Förster</i> resonance energy transfer
γ	charge balance factor
γ_{Lan}	<i>Langevin</i> bimolecular recombination rate factor
HBL	hole blocking layer
HE	hot exciton
HIL	hole-injection layer
HLCT	hybridized locally and charge-transfer
HOMO	h ighest o ccupied m olecular o rbital
HTL	hole-transport layer
IC	internal conversion
IQE	internal quantum efficiency
IR	infrared
ISC	intersystem crossing
ITO	indium tin oxide
IUPAC	<i>International Union of Pure and Applied Chemistry</i>
J	current density
k_B	<i>Boltzmann</i> constant $8.617 \cdot 10^{-5} \frac{eV}{K}$
k_{exp}	experimentally determined rate constant
L	distance over which electron exchange occurs
LE	locally excited
LUMO	l owest u noccupied m olecular o rbital
μ_e	electron mobility
μ_h	hole mobility
MCH	methylcyclohexane
M_S	spin quantum number
MTHF	2-methyltetrahydrofuran

n	refractive index
n_e	electron density
n_h	hole density
OFET	organic field-effect transistor
OLED	organic light-emitting diode
OSC	organic solar cell
π	mathematical constant 3.14159
PL	photoluminescence
PLQY	photoluminescence quantum yield
PMMA	polymethyl methacrylate
Φ_{PL}	photoluminescence quantum yield
PVD	physical vapor deposition
Φ_{Dexter}	quantum yield of the <i>Dexter</i> transfer
Φ_{FRET}	quantum yield of the FRET
R_0	<i>Förster</i> distance
r_c	<i>Coulomb</i> capture radius
R_{Lan}	<i>Langevin</i> recombination rate
rISC	reverse intersystem crossing
SOC	spin-orbit coupling
T	absolute temperature
TADF	thermally activated delayed fluorescence
T_d	decomposition temperature
T_g	glass transition temperature
TGA	thermogravimetric analysis
T_m	melting temperature
Tol	toluene
TTA	triplet-triplet annihilation
V_{bi}	built-in voltage

VTE vacuum thermal evaporation

10.2 Supplementary Data

10.2.1 Supporting Information for 4.1

ChemPhotoChem

Supporting Information

Highly Luminescent Blue Emitter with Balanced Hybridized Locally and Charge-Transfer Excited-States Emission

Julia Wiefermann⁺, Jeremy M. Kaminski⁺, Elisabeth Pankert, Dirk Hertel, Klaus Meerholz, Christel M. Marian, and Thomas J. J. Müller*

Supporting Information

Table of contents

1 General considerations.....	2
2 Absorption and emission spectra.....	3
3 Estimation of ΔE_{ST}	9
4 Lippert plot	11
4.1 Lippert-Mataga equation.....	11
5 Cyclic Voltammetry (CV)	12
6 Thermal Properties.....	13
7 OLED fabrication	13
8 Luminance-current density-voltage characteristics (L-J-V).....	13
9 External quantum efficiency (EQE) and electroluminescence (EL) spectra.....	14
10 Computational details	14
11 ω -Scan	14
12 Absorption spectrum.....	16
13 Geometries (xyz) of optimized states.....	17
13.1 S_0	17
13.2 S_1	18
13.3 T_1	20
13.4 T_2	21
Literature	23

1 General considerations

All reactions were carried out in oven dried Schlenk glassware using septa and syringes under nitrogen atmosphere. Compound **3** was prepared according to our previously published protocol.^[1] Absorption spectra were recorded in cyclohexane, toluene, diethyl ether, ethyl acetate, tetrahydrofuran, CH₂Cl₂, ethanol, DMSO, and acetonitrile high performance liquid chromatography (HPLC) grade at 293 K on a Perkin–Elmer UV/Vis/NIR Lambda 19 spectrometer. For the determination of the molar extinction coefficients ϵ absorption measurements at five different concentrations were carried out. Emission spectra and fluorescence lifetimes were recorded in cyclohexane, toluene, diethyl ether, ethyl acetate, tetrahydrofuran, CH₂Cl₂, ethanol, DMSO and acetonitrile HPLC grade at 293 K on an Edinburgh FS5 spectrometer. PLQY measurements were performed using a C9920-02 absolute PL quantum yield measurement system by *Hamamatsu*. The setup uses a L9799-01 CW Xenon light source for excitation, an A10080-01 monochromator, an integrating sphere connected to a CCD spectrometer (C10027 Photonic Multichannel Analyzer by *Hamamatsu*). Measurements in solution were performed using an UV quartz cuvette. Solid states thin films were measured on glass substrates.

2 Absorption and emission spectra

2.1 4'-(Diphenylamino)-2'-methyl-[1,1':4',1''-terphenyl]-4-carbonitrile (**3**)

The spectroscopic data ($\lambda_{abs,max}$ (ϵ) and $\lambda_{em,max}$) are compiled in Table S1.

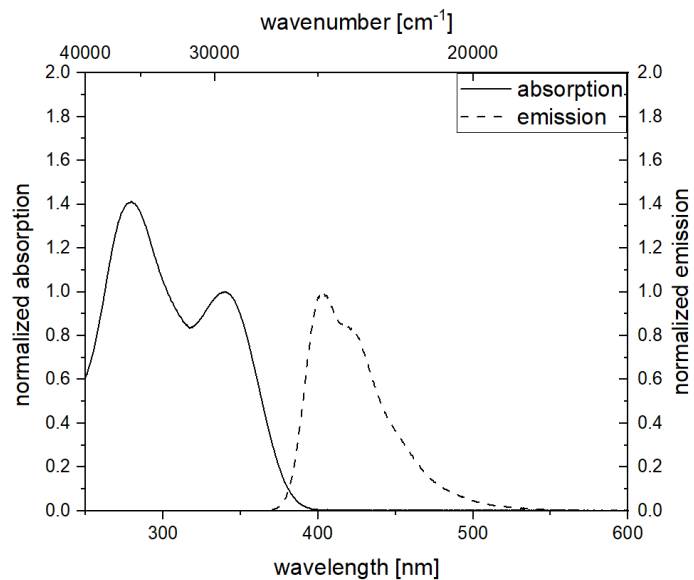


Figure S1: Recorded in cyclohexane, $T = 293\text{ K}$, $c(\mathbf{3}) = 10^{-5} - 10^{-6}\text{ M}$, $\lambda_{ex} = \lambda_{max,abs}$

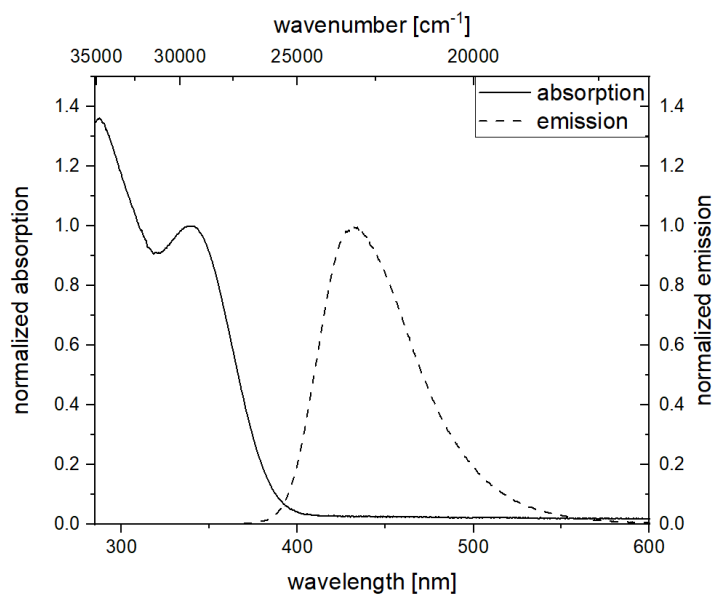


Figure S2: Recorded in toluene, $T = 293\text{ K}$, $c(\mathbf{3}) = 10^{-5} - 10^{-6}\text{ M}$, $\lambda_{ex} = \lambda_{max,abs}$

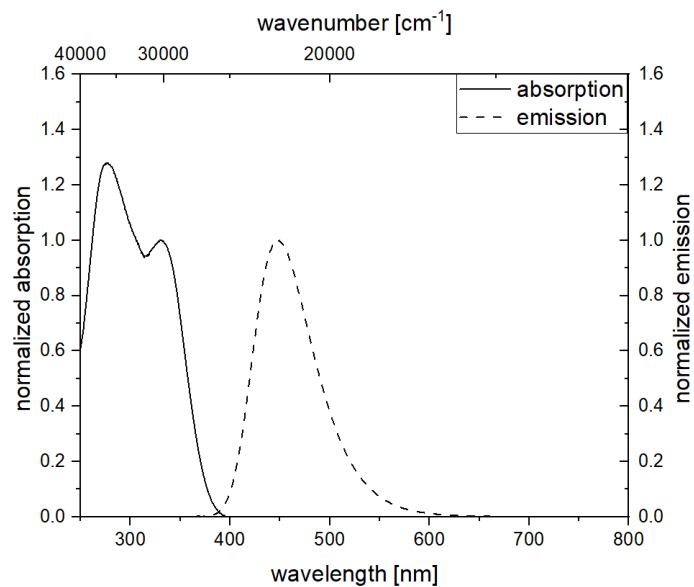


Figure S3: Recorded in diethyl ether, $T = 293$ K, $c(\mathbf{3}) = 10^{-5} - 10^{-6}$ M, $\lambda_{ex} = \lambda_{max,abs}$

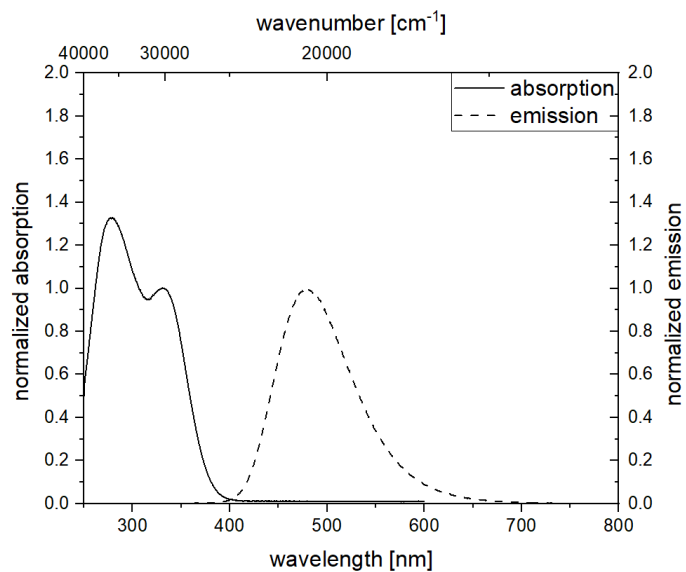


Figure S4: Recorded in ethyl acetate, $T = 293$ K, $c(\mathbf{3}) = 10^{-5} - 10^{-6}$ M, $\lambda_{ex} = \lambda_{max,abs}$

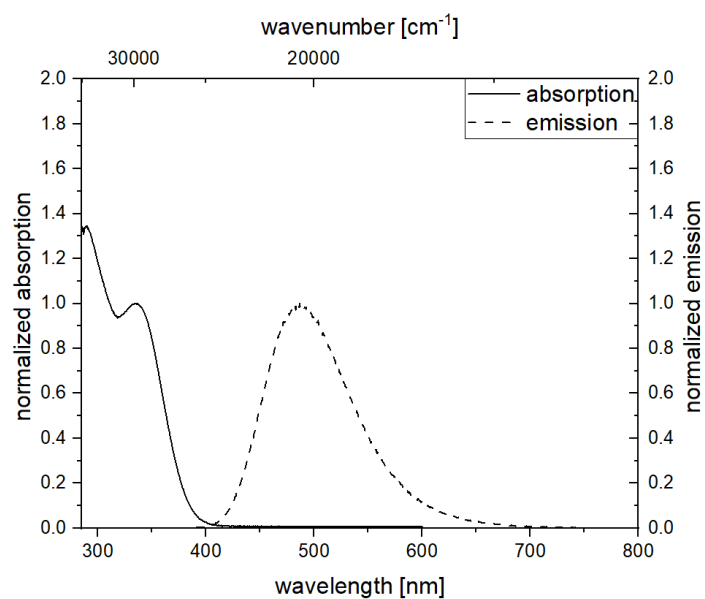


Figure S5: Recorded in tetrahydrofuran, $T = 293\text{ K}$, $c(\mathbf{3}) = 10^{-5} - 10^{-6}\text{ M}$, $\lambda_{\text{ex}} = \lambda_{\text{max,abs}}$

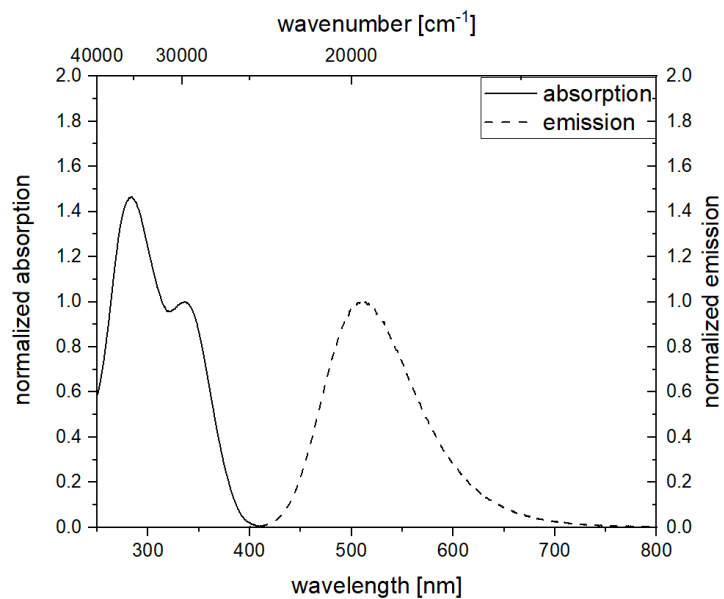


Figure S6: Recorded in dichloromethane, $T = 293\text{ K}$, $c(\mathbf{3}) = 10^{-5} - 10^{-6}\text{ M}$, $\lambda_{\text{ex}} = \lambda_{\text{max,abs}}$

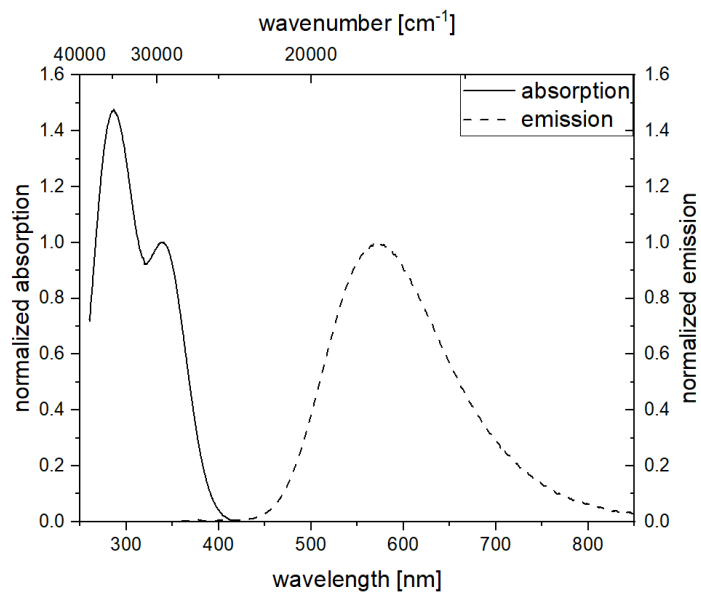


Figure S7: Recorded in DMSO, $T = 293\text{ K}$, $c(\mathbf{3}) = 10^{-5} - 10^{-6}\text{ M}$, $\lambda_{ex} = \lambda_{max,abs}$

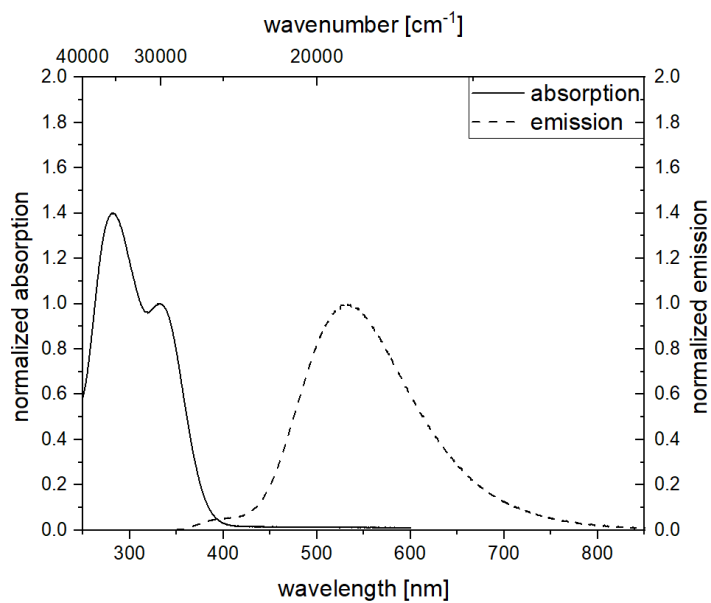


Figure S8: Recorded in ethanol, $T = 293\text{ K}$, $c(\mathbf{3}) = 10^{-5} - 10^{-6}\text{ M}$, $\lambda_{ex} = \lambda_{max,abs}$

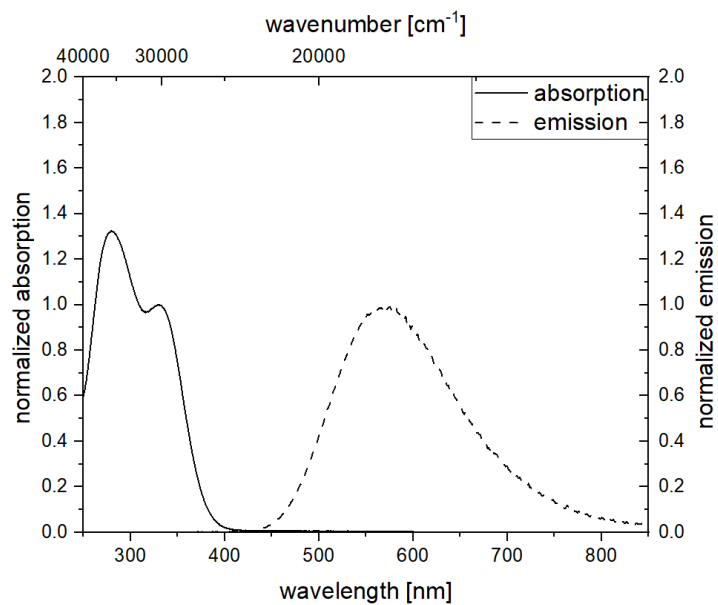


Figure S9: Recorded in acetonitrile, $T = 293$ K, $c(\mathbf{3}) = 10^{-5} - 10^{-6}$ M, $\lambda_{ex} = \lambda_{max,abs}$

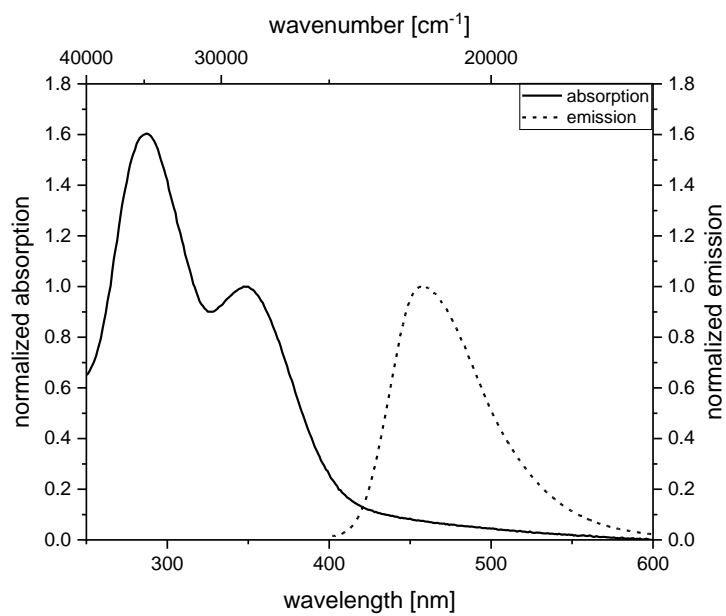


Figure S10: Recorded as 100 nm thin film on quartz glass, $T = 293$ K, $\lambda_{ex} = \lambda_{max,abs}$

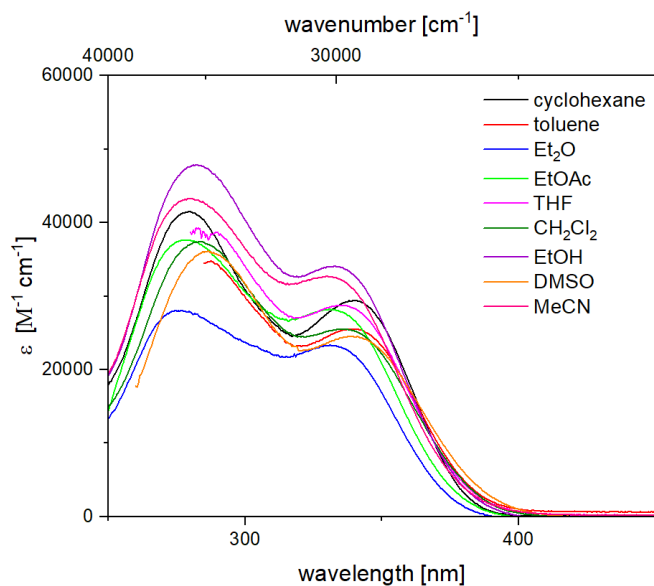


Figure S11: Absorption spectra recorded in solvents of different polarity, $T = 293\text{ K}$, $c(\mathbf{3}) = 10^{-5}\text{ M}$.

Table S1: Selected photophysical data of compound **3** in solvents of different polarity.

solvent	$\lambda_{abs, max} [nm] (\epsilon [M^{-1} cm^{-1}])$	$\lambda_{em} [nm]$
cyclohexane	340 (28620)	404
	280 (40570)	
toluene	339 (24830)	431
	287 (33750)	
Et ₂ O	331 (21650)	448
	277 (27600)	
EtOAc	330 (24360)	478
	279 (32450)	
THF	335 (29100)	487
	290 (39150)	
CH ₂ Cl ₂	336 (25580)	512
	284 (37360)	
EtOH	330 (33750)	532
	282 (47530)	
DMSO	339 (23290)	572
	286 (34300)	
MeCN	330 (32560)	571
	280 (43170)	

3 Estimation of ΔE_{ST}

For time-resolved emission measurements, the samples were placed in a cold finger cryostat (Optistat, Oxford instruments). The samples were excited using the third harmonic (355 nm) of a Nd:YAG laser (*InnoLas*) operated at a repetition rate of 10 Hz. The excitation intensity was adjusted using appropriate filters. The PL was collected and focused onto the entrance slit of a monochromator (Acton Spectra Pro 275, 150 l/mm, 2 nm spectral resolution) and detected by an intensified CCD camera (ICCD, PIMAX 4, *Roper Scientific*). The ICCD was operated in gated mode, which allows to vary and simultaneously delay the width of the detection window with respect to optical excitation. The instrument response function is about 1.7 ns. For temperature dependent measurements the sample was cooled down using liquid nitrogen. For phosphorescence lifetime measurements the repetition rate of the laser was reduced to 0.33 Hz, however, the rate could not be reduced further thus the excited molecules never depleted completely. For that reason we consider our measured lifetime as a good approximation only.

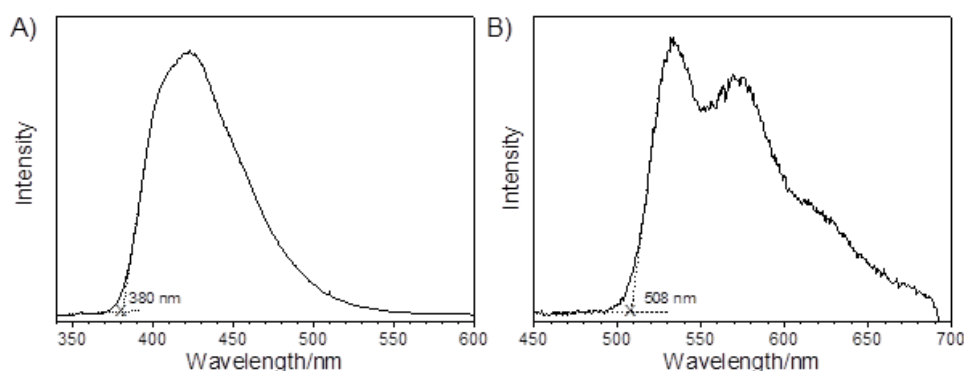


Figure S12: Fluorescence (A) and phosphorescence (B) spectra in toluene/cyclohexane (1:1) at 110 K, $c(\mathbf{3}) = 10^{-5}$ M, $\lambda_{ex} = 355$ nm. (A) was recorded with a gate of 100 ns with excitation, (B) was recorded with a gate of 200 ms and a delay of 10 ms. Cut-off wavelength of 380 nm (508 nm) for fluorescence (phosphorescence) indicate energy values of 3.26 eV (2.44 eV) and a ΔE_{ST} of 0.82 eV.

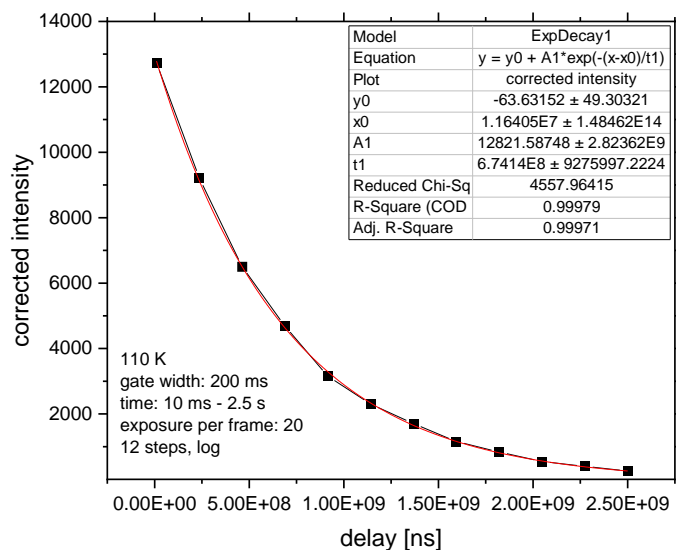


Figure S13: Phosphorescence decay in toluene/cyclohexane (1:1) at 110 K, $\alpha(3) = 10^{-5}$ M, $\lambda_{ex} = 355$ nm recorded with a gate of 200 ms and delay of 10 ms - 2.5 s. A minimum lifetime of 674 ms indicates phosphorescence type emission.

The lifetime can only be used as an order of magnitude estimate. The setup did not allow for excitation after passing of 10 lifetimes, thus the system never decays completely but remains in an equilibrium with constant T1 population. (The laser could only be operated at 0.33 Hz, not at 0.1 Hz).

4 Lippert plot

Table S2: Data for Lippert plot.

Solvent	$n_D^{20[2]}$	$\epsilon_r^{[2]}$	Δf	$\lambda_{\max, \text{abs}}$ [nm]	$\lambda_{\max, \text{em}}$ [nm]	Stokes shift [cm ⁻¹]
cyclohexane	1.4262	2.02	-0.00164973	340	404	4660
toluene	1.4969	2.38	0.01323509	339	431	6300
diethyl ether	1.3526	4.34	0.16699512	331	448	7890
EtOAc	1.3724	6.02	0.19963504	330	478	9380
THF	1.407	7.38	0.2072845	335	487	9320
DCM	1.4242	8.93	0.21710325	336	512	10230
DMSO	1.48	46.45	0.26300932	339	572	11500
EtOH	1.3614	24.55	0.28874639	330	532	12020
MeCN	1.3441	37.5	0.30541639	330	571	12790

4.1 Lippert-Mataga equation

$$\tilde{\nu}_a - \tilde{\nu}_f = \frac{2 \Delta f}{4\pi\epsilon_0 h c a^3} (\mu_E - \mu_G) + \text{const}$$

Equation S1: Lippert-Mataga equation.

$\tilde{\nu}_a$: absorption maximum

$\tilde{\nu}_f$: emission maximum

μ_E : dipole moment in the excited state

μ_G : dipole moment in the ground state

ϵ_0 : vacuum permittivity constant ($8.8542 \cdot 10^{-12}$ As V⁻¹ m⁻¹)

h: Planck's constant ($6.6256 \cdot 10^{-34}$ J s)

c: the speed of light ($2.9979 \cdot 10^{10}$ cm s⁻¹)

a: Onsager radius (5.60 Å)

5 Cyclic Voltammetry (CV)

Cyclic voltammograms were recorded with an Autolab PGSTAT302N (Metrohm) workstation under argon atmosphere with a one-compartment cell. Disk shaped platinum ($A = 0.2 \text{ mm}^2$) was used as working electrode, a platinum grid as counter electrode and a silver wire as reference electrode. Tetrabutylammonium-hexafluorophosphate (TBAPF₆) from Fluka (puriss. Electrochemical grade) was used as supporting electrolyte (0.15 mol L^{-1}). Acetonitrile (Acros Seal), bubbled with argon for 30 min was used as solvent and the emitter was dissolved with a concentration of $10^{-3} \text{ mol L}^{-1}$. The voltammogram was recorded at scan rate of 10 mV s^{-1} . Ferrocene (Aldrich, 98%) was added at the end of the measurement for calibration.

The oxidation potential $E_{\text{ox}}^{1/2}$ is calculated as the average of the anodic and cathodic peak potentials, respectively.

To estimate the HOMO energy level the following equation is used

$$E_{\text{HOMO}} = -E_{\text{ox}}^{1/2} - 5.15 \text{ eV}$$

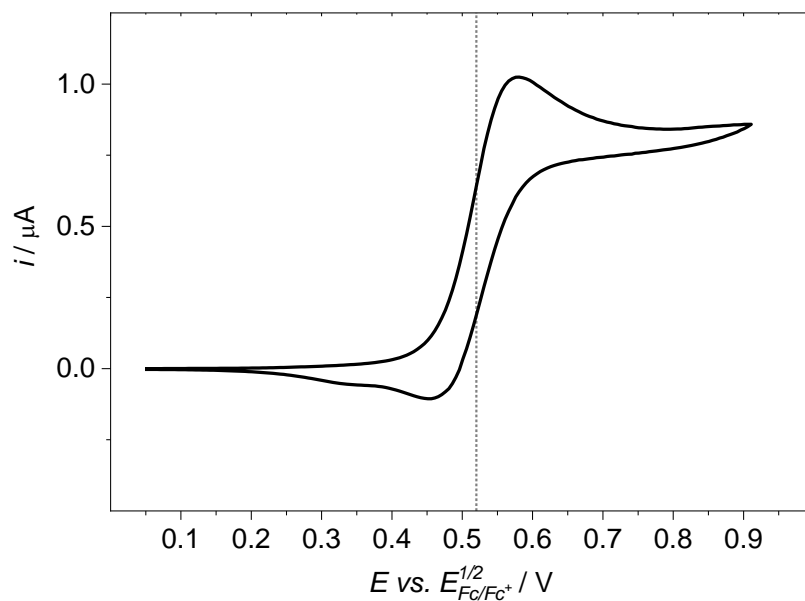


Figure S14: Cyclic voltammogram (CV) of compound **3** in MeCN/TBAPF₆ at a scan rate of 10 mV s^{-1} . The determined $E_{\text{ox}}^{1/2}$ lies at 0.52 V.

6 Thermal Properties

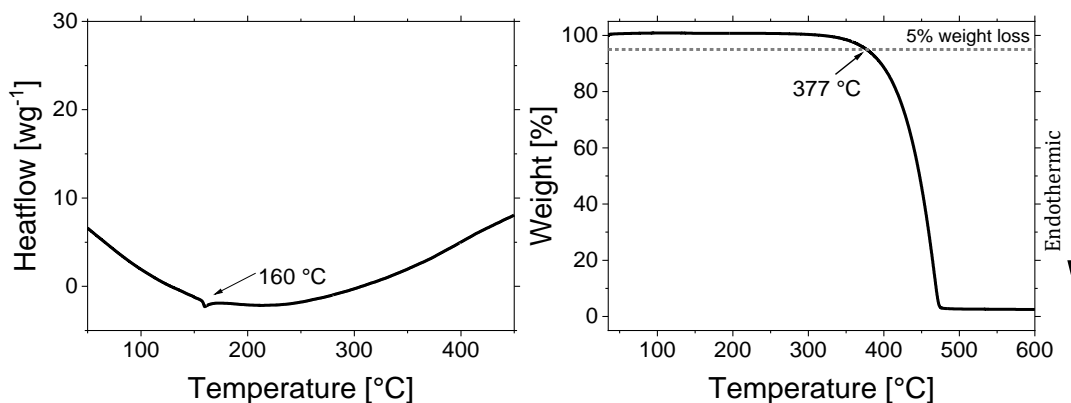


Figure S15: DSC and TGA curve of compound **3**.

Thermogravimetric analysis was performed with a TGA-DSC 1 by *Mettler-Toledo* at a heating rate of $10^{\circ}\text{C min}^{-1}$ under nitrogen flow (30 mL min^{-1}).

7 OLED fabrication

OLED devices were fabricated using commercially available ITO-coated display glass (sheet resistance: $20\ \Omega\ \text{cm}^{-2}$). Prior to film deposition the pre-patterned substrates were cleaned in different steps in an ultrasonic bath with chloroform, acetone, detergent (Mucasol®) and deionized water. After cleaning the substrates were dried in nitrogen flow.

The evaporated materials are commercially available and were used as received. MoO_3 and all organic materials were deposited in a customized *Lesker* evaporation chamber. Devices were transferred from a glovebox under dry nitrogen atmosphere into the evaporation chamber. The evaporation process was started at a maximum of 5×10^{-6} mbar and a rate of $0.2\text{--}0.3\ \text{\AA s}^{-1}$. The layer thickness was monitored via quartz sensors during the evaporation. After deposition of the organic material and without breaking the vacuum another shadow mask was used to define the active area (7.85 mm^2) of the OLED and lithium fluoride and aluminum were evaporated as cathode materials.

8 Luminance-current density-voltage characteristics (L-J-V)

LJV characteristics were determined under argon atmosphere by use of a photodiode calibrated with a luminance meter Chroma Meter *CS-100* (*Konica Minolta*). The photodiode was connected to a picoammeter (Keithley, model 6485) and a SourceMeter® (Keithley, model 2400).

9 External quantum efficiency (EQE) and electroluminescence (EL) spectra

EQE and EL measurements were performed under nitrogen atmosphere using an external quantum efficiency measurement system (C9920-11) by *Hamamatsu*. An integrating sphere, equipped with a custom-made device holder with electrical contacts is connected to a CCD spectrometer (C10027 Photonic Multichannel Analyzer by *Hamamatsu*). The voltage is increased stepwise by use of a SourceMeter® (*Keithley*, model 2400). An EL spectrum is recorded at every voltage step.

10 Computational details

The electronic ground-state geometry of the emitter was optimized with DFT at the ω B97X-D/def2-TZVP level of theory^[3] with $\omega = 0.14$ (after optimal tuning procedure in vacuo), including implicit toluene solvation via the polarizable continuum model (PCM)^[4] in the equilibrium limit using the solvent excluding surface (SES) implemented in Gaussian16.^[5]

Time-dependent DFT (TDDFT)^[6] was used for the optimization of the excited states (Tamm-Dancoff approximation (TDA) for excited triplet states^[7]). Analytic harmonic vibrational frequencies were computed by means of Gaussian16.

Excitation energies, dipole moments and photophysical properties were calculated using the DFT/MRCI method^[8] and the R2016^[9] parametrization (tight configuration selection threshold of $0.8 E_h$), which is specially designed for large multichromophoric systems. Up to 20 excited states in the singlet and triplet manifold employing closed-shell BH-LYP^[10] orbitals as the one-particle basis were considered. Kohn-Sham molecular orbitals and integrals were computed with the Turbomole suite of programs.^[11] Solute-solvent interactions were taken into consideration in this step by embedding the molecule in a field of point charges imported from preceding Gaussian16 DFT calculations.

Fragment-based analyses of the singlet and triplet DFT/MRCI wavefunctions were performed by the TheoDORE tool box.^[12] Spin-orbit coupling matrix elements (SOCMEs) between target singlet and triplet states were calculated with the spin-orbit coupling kit (SPOCK).^[13] Rate constants for ISC and rISC between excited singlet and triplet states were determined in the framework of Fermi's golden rule approximation and a time-dependent Fourier transform approach as implemented in the VIBES program.^[14] Temperature effects were accounted to the rate constants by assuming a Boltzmann distribution in the initial electronic state. Radiative rate constants were determined in Einstein's approximation.

11 ω -Scan

The accuracy of the calculated excitation energies, especially when they involved charge transfer excitations, depends on the range-separation parameter ω whose optimal values

depend on the studied system. The optimization of ω for the ω B97X-D functional was carried out by applying Koopman's theorem.^[15] The optimal value ω was determined from minimizing the target function:

$$J^2 = \sum_{i=0}^1 [\varepsilon_{HOMO}^{\omega}(N+i) + IP(N+i)]^2, \quad \text{Equation S2}$$

where $IP(N) = E(N-1) - E(N)$, and $IP(N+1) = E(N) - E(N+1)$; here N is the number of electrons of the target molecule, $\varepsilon_{HOMO}^{\omega}$ is the HOMO energy and $IP(N)$ the vertical ionization potential.^[16]

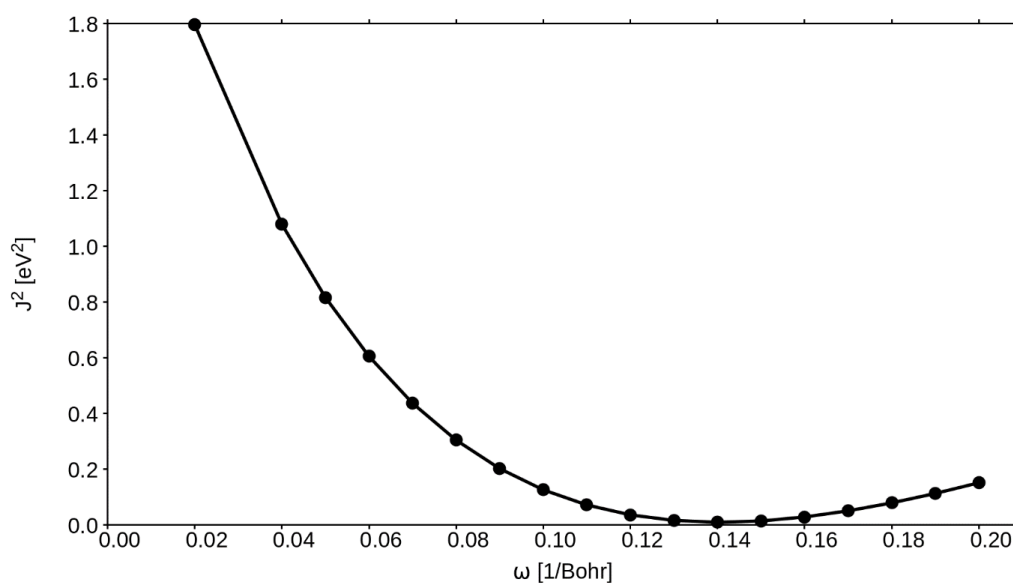


Figure S16. J^2 - ω plot in vacuo for the ω B97X-D functional and def2-TZVP basis set. The optimal value for ω is found to be 0.14 bohr⁻¹.

12 Absorption spectrum

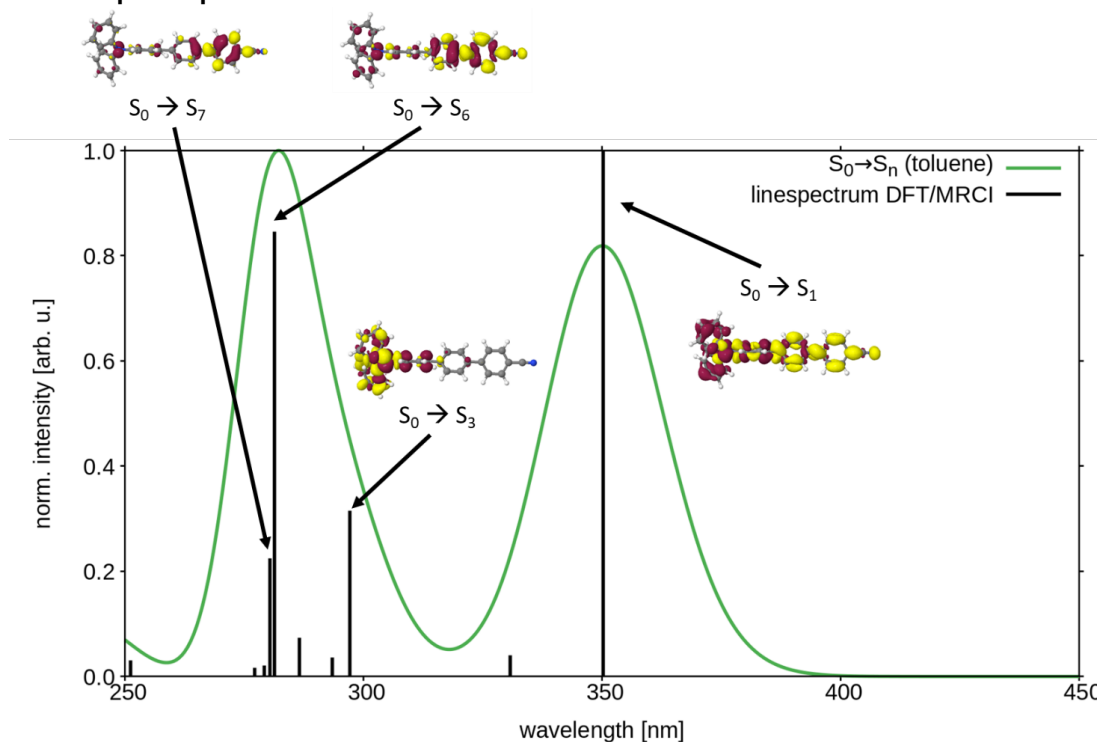


Figure S17. Calculated line spectrum (black) for $S_0 \rightarrow S_n$ transitions of the emitter with the DFT/MRCI approach and gaussian broadened (1000 cm^{-1}) spectrum (green). In the range of 250 nm and 400 nm four transitions, namely from the electronic ground state into the S_1 , S_3 , S_6 and S_7 state, produce two intense absorption bands at 350 nm and ca. 280 nm. Characterization of the transitions is done by difference densities (± 0.001). Electron density is transferred from the red to the yellow area.

13 Geometries (xyz) of optimized states

13.1 S₀

C	3.281339	8.192863	15.375076
H	3.531352	7.359586	14.730430
C	4.138365	9.282315	15.469405
H	5.062015	9.302538	14.906001
C	2.092712	8.167190	16.088291
C	3.795652	10.345558	16.295421
C	1.750648	9.229907	16.926364
H	1.424345	7.320595	16.001303
C	2.617622	10.319447	17.026097
H	4.456240	11.198856	16.384380
N	0.544612	9.203522	17.662060
H	2.362530	11.145963	17.676309
C	0.123097	8.008021	18.282672
C	-0.236046	10.375788	17.777686
C	-1.221643	7.642719	18.278094
C	1.039471	7.172538	18.918670
C	-0.826665	10.716813	18.995686
C	-0.426663	11.210890	16.675613
H	-1.938820	8.296196	17.796912
C	-1.674407	6.476176	18.885285
H	2.088375	7.436059	18.941734
C	0.601855	6.004114	19.514284
H	-0.680266	10.077196	19.856170
C	-1.597717	11.864049	19.102648
C	-1.184077	12.366061	16.795493
H	0.024438	10.952206	15.726605
C	-3.150528	6.172026	18.857970
C	-0.743045	5.630385	19.509715
H	1.324185	5.357758	19.998072
H	-2.048697	12.113459	20.054943
C	-1.778230	12.698531	18.006533
H	-1.320735	13.003097	15.930674
H	-3.405098	5.501546	18.033942
H	-3.478849	5.690670	19.779135
H	-3.726356	7.087357	18.723438

C	-1.134366	4.363161	20.177670
H	-2.374470	13.597203	18.095181
C	-1.815245	3.354759	19.494601
C	-0.796920	4.134226	21.512402
H	-2.078855	3.498177	18.454663
C	-2.148715	2.165604	20.121117
C	-1.134931	2.948068	22.143434
H	-0.266331	4.900046	22.064651
H	-2.689636	1.408500	19.567110
C	-1.817713	1.941841	21.458729
H	-0.846212	2.795948	23.176054
C	-2.179283	0.673978	22.130532
C	-2.629029	0.668685	23.454082
C	-2.079717	-0.546963	21.457104
C	-2.968860	-0.511879	24.088313
H	-2.735093	1.603920	23.987890
H	-1.712644	-0.569526	20.439420
C	-2.416835	-1.734988	22.078668
C	-2.864172	-1.722372	23.400985
H	-3.322952	-0.501115	25.110139
H	-2.327753	-2.673510	21.548762
C	-3.214772	-2.947644	24.050236
N	-3.497284	-3.934233	24.572678

13.2 S₁

C	3.598571	8.236156	15.852045
H	3.975101	7.397415	15.281155
C	4.384700	9.368551	16.030565
H	5.379833	9.412117	15.608196
C	2.323136	8.176116	16.388731
C	3.885072	10.445887	16.754608
C	1.824995	9.257032	17.119632
H	1.703660	7.302265	16.236738
C	2.614393	10.394927	17.301664
H	4.493544	11.328277	16.904204
N	0.526684	9.197348	17.679271
H	2.230389	11.227394	17.876011

S18

C	0.083813	8.042806	18.300976
C	-0.307392	10.338696	17.597551
C	-1.279279	7.677182	18.267471
C	0.978404	7.210518	19.011631
C	-1.047968	10.745561	18.709281
C	-0.394180	11.057846	16.403848
H	-1.973642	8.328009	17.752284
C	-1.761997	6.537184	18.862014
H	2.024904	7.474340	19.077036
C	0.515700	6.086232	19.626139
H	-0.966880	10.194035	19.636509
C	-1.868232	11.858047	18.621118
C	-1.212552	12.172291	16.329531
H	0.174280	10.735460	15.541631
C	-3.249006	6.308741	18.812372
C	-0.850131	5.662255	19.562651
H	1.229023	5.462521	20.145901
H	-2.433759	12.172099	19.488754
C	-1.954626	12.576388	17.434124
H	-1.279215	12.722289	15.399901
H	-3.532327	5.603671	18.027477
H	-3.624964	5.915361	19.756944
H	-3.762282	7.246708	18.603268
C	-1.213707	4.430350	20.191770
H	-2.595190	13.445973	17.370192
C	-2.269847	3.582396	19.740307
C	-0.470207	3.930572	21.308642
H	-2.834437	3.853424	18.862202
C	-2.548610	2.385248	20.333701
C	-0.774692	2.750133	21.920777
H	0.326146	4.530177	21.728560
H	-3.349939	1.793995	19.913951
C	-1.828830	1.905252	21.468061
H	-0.178513	2.459654	22.774196
C	-2.140389	0.655106	22.104834
C	-1.525114	0.255268	23.324068
C	-3.084668	-0.256474	21.554798

C	-1.823650	-0.936343	23.935408
H	-0.811796	0.904626	23.810344
H	-3.579505	-0.028482	20.622057
C	-3.383716	-1.451032	22.160579
C	-2.760013	-1.818162	23.366205
H	-1.339551	-1.201032	24.866324
H	-4.102265	-2.120849	21.706621
C	-3.069057	-3.051314	23.995110
N	-3.320994	-4.056327	24.507597

13.3 T₁

C	3.648027	8.325478	15.882932
H	4.043180	7.508971	15.292253
C	4.418183	9.459595	16.108929
H	5.418562	9.529062	15.702389
C	2.362945	8.236062	16.395265
C	3.893191	10.504997	16.858834
C	1.840565	9.280698	17.157275
H	1.758144	7.358831	16.206212
C	2.614545	10.417530	17.387206
H	4.485935	11.391573	17.044284
N	0.526897	9.195146	17.684873
H	2.210082	11.228733	17.978270
C	0.088266	8.031134	18.307356
C	-0.326295	10.322711	17.568105
C	-1.266184	7.655613	18.270834
C	0.980821	7.202265	19.012594
C	-1.062242	10.765765	18.666516
C	-0.423155	11.003850	16.355672
H	-1.967150	8.304677	17.762214
C	-1.745830	6.508985	18.865338
H	2.027856	7.464757	19.075366
C	0.524385	6.067352	19.621584
H	-0.978258	10.243621	19.610670
C	-1.893213	11.868842	18.546058
C	-1.245337	12.114922	16.247530
H	0.148172	10.660535	15.503153

S20

C	-3.234353	6.279101	18.812308
C	-0.834806	5.640129	19.560353
H	1.244558	5.445568	20.134627
H	-2.459318	12.205039	19.405282
C	-1.987215	12.550192	17.338767
H	-1.313744	12.636272	15.301386
H	-3.516404	5.597427	18.006505
H	-3.612640	5.861669	19.745167
H	-3.748837	7.221760	18.628752
C	-1.194761	4.404148	20.185253
H	-2.631852	13.414705	17.249794
C	-2.255316	3.552988	19.727341
C	-0.448776	3.899333	21.308663
H	-2.803250	3.823026	18.838307
C	-2.545622	2.366502	20.318286
C	-0.750678	2.727496	21.919770
H	0.343417	4.504206	21.728698
H	-3.323201	1.760669	19.876671
C	-1.824555	1.878521	21.469205
H	-0.176061	2.449370	22.791110
C	-2.145030	0.651630	22.105292
C	-1.355340	0.120793	23.175542
C	-3.280432	-0.130159	21.717326
C	-1.664864	-1.061372	23.788845
H	-0.476467	0.649361	23.513217
H	-3.930126	0.214590	20.926918
C	-3.593968	-1.310365	22.332839
C	-2.792944	-1.805947	23.383150
H	-1.041782	-1.434853	24.590489
H	-4.463712	-1.871159	22.017480
C	-3.115675	-3.030083	24.019737
N	-3.379113	-4.028383	24.538741

13.4 T₂

C	3.533959	8.258766	15.708688
H	3.886697	7.417250	15.126287
C	4.328597	9.391260	15.849643

H	5.305972	9.433015	15.387424
C	2.281887	8.200244	16.297439
C	3.857777	10.470402	16.593177
C	1.808688	9.284429	17.044393
H	1.657242	7.325272	16.176960
C	2.612019	10.420647	17.192845
H	4.472403	11.352866	16.716931
N	0.545672	9.215118	17.670349
H	2.255394	11.253458	17.784209
C	0.129214	8.031278	18.268521
C	-0.289499	10.352663	17.688319
C	-1.237946	7.628707	18.214466
C	1.051893	7.199482	18.965357
C	-1.033278	10.658618	18.833539
C	-0.408219	11.163425	16.553846
H	-1.944921	8.260554	17.692058
C	-1.677343	6.463080	18.789416
H	2.088834	7.496290	19.046589
C	0.614374	6.045089	19.549499
H	-0.935448	10.035531	19.712396
C	-1.874710	11.758372	18.839257
C	-1.246024	12.264048	16.574555
H	0.152972	10.919121	15.661670
C	-3.138211	6.108549	18.711596
C	-0.741289	5.625602	19.476025
H	1.322124	5.421565	20.082019
H	-2.439237	11.990573	19.733250
C	-1.986179	12.568484	17.714476
H	-1.332431	12.883063	15.690720
H	-3.327007	5.312584	17.987802
H	-3.511694	5.757199	19.675328
H	-3.725992	6.974999	18.410030
C	-1.129535	4.366631	20.140749
H	-2.644203	13.427295	17.723714
C	-1.793080	3.334605	19.462208
C	-0.805578	4.144643	21.487097
H	-2.019959	3.450055	18.410521

C	-2.135549	2.158481	20.096828
C	-1.130340	2.964080	22.123126
H	-0.305745	4.926805	22.045146
H	-2.621608	1.383097	19.519898
C	-1.815692	1.931898	21.450953
H	-0.884425	2.856891	23.171114
C	-2.173019	0.693070	22.121114
C	-1.479828	0.249603	23.281193
C	-3.232956	-0.128172	21.646845
C	-1.811292	-0.916832	23.916159
H	-0.646285	0.824839	23.659213
H	-3.808205	0.184051	20.786468
C	-3.579671	-1.292216	22.278116
C	-2.873252	-1.714336	23.428838
H	-1.258768	-1.240836	24.787534
H	-4.400662	-1.891050	21.908106
C	-3.224853	-2.918321	24.084126
N	-3.512563	-3.902006	24.619389

Literature

- [1] J. Wiefermann, P. Schmeinck, C. Ganter, T. J. J. Müller, *Chem. Eur. J.* **2022**, 28, e202200576.
- [2] C. Reichardt, T. Welton, *Solvents and Solvent Effects in Organic Chemistry*; Wiley-VCH Verlag GmbH & Co. KGaA, Weinheim, Germany, **2010**.
- [3] a) J.-D. Chai, M. Head-Gordon, *Phys. Chem. Chem. Phys.* **2008**, 10, 6615–6620; b) J.-D. Chai, M. Head-Gordon, *J. Chem. Phys.* **2008**, 128, 84106; c) A. Schäfer, H. Horn, R. Ahlrichs, *J. Chem. Phys.* **1992**, 97, 2571–2577; d) F. Weigend, *Phys. Chem. Chem. Phys.* **2006**, 8, 1057–1065.
- [4] a) R. Cammi, S. Corni, B. Mennucci, J. Tomasi, *J. Chem. Phys.* **2005**, 122, 104513; b) E. Cancès, B. Mennucci, J. Tomasi, *J. Chem. Phys.* **1997**, 107, 3032–3041; c) G. Scalmani, M. J. Frisch, B. Mennucci, J. Tomasi, R. Cammi, V. Barone, *J. Chem. Phys.* **2006**, 124, 94107.
- [5] M. J. Frisch, G. W. Trucks, H. B. Schlegel, G. E. Scuseria, M. A. Robb, J. R. Cheeseman, G. Scalmani, V. Barone, G. A. Petersson, H. Nakatsuji, X. Li, M. Caricato, A. V. Marenich, J. Bloino, B. G. Janesko, R. Gomperts, B. Mennucci, H. P. Hratchian, J. V. Ortiz, A. F. Izmaylov, J. L. Sonnenberg, D. Williams-Young, F. Ding, F. Lipparini, F. Egidi, J. Goings, B. Peng, A. Petrone, T. Henderson, D. Ranasinghe, V. G. Zakrzewski, J. Gao, N. Rega, G. Zheng, W. Liang, M. Hada, M. Ehara, K. Toyota, R. Fukuda, J. Hasegawa, M. Ishida, T. Nakajima, Y. Honda, O. Kitao, H. Nakai, T. Vreven, K. Throssell, J. A. Montgomery, Jr, J. E. Peralta, F. Ogliaro, M. J. Bearpark, J. J. Heyd, E. N. Brothers, K. N. Kudin, V. N. Staroverov, T. A. Keith, R. Kobayashi, J. Normand, K. Raghavachari, A. P. Rendell, J. C. Burant, S. S. Iyengar, J. Tomasi, M. Cossi, J. M. Millam, M. Klene, C. Adamo, R. Cammi, J. W. Ochterski, R. L. Martin, K. Morokuma, O.

- Farkas, J. B. Foresman, and D. J. Fox, *Gaussian 16, Revision A.03, Gaussian Inc. 2016*.
- [6] a) A. Dreuw, M. Head-Gordon, *J. Am. Chem. Soc.* **2004**, *126*, 4007–4016; b) C. Fiolhais, Ed, *A Primer in Density Functional Theory*; Springer-Verlag Berlin Heidelberg, Berlin, Heidelberg, **2003**; c) F. Furche, R. Ahlrichs, *J. Chem. Phys.* **2002**, *117*, 7433–7447; d) E. Runge, E. K. U. Gross, *Phys. Rev. Lett.* **1984**, *52*, 997–1000.
 - [7] S. Hirata, M. Head-Gordon, *Chem. Phys. Lett.* **1999**, *314*, 291–299.
 - [8] a) S. Grimme, M. Waletzke, *J. Chem. Phys.* **1999**, *111*, 5645–5655; b) M. Kleinschmidt, C. M. Marian, M. Waletzke, S. Grimme, *J. Chem. Phys.* **2009**, *130*, 44708; c) C. M. Marian, A. Heil, M. Kleinschmidt, *WIREs Comput. Mol. Sci.* **2019**, *9*,
 - [9] I. Lyskov, M. Kleinschmidt, C. M. Marian, *J. Chem. Phys.* **2016**, *144*, 34104.
 - [10] a) A. D. Becke, *J. Chem. Phys.* **1993**, *98*, 1372–1377; b) C. Lee, W. Yang, R. G. Parr, *Phys. Rev. B.* **1988**, *37*, 785–789.
 - [11] TURBOMOLE V7.5 2020. A development of University of Karlsruhe and Forschungszentrum Karlsruhe GmbH, 1989–2007, TURBOMOLE GmbH, since 2007; available from <http://www.turbomole.com>.
 - [12] F. Plasser, *J. Chem. Phys.* **2020**, *152*, 84108.
 - [13] a) B. A. Heß, C. M. Marian, U. Wahlgren, O. Gropen, *Chem. Phys. Lett.* **1996**, *251*, 365–371; b) M. Kleinschmidt, C. M. Marian, *Chem. Phys.* **2005**, *311*, 71–79; c) M. Kleinschmidt, J. Tatchen, C. M. Marian, *J. Comput. Chem.* **2002**, *23*, 824–833; d) M. Kleinschmidt, J. Tatchen, C. M. Marian, *J. Chem. Phys.* **2006**, *124*, 124101; e) B. Schimmelpfennig, *University of Stockholm* **1996**.
 - [14] a) M. Etinski, J. Tatchen, C. M. Marian, *J. Chem. Phys.* **2011**, *134*, 154105; b) M. Etinski, J. Tatchen, C. M. Marian, *Phys. Chem. Chem. Phys.* **2014**, *16*, 4740–4751;
 - [15] D. Jacquemin, B. Moore, A. Planchat, C. Adamo, J. Autschbach, *J. Chem. Theory Comput.* **2014**, *10*, 1677–1685.
 - [16] a) R. Baer, E. Livshits, U. Salzner, *Annu. Rev. Phys. Chem.* **2010**, *61*, 85–109; b) L. Kronik, T. Stein, S. Refaely-Abramson, R. Baer, *J. Chem. Theory Comput.* **2012**, *8*, 1515–1531.

10.2.2 Supplementary Data for Chapter 5

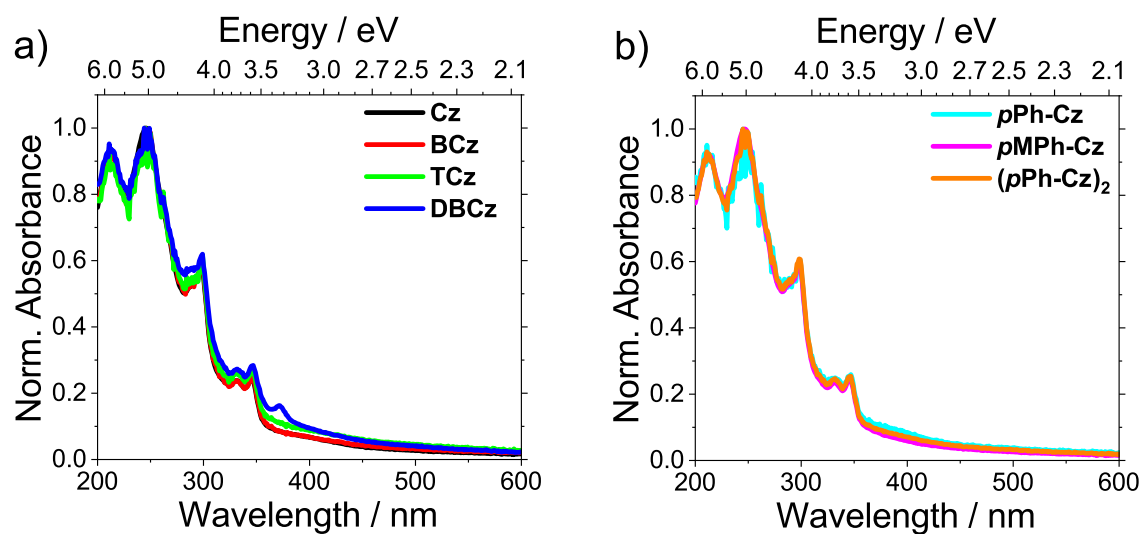


Figure 10.1: Thin film absorbance of 8wt% of a) Cz, BCz, TCz, DBCz and b) *p*Ph-Cz, *p*MPh-Cz, (*p*Ph-Cz)₂ in mCBP.

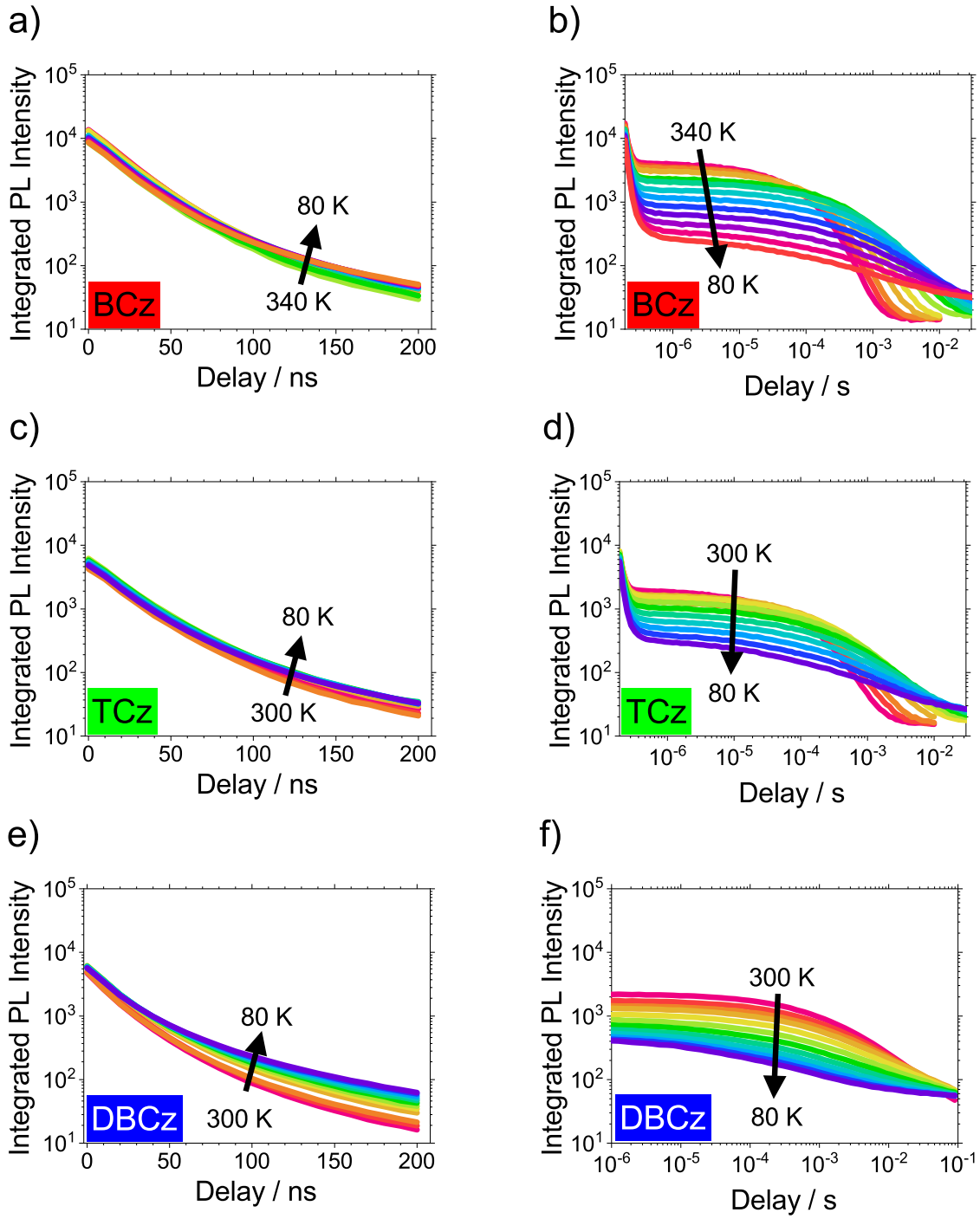


Figure 10.2: Prompt (left) and delayed (right) integrated PL intensity recorded with gate width of 100 ns (prompt) and 1 ms (delayed) at different temperatures for 8 wt%, **BCz** (top), **TCz** (middle) and **DBCz** (bottom) in mCBP film. Fitted decay curves can be found in Fig.10.9-10.20.

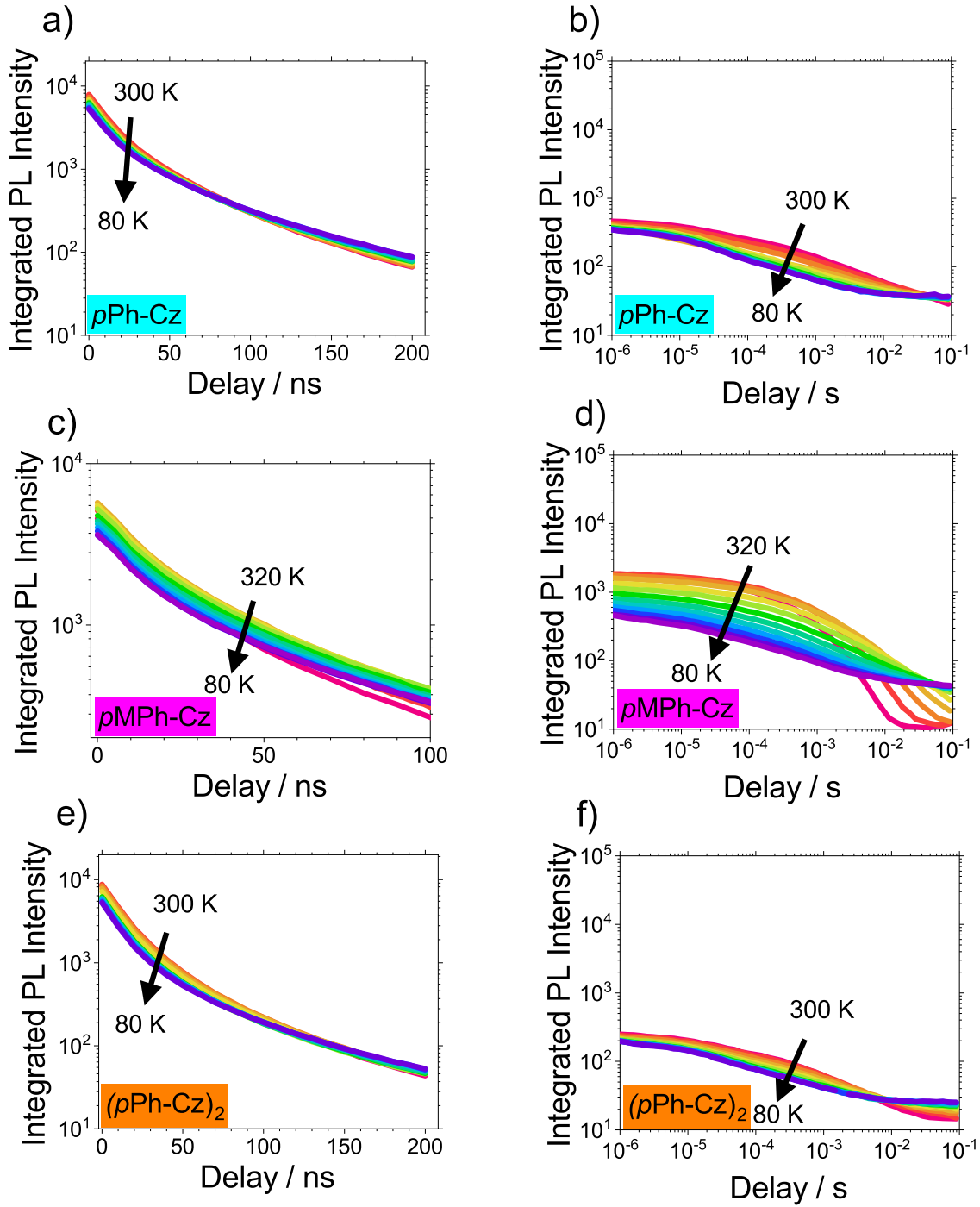


Figure 10.3: Prompt (left) and delayed (right) integrated PL intensity recorded with gate width of 100 ns (prompt) and 1 ms (delayed) at different temperatures for 8 wt%, **pPh-Cz** (top), **pMPh-Cz** (middle) and **(pPh-Cz)₂** (bottom) in mCBP film. Fitted decay curves can be found in Fig.10.21-10.32.

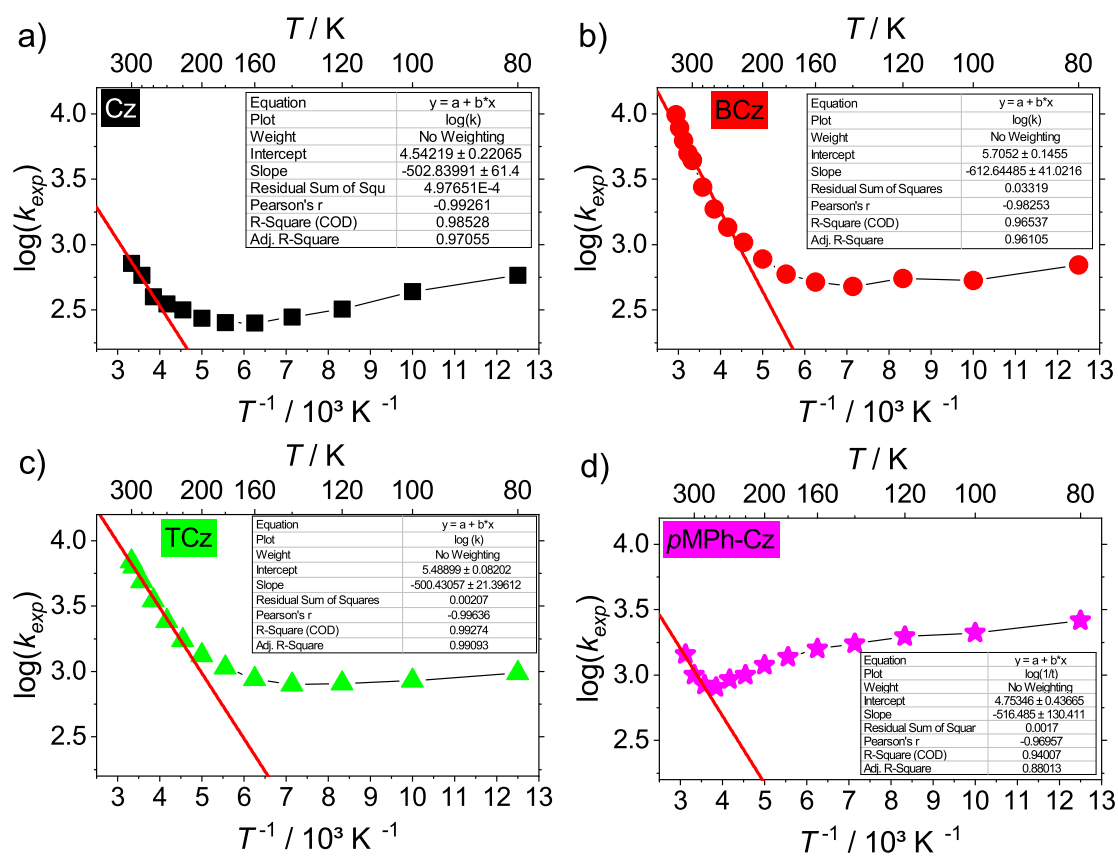


Figure 10.4: Arrhenius plots for a) **Cz** b) **BCz** c) **TCz** d) **pMPh-Cz** with corresponding fit. The slope is used for calculation of ΔE_{ST} according to Eq. 5.2.

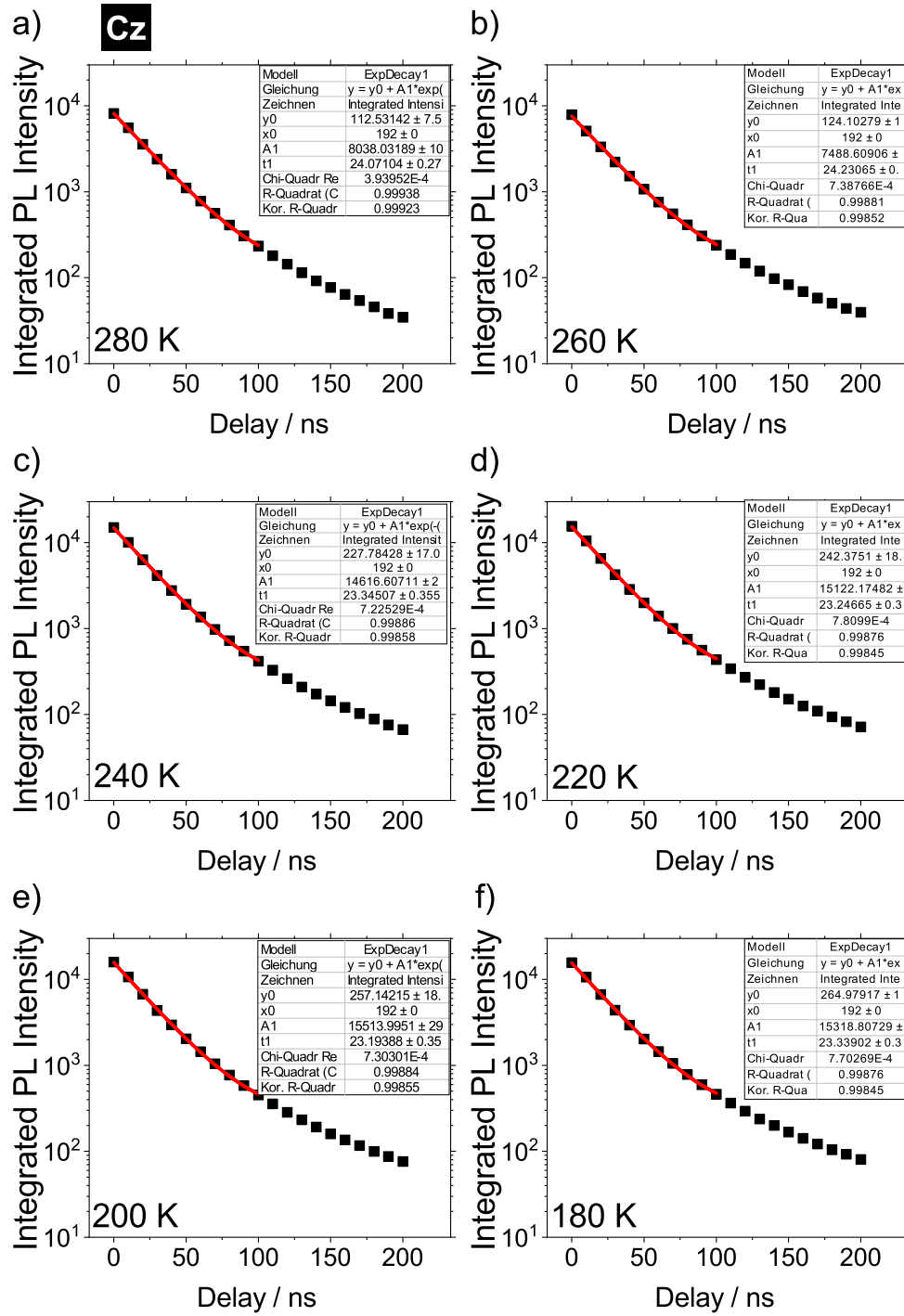


Figure 10.5: Time resolved prompt PL decay of 8wt% Cz in mCBP detected with a gate width of 100 ns. a) 280 K, b) 260 K, c) 240 K, d) 220 K, e) 200 K, f) 180 K. The fit parameters are summarized in Tab. 10.1.

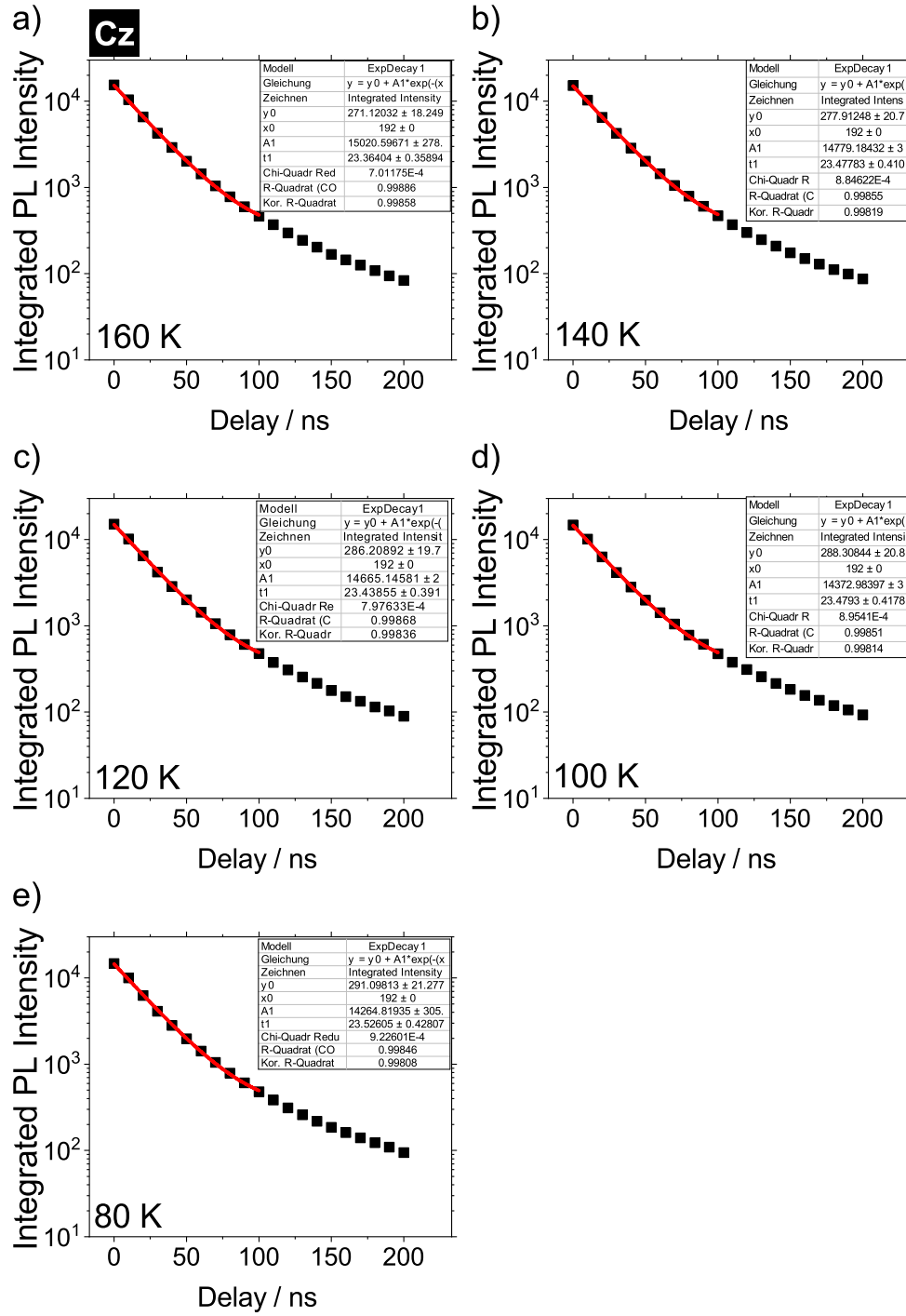


Figure 10.6: Time resolved prompt PL decay of 8wt% **Cz** in mCBP detected with a gate width of 100 ns. a) 160 K, b) 140 K, c) 120 K, d) 100 K, e) 80 K. The fit parameters are summarized in Tab. 10.1.

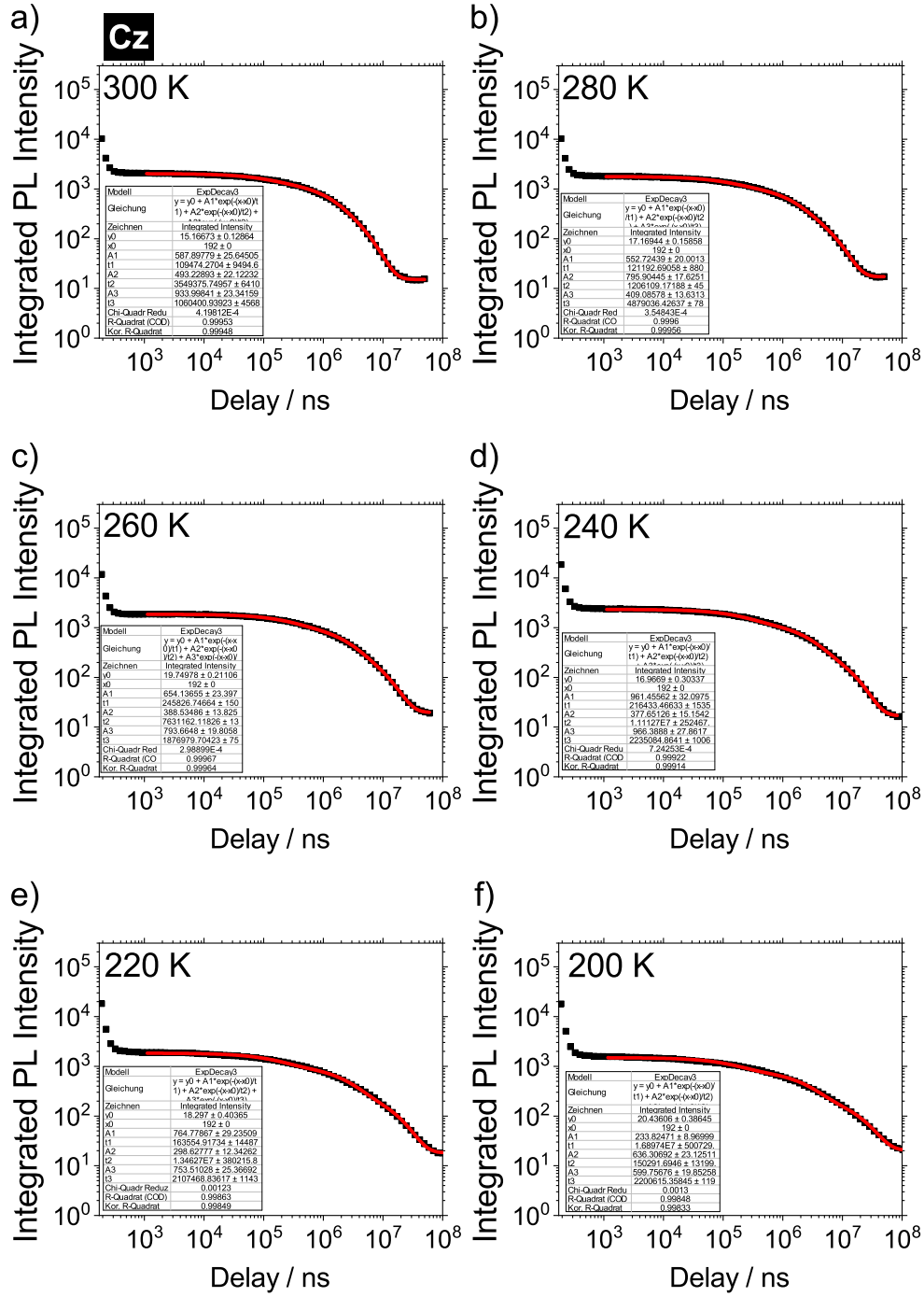


Figure 10.7: Time resolved delayed PL decay of 8wt% **Cz** in mCBP detected with a gate width of 1 ms. a) 300 K, b) 280 K, c) 260 K, d) 240 K, e) 220 K, f) 200 K. The fit parameters are summarized in Tab. 10.1.

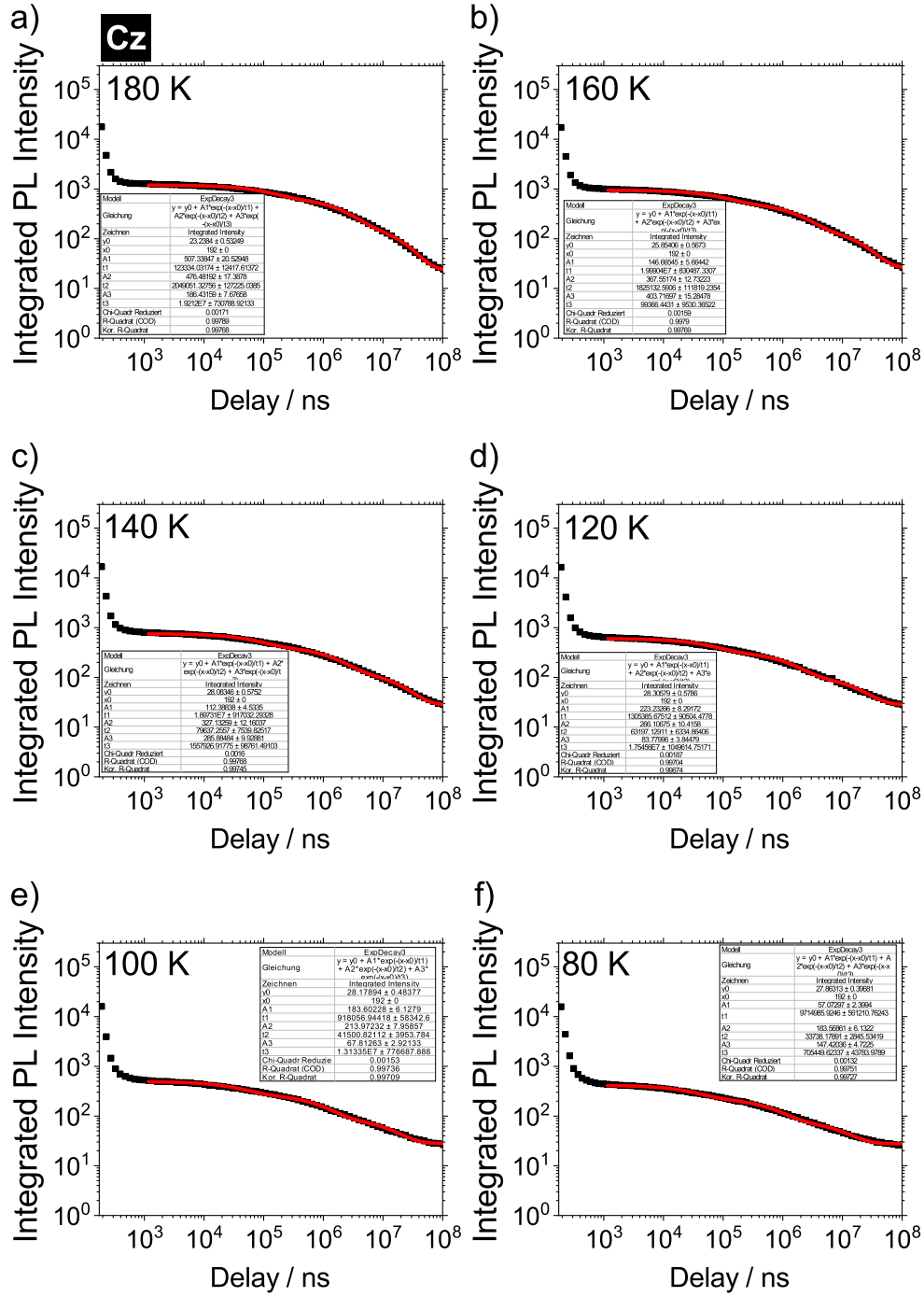


Figure 10.8: Time resolved delayed PL decay of 8wt% Cz in mCBP detected with a gate width of 1 ms. a) 180 K, b) 160 K, c) 140 K, d) 120 K, e) 100 K, f) 80 K. The fit parameters are summarized in Tab. 10.1.

Table 10.1: Fit parameter of PL decay for **Cz** in mCBP at different temperatures. $\tau_{delayed}$ is the amplitude weighted average of the three decay times according to Eq. 9.2.

T K	prompt	delayed						$\tau_{delayed}$
	τ_{prompt} ns	A1	t1	A2	t2	A3	t3	
300		588	1.09E+05	493	3.55E+06	934	1.06E+06	1.39
280	24.07	553	1.21E+05	796	1.21E+06	409	4.88E+06	1.72
260	24.23	654	2.46E+05	389	7.63E+06	794	1.88E+06	2.51
240	23.35	961	2.16E+05	378	1.11E+07	966	2.24E+06	2.85
220	23.25	765	1.64E+05	299	1.35E+07	754	2.11E+06	3.16
200	23.19	234	1.69E+07	636	1.50E+05	600	2.20E+06	3.65
180	23.34	507	1.23E+05	476	2.05E+06	186	1.92E+07	3.95
160	23.36	147	2.00E+07	368	1.83E+06	404	9.94E+04	3.97
140	23.48	112	1.90E+07	327	7.96E+04	286	1.56E+06	3.59
120	23.44	223	1.31E+06	266	6.32E+04	84	1.75E+07	3.10
100	23.48	184	9.18E+05	214	4.15E+04	68	1.31E+07	2.29
80	23.53	57	9.71E+06	184	3.37E+04	147	7.05E+05	1.71

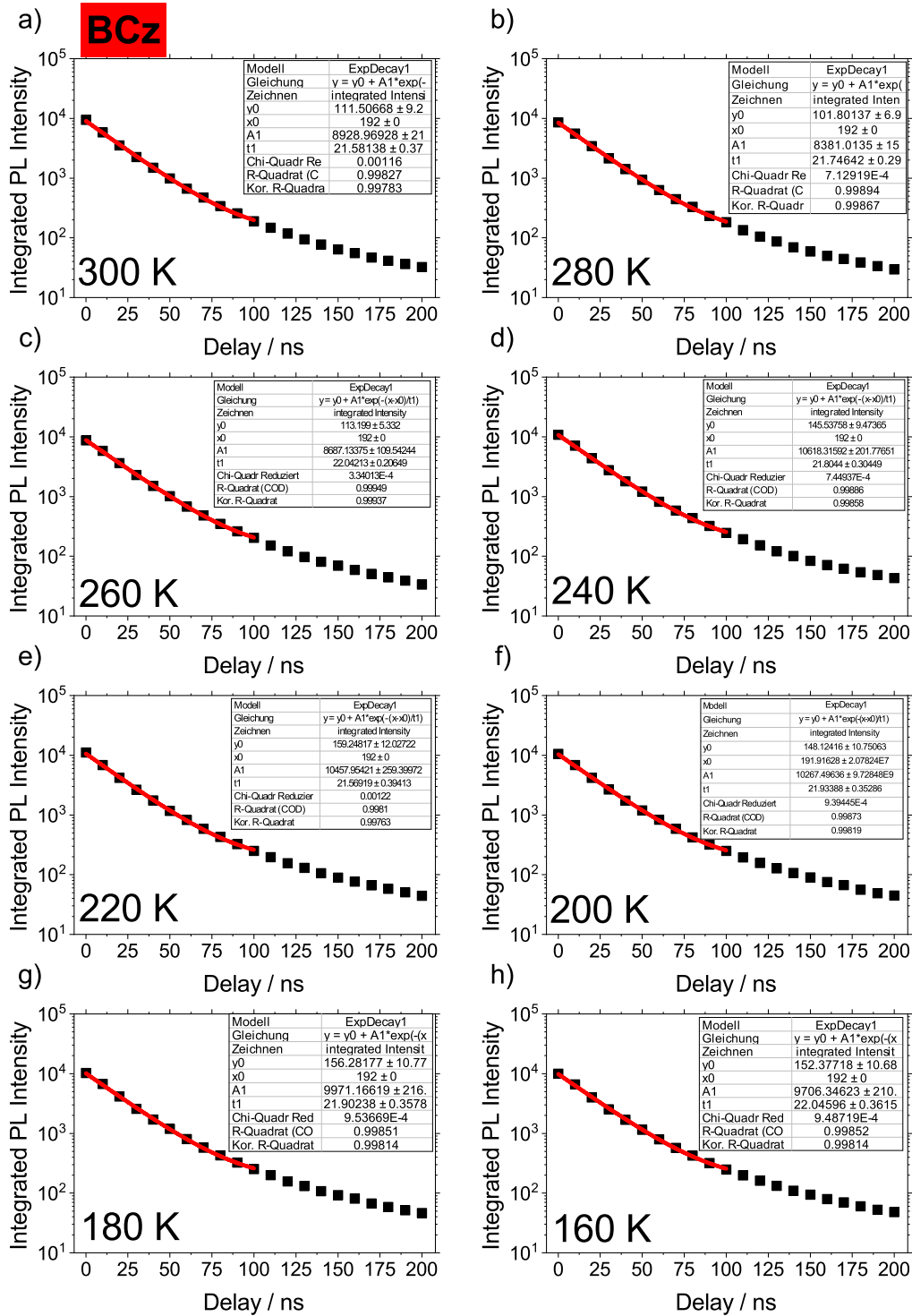


Figure 10.9: Time resolved prompt PL decay of 8wt% **BCz** in mCBP detected with a gate width of 100 ns. a) 300 K, b) 280 K, c) 260 K, d) 240 K, e) 220 K, f) 200 K, g) 180 K, h) 160 K. The fit parameters are summarized in Tab. 10.2.

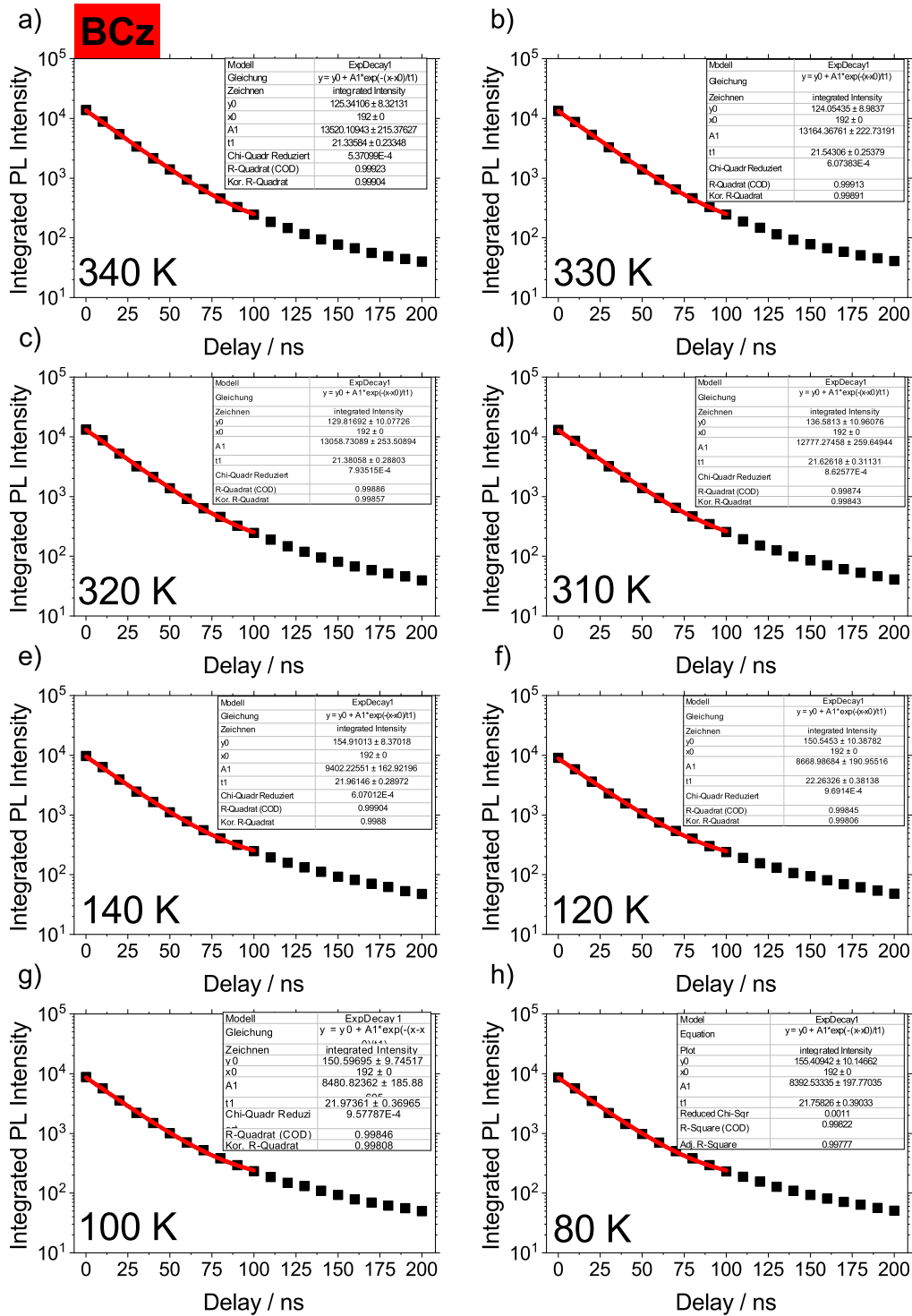


Figure 10.10: Time resolved prompt PL decay of 8wt% **BCz** in mCBP detected with a gate width of 100 ns. a) 340 K, b) 330 K, c) 320 K, d) 310 K, e) 140 K, f) 120 K, g) 100 K, h) 80 K. The fit parameters are summarized in Tab.10.2.

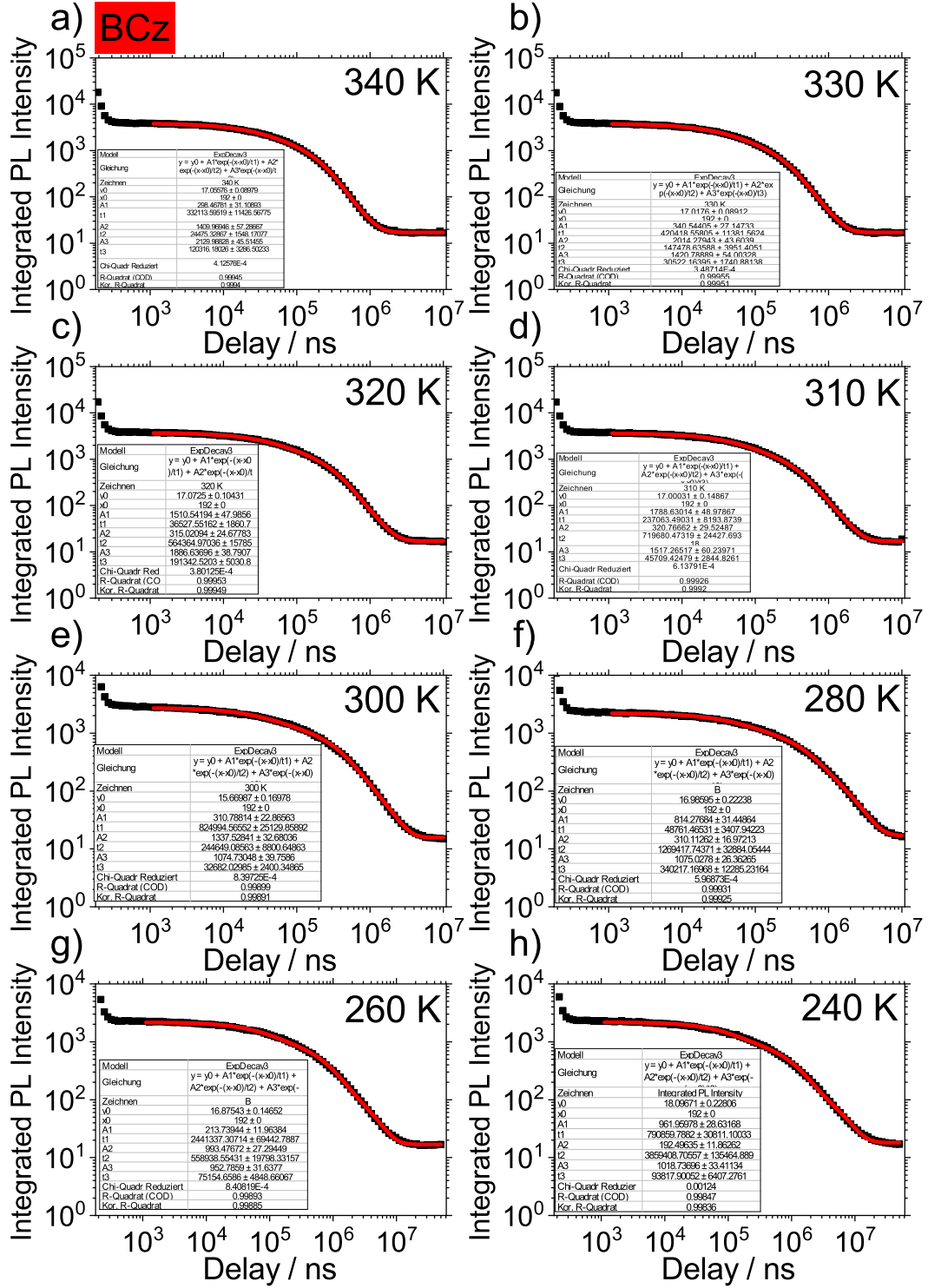


Figure 10.11: Time resolved delayed PL decay of 8wt% **BCz** in mCBP detected with a gate width of 1 ms. a) 340 K, b) 330 K, c) 320 K, d) 310 K, e) 300 K, f) 280 K, g) 260 K, h) 240 K. The fit parameters are summarized in Tab. 10.2.

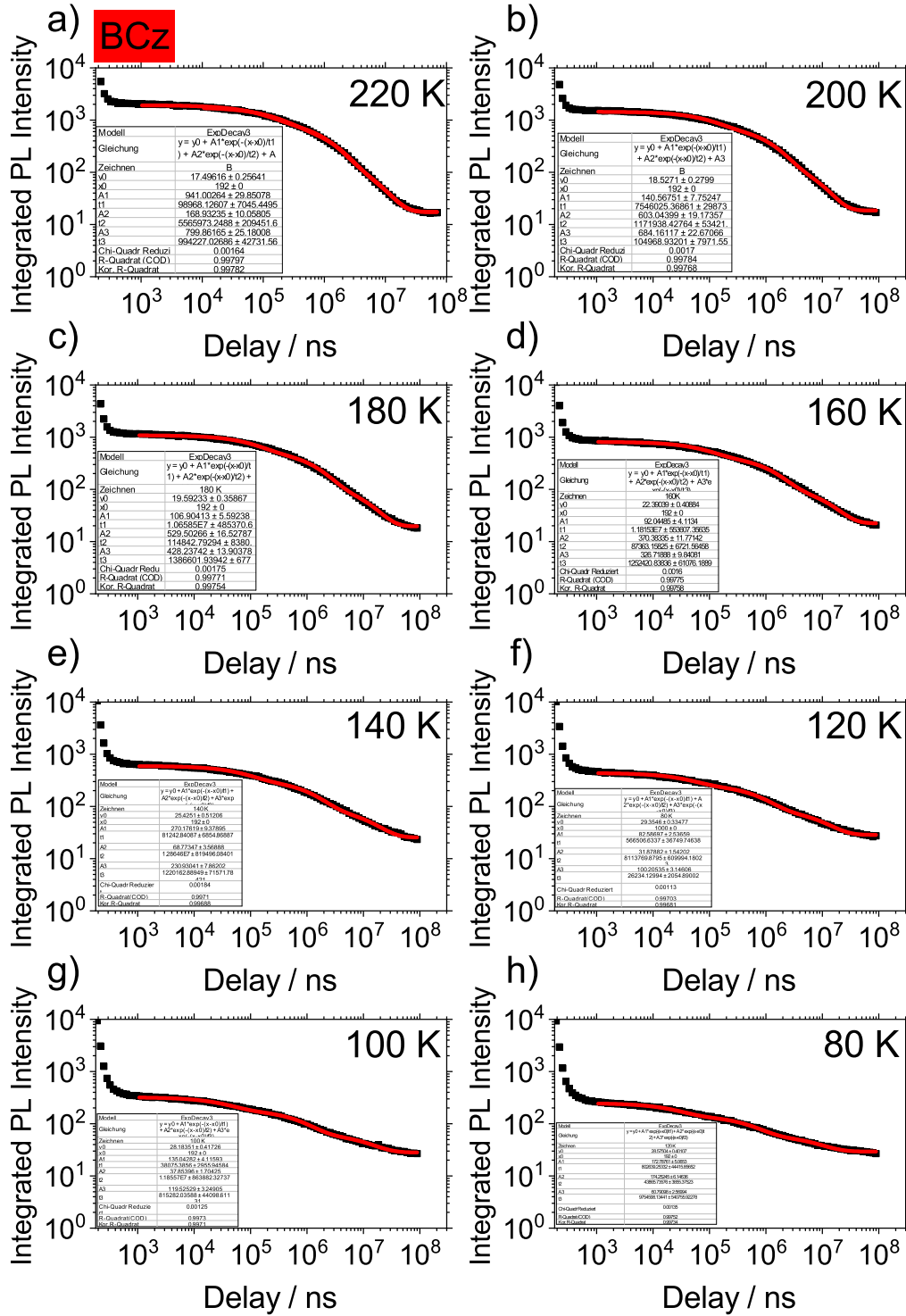


Figure 10.12: Time resolved delayed PL decay of 8wt% BCz in mCBP detected with a gate width of 1 ms. a) 220 K, b) 200 K, c) 180 K, d) 160 K, e) 140 K, f) 120 K, g) 100 K, h) 80 K. The fit parameters are summarized in Tab. 10.2.

Table 10.2: Fit parameter of PL decay for **BCz** in mCBP at different temperatures. $\tau_{delayed}$ is the amplitude weighted average of the three decay times according to Eq. 9.2.

T K	prompt	delayed						$\tau_{delayed}$ ms
	τ_{prompt} ns	A1	t1	A2	t2	A3	t3	
340	21.34	298	3.32E+05	1410	2.45E+04	2130	1.20E+05	0.10
330	21.54	341	4.20E+05	2014	1.47E+05	1421	3.05E+04	0.13
320	21.38	1511	3.65E+04	315	5.64E+05	1887	1.91E+05	0.16
310	21.63	1789	2.37E+05	321	7.20E+05	1517	4.57E+04	0.20
300	21.58	311	8.25E+05	1338	2.45E+05	1075	3.27E+04	0.23
280	21.75	814	4.88E+04	310	1.27E+06	1075	3.40E+05	0.36
260	22.04	214	2.44E+06	993	5.59E+05	953	7.52E+04	0.53
240	21.80	962	7.91E+05	192	3.86E+06	1019	9.38E+04	0.74
220	21.57	941	9.90E+04	169	5.57E+06	800	9.94E+05	0.96
200	21.93	141	7.55E+06	603	1.17E+06	684	1.05E+05	1.29
180	21.90	107	1.07E+07	530	1.15E+05	428	1.39E+06	1.69
160	22.05	92	1.18E+07	370	8.74E+04	327	1.25E+06	1.94
140	21.96	270	8.12E+04	69	1.29E+07	231	1.22E+06	2.09
120	22.26	173	8.03E+05	174	4.39E+04	61	9.75E+06	1.81
100	21.97	135	3.81E+04	38	1.19E+07	120	8.15E+05	1.89
80	21.76	83	5.67E+05	32	8.11E+06	100	2.62E+04	1.44

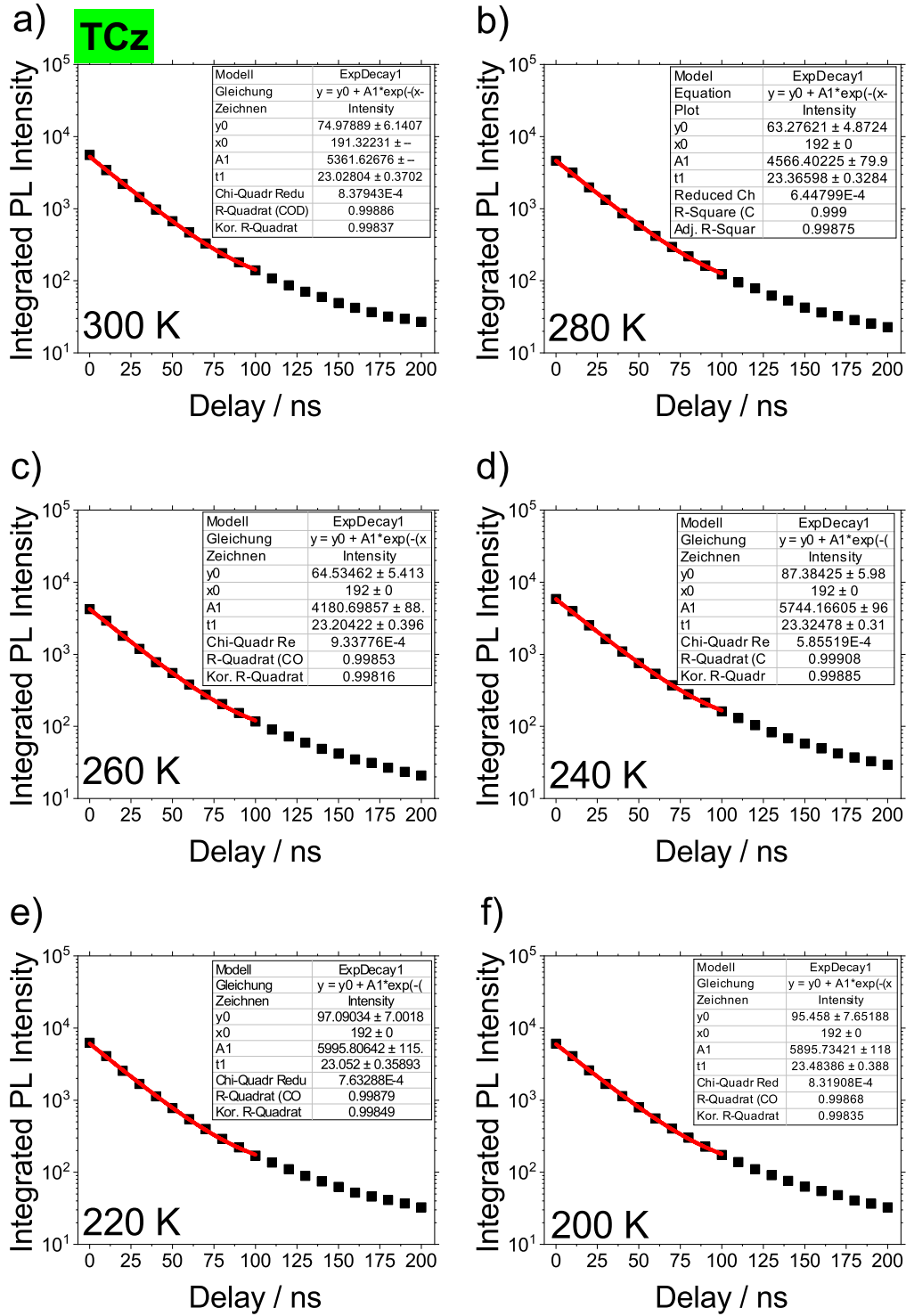


Figure 10.13: Time resolved prompt PL decay of 8wt% **TCz** in mCBP detected with a gate width of 100 ns. a) 300 K, b) 280 K, c) 260 K, d) 240 K, e) 220 K, f) 200 K. The fit parameters are summarized in Tab. 10.3.

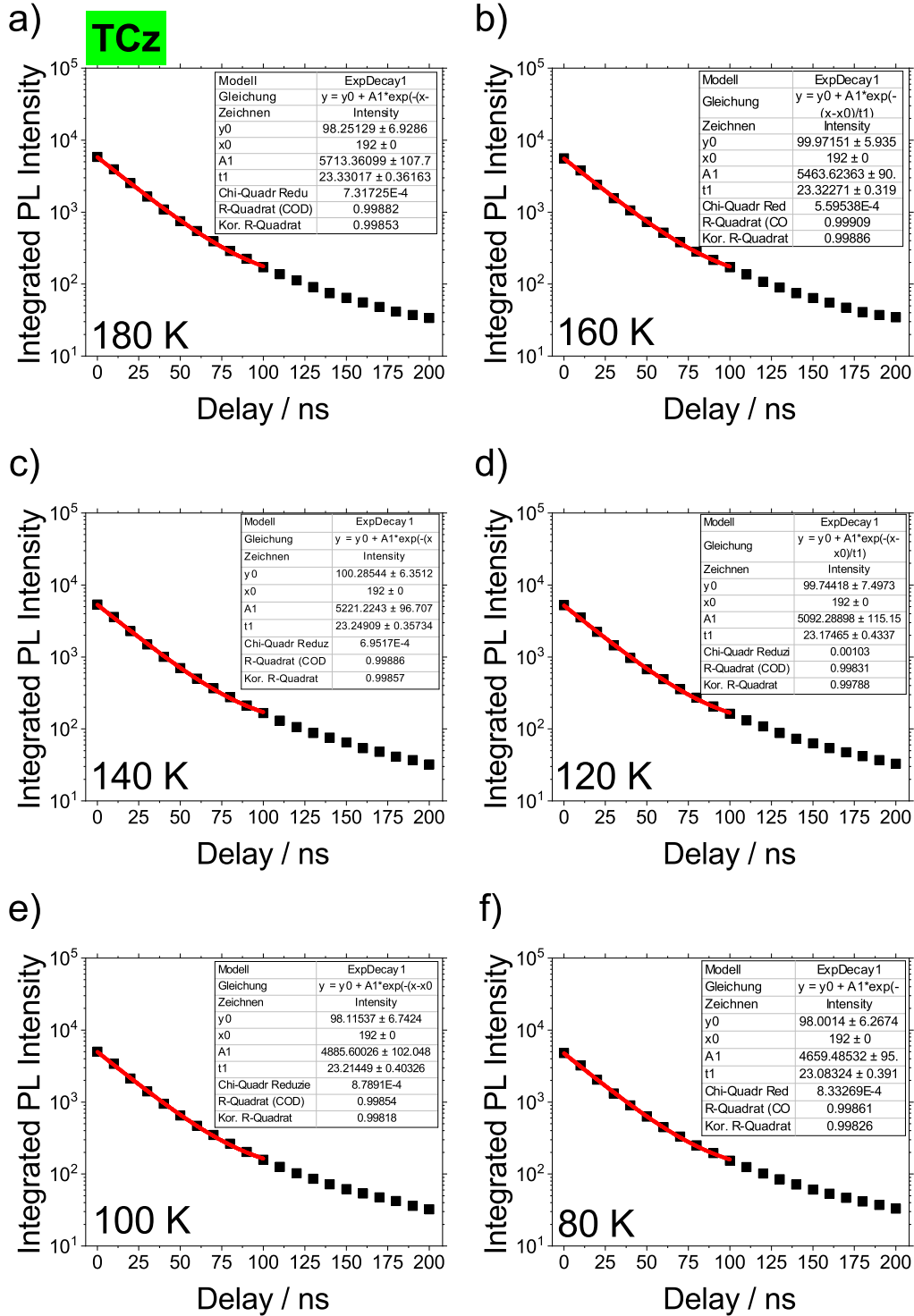


Figure 10.14: Time resolved prompt PL decay of 8wt% **TCz** in mCBP detected with a gate width of 100 ns. a) 180 K, b) 160 K, c) 140 K, d) 120 K, e) 100 K, f) 80 K. The fit parameters are summarized in Tab. 10.3.

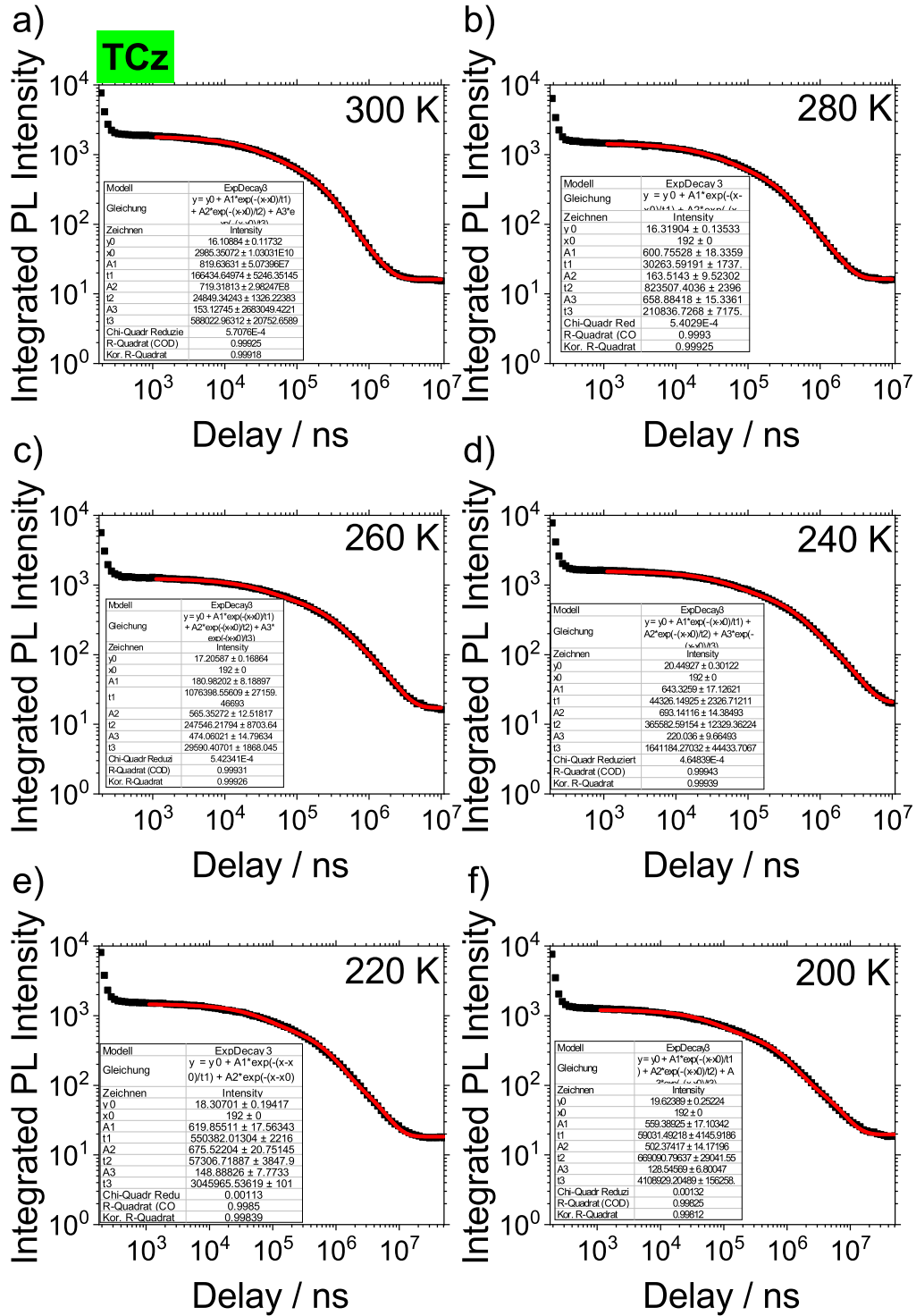


Figure 10.15: Time resolved delayed PL decay of 8wt% **TCz** in mCBP detected with a gate width of 1 ms. a) 300 K, b) 280 K, c) 260 K, d) 240 K, e) 220 K, f) 200 K. The fit parameters are summarized in Tab. 10.3.

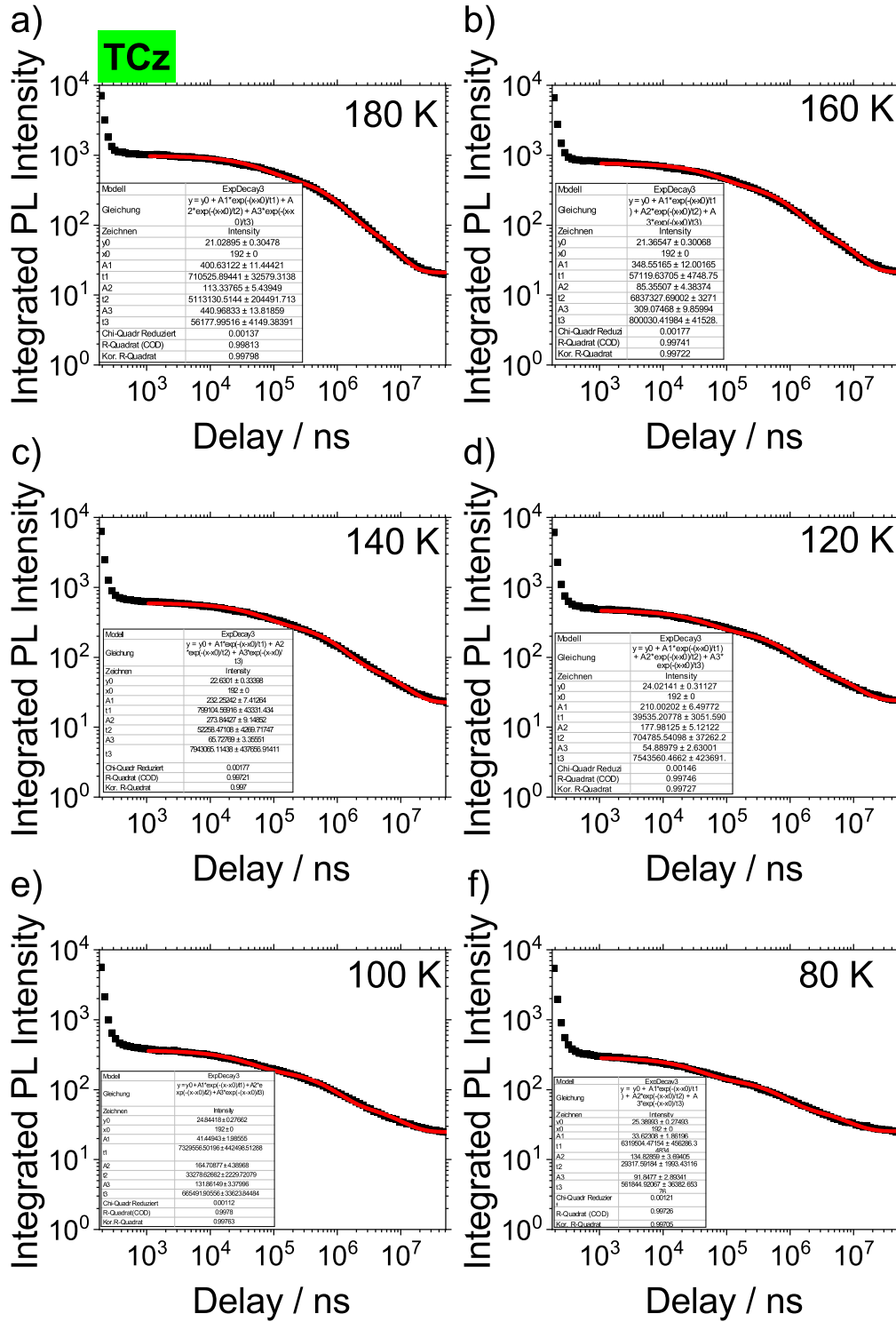


Figure 10.16: Time resolved delayed PL decay of 8wt% **TCz** in mCBP detected with a gate width of 1 ms. a) 180 K, b) 160 K, c) 140 K, d) 120 K, e) 100 K, f) 80 K. The fit parameters are summarized in Tab. 10.3.

Table 10.3: Fit parameter of PL decay for **TCz** in mCBP at different temperatures. $\tau_{delayed}$ is the amplitude weighted average of the three decay times according to Eq. 9.2.

T K	prompt	delayed						$\tau_{delayed}$ ms
	τ_{prompt} ns	A1	t1	A2	t2	A3	t3	
300	23.03	820	1.66E+05	719	2.48E+04	153	5.88E+05	0.14
280	23.37	601	3.03E+04	164	8.24E+05	659	2.11E+05	0.21
260	23.20	181	1.08E+06	565	2.48E+05	474	2.96E+04	0.29
240	23.32	643	4.43E+04	693	3.66E+05	220	1.64E+06	0.41
220	23.05	620	5.50E+05	676	5.73E+04	149	3.05E+06	0.58
200	23.48	559	5.90E+04	502	6.69E+05	129	4.11E+06	0.75
180	23.33	401	7.11E+05	113	5.11E+06	441	5.62E+04	0.93
160	23.32	349	5.71E+04	85	6.84E+06	309	8.00E+05	1.15
140	23.25	232	7.99E+05	274	5.23E+04	66	7.94E+06	1.26
120	23.17	210	3.95E+04	178	7.05E+05	55	7.54E+06	1.24
100	23.21	41	7.33E+06	165	3.33E+04	132	6.65E+05	1.17
80	23.08	34	6.32E+06	135	2.93E+04	92	5.62E+05	1.03

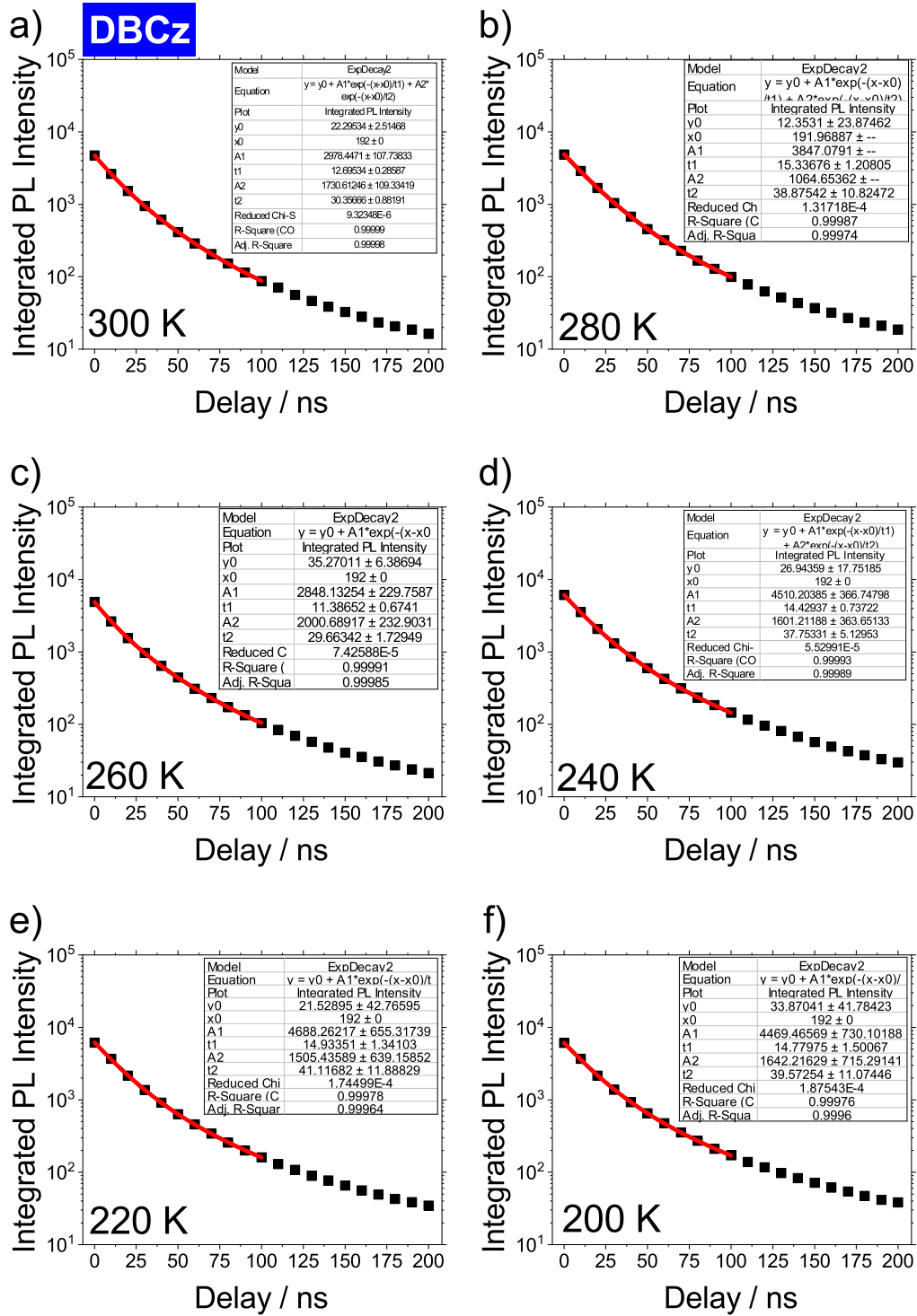


Figure 10.17: Time resolved prompt PL decay of 8wt% DBCz in mCBP detected with a gate width of 100 ns. a) 300 K, b) 280 K, c) 260 K, d) 240 K, e) 220 K, f) 200 K. The fit parameters are summarized in Tab. 10.4.

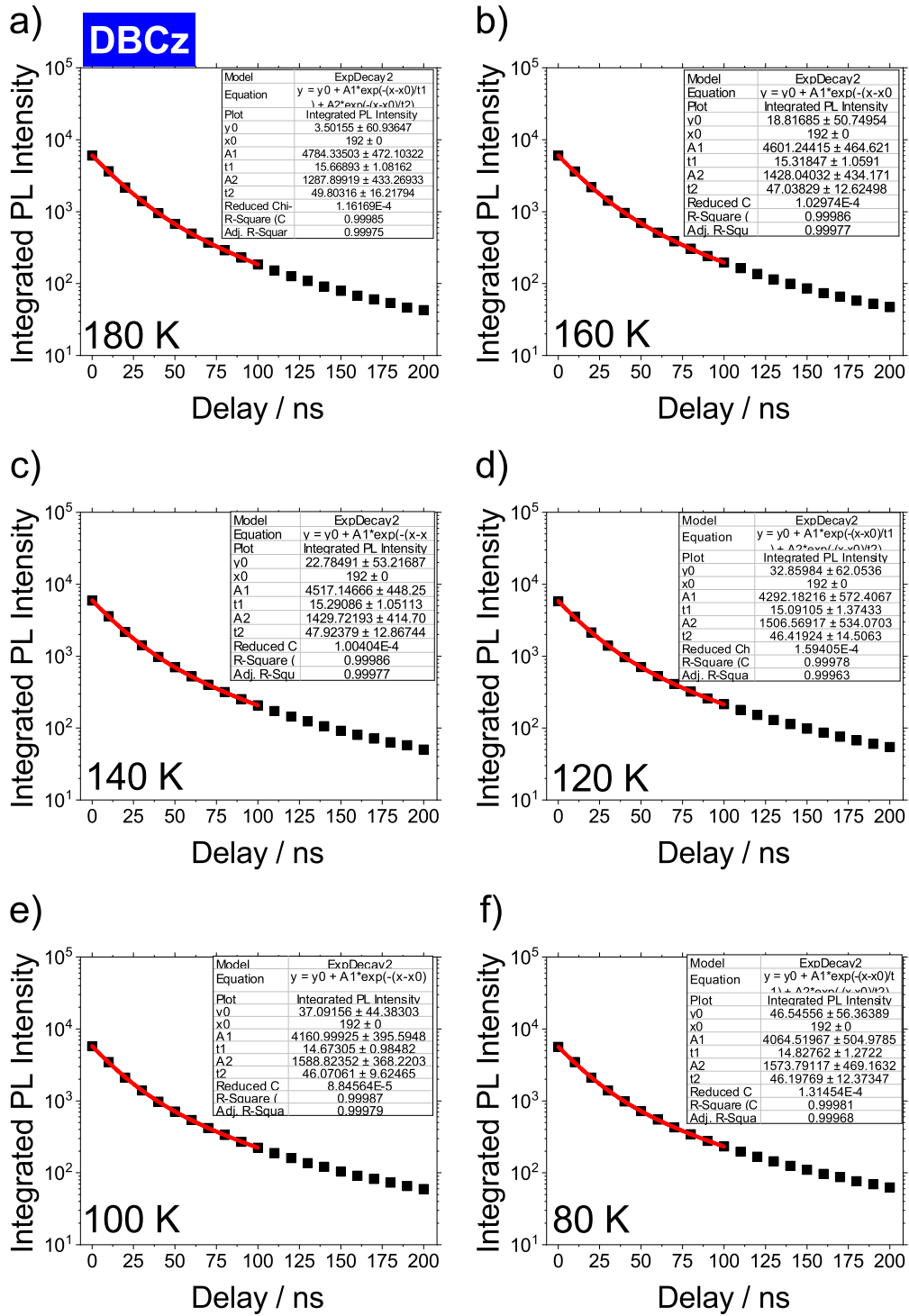


Figure 10.18: Time resolved prompt PL decay of 8wt% **DBCz** in mCBP detected with a gate width of 100 ns. a) 180 K, b) 160 K, c) 140 K, d) 120 K, e) 100 K, f) 80 K. The fit parameters are summarized in Tab. 10.4.

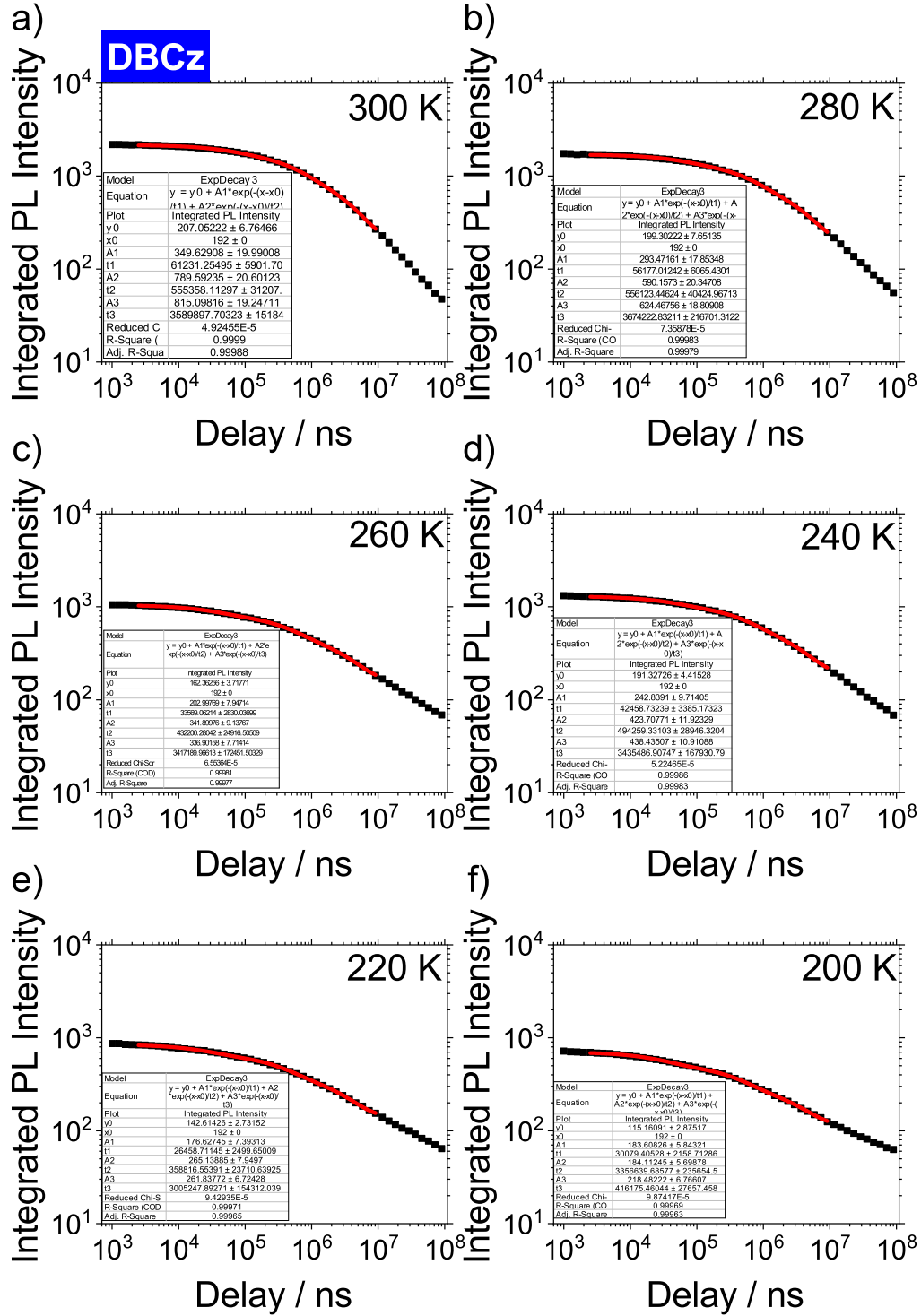


Figure 10.19: Time resolved delayed PL decay of 8wt% **DBCz** in mCBP detected with a gate width of 1 ms. a) 300 K, b) 280 K, c) 260 K, d) 240 K, e) 220 K, f) 200 K. The fit parameters are summarized in Tab. 10.4.

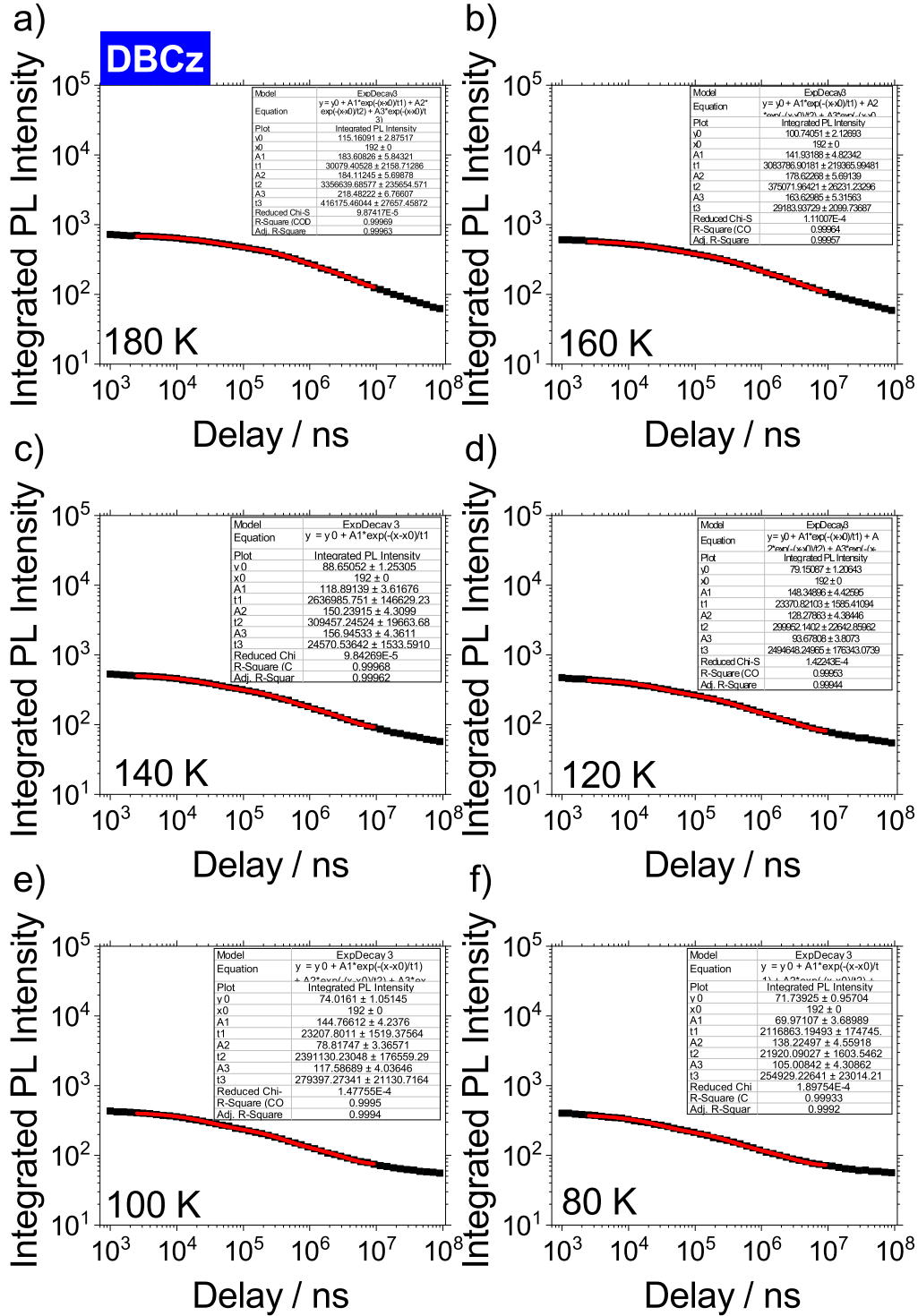


Figure 10.20: Time resolved delayed PL decay of 8wt% **DBCz** in mCBP detected with a gate width of 1 ms. a) 180 K, b) 160 K, c) 140 K, d) 120 K, e) 100 K, f) 80 K. The fit parameters are summarized in Tab. 10.4.

Table 10.4: Fit parameter of PL decay for **DBCz** in mCBP at different temperatures.
 τ_{prompt} , $\tau_{delayed}$ is the amplitude weighted average of the two/three decay times according to Eq.9.2.

prompt							τ_{prompt}
T	A1	t1	A2	t2			
K	ns		ns				ns
300	2978	1.27E+01	1731	3.04E+01			19.19
280	3839	1.53E+01	1064	3.89E+01			20.44
260	2848	1.14E+01	2001	2.97E+01			18.93
240	4510	1.44E+01	1601	3.78E+01			20.54
220	4688	1.49E+01	1505	4.11E+01			21.30
200	4469	1.48E+01	1642	3.96E+01			21.44
180	4784	1.57E+01	1288	4.98E+01			22.91
160	4601	1.53E+01	1428	4.70E+01			22.83
140	4517	1.53E+01	1430	4.79E+01			23.14
120	4292	1.51E+01	1507	4.64E+01			23.23
100	4161	1.47E+01	1589	4.61E+01			23.35
80	4065	1.48E+01	1574	4.62E+01			23.58
delayed							
T	A1	t1	A2	t2	A3	t3	$\tau_{delayed}$
K	ns		ns		ns		ms
300	302	1.95E+07	897	2.53E+05	875	2.57E+06	4.03
280	270	2.01E+07	656	2.05E+05	697	2.38E+06	4.45
260	544	2.11E+05	559	2.44E+06	232	2.18E+07	4.90
240	233	1.93E+07	443	1.25E+05	530	1.80E+06	4.57
220	409	1.64E+06	360	1.04E+05	184	1.91E+07	4.43
200	325	1.44E+06	296	7.61E+04	142	1.89E+07	4.17
180	118	1.55E+07	247	5.22E+04	265	1.09E+06	3.39
160	91	1.46E+07	219	4.45E+04	214	9.55E+05	2.94
140	179	8.17E+05	71	1.25E+07	204	3.70E+04	2.29
120	59	1.04E+07	153	6.73E+05	183	3.03E+04	1.82
100	134	5.55E+05	53	8.27E+06	173	2.84E+04	1.43
80	122	4.98E+05	166	2.51E+04	45	7.42E+06	1.20

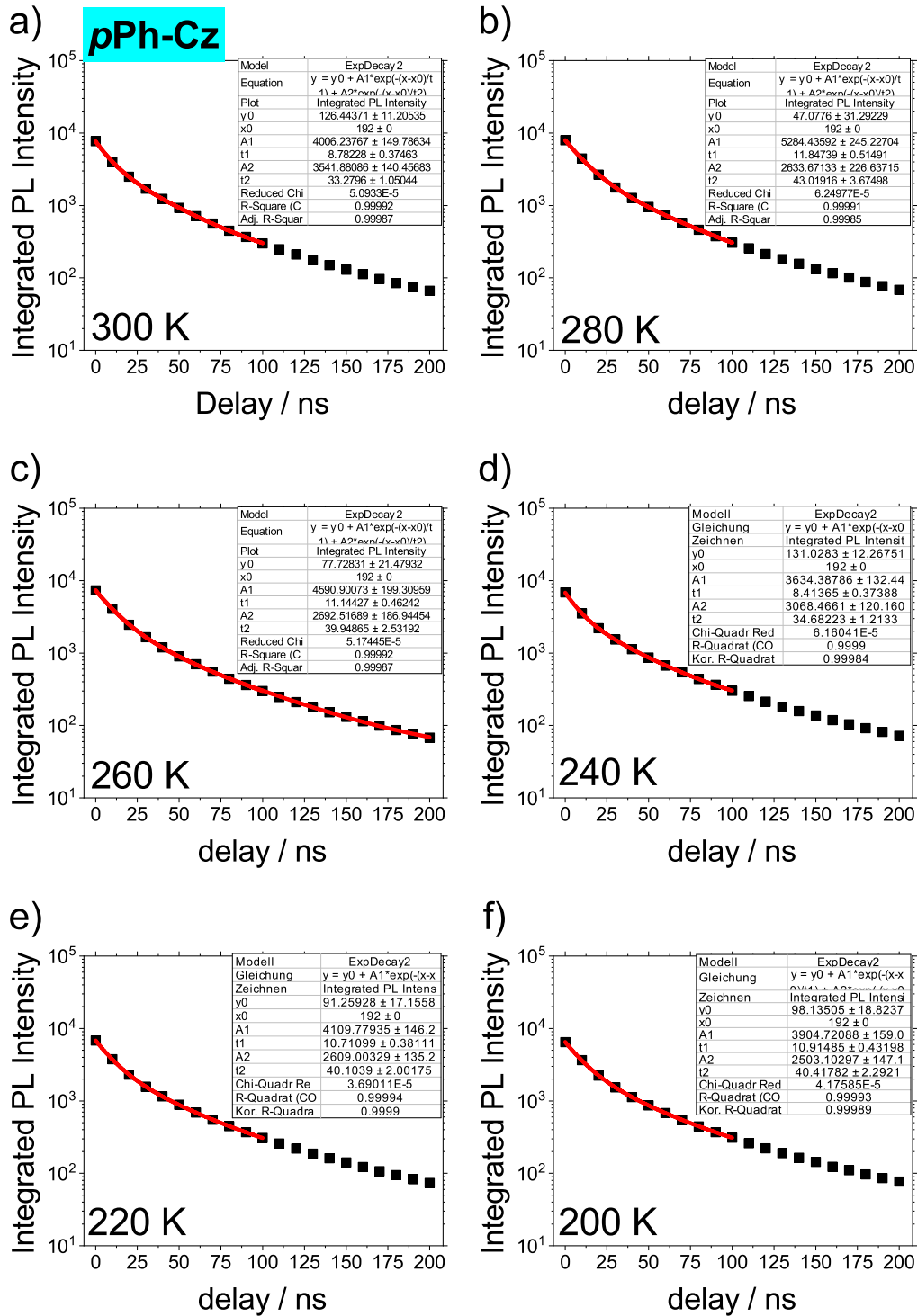


Figure 10.21: Time resolved prompt PL decay of 8wt% **pPh-Cz** in mCBP detected with a gate width of 100 ns. a) 300 K, b) 280 K, c) 260 K, d) 240 K, e) 220 K, f) 200 K. The fit parameters are summarized in Tab. 10.5.

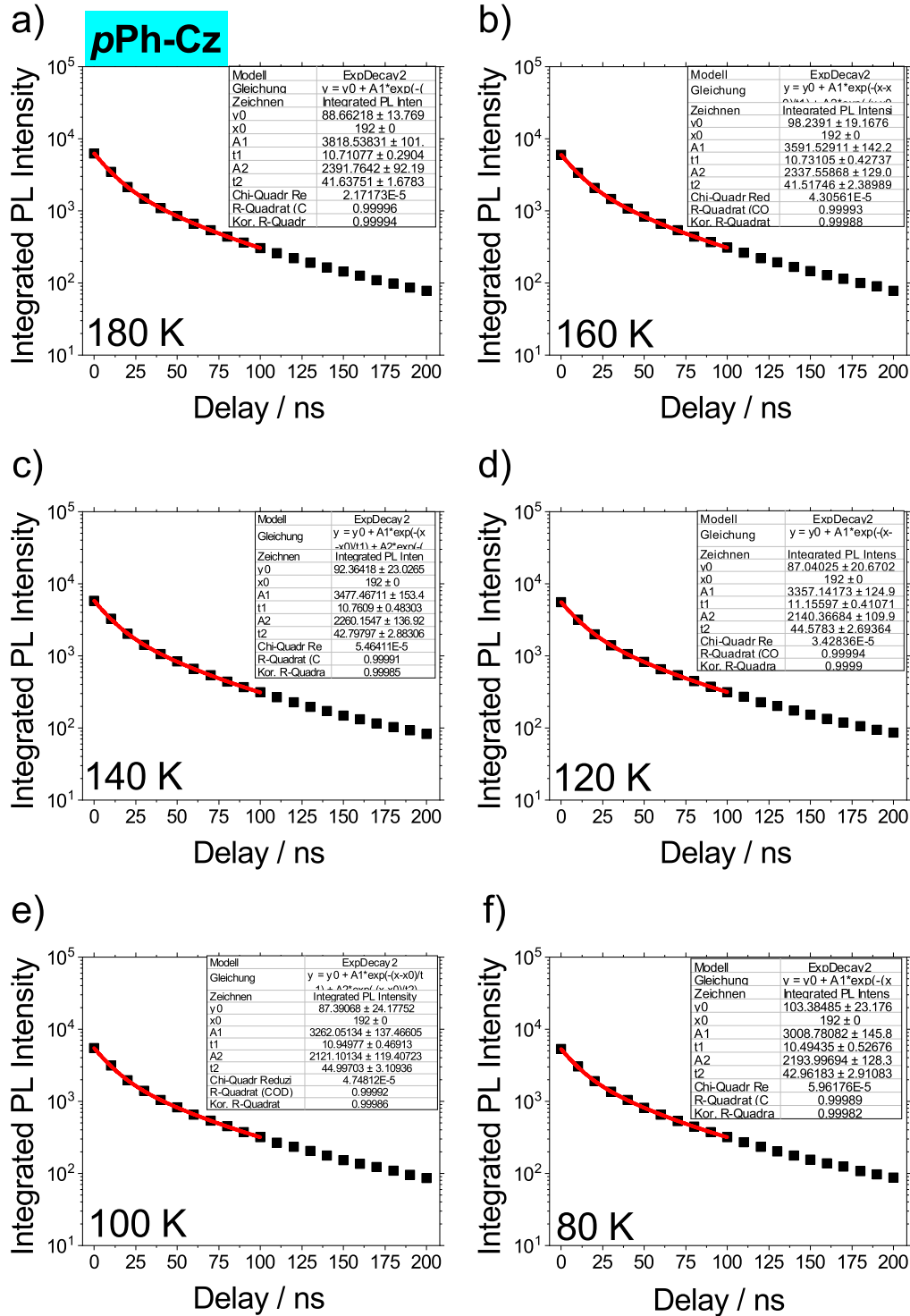


Figure 10.22: Time resolved prompt PL decay of 8wt% **pPh-Cz** in mCBP detected with a gate width of 100 ns. a) 180 K, b) 160 K, c) 140 K, d) 120 K, e) 100 K, f) 80 K. The fit parameters are summarized in Tab. 10.5.

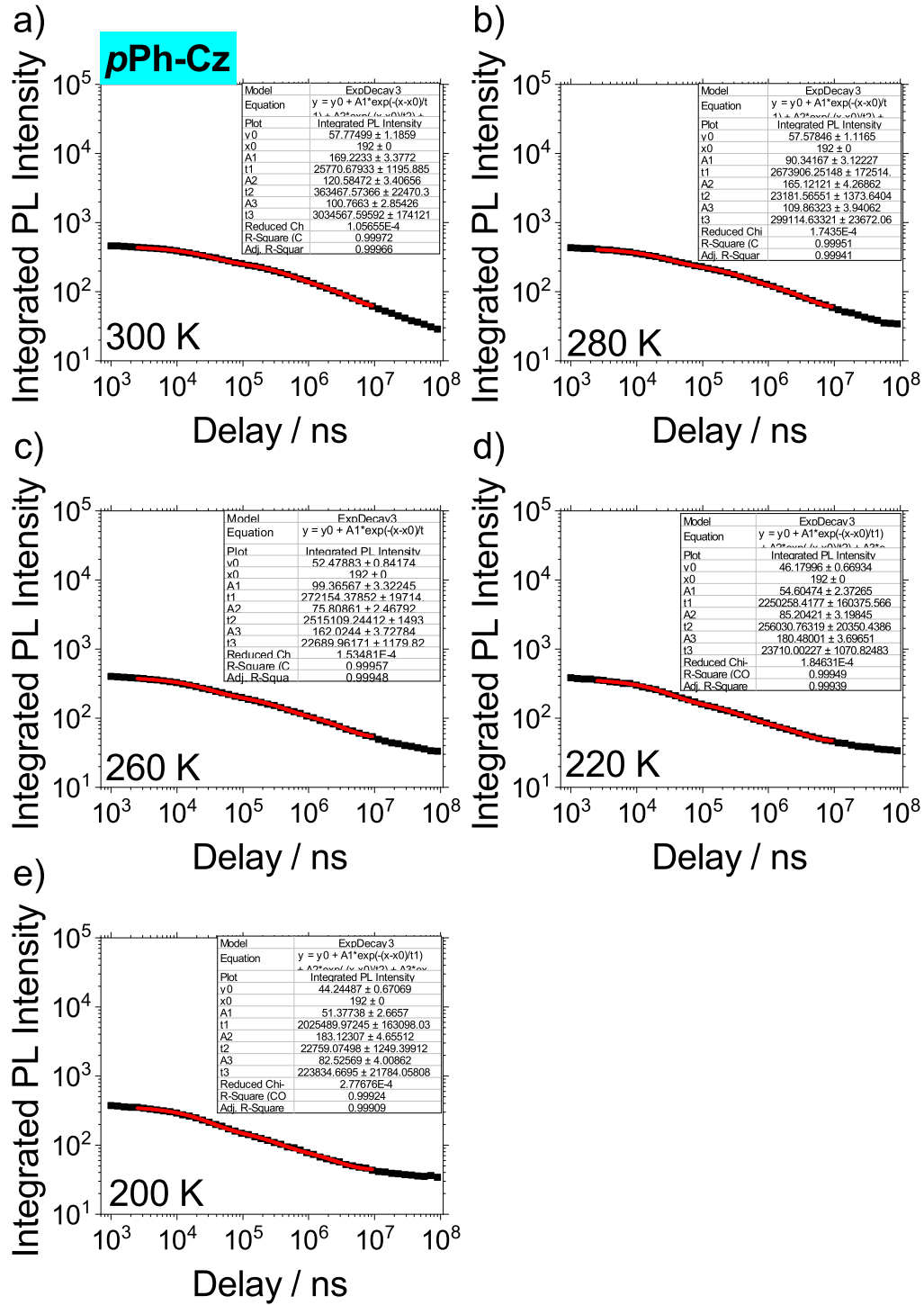


Figure 10.23: Time resolved delayed PL decay of 8wt% **pPh-Cz** in mCBP detected with a gate width of 1 ms. a) 300 K, b) 280 K, c) 260 K, d) 240 K, e) 220 K, f) 200 K. The fit parameters are summarized in Tab. 10.5.

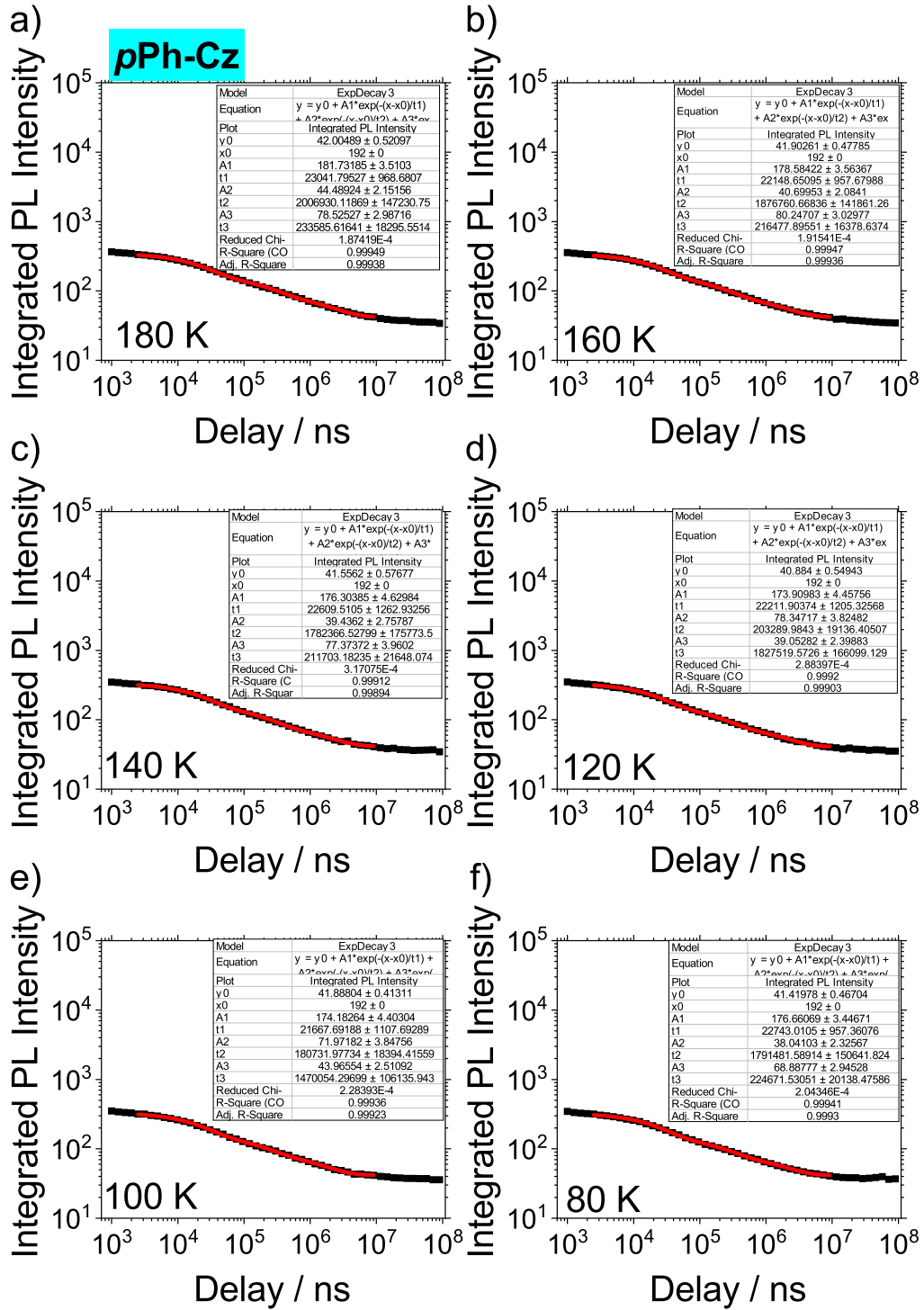


Figure 10.24: Time resolved delayed PL decay of 8wt% **pPh-Cz** in mCBP detected with a gate width of 1 ms. a) 180 K, b) 160 K, c) 140 K, d) 120 K, e) 100 K, f) 80 K. The fit parameters are summarized in Tab. 10.5.

Table 10.5: Fit parameter of PL decay for **pPh-Cz** in mCBP at different temperatures.
 τ_{prompt} , $\tau_{delayed}$ is the amplitude weighted average of the two/three decay times according to Eq. 9.2.

	prompt						
T	A1	t1	A2	t2			τ_{prompt}
K		ns		ns			ns
300	4006	8.78	3542	33.28			20.28
280	5284	11.85	2634	43.02			22.22
260	4591	11.14	2693	39.95			21.79
240	3634	8.41	3068	34.68			20.44
220	4110	10.71	2609	40.10			22.12
200	3905	10.91	2503	40.42			22.44
180	3819	10.71	2392	41.64			22.62
160	3592	10.73	2338	41.52			22.87
140	3477	10.76	2260	42.80			23.38
120	3357	11.16	2140	44.58			24.17
100	3262	10.95	2121	45.00			24.37
80	3009	10.49	2194	42.96			24.19
	delayed						
T	A1	t1	A2	t2	A3	t3	$\tau_{delayed}$
K		ns		ns		ns	ms
300	63	1.50E+07	205	3.60E+04	149	9.84E+05	2.62
280	132	8.10E+05	198	3.18E+04	56	1.21E+07	2.06
260	192	2.90E+04	49	1.02E+07	115	6.76E+05	1.63
220	35	8.21E+06	205	2.70E+04	95	5.33E+05	1.03
200	205	2.57E+04	88	4.35E+05	34	5.90E+06	0.75
180	33	4.70E+06	85	3.65E+05	200	2.37E+04	0.59
160	85	3.43E+05	196	2.35E+04	29	4.80E+06	0.56
140	29	4.08E+06	82	3.22E+05	193	2.35E+04	0.48
120	30	3.57E+06	82	2.90E+05	190	2.27E+04	0.45
100	194	2.28E+04	78	3.13E+05	29	3.41E+06	0.42
80	30	3.19E+06	75	2.97E+05	190	2.21E+04	0.41

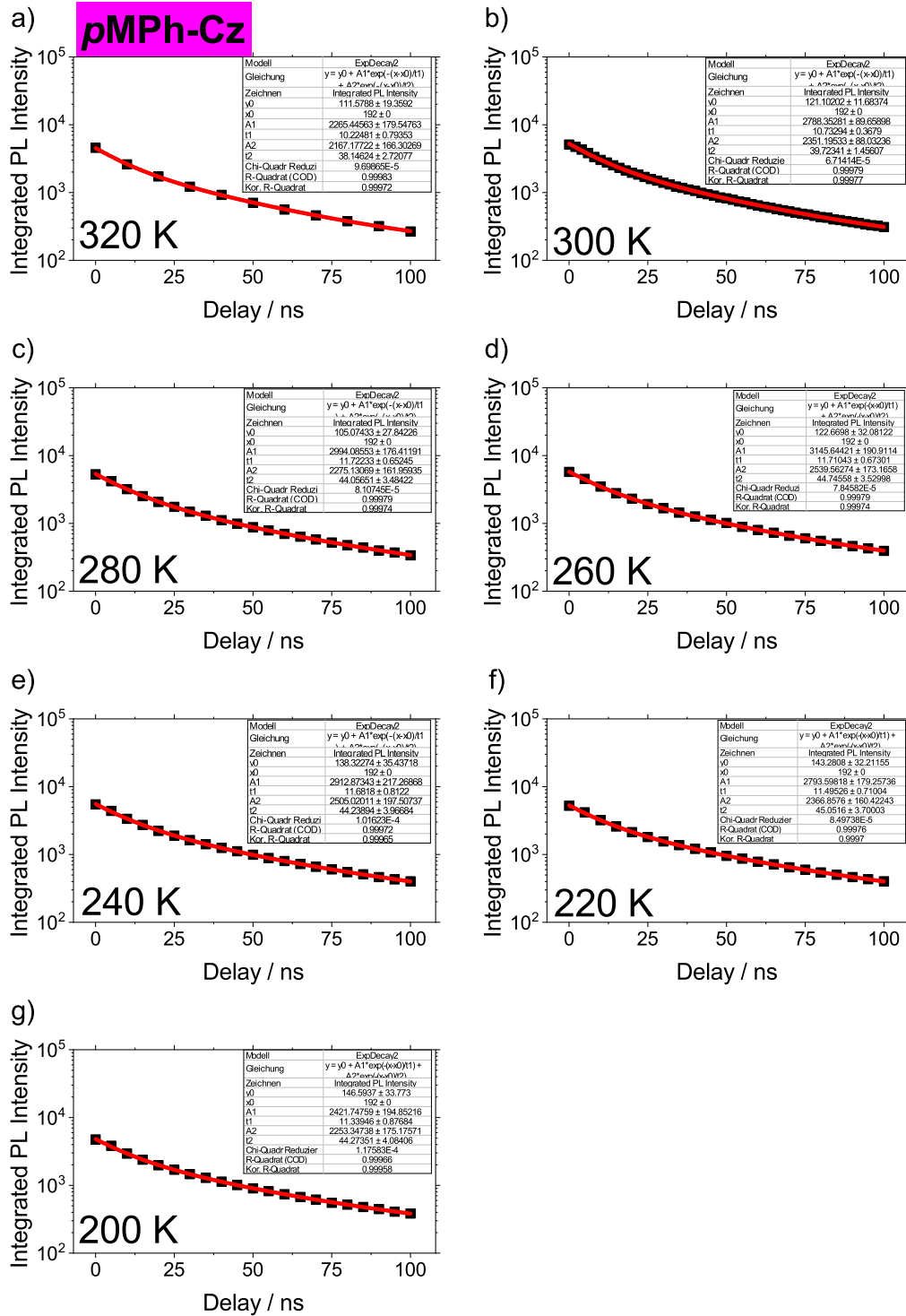


Figure 10.25: Time resolved prompt PL decay of 8wt% *p*MPh-Cz in mCBP detected with a gate width of 100 ns. a) 320 K, b) 300 K, c) 280 K, d) 260 K, e) 240 K, f) 220 K, g) 200 K. The fit parameters are summarized in Tab. 10.6.

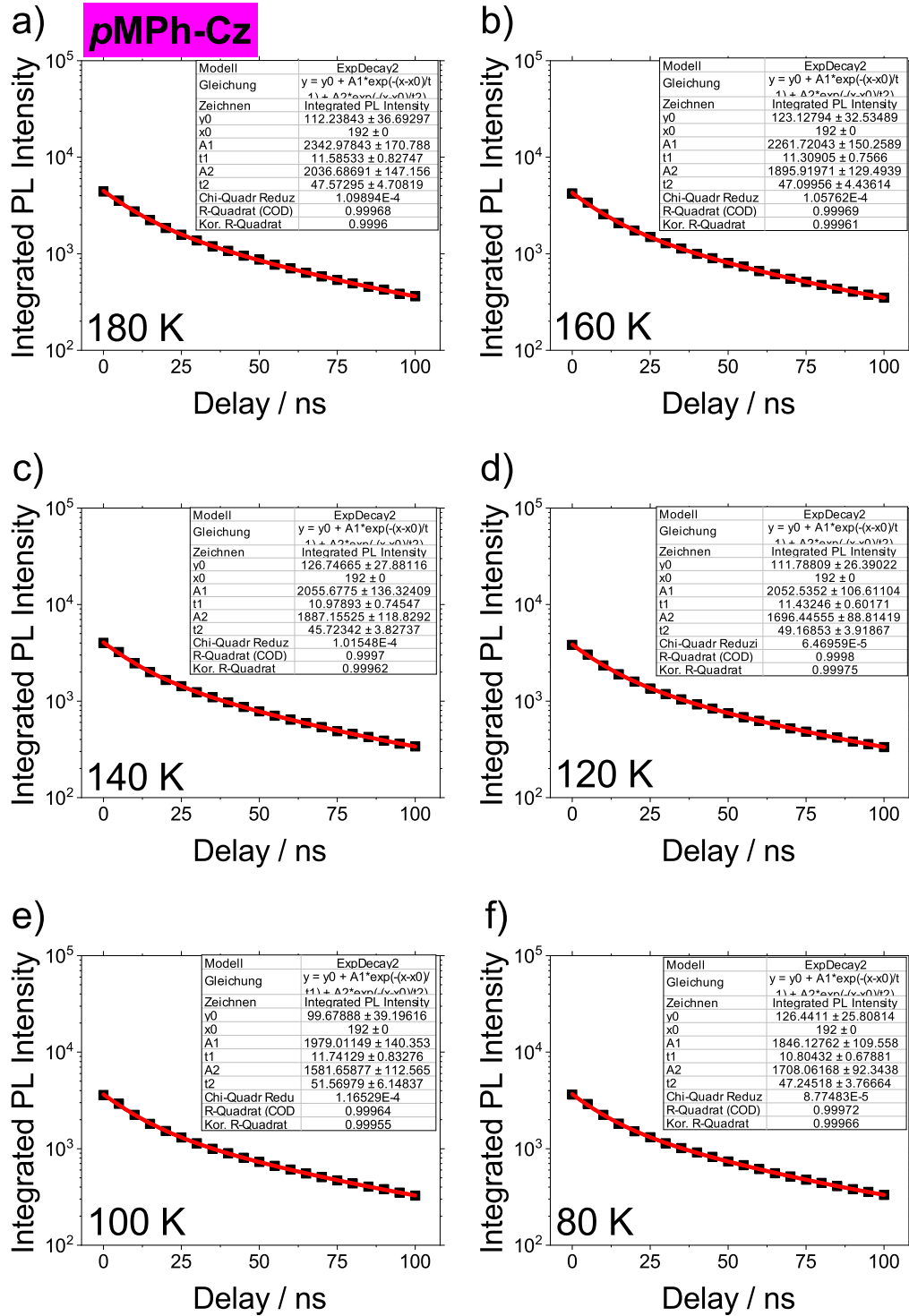


Figure 10.26: Time resolved prompt PL decay of 8wt% **pMPh-Cz** in mCBP detected with a gate width of 100 ns. a) 180 K, b) 160 K, c) 140 K, d) 120 K, e) 100 K, f) 80 K. The fit parameters are summarized in Tab. 10.6.

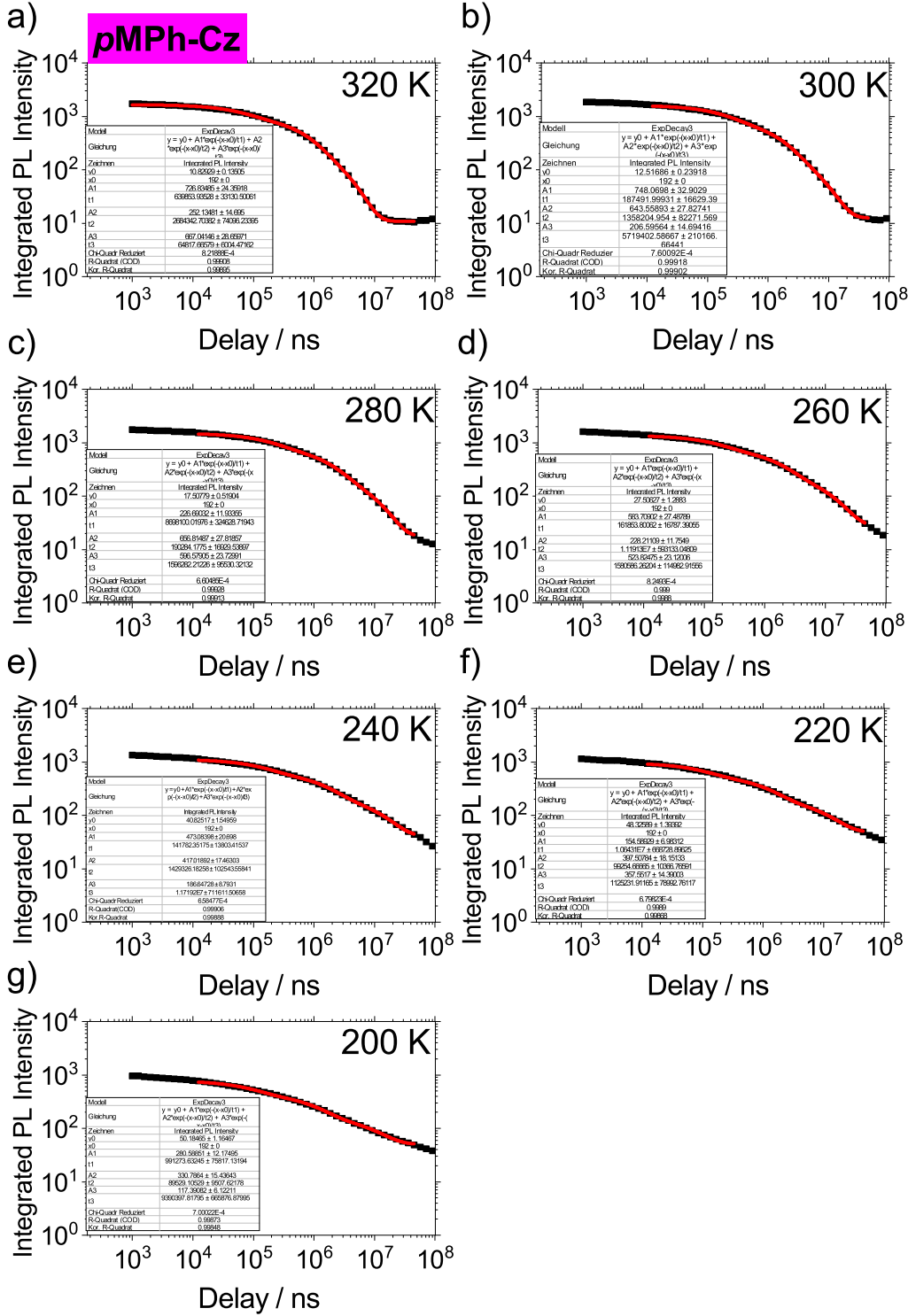


Figure 10.27: Time resolved delayed PL decay of 8wt% **pMPh-Cz** in mCBP detected with a gate width of 1 ms. a) 320 K, b) 300 K, c) 280 K, d) 260 K, e) 240 K, f) 220 K, g) 200 K. The fit parameters are summarized in Tab. 10.6.

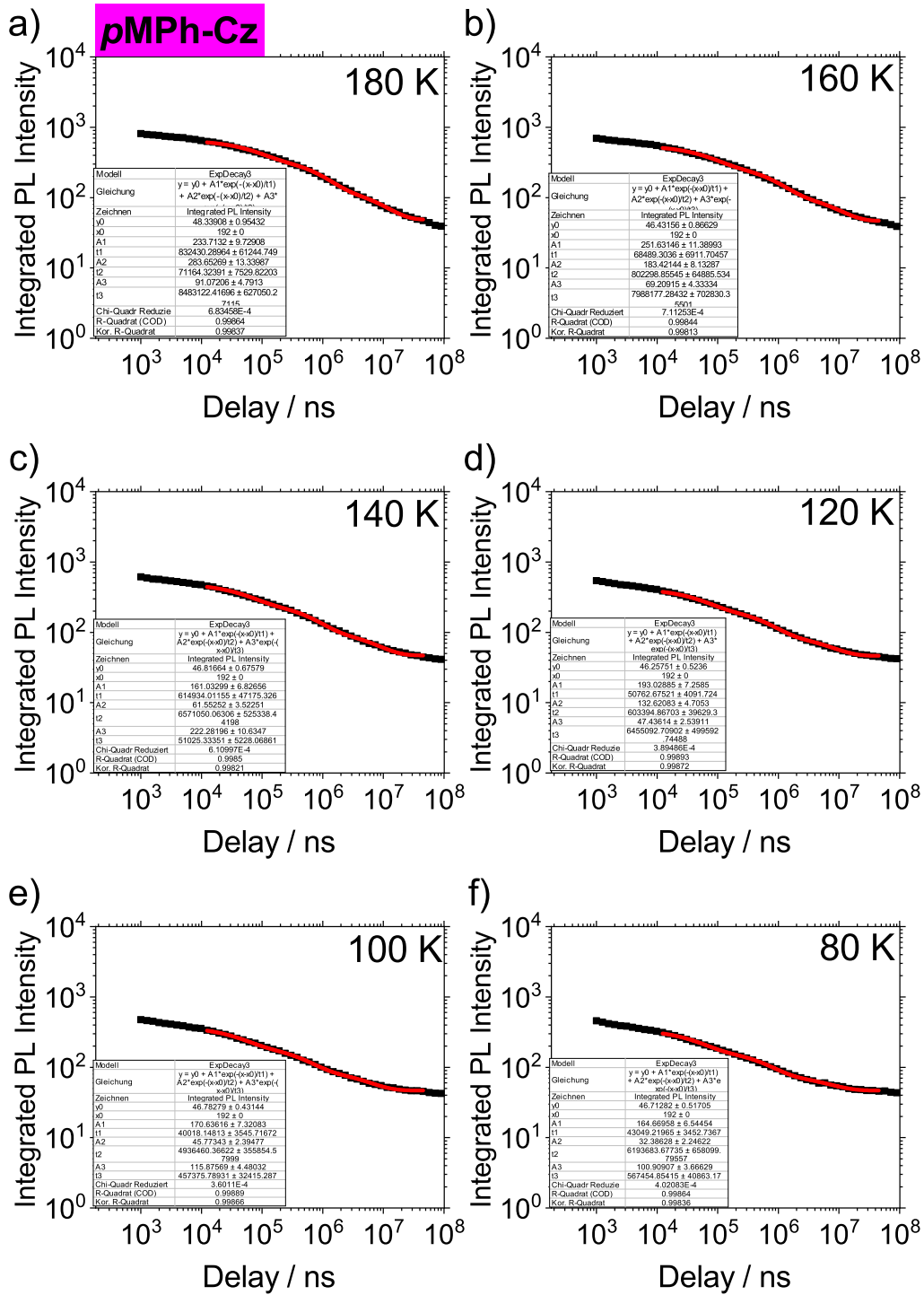


Figure 10.28: Time resolved delayed PL decay of 8wt% *p*MPh-Cz in mCBP detected with a gate width of 1 ms. a) 180 K, b) 160 K, c) 140 K, d) 120 K, e) 100 K, f) 80 K. The fit parameters are summarized in Tab. 10.6.

Table 10.6: Fit parameter of PL decay for *p*MPh-Cz in mCBP at different temperatures.
 τ_{prompt} , $\tau_{delayed}$ is the amplitude weighted average of the two/three decay times according to Eq. 9.2.

		prompt					
T	A1	t1	A2	t2			τ_{prompt}
K		ns		ns			ns
320	5597	10.22	2762	38.15			19.45
300	2788	10.73	2351	39.72			24.00
280	2994	11.72	2275	44.06			25.68
260	3146	11.71	2540	44.75			26.47
240	2913	11.68	2505	44.24			26.73
220	2794	11.50	2367	45.05			26.89
200	2422	11.34	2253	44.27			27.21
180	2343	11.59	2037	47.57			28.32
160	2262	11.31	1896	47.10			27.63
140	2056	10.98	1887	45.72			27.61
120	2053	11.43	1696	49.17			28.51
100	1979	11.74	1582	51.57			28.51
80	1846	10.80	1708	47.25			28.32
		delayed					
T	A1	t1	A2	t2	A3	t3	$\tau_{delayed}$
K		ns		ns		ns	ms
320	727	6.40E+05	252	2.68E+06	667	6.48E+04	0.72
300	748	1.87E+05	644	1.36E+06	207	5.72E+06	1.37
280	227	8.70E+06	657	1.90E+05	597	1.60E+06	2.06
260	584	1.62E+05	228	1.12E+07	524	1.58E+06	2.60
240	473	1.42E+05	417	1.43E+06	187	1.17E+07	2.65
220	155	1.06E+07	398	9.93E+04	358	1.13E+06	2.29
200	281	9.91E+05	331	8.95E+04	117	9.39E+06	1.93
180	234	8.32E+05	284	7.12E+04	91	8.48E+06	1.62
160	252	6.85E+04	183	8.02E+05	69	7.99E+06	1.42
140	161	6.15E+05	62	6.57E+06	222	5.10E+04	1.16
120	193	5.08E+04	133	6.03E+05	47	6.46E+06	1.06
100	171	4.00E+04	46	4.94E+06	116	4.57E+05	0.86
80	165	4.30E+04	32	6.19E+06	101	5.67E+05	0.89

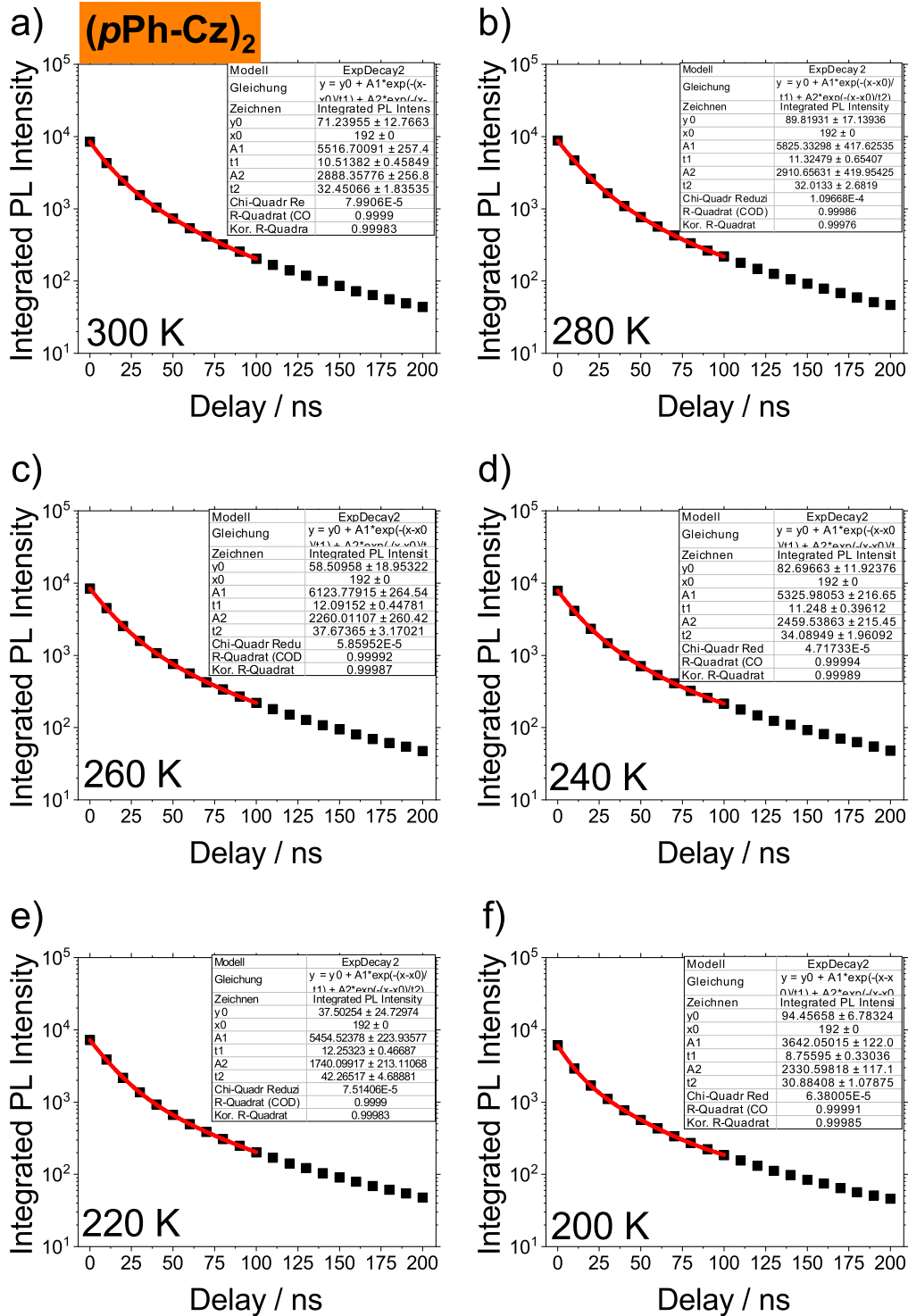


Figure 10.29: Time resolved prompt PL decay of 8wt% (pPh-Cz)₂ in mCBP detected with a gate width of 100 ns. a) 300 K, b) 280 K, c) 260 K, d) 240 K, e) 220 K, f) 200 K. The fit parameters are summarized in Tab. 10.7.

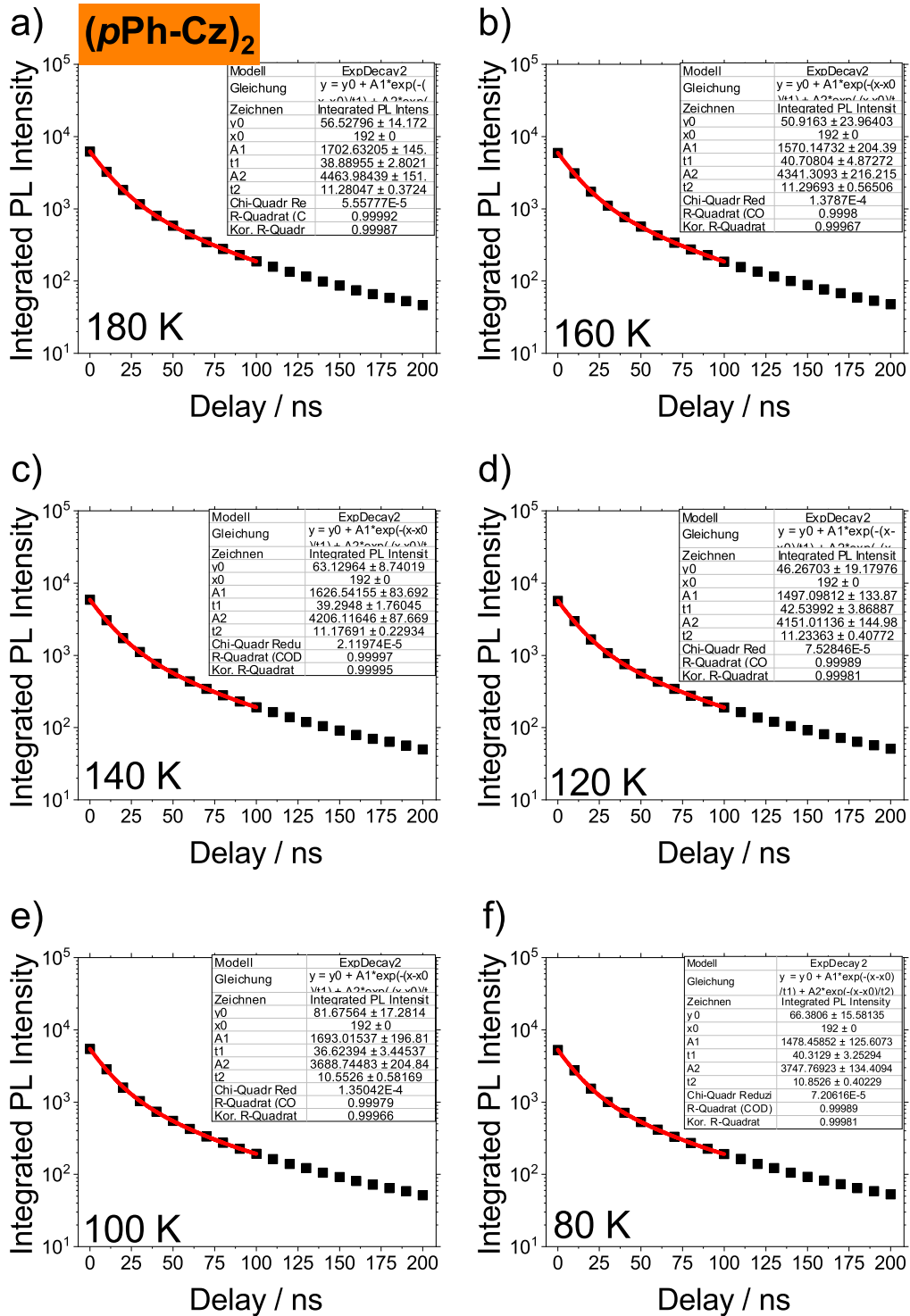


Figure 10.30: Time resolved prompt PL decay of 8wt% (pPh-Cz)₂ in mCBP detected with a gate width of 100 ns. a) 180 K, b) 160 K, c) 140 K, d) 120 K, e) 100 K, f) 80 K. The fit parameters are summarized in Tab. 10.7.

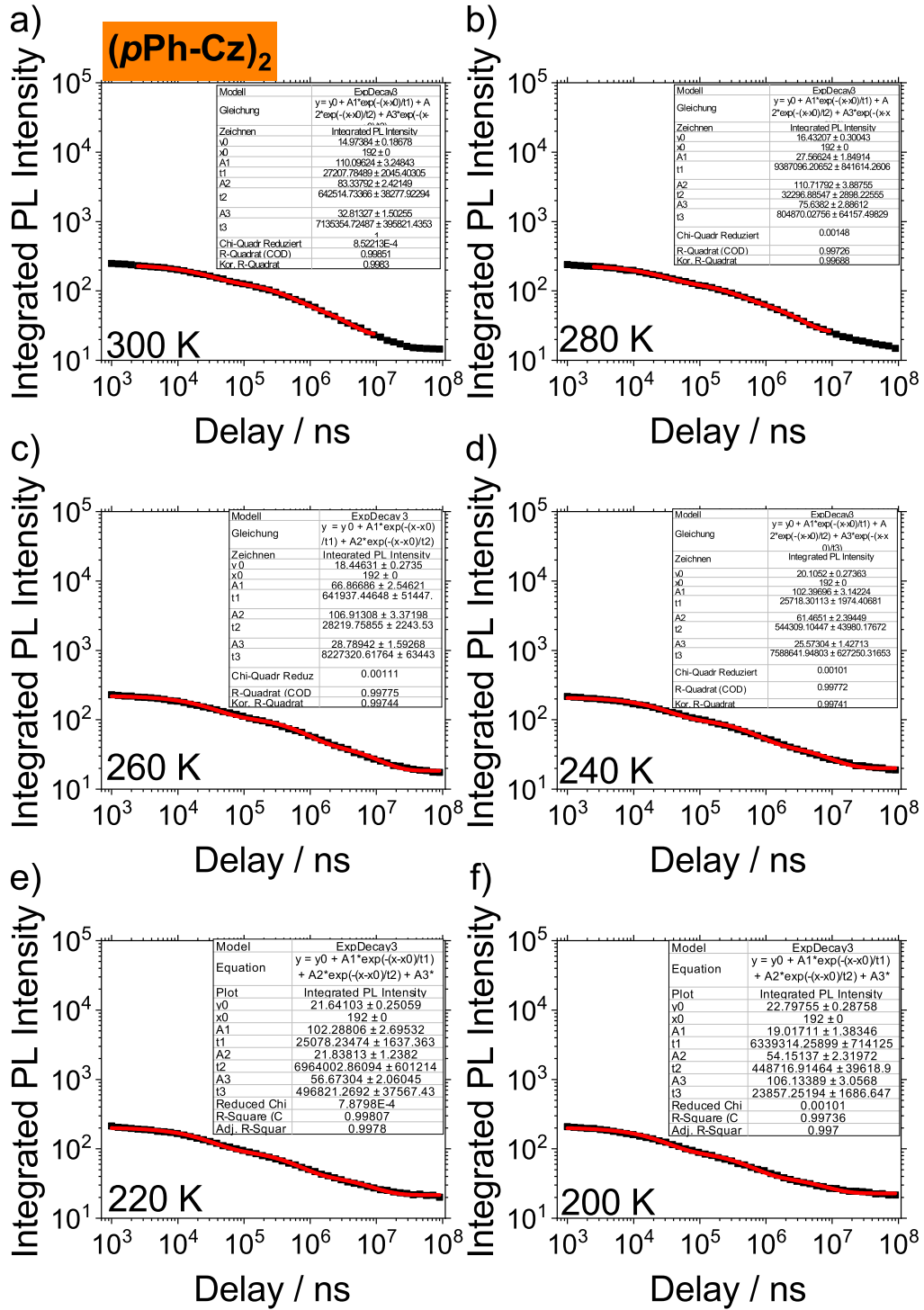


Figure 10.31: Time resolved delayed PL decay of 8wt% (pPh-Cz)₂ in mCBP detected with a gate width of 1 ms. a) 300 K, b) 280 K, c) 260 K, d) 240 K, e) 220 K, f) 200 K. The fit parameters are summarized in Tab. 10.7.

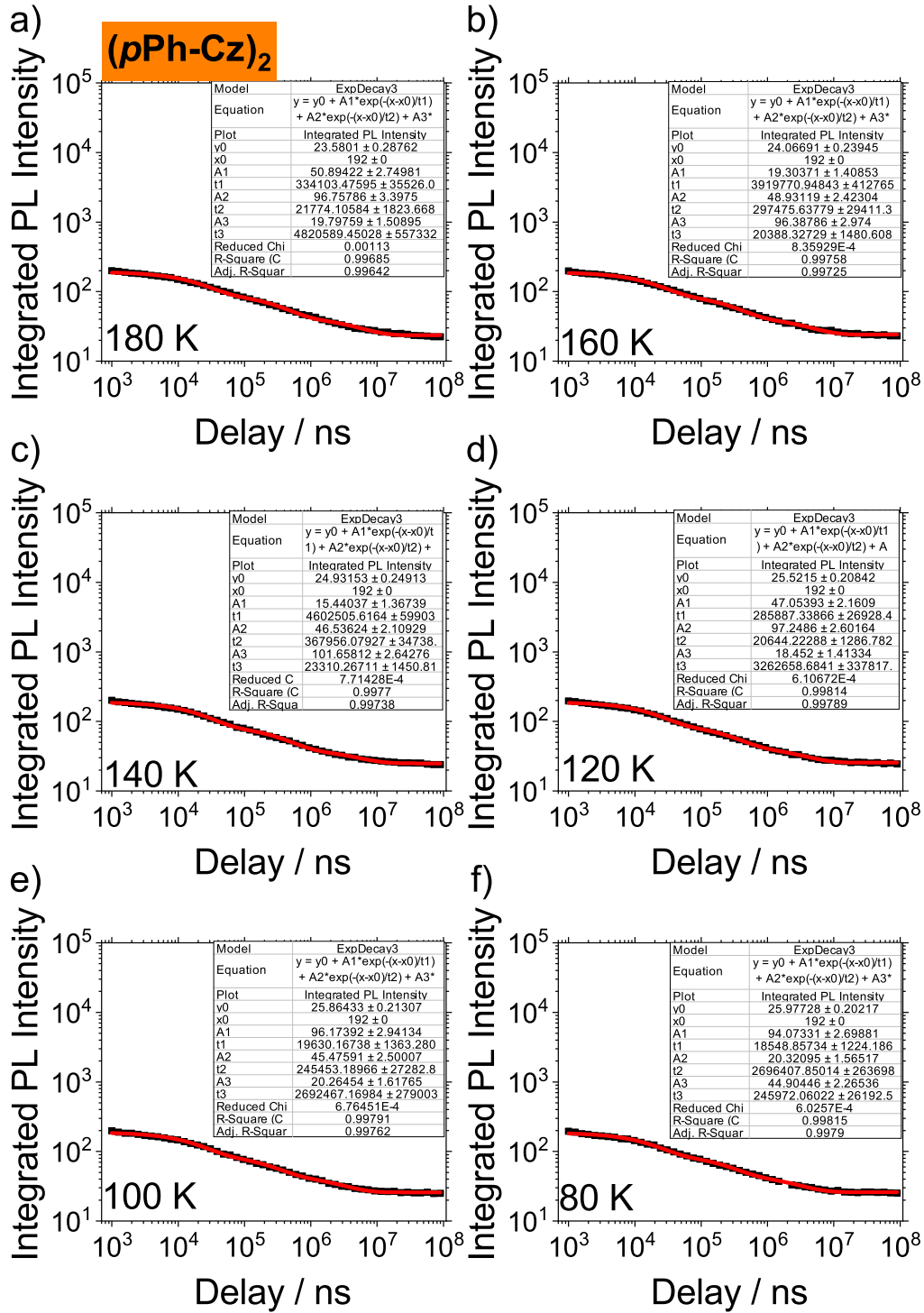


Figure 10.32: Time resolved delayed PL decay of 8wt% (pPh-Cz)₂ in mCBP detected with a gate width of 1 ms. a) 180 K, b) 160 K, c) 140 K, d) 120 K, e) 100 K, f) 80 K. The fit parameters are summarized in Tab. 10.7.

Table 10.7: Fit parameter of PL decay for (*p*Ph-Cz)₂ in mCBP at different temperatures.
 τ_{prompt} , $\tau_{delayed}$ is the amplitude weighted average of the two/three decay times according to Eq. 9.2.

prompt							
T	A1	t1	A2	t2			τ_{prompt}
K		ns		ns			ns
300	5517	10.51	2888	32.45			18.05
280	5825	11.32	2911	32.01			18.22
260	6124	12.09	2260	37.67			18.99
240	5326	11.25	2460	34.09			18.46
220	5455	12.25	1740	42.27			19.51
200	3642	8.76	2331	30.88			17.39
180	1703	38.89	4464	11.28			18.90
160	1570	40.71	4341	11.30			19.11
140	1627	39.29	4206	11.18			19.02
120	1497	42.54	4151	11.23			19.53
100	1693	36.62	3689	10.55			18.75
80	1478	40.31	3748	10.85			19.19
delayed							
T	A1	t1	A2	t2	A3	t3	$\tau_{delayed}$
K		ns		ns		ns	ms
300	110	2.72E+04	83	6.43E+05	33	7.14E+06	1.28
280	28	9.39E+06	111	3.23E+04	76	8.05E+05	1.51
260	67	6.42E+05	107	2.82E+04	29	8.23E+06	1.40
240	102	2.57E+04	61	5.44E+05	26	7.59E+06	1.21
220	102	2.51E+04	22	6.96E+06	57	4.97E+05	1.01
200	19	6.34E+06	54	4.49E+05	106	2.39E+04	0.82
180	51	3.34E+05	97	2.18E+04	20	4.82E+06	0.68
160	19	3.92E+06	49	2.97E+05	96	2.04E+04	0.56
140	15	4.60E+06	47	3.68E+05	102	2.33E+04	0.55
120	47	2.86E+05	97	2.06E+04	18	3.26E+06	0.46
100	96	1.96E+04	45	2.45E+05	20	2.69E+06	0.42
80	94	1.85E+04	20	2.70E+06	45	2.46E+05	0.42

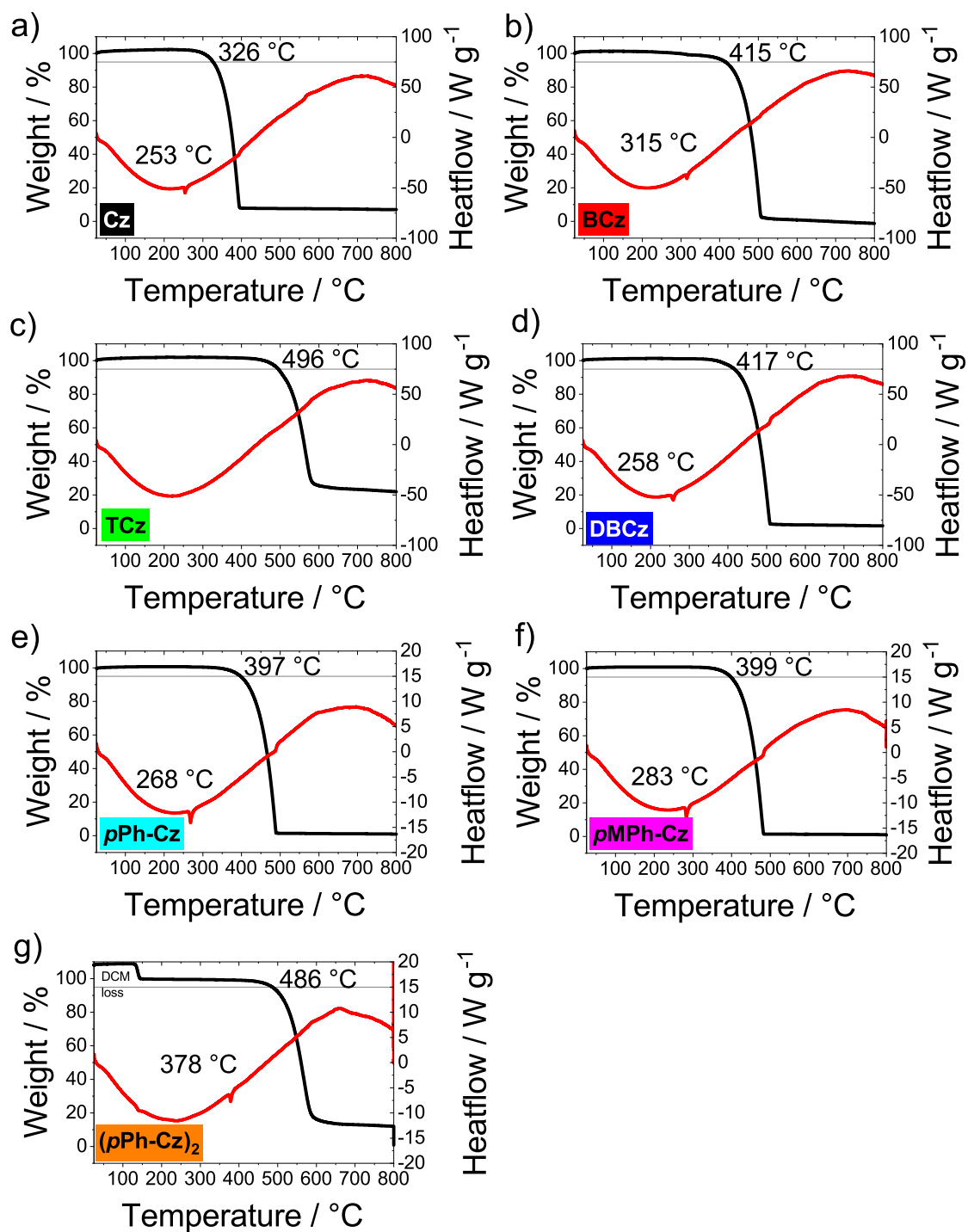


Figure 10.33: TGA-DSC with melting temperature T_m and decomposition temperature (5% weight loss) T_d : a) **Cz**, b) **BCz**, c) **TCz**, d) **DBCz**, e) **pPh-Cz**, f) **pMPh-Cz**, g) **(pPh-Cz)₂**.

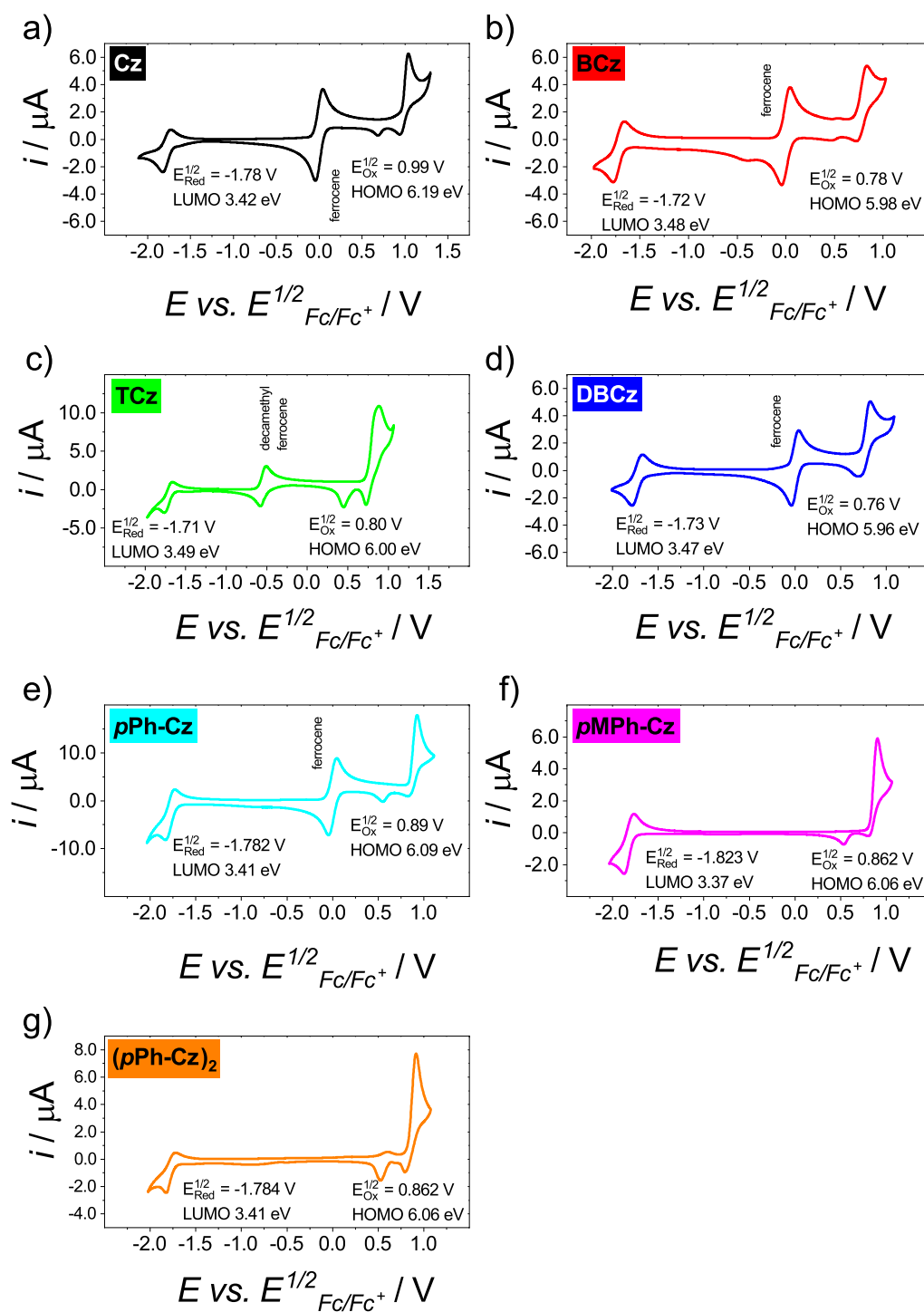


Figure 10.34: CV in DCM of a) Cz, b) BCz, c) TCz, d) DBCz, e) *p*Ph-Cz, f) *p*MPh-Cz, g) (*p*Ph-Cz)₂. The irreversible reduction signal between 0.7 and 0.4 V is attributed to dimerisation of carbazole units.^[106]

10.2.3 Supplementary Data for Chapter 6

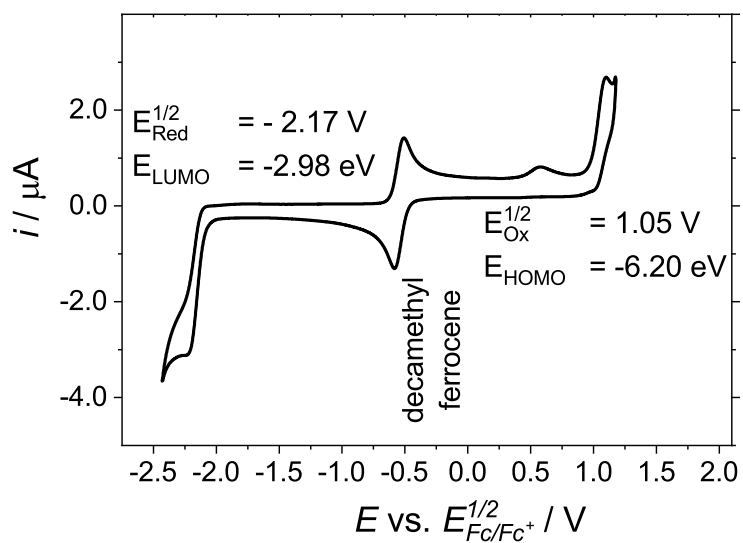


Figure 10.35: CV of NMAAdF in DCM with decamethyl ferrocene reference.

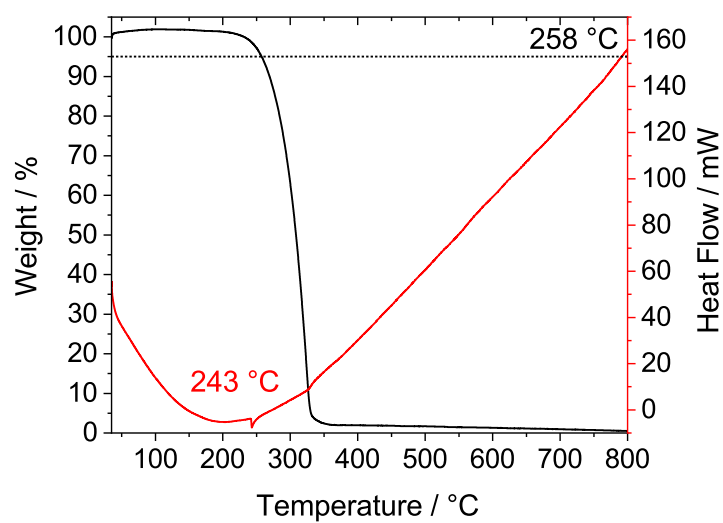


Figure 10.36: TGA/DSC of NMAAdF with $T_m=243^\circ\text{C}$ and $T_d=258^\circ\text{C}$ (5% weight loss).

10.2.4 Supplementary Data for Chapter 7

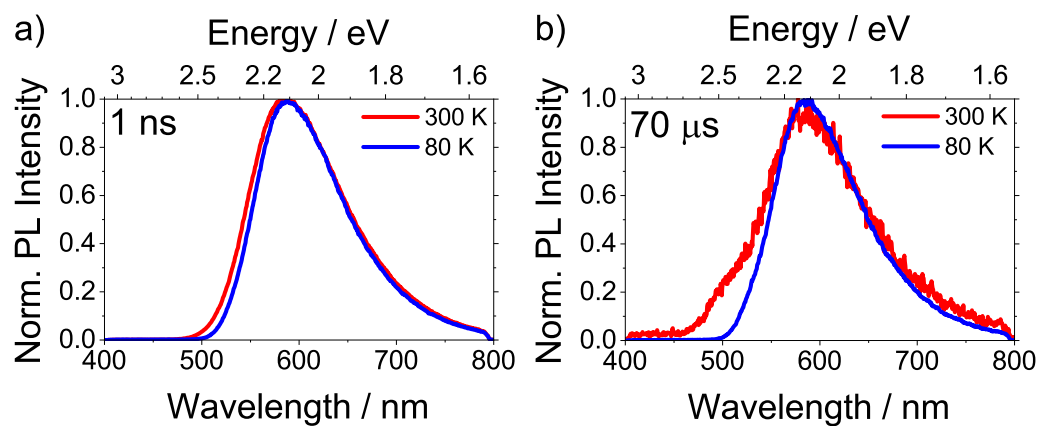


Figure 10.37: Normalized PL spectra of 6 wt% (*S*)-DHPZ-BTZ in mCBP at 300 K and 80 K at delay times of a) 10 ns (100 ns gate width) and b) 70 μ s (1 ms gate width).

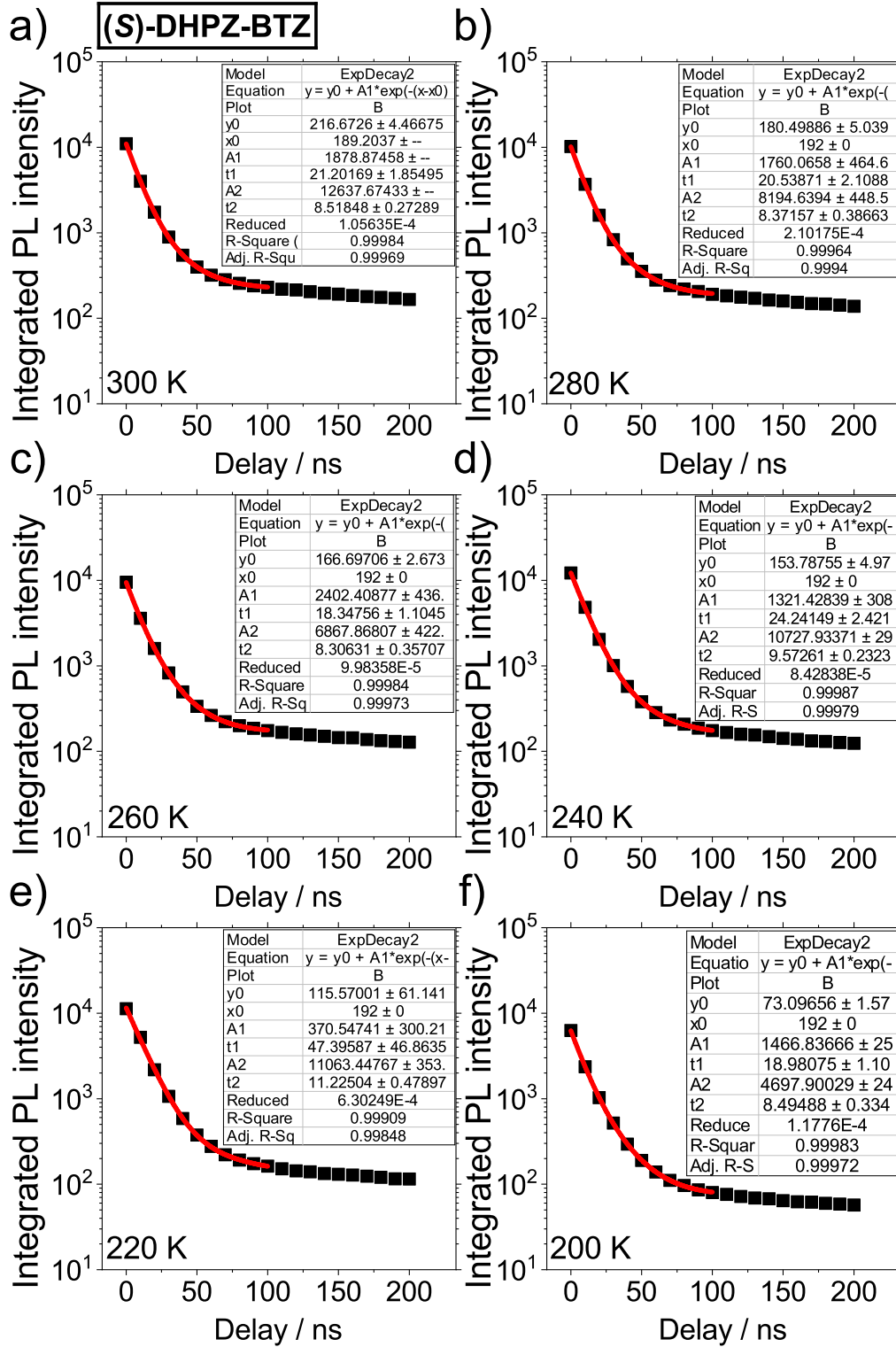


Figure 10.38: Time resolved prompt PL decay of 6wt% (S)-DHPZ-BTZ in mCBP detected with a gate width of 100 ns. a) 300 K, b) 280 K, c) 260 K, d) 240 K, e) 220 K, f) 200 K. The fit parameters are summarized in Tab. 10.8.

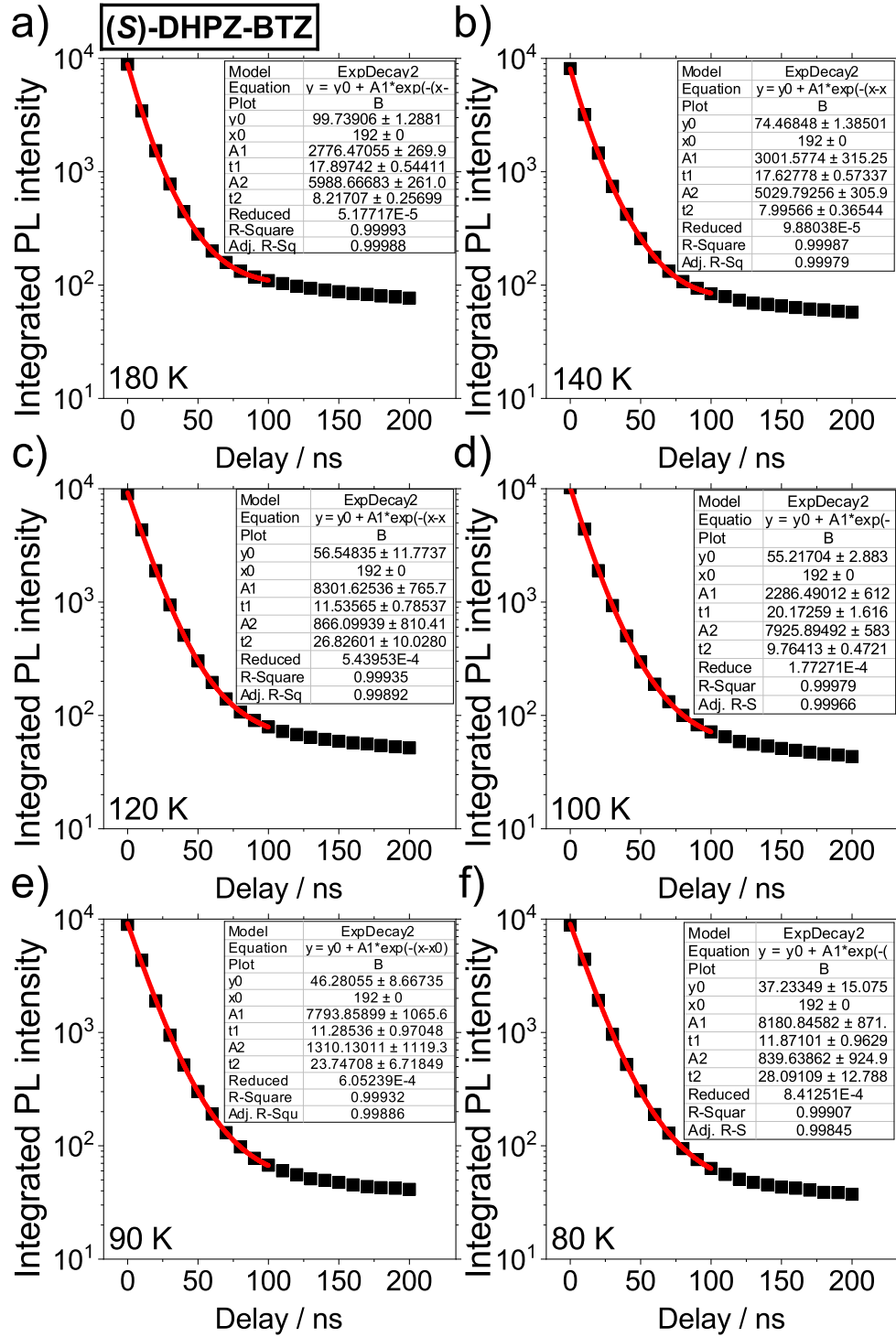


Figure 10.39: Time resolved prompt PL decay of 6wt% (S)-DHPZ-BTZ in mCBP detected with a gate width of 100 ns. a) 180 K, b) 140 K, c) 120 K, d) 100 K, e) 90 K, f) 80 K. The fit parameters are summarized in Tab.10.8.

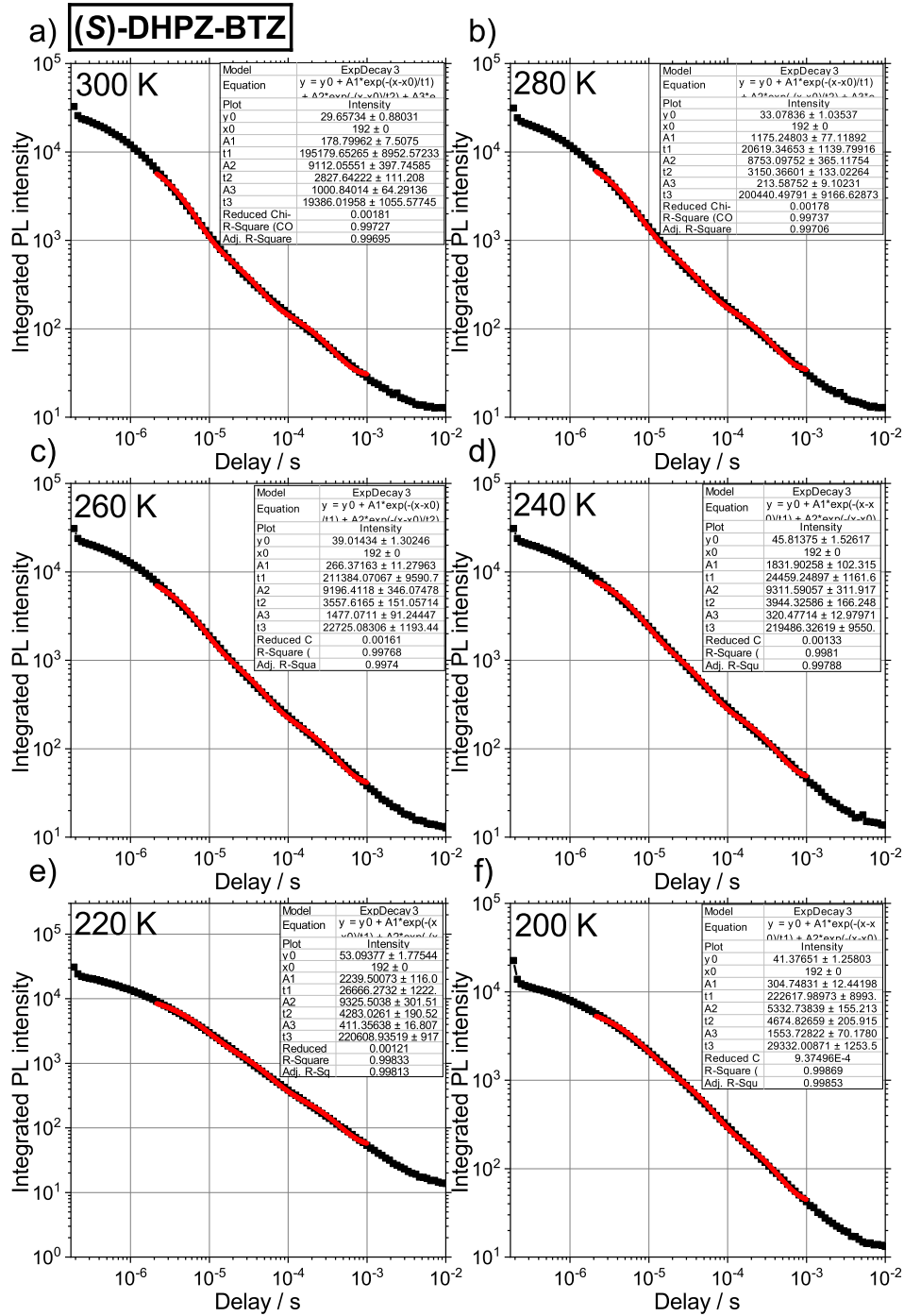


Figure 10.40: Time resolved delayed PL decay of 6wt% (S)-DHPZ-BTZ in mCBP detected with a gate width of 1 ms. a) 300 K, b) 280 K, c) 260 K, d) 240 K, e) 220 K, f) 200 K. The fit parameters are summarized in Tab.10.8.

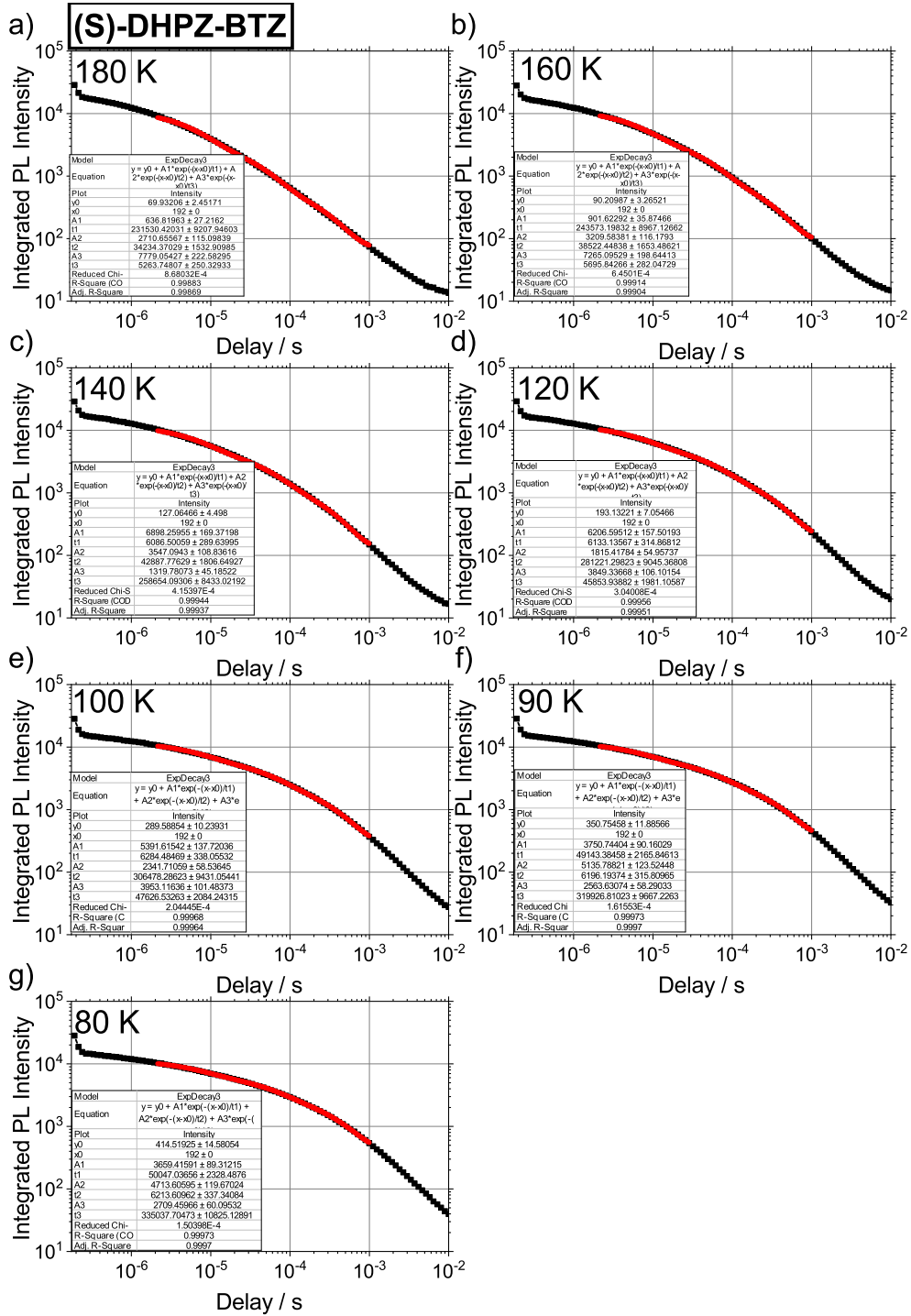


Figure 10.41: Time resolved delayed PL decay of 6wt% (S)-DHPZ-BTZ in mCBP detected with a gate width of 1 ms. a) 180 K, b) 160 K, c) 140 K, d) 120 K, e) 100 K, f) 90 K g) 80 K. The fit parameters are summarized in Tab.10.8.

Table 10.8: Fit parameter of PL decay for (*S*)-DHPZ-BTZ in mCBP at different temperatures. τ_{prompt} and $\tau_{delayed}$ is the amplitude weighted average of the two/three decay times according to Eq. 9.2.

prompt							τ_{prompt}
T	A1	t1	A2	t2			
K		ns		ns			ns
300	1879	21.20	12638	8.52			10.16
280	1760	20.54	8195	8.37			10.52
260	2402	18.35	6868	8.31			10.91
240	1321	24.24	10728	9.57			11.18
220	371	47.40	11063	11.23			12.40
200	1467	18.98	4698	8.49			10.99
180	2776	17.90	5989	8.22			11.28
160							
140	3002	17.63	5030	8.00			11.60
120	8302	11.54	866	26.83			12.98
100	2286	20.17	7926	9.76			12.09
90	7794	11.29	1310	23.75			13.08
80	8181	11.87	840	28.09			13.08
delayed							$\tau_{delayed}$
T	A1	t1	A2	t2	A3	t3	
K		ns		ns		ns	μs
300	179	1.95E+05	9112	2.83E+03	1001	1.94E+04	7.78
280	1175	2.06E+04	8753	3.15E+03	214	2.00E+05	9.33
260	266	2.11E+05	9196	3.56E+03	1477	2.27E+04	11.21
240	1832	2.45E+04	9312	3.94E+03	320	2.19E+05	13.25
220	2240	2.67E+04	9326	4.28E+03	411	2.21E+05	15.90
200	305	2.23E+05	5333	4.67E+03	1554	2.93E+04	19.24
180	637	2.32E+05	2711	3.42E+04	7779	5.26E+03	25.27
160	902	2.44E+05	3210	3.85E+04	7265	5.70E+03	33.81
140	6898	6.09E+03	3547	4.29E+04	1320	2.59E+05	45.51
120	6207	6.13E+03	1815	2.81E+05	3849	4.59E+04	61.08
100	5392	6.28E+03	2342	3.06E+05	3953	4.76E+04	80.42
90	3751	4.91E+04	5136	6.20E+03	2564	3.20E+05	90.51
80	3659	5.00E+04	4714	6.21E+03	2709	3.35E+05	101.08

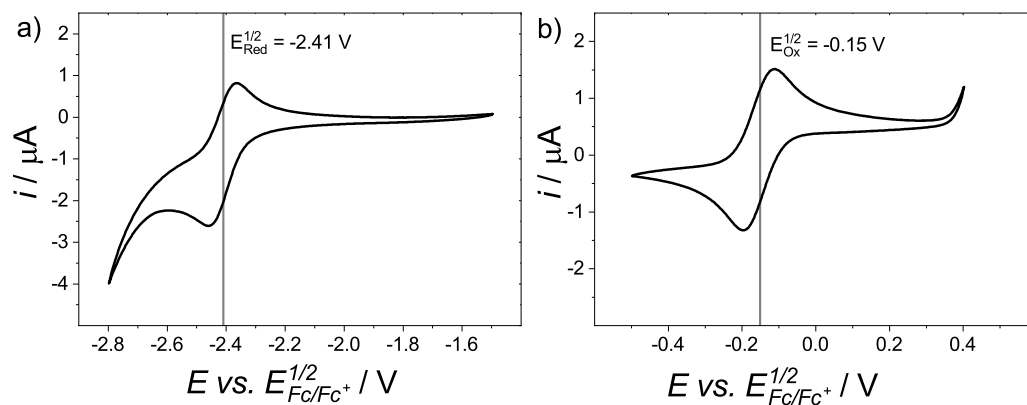


Figure 10.42: Cyclic voltammogram of (*S*)-DHPZ-BTZ (1 mmol L⁻¹ in THF at RT) with a) reduction and b) oxidation vs ferrocen/ferrocenium.

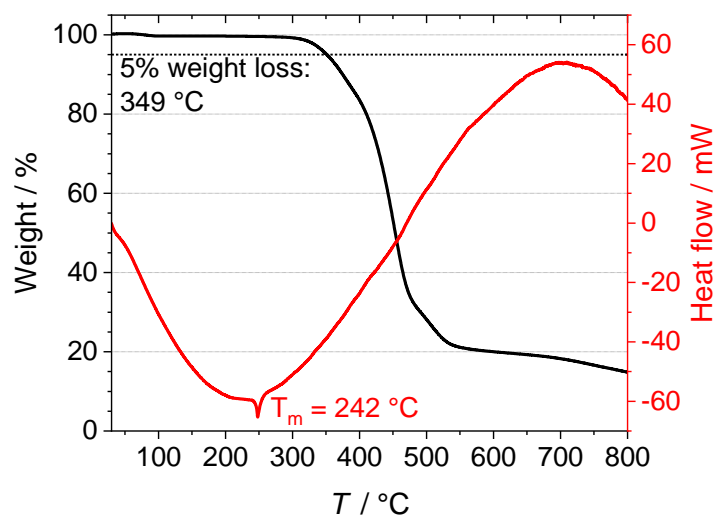


Figure 10.43: TGA/DSC of (*S*)-DHPZ-BTZ with $T_m = 243 ^\circ\text{C}$ and $T_d = 258 ^\circ\text{C}$

Bibliography

- [1] Bernanose, A.; Comte, M.; Vouaux, P. *J. Chim. Phys.* **1953**, *50*, 64–68.
- [2] Tang, C. W.; Vanslyke, S. A. *Appl. Phys. Lett.* **1987**, *51*, 913–915.
- [3] Burroughes, J. H.; Bradley, D. D. C.; Brown, A. R.; Marks, R. N.; Mackay, K.; Friend, R. H.; Burns, P. L.; Holmes, A. B. *Nature* **1990**, *347*, 539–541.
- [4] Baldo, M. A.; O'Brien, D. F.; You, Y.; Shoustikov, A.; Sibley, S.; Thompson, M. E.; Forrest, S. R. *Nature* **1998**, *395*, 1–12.
- [5] Baldo, M. A.; Lamansky, S.; Burrows, P. E.; Thompson, M. E.; Forrest, S. R. *Appl. Phys. Lett.* **1999**, *75*, 59–68.
- [6] Adachi, C.; Baldo, M. A.; Thompson, M. E.; Forrest, S. R. *J. Appl. Phys.* **2001**, *90*, 5048–5051.
- [7] Endo, A.; Ogasawara, M.; Takahashi, A.; Yokoyama, D.; Kato, Y.; Adachi, C. *Adv. Mater.* **2009**, *21*, 4802–4806.
- [8] Endo, A.; Sato, K.; Yoshimura, K.; Kai, T.; Kawada, A.; Miyazaki, H.; Adachi, C. *Appl. Phys. Lett.* **2011**, *98*, 1–3.
- [9] Uoyama, H.; Goushi, K.; Shizu, K.; Nomura, H.; Adachi, C. *Nature* **2012**, *492*, 234–238.
- [10] Köhler, A.; Bassler, H. *Electronic Processes in Organic Semiconductors*; Wiley-VCH Verlag GmbH: Weinheim, 2015; pp 1–414.
- [11] Hertel, D.; Müller, C. D.; Meerholz, K. *Chem. Unserer Zeit* **2005**, *39*, 336–347.
- [12] Deussen, M.; Bässler, H. *Chem. Unserer Zeit* **1997**, *31*, 76–86.
- [13] Nordheim, L. W.; Fowler, R. H. *Proc. R. Soc. Lond.* **1928**, *121*, 304–308.

- [14] Schottky, W. *Z. Phys.* **1939**, *113*, 367–414.
- [15] Simmons, J. G. *Phys. Rev. Lett.* **1965**, *15*, 967–968.
- [16] Arkhipov, V. I.; Wolf, U.; Bässler, H. *PhysRevB* **1999**, *59*, 7514–7520.
- [17] Wolf, U.; Arkhipov, V. I.; Bässler, H. *PhysRevB*. **1999**, *59*, 7507–7513.
- [18] Gartstein, Y. N.; Conwell, E. M. *Chem Phys Lett* **1995**, *245*, 351–358.
- [19] Bässler, H. *phys. stat. sol.* **1993**, *175*, 15–56.
- [20] Coropceanu, V.; Cornil, J.; da Silva Filho, D. A.; Olivier, Y.; Silbey, R.; Bredas, J. L. *Chem. Rev.* **2007**, *107*, 926–952.
- [21] Van Der Holst, J. J.; Van Oost, F. W.; Coehoorn, R.; Bobbert, P. A. *Phys. Rev. B Condens. Matter* **2009**, *80*, 1–8.
- [22] Atkins, P. W.; de Paula, J.; Keeler, J. J. *Physikalische Chemie*, 6th ed.; Wiley-VCH Verlag GmbH: Weinheim, 2021; pp 399–428.
- [23] Montalti, M.; Credi, A.; Prodi, L.; Gandolfi, M. T. *Handb. Photochem.*, 3rd ed.; Taylor and Francis Group: Boca Raton, FL, 2006; pp 1–632.
- [24] Franck, J.; Dymond, E. G. *Trans. Faraday Soc.* **1926**, *21*, 536–542.
- [25] Condon, E. *Phys. Rev.* **1926**, *28*, 1182–1201.
- [26] Jablonski, A. *Nature* **1933**, *131*, 839–840.
- [27] Kasha, M. *Discuss. Faraday Soc.* **1950**, *9*, 14–19.
- [28] Tétreault, N.; Muthyala, R. S.; Liu, R. S.; Steer, R. P. *J. Phys. Chem. A* **1999**, *103*, 2524–2531.
- [29] Veys, K.; Escudero, D. *Acc. Chem. Res.* **2022**, *55*, 2698–2707.
- [30] Parker, C. A.; Hatchard, C. G. *Trans. Faraday Soc.* **1961**, *57*, 1894–1904.
- [31] Parker, C. A.; Hatchard, C. G. *J. Phys. Chem.* **1962**, *66*, 2506–2511.
- [32] Parker, C. A.; Hatchard, C. G. *Trans. Faraday Soc.* **1963**, *59*, 284–295.

- [33] Hong, G.; Gan, X.; Leonhardt, C.; Zhang, Z.; Seibert, J.; Busch, J. M.; Bräse, S. *Adv. Mater.* **2021**, *33*, 1–24.
- [34] Baldo, M. A.; Thompson, M. E.; Forrest, S. R. *Nature* **2000**, *403*, 91–102.
- [35] Valeur, B.; Berberan-Santos, M. N. *Molecular Fluorescence -Principles and Applications*; Wiley-VCH Verlag and Co. KGaA: Weinheim, 2012; pp 1–569.
- [36] Förster, T. *Ann. Phys.* **1948**, *437*, 55–75.
- [37] Förster, T. *Discuss. Faraday Soc.* **1959**, *27*, 7–17.
- [38] Calcada, M.; Lunardi, J. T.; Manzoni, L. A.; Monteiro, W.; Pereira, M. *Front. Phys.* **2019**, *7*, 1–19.
- [39] Dexter, D. L. *J. Chem. Phys.* **1953**, *21*, 836–850.
- [40] Parker, C. A.; Hatchard, C. G. *Proc. R. Soc. Lond. A* **1962**, *269*, 574–584.
- [41] Baldo, M. A.; Adachi, C.; Forrest, S. R. *Phys. Rev. B* **2000**, *62*, 10967–10977.
- [42] Chou, P. Y.; Chou, H. H.; Chen, Y. H.; Su, T. H.; Liao, C. Y.; Lin, H. W.; Lin, W. C.; Yen, H. Y.; Chen, I. C.; Cheng, C. H. *Chem. Commun.* **2014**, *50*, 6869–6871.
- [43] Kuma, H.; Hosokawa, C. *Sci. Technol. Adv. Mater.* **2014**, *15*.
- [44] Engmann, S.; Barito, A. J.; Bittle, E. G.; Giebink, N. C.; Richter, L. J.; Gundlach, D. J. *Nat Commun* **2019**, *10*.
- [45] Brütting, W.; Adachi, C. *Physics of Organic Semiconductors*, 2nd ed.; Wiley-VCH Verlag and Co. KGaA: Weinheim, 2012; pp 1–634.
- [46] Kim, J. S.; Ho, P. K.; Greenham, N. C.; Friend, R. H. *J. Appl. Phys.* **2000**, *88*, 1073–1081.
- [47] Brütting, W.; Frischeisen, J.; Scholz, B. J.; Schmidt, T. D. *Eur. News* **2011**, *42*, 20–24.
- [48] Walzer, K.; Männig, B.; Pfeiffer, M.; Leo, K. *Chem. Rev.* **2007**, *107*, 1233–1271.
- [49] Huang, J.; Pfeiffer, M.; Werner, A.; Blochwitz, J.; Leo, K.; Liu, S. *Appl. Phys. Lett.* **2002**, *80*, 139–141.

- [50] Bender, V. C.; Marchesan, T. B.; Alonso, J. M. *IEEE Ind. Electron. Mag.* **2015**, *9*, 6–16.
- [51] Meerheim, R.; Lüssem, B.; Leo, K. *Proc. IEEE* **2009**, *97*, 1606–1626.
- [52] Olthof, S.; Meerholz, K. *Sci. Rep.* **2017**, *7*, 1–10.
- [53] Park, Y.; Choong, V.; Gao, Y.; Hsieh, B. R.; Tang, C. W. *Appl. Phys. Lett.* **1996**, *68*, 2699–2701.
- [54] Lee, S.; Lee, J. H.; Kim, K. H.; Yoo, S. J.; Kim, T. G.; Kim, J. W.; Kim, J. J. *Org. Electron.* **2012**, *13*, 2346–2351.
- [55] Shirota, Y. *J. Mater. Chem.* **2005**, *15*, 75–93.
- [56] Morgado, J.; Friend, R. H.; Cacialli, F. *Appl. Phys. Lett.* **2002**, *80*, 2436–2438.
- [57] He, Y.; Gong, S.; Hattori, R.; Kanicki, J. *Appl. Phys. Lett.* **1999**, *74*, 2265–2267.
- [58] Shi, J.; Tang, C. W. *Appl. Phys. Lett.* **1997**, *70*, 1665–1667.
- [59] Okumoto, K.; Kanno, H.; Hamaa, Y.; Takahashi, H.; Shibata, K. *Appl. Phys. Lett.* **2006**, *89*, 063504.
- [60] Li, W.; Zhang, X.; Zhang, Y.; Xu, K.; Xu, J.; Wang, H.; Li, H.; Guo, J.; Mo, J.; Yang, P. *Synth. Met.* **2018**, *245*, 111–115.
- [61] Moon, C. B.; Song, W.; Meng, M.; Kim, N. H.; Yoon, J. A.; Kim, W. Y.; Wood, R.; Mascher, P. *J. Lumin.* **2014**, *146*, 314–320.
- [62] Guo, Z.; Zhu, W.; Tian, H. *Chem. Commun* **2012**, *48*, 6073–6084.
- [63] Li, Y.; Zhou, L.; Cui, R.; Jiang, Y.; Zhao, X.; Liu, W.; Zhu, Q.; Cui, Y.; Zhang, H. *RSC Adv.* **2016**, *6*, 71282–71286.
- [64] Adachi, C.; Kwong, R.; Forrest, S. R. *Org. Electron.* **2001**, *2*, 37–43.
- [65] Nakanotani, H.; Masui, K.; Nishide, J.; Shibata, T.; Adachi, C. *Sci. Rep.* **2013**, *3*, 1–6.
- [66] Zhang, Q.; Li, B.; Huang, S.; Nomura, H.; Tanaka, H.; Adachi, C. *Nat. Photonics* **2014**, *8*, 326–332.

- [67] Zhang, Q.; Tsang, D.; Kuwabara, H.; Hatae, Y.; Li, B.; Takahashi, T.; Lee, S. Y.; Yasuda, T.; Adachi, C. *Adv. Mater.* **2015**, *27*, 2096–2100.
- [68] Holmes, R. J.; Forrest, S. R.; Tung, Y. J.; Kwong, R. C.; Brown, J. J.; Garon, S.; Thompson, M. E. *Appl. Phys. Lett.* **2003**, *82*, 2422–2424.
- [69] Gong, S.; He, X.; Chen, Y.; Jiang, Z.; Zhong, C.; Ma, D.; Qin, J.; Yang, C. *J. Mater. Chem.* **2012**, *22*, 2894–2899.
- [70] Zhang, J.; Ding, D.; Wei, Y.; Xu, H. *Chem. Sci.* **2016**, *7*, 2870–2882.
- [71] Shaheen, S. E.; Jabbour, G. E.; Morrell, M. M.; Kawabe, Y.; Kippelen, B.; Peyghambarian, N.; Nabor, M. F.; Schlaf, R.; Mash, E. A.; Armstrong, N. R. *J. Appl. Phys.* **1998**, *84*, 2324–2327.
- [72] Yang, X.; Mo, Y.; Yang, W.; Yu, G.; Cao, Y. *Appl. Phys. Lett.* **2001**, *79*, 563–565.
- [73] Piromreun, P.; Oh, H. S.; Shen, Y.; Malliaras, G. G.; Scott, J. C.; Brock, P. J. *Appl. Phys. Lett.* **2000**, *77*, 2403–2405.
- [74] Meerholz, K. *Nature* **2005**, *437*, 327–328.
- [75] Zacharias, P.; Gather, M. C.; Rojahn, M.; Nuyken, O.; Meerholz, K. *Angew. Chem. Int. Ed.* **2007**, *46*, 4388–4392.
- [76] Abbel, R.; Galagan, Y.; Groen, P. *Adv. Eng. Mater.* **2018**, *20*, 1–30.
- [77] Li, W.; Pan, Y.; Xiao, R.; Peng, Q.; Zhang, S.; Ma, D.; Li, F.; Shen, F.; Wang, Y.; Yang, B.; Ma, Y. *Adv. Funct. Mater.* **2014**, *24*, 1609–1614.
- [78] Yao, L.; Zhang, S.; Wang, R.; Li, W.; Shen, F.; Yang, B.; Ma, Y. *Angew. Chem.* **2014**, *126*, 2151–2155.
- [79] Fu, C.; Luo, S.; Li, Z.; Ai, X.; Pang, Z.; Li, C.; Chen, K.; Zhou, L.; Li, F.; Huang, Y.; Lu, Z. *Chem. Commun.* **2019**, *55*, 6317–6320.
- [80] Tian, X.; Sheng, J.; Zhang, S.; Xiao, S.; Gao, Y.; Liu, H.; Yang, B. *Molecules* **2021**, *26*.
- [81] Xu, Y.; Xu, P.; Hu, D.; Ma, Y. *Chem. Soc. Rev.* **2021**, *50*, 1030–1069.

- [82] Wiefermann, J.; Schmeinck, P.; Ganter, C.; Müller, T. J. *Chem. Eur. J.* **2022**, *28*, 1–9.
- [83] Wiefermann, J.; Kaminski, J. M.; Pankert, E.; Hertel, D.; Meerholz, K.; Marian, C. M.; Müller, T. J. *ChemPhotoChem* **2023**, *7*, 2–7.
- [84] Alba, C.; Busse, L. E.; List, D. J.; Angell, C. A. *J. Chem. Phys.* **1990**, *92*, 617–624.
- [85] Ginzburg, B. M.; Tuichiev, S. *Russ. J. Appl. Chem.* **2009**, *82*, 1178–1187.
- [86] Migulin, V. A.; Lvov, A. G.; Krayushkin, M. M. *Tetrahedron* **2017**, *73*, 4439–4449.
- [87] Mandanici, A.; Cutroni, M.; Triolo, A.; Rodriguez-Mora, V.; Ramos, M. A. *J. Chem. Phys.* **2006**, *125*.
- [88] Pina, J.; Sarmiento, D.; Accoto, M.; Gentili, P. L.; Vaccaro, L.; Galvão, A.; Seixas De Melo, J. S. *J. Phys. Chem. B* **2017**, *121*, 2308–2318.
- [89] Nielsen, A. I.; Christensen, T.; Jakobsen, B.; Niss, K.; Olsen, N. B.; Richert, R.; Dyre, J. C. *J. Chem. Phys.* **2009**, *130*.
- [90] Lebedeva, N. P.; Boon-Brett, L. *J. Electrochem. Soc.* **2016**, *163*, A821–A830.
- [91] Goes, M. Photo- and Electroluminescence Generated by Intramolecular Charge Transfer. Ph.D. thesis, Universiteit van Amsterdam, 2002.
- [92] Zoon, P. D.; Brouwer, A. M. *Photochem. Photobiol. Sci.* **2009**, *8*, 345–353.
- [93] Suppan, P.; Tsiamis, C. *J. Chem. Soc., Faraday Trans. 2* **1981**, *77*, 1553–1562.
- [94] Zoon, P. D. Fluorescent Probe Molecules with Individual Detection Capability. Ph.D. thesis, University of Amsterdam, 2009.
- [95] Munshi, M. U.; Berden, G.; Martens, J.; Oomens, J. *Phys. Chem. Chem. Phys.* **2017**, *19*, 19881–19889.
- [96] Yang, Z.; Mao, Z.; Xie, Z.; Zhang, Y.; Liu, S.; Zhao, J.; Xu, J.; Chi, Z.; Aldred, M. P. *Chem. Soc. Rev.* **2017**, *46*, 915–1016.
- [97] Im, Y.; Kim, M.; Cho, Y. J.; Seo, J. A.; Yook, K. S.; Lee, J. Y. *Chem. Mater.* **2017**, *29*, 1946–1963.

- [98] Liu, Y.; Li, C.; Ren, Z.; Yan, S.; Bryce, M. R. *Nat. Rev. Mater.* **2018**, *3*.
- [99] Li, M.; Liu, Y.; Duan, R.; Wei, X.; Yi, Y.; Wang, Y.; Chen, C. F. *Angew. Chemie - Int. Ed.* **2017**, *56*, 8818–8822.
- [100] Gonda, Z.; Földesi, T.; Nagy, B.; Novák, Z. *Synth.* **2022**, *54*, 3771–3784.
- [101] Zhang, Y.; Wu, Y.; Mao, Z.; Yang, Z.; Jiang, X.; Liu, S.; Yang, Z.; Chi, Z.; Xu, J. Organic room-temperature phosphorescent material containing imide structure, and preparing method and application thereof. Sun Yat-Sen University, China. Patent: CN-111303010. 2020.
- [102] Liu, X.; Wang, Y. F.; Li, M.; Zhu, Y.; Chen, C. F. *Org. Electron.* **2021**, *88*, 106017.
- [103] Feng, Q.; Rao, J.; Wang, H.; Ma, J.; Yu, F.; Zhang, Y.; Wang, B.; Zhang, J.; Cao, H.; Wang, H.; Peng, X.; Yang, L.; Xie, L. *Chem. Eng. J.* **2023**, *471*, 144352.
- [104] Xie, Linghai; Zheng, Xiaojun; Feng, Quanyou; Zhou, Tao; Wang, Hongjian; Qian, Y. Preparation method of fluorene-based thermally activated delayed fluorescent material, and its application in OLED. Nanjing University of Posts and Telecommunications, China. Patent: CN113214229. 2021.
- [105] Sommer, G. A.; Mataranga-Popa, L. N.; Czerwieniec, R.; Hofbeck, T.; Homier, H. H.; Müller, T. J.; Yersin, H. *J. Phys. Chem. Lett.* **2018**, *9*, 3692–3697.
- [106] Karon, K.; Lapkowski, M. *J. Solid State Electrochem.* **2015**, *19*, 2601–2610.
- [107] Thom, K. A.; Wieser, F.; Diestelhorst, K.; Reiffers, A.; Czekelius, C.; Kleinschmidt, M.; Bracker, M.; Marian, C. M.; Gilch, P. *J. Phys. Chem. Lett.* **2021**, *12*, 5703–5709.
- [108] Ziegenbein, C. T.; Fröbel, S.; Glöß, M.; Nobuyasu, R. S.; Data, P.; Monkman, A.; Gilch, P. *ChemPhysChem* **2017**, *18*, 2314–2317.
- [109] Ren, X.; Li, J.; Holmes, R. J.; Djurovich, P. I.; Forrest, S. R.; Thompson, M. E. *Chem. Mater.* **2004**, *16*, 4743–4747.
- [110] Jeon, S. O.; Jang, S. E.; Son, H. S.; Lee, J. Y. *Adv. Mater.* **2011**, *23*, 1436–1441.
- [111] Sun, D.; Ren, Z.; Bryce, M. R.; Yan, S. *J. Mater. Chem. C* **2015**, *3*, 9496–9508.

- [112] Huang, S.; Ling, X.; Liang, L.; Song, Y.; Fang, W.; Zhang, J.; Kong, J.; Meunier, V.; Dresselhaus, M. S. *Nano Lett.* **2015**, *15*, 2892–2901.
- [113] Kotadiya, N. B.; Lu, H.; Mondal, A.; Ie, Y.; Andrienko, D.; Blom, P. W.; Wetzel, G. J. A. *Nat. Mater.* **2018**, *17*, 329–334.
- [114] Püschel, D.; Wiefermann, J.; Hédé, S.; Heinen, T.; Pfeifer, L.; Weingart, O.; Suta, M.; Müller, T. J.; Janiak, C. *J. Mater. Chem.* **2023**, *11*, 8982–8991.
- [115] Lee, J.; Shizu, K.; Tanaka, H.; Nakanotani, H.; Yasuda, T.; Kaji, H.; Adachi, C. *J. Mater. Chem. C* **2015**, *3*, 2175–2181.
- [116] ying Fu, H.; dong Gao, X.; yu Zhong, G.; yang Zhong, Z.; Xiao, F.; xian Shao, B. *J. Lumin.* **2009**, *129*, 1207–1214.
- [117] Chen, C. H.; Tang, C. W. *Appl. Phys. Lett.* **2001**, *79*, 3711–3713.
- [118] Wu, I. W.; Chen, Y. H.; Wang, P. S.; Wang, C. G.; Hsu, S. H.; Wu, C. I. *Appl. Phys. Lett.* **2010**, *96*.
- [119] Nishita, N.; Okada, H. Organic electroluminescent elements with luminescent layers employing multiple hosts and buffer layers including charge-trapping materials. Fuji Photo Film Co., Ltd., Japan. Patent: US-20070057630. 2007.
- [120] Aonuma, M.; Oyamada, T.; Sasabe, H.; Miki, T.; Adachi, C. *Appl. Phys. Lett.* **2007**, *90*, 1–4.
- [121] Chang, C. H.; Hsu, M. K.; Wu, S. W.; Chen, M. H.; Lin, H. H.; Li, C. S.; Pi, T. W.; Chang, H. H.; Chen, N. P. *Phys.Chem.Chem.Phys.* **2015**, *17*, 13123–13128.

Personal Bibliography

Journal Articles

J. Wiefermann, J. M. Kaminski, E. Pankert, D. Hertel, K. Meerholz, C. M. Marian, T. J. J. Müller. *Highly Luminescent Blue Emitter with Balanced Hybridized Locally and Charge-Transfer Excited-States Emission*, ChemPhotoChem 2023, 7.

Conference Contributions

E. Pankert, C. Wallerius, F. Scharbert, D. Hertel K. Meerholz. *Transition from TADF to Room Temperature Phosphorescence: Finetuning of Donor-Acceptor Molecules*. ICEL, Kyoto, Japan, 2024. (Poster)

E. Pankert, F. Scharbert, C. Wallerius, K. Meerholz. *Structure-Property Studies of N-Phenyl-phthalimide based Donor-Acceptor Compounds and their Implementation in Solution Processed Organic Light-Emitting Diodes*. TIDE Conference, Cologne, Germany, 2024. (Poster)

E. Pankert, J. Wiefermann, J. Kaminski, D. Hertel, C. Marian, T.J.J. Müller, K.Meerholz. *Highly Luminescent Blue Emitter with Balanced Hybridized Locally and Charge-Transfer Excited-States Emission*. Optical Probes, Como, Italy, 2023. (Talk & Poster)

E. Pankert, K. Singh Ghorta, C. Wallerius, K. Meerholz. *Investigation of Thermally Activated Ring-Opening of Photochromic Dithienylethenes in Organic Light-Emitting Memory Diodes*. ICSM, Glasgow, UK, 2022. (Poster)